Planetary cooling, tectonics, and weathering from 1 billion years ago to the present

by

Yuem Park

A dissertation submitted in partial satisfaction of the

requirements for the degree of

Doctor of Philosophy

in

Earth & Planetary Science

in the

Graduate Division

of the

University of California, Berkeley

Committee in charge:

Professor Nicholas L. Swanson-Hysell, Chair
Professor Daniel A. Stolper
Professor Seth Finnegan

Fall 2020

Planetary cooling, tectonics, and weathering from 1 billion years ago to the present

Abstract

Planetary cooling, tectonics, and weathering from 1 billion years ago to the present

by

Yuem Park

Doctor of Philosophy in Earth & Planetary Science

University of California, Berkeley

Professor Nicholas L. Swanson-Hysell, Chair

Over the past one billion years, Earth's climate has fluctuated between three stable states on million year time-scales: a warm state in which the poles are ice-free, a cold state in which finite ice caps exist at the poles, and a "snowball" state in which ice sheets extended to the equator. Changes in global weatherability could be responsible for driving transitions between these climate states by modulating the atmospheric CO_2 concentration (pCO_2) at which CO_2 input from volcanism into Earth's ocean/atmosphere system is removed via silicate weathering. Since the presence of mafic and ultramafic rocks in the warm and wet tropics increases global weatherability, it has both been hypothesized that island arc exhumation and large igneous province eruption at low latitudes have driven cooling on million year time-scales. In the chapters presented in this dissertation, I evaluate these two hypotheses.

In Chapter 1, we reconstruct the paleogeographic position of major arc-continent collisions and large igneous provinces to assess whether a first-order correlation between these two tectonic settings and changes in Earth's climate state can be established for the Phanerozoic. Arc-continent collisions are quantified as the length of sutures that are active at any given time, and large igneous provinces are quantified as the area of surface volcanics remaining following eruption after a parameterization of erosion has been applied. The latitudinal distribution of continental ice sheets is used as a proxy for Earth's climate state. Our analyses reveal a strong correlation between active suture length in the tropics and the extent of glaciation, and no significant correlation between large igneous province area in the tropics and the extent of glaciation. The key difference between large igneous provinces and active orogens involving island arcs is continuous exhumation and the creation of steep topography in the orogens. Therefore, our results suggest that changes in Earth's climate state are primarily driven by island arc exhumation in the tropics due to the combination of mafic and ultramafic lithologies, a warm and wet tropical environment, high erosion rates, and a lack of thick regoliths in this tectonic setting. In contrast, large igneous provinces

have low erosion rates and develop thick regoliths, dampening their influence on global weatherability and Earth's climate state.

However, this correlation between arc-continent collisions in the tropics and Earth's climate state over the Phanerozoic does not necessitate causation. The magnitude of decrease in steady-state pCO_2 associated with specific instances of arc-continent collision in the tropics needs to be quantified. Ongoing arc–continent collision in the tropical Southeast Asian islands has increased the area of subaerially exposed land in the region since the mid-Miocene. Concurrently, Earth's climate has cooled since the Miocene Climatic Optimum, leading to growth of the Antarctic ice sheet and the onset of Northern Hemisphere glaciation. In Chapter 2, we compile paleoshoreline data and incorporate them into a numerical model that couples a global climate model to a silicate weathering model with spatially resolved lithology. We find that without the increase in area of the Southeast Asian islands over the Neogene, pCO_2 would have been significantly higher than pre-industrial values, remaining above the levels necessary for initiating Northern Hemisphere ice sheets.

As such, there is accumulating evidence that supports the notion that transitions between ice-free and ice-cap climate states is primarily driven by island arc exhumation in the tropics. However, it remains unclear whether transitions into the snowball climate state are driven by the same mechanism. In Chapter 3, we investigate the Tonian-Cryogenian Tambien Group of northern Ethiopia – a mixed carbonate-siliciclastic sequence that culminates in glacial deposits associated with the ca. 717–660 Ma Sturtian "Snowball Earth." The presence of intercalated tuffs suitable for high-precision geochronology within the Tambien Group enable temporal constraints on stratigraphic data sets of the interval preceding, and leading into, the Sturtian glaciation. $\delta^{13}C$ and $^{87}Sr/^{86}Sr$ data and U-Pb chemical abrasion isotope dilution thermal ionization mass spectrometry (CA-ID-TIMS) dates from the Tambien Group are used in conjunction with previously published isotopic and geochronologic data to construct newly time-calibrated composite Tonian carbon and strontium isotope curves. Tambien Group $\delta^{13}C$ data and U-Pb CA-ID-TIMS ages reveal that a pre-Sturtian sharp negative $\delta^{13}C$ excursion precedes the Sturtian glaciation by ∼18 Myr and is followed by a prolonged interval of positive $\delta^{13}C$ values, suggesting that perturbations to the carbon cycle that lead to sharp negative $\delta^{13}C$ excursions are unrelated to the initiation of the Sturtian glaciation. The composite Tonian $^{87}Sr/^{86}Sr$ curve shows that, following an extended interval of low and relatively invariant values, inferred seawater $^{87}Sr/^{86}Sr$ rose ca. 880–770 Ma, and then decreased to the ca. 717 Ma initiation of the Sturtian glaciation. These data, when combined with a simple global weathering model and analyses of the timing and paleolatitude of large igneous province eruptions and island arc exhumation events, suggest that the $^{87}Sr/^{86}Sr$ increase was influenced by increased subaerial weathering of radiogenic lithologies as the (super)continent Rodinia rifted apart at low latitudes. While interpretations of $^{87}Sr/^{86}Sr$ data are non-unique, the following $^{87}Sr/^{86}Sr$ decrease is consistent with enhanced subaerial weathering of island arc lithologies accreting in the tropics within the assembling Arabian-Nubian Shield over tens of millions of years, lowering pCO_2 and contributing to the initiation

of the Sturtian glaciation.

However, a lack of paleomagnetic data to constrain the paleolatitude and configuration of tectonic blocks during the Tonian, especially those associated with island arc exhumation, hampers efforts to quantify changes in global weatherability during the lead up to the Sturtian glaciation. For example, a series of arc terranes were exhumed as the Yangtze and Cathaysia blocks that make up South China collided in the Tonian. However, the timing and paleolatitude of this collision is poorly constrained. South China's association with Rodinia is also a matter of debate, with competing models variably placing the block at the core or periphery of Rodinia, or separated from it entirely. Tonian paleogeographic models also vary in whether they incorporate proposed large and rapid oscillatory true polar wander associated with the ca. 810–795 Ma Bitter Springs Stage. In Chapter 4, we develop new paleomagnetic data paired with U-Pb CA-ID-TIMS geochronology from the Tonian Xiajiang Group in South China to establish the block's position and test the Bitter Springs Stage true polar wander hypothesis. The data constrain folding associated with the collision of the Yangtze and Cathaysia blocks to have occurred between ca. 830 and 816 Ma. The data also constrain South China to high latitudes ca. 813 Ma, and when considered in conjunction with other paleomagnetic poles from South China, indicate a relatively stable high-latitude position ca. 821–805 Ma. Together, these geochronologic and paleomagnetic constraints indicate that island arc exhumation associated with the collision of the Yangtze and Cathaysia blocks occurred at high latitudes ∼100 m.y. before the onset of the Sturtian glaciation and ∼50 m.y. before marine $^{87}Sr/^{86}Sr$ started to decrease. This result is consistent with the hypothesis that island arc exhumation needs to occur in the warm and wet tropics to have a significant impact on global weatherability and Earth's climate state. Additionally, the difference in pole position between the pre-Bitter Springs Stage Xiajiang Group pole and the syn-Bitter Springs Stage Madiyi Formation pole is significantly less than that predicted for the Bitter Springs Stage true polar wander hypothesis. These constraints place the craton at higher latitudes connected to Rodinia along its periphery, or disconnected from Rodinia entirely. If this pole difference is interpreted as true polar wander superimposed upon differential plate motion, it requires South China to have been separate from Rodinia.

Put together, we find that the exhumation of island arcs and oceanic crust during arc-continent collision and arc-accretion events in the tropics is important, and perhaps the most important, for driving shifts in Earth's climate state over the past one billion years.

Contents

List of Figures

List of Tables

Preface

The material within the chapters of this dissertation are largely taken from previously published (or soon to be published) articles. The following text identifies these articles, and provides some additional context about how they relate to one another.

Chapter 1 - Evaluating the relationship between the area and latitude of large igneous provinces and Earth's long-term climate state

Macdonald, F. A., Swanson-Hysell, N. L., Park, Y., Lisiecki, L., and Jagoutz, O., 2019, Arc-continent collisions in the tropics set Earth's climate state: Science, vol. 364, pp. 181–184, doi: 10.1126/science.aav5300

Park, Y., Swanson-Hysell, N. L., Macdonald, F. A., and Lisiecki, L., 2019, Evaluating the relationship between the area and latitude of large igneous provinces and Earth's long-term climate state: EarthArXiv, doi: 10.31223/osf.io/p9ndf

In Macdonald et al. (2019), I developed a workflow built on pyGPlates (software for the analysis of paleogeographic models) that allowed us to calculate the area/length of paleogeographically reconstructed polygons/lines within different latitude bands through time. By pairing this workflow with a database of ophiolite-bearing sutures and a paleogeographic model, we were able to identify a strong correlation between arc-continent collisions in the tropics (measured as active suture length in the tropics) and times of glacial climate over the past ∼520 m.y. This correlation led to our proposal that Earth's climate state is set primarily by global weatherability, which changes with the latitudinal distribution of arc-continent collisions. Similarly, it has been proposed elsewhere that the eruption/drift of large igneous provinces into the tropics has driven global cooling. The pyGPlates workflow that I developed provided a means through which we could evaluate this hypothesis. Park et al. (2019) builds upon the zonal large igneous province area analysis that I conducted and presented in the supplementary materials for Macdonald et al. (2019) by more rigorously developing parameterizations of large igneous province erosion and exploring several geologically reasonable large igneous province post-emplacement scenarios.

Park et al. (2019) is currently available as a preprint on EarthArXiv, but a slightly modified version of the article is scheduled to be formally published as Chapter 7 of AGU Geophysical Monograph Series 255, titled *Large Igneous Provinces: A Driver of Global Environmental and Biotic Changes*, edited by Richard E. Ernst, Alexander J. Dickson, and Andrey Bekker.

Code used to perform the analyses presented in these articles are available on GitHub at https://github.com/Swanson-Hysell-Group/Arc_Continent_Analysis and https://github.com/Swanson-Hysell-Group/2020_large_igneous_provinces, or on Zenodo at https://doi.org/10.5281/zenodo.2636731 and https://doi.org/10.5281/zenodo.3981262.

Chapter 2 - Emergence of the Southeast Asian islands as a driver for Neogene cooling

Park, Y., Maffre, P., Goddéris, Y., Macdonald, F. A., Anttila, E. S. C., and Swanson-Hysell, N. L., 2020a, Emergence of the Southeast Asian islands as a driver for Neogene cooling: Proceedings of the National Academy of Sciences, p. 202011033, doi: 10.1073/pnas.2011033117

This article was the result of a collaboration between Goddéris' and Swanson-Hysell's research groups supported by the France-Berkeley Fund. Broadly speaking, the collaboration was intended to investigate whether numerical Earth system models quantitatively support the hypothesis put forward in Macdonald et al. (2019) and Swanson-Hysell and Macdonald (2017) that tropical arc-continent collisions set Earth's climate state. The model that we use is the global spatially resolved GEOCLIM model, which estimates changes in steady-state $p\mathrm{CO}_2$ associated with coupled changes in erosion, chemical weathering, and climatology by linking a silicate weathering model to climate model runs at multiple $p\mathrm{CO}_2$ levels. In previous versions of the model, Goddéris and his collaborators parameterized silicate weathering to be a function of temperature and runoff only, and all bedrock was assigned identical chemical compositions. In a more recent version of the model, Maffre implemented regolith development and soil shielding, which introduced a dependence on erosion rate (and, therefore, topographic slope). While this introduction of regolith development into GEOCLIM is important for assessing the impact of tropical arc–continent collisions on $p\mathrm{CO}_2$, the relatively high Ca+Mg concentration in arc rocks relative to other lithologies must also be considered. Therefore, in Park et al. (2020a), I implemented variable bedrock Ca+Mg concentration into GEOCLIM and quantified the uncertainty in steady-state $p\mathrm{CO}_2$ that arises from poorly constrained model parameters.

The code for the GEOCLIM model used in this study can be found at https://github.com/piermafrost/GEOCLIM-dynsoil-steady-state/releases/tag/v1.0. The code that generated the inputs and analyzed the output of the GEOCLIM model can be found at https://github.com/Swanson-Hysell-Group/2020_Southeast_Asian_Islands or https://doi.org/10.5281/zenodo.4021653.

Chapter 3 - The lead-up to the Sturtian Snowball Earth: Neoproterozoic chemostratigraphy time-calibrated by the Tambien Group of Ethiopia

MacLennan, S. A., Park, Y., Swanson-Hysell, N. L., Maloof, A. C., Schoene, B., Gebreslassie, M., Antilla, E., Tesema, T., Alene, M., and Haileab, B., 2018, The arc of the Snowball: U-Pb dates constrain the Islay anomaly and the initiation of the Sturtian glaciation: Geology, vol. 46, pp. 539–542, doi: 10.1130/G40171.1

Park, Y., Swanson-Hysell, N. L., MacLennan, S. A., Maloof, A. C., Gebreslassie, M., Tremblay, M. M., Schoene, B., Alene, M., Anttila, E. S., Tesema, T., and Haileab, B., 2020b, The lead-up to the Sturtian Snowball Earth: Neoproterozoic chemostratigraphy time-calibrated by the Tambien Group of Ethiopia: GSA Bulletin, vol. 132, pp. 1119–1149, doi: 10.1130/b35178.1

Chronologically, the work that lead to MacLennan et al. (2018) and Park et al. (2020b) largely preceded the projects presented in Chapters 1 and 2. In MacLennan et al. (2018), we presented the initial geochronologic results that placed temporal constraints on large excursions in the marine $\delta^{13}C$ record and the initiation of the Sturtian glaciation in a short-format journal. Park et al. (2020b) built upon this work by: thoroughly documenting the geology of the Tambien Group in northern Ethiopia (including the discovery of vast areas of exposures of Sturtian glacial deposits and underlying strata near the town of Samre), presenting additional geochronologic results, assessing diagenesis in carbonate samples, presenting the complete $\delta^{13}C$ and $^{87}Sr/^{86}Sr$ data from the Tambien Group, developing a composite Tonian-Cryogenian $\delta^{13}C$ and $^{87}Sr/^{86}Sr$ chemostratigraphic record, and proposing a model for the initiation of the Sturtian glaciation based on the composite $^{87}Sr/^{86}Sr$ chemostratigraphic record, a simple global weathering model, and analyses of the timing and paleolatitude of large igneous province eruptions and arc accretion events. As in Swanson-Hysell and Macdonald (2017) and Macdonald et al. (2019), the model for the initiation of the Sturtian glaciation proposed in Park et al. (2020b) called upon island arc exhumation in the tropics, and was part of the motivation to initiate a collaboration with Goddéris' research group.

Code used to perform the analyses presented in these articles is available on GitHub at https://github.com/Swanson-Hysell-Group/2019_Tambien_Group, or on Zenodo at https://doi.org/10.5281/zenodo.3403180.

Chapter 4 - Tonian paleomagnetism from South China permits an inclusive Rodinia or Bitter Springs Stage true polar wander, but not both

Park, Y., Swanson-Hysell, N. L., Xian, H., Zhang, S., Condon, D. J., Fu, H., and Macdonald, F. A., submitted, Tonian paleomagnetism from South China permits an inclusive Rodinia or Bitter Springs Stage true polar wander, but not both: Journal of Geophysical Research: Solid Earth

Although Park et al. (2020b) called upon island arc exhumation in the tropics as a critical tectonic boundary condition that allowed for the Sturtian glaciation to take place, a lack of paleomagnetic data to constrain the paleolatitude and configuration of tectonic blocks during the Tonian hampers efforts to quantify changes in global weatherability associated with island arc exhumation during the lead up to the Sturtian glaciation. Park et al. (submitted) develops paleomagnetic data to better constrain the location of one of these tectonic blocks, South China, in the Tonian. South China is a particularly important block to investigate with paleomagnetic data in the context of the Sturtian glaciation because arc-continent collisions are hypothesized to have occurred both within and along the margin of the block during the Tonian. Furthermore, sediments from which paleomagnetic data can be developed exist in South China that span a hypothesized major global tectonic event (Bitter Springs Stage true polar wander) that, if real, has far-reaching implications for the paleogeography of the time.

Park et al. (submitted) has been submitted to the *Journal of Geophysical Research: Solid Earth* for review.

Code used to perform the analyses presented in this study is available on GitHub at https://github.com/Swanson-Hysell-Group/Banxi_Paleomagnetism.

Acknowledgments

None of what is presented in this dissertation would have been possible without the support of innumerable people. It would be impossible to list every one of these people here, but nevertheless I note some of the individuals who were key to making the research possible below.

I sincerely appreciate the expert guidance and advice from the professors with whom I worked to push the research forward throughout the years: Mulugeta Alene, Dan Condon, Seth Finnegan, Yves Goddéris, Bereket Haileab, Oli Jagoutz, Lorraine Lisiecki, Francis Macdonald, Adam Maloof, Blair Schoene, Daniel Stolper, and Shihong Zhang.

I thank my graduate student and post-doc collaborators, the Swanson-Hysell Group, and my Ph.D. class, not only for discussing research with me, but also for being great friends: Eliel Anttila, Maggie Avery, Alex Charn, Luke Fairchild, Isabel Fendley, Hairuo Fu, Mulubrhan Gebreslassie, Blake Hodgin, Taylor Kilian, Jinsol Kim, Tanis Leonhardi, Nate Lindsey, Scott MacLennan, Pierre Maffre, Alex Robson, Allison Sharrar, Sarah Slotznick, Tadele Tesema, Marissa Tremblay, Hanbiao Xian, and Yiming Zhang.

I thank the EPS staff for dealing with the logistics of research and being a graduate student: Rachel Kowalik and Margie Winn.

And of course a big thank you to the rest of the undergraduate students, graduate students, post-docs, staff, and faculty in the Department of Earth & Planetary Science at UC Berkeley and elsewhere, who I didn't have the chance to list here.

In terms of the non-Earth Science people in my life, I thank my friends and my partner Yudith Dian for putting up with me through the years. And of course a huge thank you to my family, who dedicated everything to raising me and getting me to where I am today.

Finally, and most importantly, thank you to my advisor Nick Swanson-Hysell, for accepting me into the program to begin with and then tirelessly mentoring me throughout the years. I'm endlessly appreciative that I was able to work with him and learn from him, and honestly I don't think I could have asked for a better advisor. As his first graduating Ph.D. student, I hope that I didn't set the bar too low for those to follow.

Chapter 1

Evaluating the relationship between the area and latitude of large igneous provinces and Earth's long-term climate state

1.1 Abstract

One of the hypothesized effects of large igneous provinces (LIPs) is planetary cooling on million-year timescales associated with enhanced silicate weathering of freshly-emplaced basalt. This study combines reconstructions of the original surface extent and emplacement ages of LIPs, a paleogeographic model, and a parameterization of LIP erosion to estimate LIP area in all latitudinal bands through the Phanerozoic. This analysis reveals no significant correlation between total LIP area, nor LIP area in the tropics, and the extent of continental ice sheets. The largest peaks in tropical LIP area are at times of non-glacial climate. These results suggest that changes in planetary weatherability associated with LIPs are not the fundamental control on whether Earth is in a glacial or non-glacial climate, although they could provide a secondary modulating effect in conjunction with other processes $p\mathrm{CO}_2$.

1.2 Introduction

Global weatherability is the sum of factors aside from climate itself that contribute to overall global weathering and associated CO_2 consumption, such as the latitudinal distribution of continents and mountain belts (Kump and Arthur, 1997). On a planet with high weatherability, the CO_2 input from volcanism can be removed via silicate weathering at a lower atmospheric CO_2 concentration than on a less weatherable planet. Basaltic regions consume more CO_2 than regions where the bedrock composition is closer to bulk continental crust because mafic lithologies have relatively high concentrations of Ca and Mg (that ultimately

sequester carbon through precipitation as carbonate), constitute minerals with relatively high reactivity (Gislason and Oelkers, 2003), and have relatively high weathering rates (Dessert et al., 2003; Ibarra et al., 2016). Furthermore, data from basaltic watersheds show that chemical weathering rates are highest in regions with high runoff and temperature. As a result, CO_2 consumption in basaltic regions is most pronounced in the tropical rain belt (Dessert et al., 2003; Hartmann et al., 2009, 2014).

One aspect of large igneous province (LIP) emplacement that has been hypothesized to relate to long-term global climate is the effect that associated mafic lithologies could have on increasing global weatherability and driving cooling. In particular, the emplacement of LIPs in the tropics has been hypothesized to be associated with specific episodes of climatic cooling on Earth. In the Neoproterozoic, the emplacement of the ca. 720 Ma Franklin LIP in the tropics, in concert with elevated runoff rates associated with supercontinent break-up, has been implicated as a major contributor to the cooling that initiated the Sturtian 'Snowball Earth' (Donnadieu et al., 2004a; Macdonald et al., 2010; Cox et al., 2016). In the Cenozoic, the movement of the Deccan LIP into the tropical rain belt, together with the low-latitude emplacement of the Ethiopian Traps, has been implicated in drawing down CO_2 levels in the lead-up to Oligocene glaciation of Antarctica (Kent and Muttoni, 2008, 2013). More recently, Johansson et al. (2018) used paleogeographic reconstructions to suggest that tropical LIP area correlates with Phanerozoic climate change through comparison with a pCO_2 proxy compilation.

This chapter seeks to address two interconnected questions: 1) how unique are the peaks in low-latitude LIP area that have been proposed to be associated with climatic cooling?; and 2) how strong is the overall relationship between tropical LIP area and glaciation?

1.3 Methods

This study combines reconstructions of the original surface extent and emplacement ages of LIPs, a paleogeographic model, and a parameterization of LIP erosion to estimate LIP area in all latitudinal bands through the Phanerozoic. We then compare these time series of zonal LIP area to the latitudinal extent of continental ice sheets - a proxy for Earth's long term climate state. This study builds upon a zonal LIP area analysis presented in the supplementary materials for Macdonald et al. (2019) by more rigorously developing parameterizations of LIP erosion and exploring several geologically reasonable LIP post-emplacement scenarios.

Outlines of the original surface extent of continental LIPs through the Phanerozoic (Fig. 1.1) were slightly modified (to ensure that all currently exposed volcanic lithologies are encapsulated by the initial LIP area polygons) from the compilation of Ernst and Youbi (2017) and Ernst et al. (2019), and emplacement ages were taken from the literature (Table 1.1). The LIP original surface extent compilation seeks to reconstruct the original surface extent of LIPs with the caveat that there can be significant uncertainty with doing so, particularly for older more deeply eroded LIPs. These polygons encapsulate all of the preserved rocks asso-

Table 1.1: Phanerozoic large igneous provinces (and the Franklin).

name	age (Ma)	age ref.	original[1] area (Mm^2)	present[2] area (Mm^2)	present area ref.	present/[3] original	half-life[4] (Myr)	buried?
Columbia River	16	Kasbohm and Schoene (2018)	0.68	0.38	Buchan and Ernst (2004)	0.56	19.2	no
Afar	30	Courtillot and Renne (2003)	2.05	0.63	Coffin et al. (2006)	0.31	17.7	partial
NAIP	62	Larsen et al. (2015)	1.07	0.29	Buchan and Ernst (2004); Coffin et al. (2006)	0.27	33.0	partial
Deccan	66	Schoene et al. (2014)	0.83	0.56	Coffin et al. (2006)	0.68	116.6	no
Seychelles	66	Schoene et al. (2014)	0.46	0.00	Coffin et al. (2006)	0.00	0.0	yes
Madagascar	90	Cucciniello (2010)	0.63	0.03	Coffin et al. (2006)	0.05	20.8	no
Caribbean-Colombian	94	Loewen et al. (2013)	0.71	0.13	Coffin et al. (2006)	0.18	37.6	no
HALIP	95	Kingsbury et al. (2018)	3.60	0.15	Hartmann and Moosdorf (2012)	0.04	20.7	no
EQUAMP	131	Hollanda et al. (2016)	0.66	0.01	Hollanda et al. (2016)	0.01	20.5	no
Comei	132	Zhu et al. (2009)	0.11	-	-	-	-	no
Bunbury	132	Zhu et al. (2009)	0.03	0.00	Thorne et al. (2014)	0.05	30.9	no
Parana-Etendeka	135	Florisbal et al. (2014); Almeida et al. (2018)	3.12	0.40	Coffin et al. (2006)	0.13	45.7	partial
Trap	140	Ernst and Buchan (2001)	0.03	0.00	Ernst and Buchan (2001)	0.00	0.0	no
NW Australia Margin	160	Pirajno and Hoatson (2012)	0.62	0.00	Coffin et al. (2006)	0.00	0.0	yes
Karoo	183	Burgess et al. (2015)	3.21	0.15	de Kock compilation[5]	0.05	41.3	no
Ferrar	183	Burgess et al. (2015)	0.18	-	-	-	-	no
CAMP	201	Blackburn et al. (2013)	11.46	0.23	Marzoli and Parisio compilation[6]	0.02	35.7	partial
Siberia	252	Burgess and Bowring (2015)	3.46	0.47	Coffin et al. (2006)	0.14	87.5	no
Emeishan	259	Zhou et al. (2002)	0.71	0.06	Coffin et al. (2006)	0.09	72.9	no
Panjal-Qiangtang	283	Zhai et al. (2013)	0.11	-	-	-	-	no
Tarim	290	Xu et al. (2014)	0.35	-	-	-	-	no
Magdalen	360	Murphy et al. (1999)	0.42	-	-	-	-	no
Vilyui	374	Ricci et al. (2013)	1.14	-	-	-	-	no
Kola-Dnieper	380	Arzamastsev and Wu (2014)	5.90	-	-	-	-	no
Suordakh	450	Khudoley et al. (2013)	0.02	-	-	-	-	no
Kalkarindji	511	Jourdan et al. (2014)	3.54	0.17	Thorne et al. (2014)	0.05	116.3	no
Franklin	720	Denyszyn et al. (2009)	2.62	0.04	Buchan and Ernst (2004)	0.02	121.8	no

[1]obtained via calculating the area of the continental portions of polygons within the LIP original surface extent compilation of Ernst and Youbi (2017) and Ernst et al. (2019), shown as blue polygons in Fig. 1.1.

[2]obtained via calculating the area of polygons from the noted reference of presently-exposed volcanics associated with LIPs, shown as orange polygons in Fig. 1.1.

[3]present area / original area

[4]assuming exponential decay with form $N(t) = 2^{t/t_{1/2}}$.

[5]from ArcGIS compilation produced by M. de Kock for the LIPs Reconstruction Project (Ernst et al., 2013).

[6]from ArcGIS compilation produced by A. Marzoli and L. Parisio for the LIPs Reconstruction Project (Ernst et al., 2013).

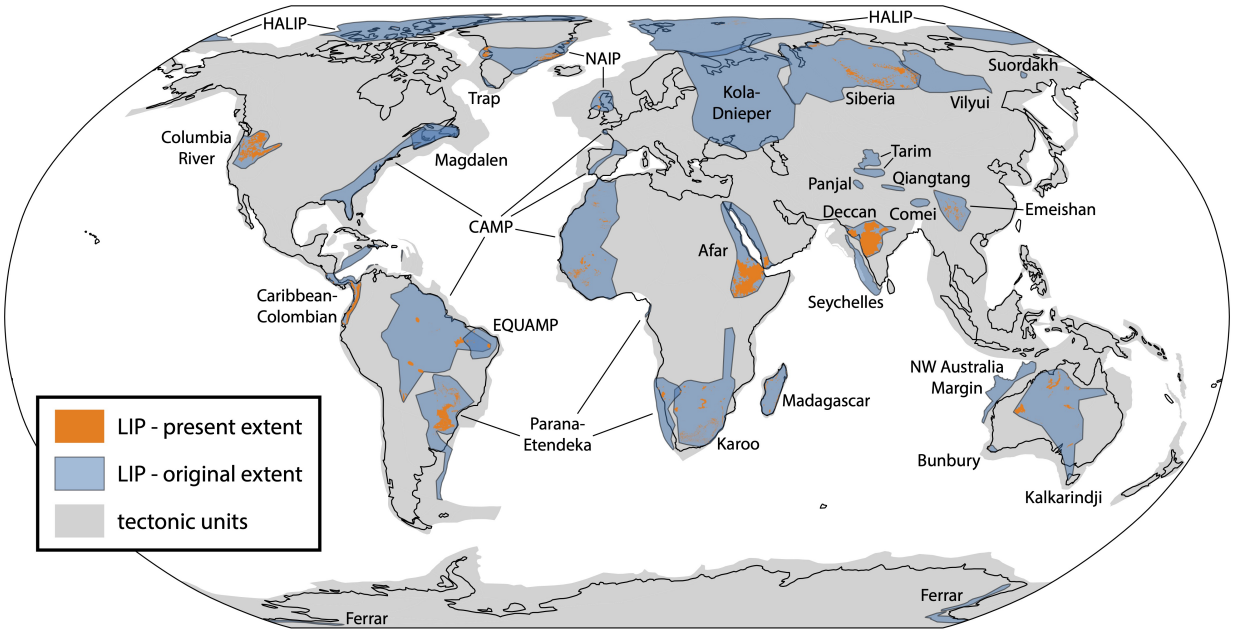

Figure 1.1: Map of current surface extent of volcanic lithologies associated with LIPs that erupted between 520 Ma and the present, as well as the estimates of the initial LIP surface extent used in the area analysis (modified slightly from Ernst and Youbi, 2017 and Ernst et al., 2019 to ensure that all currently exposed volcanic lithologies are encapsulated by the initial LIP surface area polygons).

ciated with a given LIP, including dikes, sills, and layered intrusions, in addition to subaerial volcanics (Fig. 1.1). For some LIPs, this approach may lead to an over-estimate of original surface extent, given that subsurface intrusions could extend over a broader area than the surface volcanics. The polygons also assume complete surface coverage between wide-spread remnants, creating further potential for these original extent outlines to be over-estimates. These original extent outlines could also under-estimate the surface area for some LIPs where flows have been eroded and feeder dikes are not exposed or poorly documented. However, despite these uncertainties, this approach likely provides the best estimates available of original surface extent for ancient LIPs. The extents of presently-exposed volcanics associated with LIPs that were used for present-day area estimates (Fig. 1.1) and the sources that went into the construction of the original extent polygons by Ernst and Youbi (2017) and Ernst et al. (2019) were taken from a number of resources including the PLATES compilation (Coffin et al., 2006) and more recent compilation efforts associated with the LIPs Reconstruction Project (Ernst et al., 2013; Table 1.1).

After LIPs are emplaced, they progressively erode. In order to account for the associated decrease in area with time, Goddéris et al. (2017b) took the approach of fitting an exponential decay function to estimates of the original surface extent and the current surface extent of 5 LIPs. They used the resulting exponential decay constants to develop a first-order

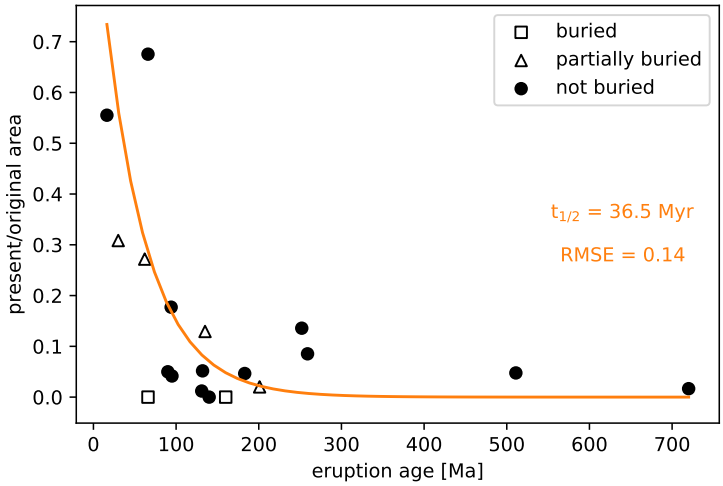

Figure 1.2: LIP erosion through time. The ratio of estimates of the present-day surface area to that of the original surface area are shown for 19 basaltic LIPs. An exponential fit is made to the 13 basaltic LIPs that are interpreted to not have been buried after emplacement (Table 1.1), which yields a half-life of ∼36 Myr. RMSE = root mean square error.

parameterization of changing LIP area through time. We extend this approach to 19 basaltic LIPs for which there are estimates of the original surface extent of the province and the current surface extent of rocks associated with the province (Fig. 1.2). While there are significant uncertainties associated with the area estimates, this compilation suggests that an exponential decay function is an appropriate first-order representation of the progressive reduction in LIP area (Fig. 1.2). The best-fit exponential function results in a LIP area half-life of 29 Myr. However, since we explicitly account for LIP burial separately in our area analysis (see below), we exclude from our estimation of a representative LIP area half-life the 6 of 19 LIPs which are inferred to have been partially or completely buried. This latter approach yields a slightly longer best-fit half-life of 36 Myr (Fig. 1.2). Although the exponential fit to the 13 unburied LIPs is good (i.e. it yields a low root mean square error of 0.14), if each LIP is fit individually with an exponential decay function, there is variability in the estimated half-lives from ∼20 Myr up to ∼120 Myr for the Deccan Traps (Table 1.1). In the analysis of LIP area through time, we implement decay scenarios informed by these results: the '$t_{1/2}$ = 36 Myr' scenario uses the best-fit half-life of 36 Myr, while the '$t_{1/2}$ = 120 Myr' scenario uses the slower decay. Given that the post-emplacement weathering and erosional history of each LIP should be dependent on the tectonic and climatic setting that each LIP experiences during and after emplacement, this approach is simplistic, but it provides a framework for analysis. The LIP reconstructions used in this study also include pre-Phanerozoic LIPs. However, given the imposed exponential decay since emplacement, the inclusion of these LIPs does not significantly influence the calculated LIP areas through

the Phanerozoic, which is the focus of this analysis.

Of the tectonic factors that could alter exposed LIP area, the most consequential is near-immediate burial by sediment of LIP volcanics that are co-located with a rift basin. There are numerous examples in the record where there is partial or complete burial of a LIP associated with rifting and thermal subsidence (Table 1.1). For example, the Afar LIP is both associated with the Ethiopian Traps which form plateau flood basalts as well as successful rifting in the region of the Red Sea that has resulted in burial (Fig. 1.1). To account for the rapid decrease in exposed surface area that would result from burial by sediments in a rift basin, we impose two different burial scenarios for LIPs that are co-located with rifting. The '50% burial' scenario imposes instantaneous burial of 50% of the LIP area while the '100% burial' imposes instantaneous burial of the entire LIP as an end-member scenario. A limitation of our treatment of LIPs that are co-located with rifting is that we 'bury' all of these LIPs instantly at the time of emplacement and to the same degree when in fact the degree and timing of burial of these LIPs may vary substantially. The LIP area analysis uses all of the available combinations of the distinct decay and burial scenarios described above.

Our LIP reconstruction differs from that of Johansson et al. (2018). In contrast to the decay and decay+burial scenarios implemented on estimates of original LIP extent in this study, Johansson et al. (2018) uses a static extent for each LIP throughout the reconstruction. In their analysis, some of the polygons correspond to the present-day surface extent and some represent the original extent that includes currently buried portions of the LIP. An example of this treatment is the Keweenawan Midcontinent Rift for which the implemented extent in Johansson et al. (2018) is from geophysical data that largely corresponds to buried subsurface exposures.

The original surface extent LIP polygons were assigned a plate ID corresponding to a tectonic unit on Earth using the polygons of Torsvik and Cocks (2016) for the Phanerozoic. The LIP polygons and tectonic units were reconstructed from 520 Ma to the present (e.g. Fig. 1.5) utilizing the paleogeographic model of Torsvik and Cocks (2016) in the spin axis reference frame (anchor plate ID of 1). This paleogeographic model was updated to include revisions to Ordovician Laurentia (Swanson-Hysell and Macdonald, 2017) and Paleozoic Asia (Domeier, 2018). Reconstructions and area calculations within latitude bands utilized the pyGPlates function library and custom Python scripts. The total LIP area and the LIP area reconstructed within the tropical rain belt were calculated for the various decay and burial scenarios at a resolution of 5 Myr (Fig. 1.4B and C). All the data and code necessary to reproduce the analyses and figures presented in this study can be downloaded from GitHub (https://github.com/Swanson-Hysell-Group/2020_large_igneous_provinces) or Zenodo (https://doi.org/10.5281/zenodo.3981262).

The ascent of air near the equator associated with Earth's large-scale Hadley circulation promotes precipitation and leads to a low-latitude band of high rainfall known as the tropical rain belt. In contrast, the descending branches of the Hadley circulation in the subtropics are associated with aridity (Manabe, 1969). We use 15° S to 15° N as a working definition of the tropical rain belt, as these latitudes approximately correspond with a sharp increase in zonal mean precipitation when approaching the equator to values greater than 1.0 m/yr in

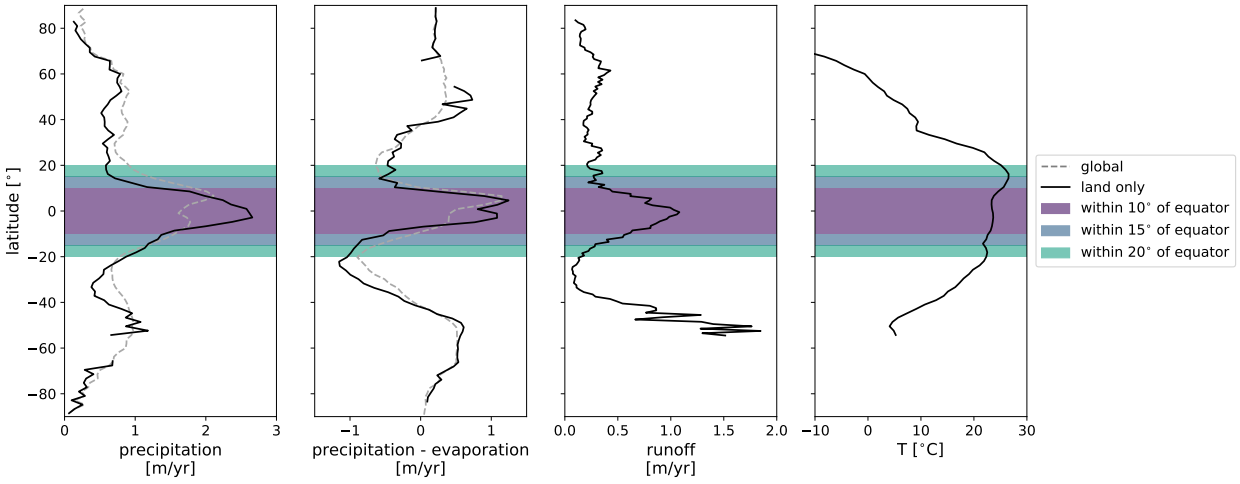

Figure 1.3: Zonally averaged modern climatological data used to define the tropical rain belt. The global precipitation (Kalnay et al., 1996) and precipitation minus evaporation (Trenberth et al., 2011) data include land and ocean pixels, global temperature data (Kalnay et al., 1996) are from land only, and runoff data (Fekete et al., 1999) are from land only excluding Antarctica. The peak in runoff ∼-50° is due to anomalously high orographically-induced runoff in the southern Andes, which represents almost all of the land in that latitude belt. Temperature data for Antarctica are off scale. Precipitation, precipitation minus evaporation, and runoff all increase sharply between ±10° and ±15°.

Table 1.2: Statistics of correlation between large igneous province area and ice extent.

	within tropics ±15°				total[5]				within tropics ±10°				within tropics ±20°			
	correlation[1]		% overlap[2]		correlation		% overlap		correlation		% overlap		correlation		% overlap	
scenario	val.[3]	p-val.[4]	val.	p-val.	val.	p-val.	val.	p-val.	val.	p-val.	val.	p-val.	val.	p-val.	val.	p-val.
$t_{1/2}$ = 36 Myr	-0.19	0.81	13	0.94	-0.26	0.85	30	0.95	-0.22	0.86	13	0.95	-0.17	0.77	9	0.96
$t_{1/2}$ = 36 Myr + 50% burial	-0.14	0.73	22	0.85	-0.25	0.84	52	0.97	-0.17	0.79	9	0.90	-0.10	0.67	26	0.86
$t_{1/2}$ = 36 Myr + 100% burial	-0.02	0.45	22	0.65	-0.14	0.74	65	0.94	-0.08	0.54	9	0.76	0.04	0.37	22	0.65
$t_{1/2}$ = 120 Myr + 100% burial	0.10	0.32	35	0.72	0.00	0.51	100	1.00	0.02	0.40	26	0.77	0.19	0.24	48	0.66

[1]Pearson correlation coefficient between LIP area and the actual ice extent record.

[2]% of time when both LIP area is >30% of the maximum and ice extent is >10° from the poles.

[3]'val.' refers to the computed correlation coefficient/% overlap between LIP area and the actual ice extent record.

[4]'p-val.' refers to the fraction of randomly timed glacial interval simulations that correlate/overlap better with LIP area than the actual ice extent record (i.e. the p-value with respect to the null hypothesis of no correlation/overlap). P-values <0.05 indicate that we can reject the null hypothesis at the 95% confidence level.

[5]all latitudes.

modern climatalogical data (Kalnay et al., 1996; Fig. 1.3). Other parameters that could be

used to define the tropical rain belt are runoff and precipitation minus evaporation (P–E). When approaching the equator in modern climatological data, zonal mean runoff sharply increases to values above 0.25 m/yr between approximately ±10° and ±15° (Fekete et al., 1999; Fig. 1.3), and zonal mean P–E sharply increases to values above 0.5 m/yr also between approximately ±10° and ±15° (Trenberth et al., 2011; Fig. 1.3). While seasonally high precipitation within ±15° of the equator associated with migration of the intertropical convergence zone could be a driver of high chemical weathering, annual mean runoff is often the value that is used within parameterizations of chemical weathering (e.g. West, 2012). Using runoff or P–E favors a definition of the tropical rain belt that is closer to ±10° rather than ±15°. Therefore, we tested the sensitivity of our results to the assumed width of the tropical rain belt by performing the tropical LIP area calculations with a tropical rain belt width of ±10°. We also calculated the area of LIPs within ±20° of the equator (a width that includes part of the arid subtropics) in order to account for uncertainties in the paleolatitude of LIPs in the paleogeographic model. We find that both of these additional analyses (LIP area calculated within ±10° and ±20° of the equator) yield similar results to those obtained when LIP area is calculated within ±15° of the equator (Table 1.2).

In Evans (2006), the reconstructed paleolatitudes of basins with thick, basin-wide evaporite deposition are shown to be consistently in the subtropics throughout the Phanerozoic and the Proterozoic, suggesting that the large-scale atmospheric circulation that gives rise to intense precipitation in the tropical rain belt and an arid subtropical climate is stable through time. However, subsequent work by Boucot et al. (2013) and Cao et al. (2018) has interpreted evaporite deposits to have formed at or near the equator at times in the Phanerozoic. While some of this variability could be attributed to waxing/waning of the width of the tropical rain belt as a whole, it is important to note that there can be large deviations in local precipitation from the zonal mean due to factors such as monsoon-related precipitation (Trenberth et al., 2000), or continentality (i.e. how dispersed or amalgamated the continents are) which can lead to aridity in continental interiors. For instance, much of the Early Cretaceous low-latitude evaporite deposits were formed in basins that were located deep within arid continental interiors at the time of deposition (Boucot et al., 2013; Cao et al., 2018). In contrast to Evans (2006), the compilation of evaporite deposits of Boucot et al. (2013) contains sedimentary sequences in which the occurrence of evaporitic minerals is limited (e.g. to disseminated gypsum pseudomorphs). Such limited evaporitic mineral precipitation could be attributed to seasonal evaporation that transiently led to saturation states that otherwise would not be expected for that latitude. Nevertheless, a limitation of the LIP analysis described in this study is that it does not account for deviations in local precipitation from the zonal mean (due to the infeasibility of running a highly-resolved global climate model at each time-step in the analysis). However, evaporite deposits, including those in which the occurrence of evaporitic minerals is limited, are distributed bimodally about the equator in the subtropics for the vast majority of the past ∼420 Myr (Cao et al., 2018) and overall stability of the large-scale atmospheric circulation is predicted by climate dynamics (Donohoe and Voigt, 2017). Therefore, the assumption of enhanced precipitation and runoff in the tropics throughout the Phanerozoic is warranted.

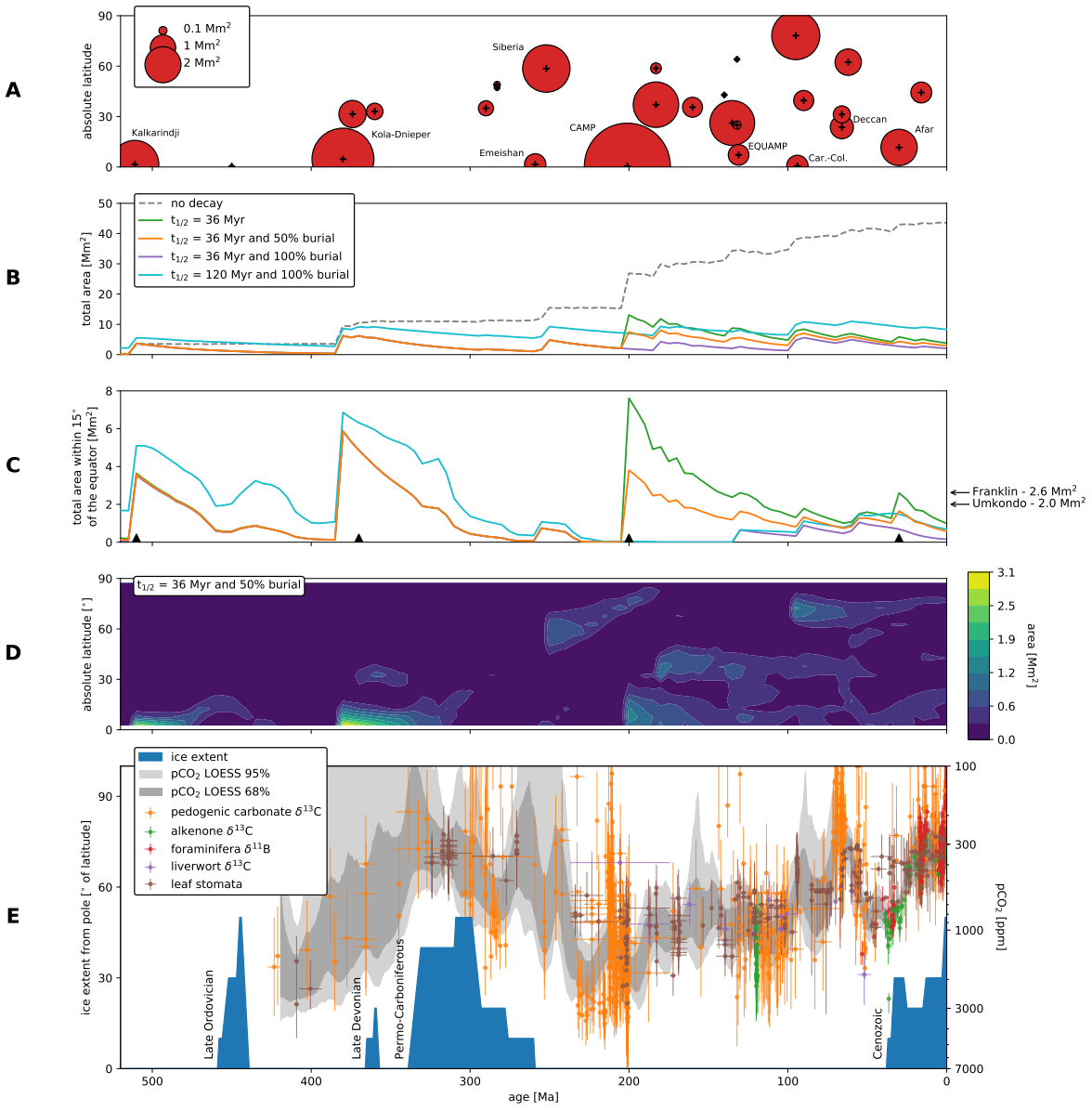

Figure 1.4: **A)** LIPs included in this analysis. The size of each circle reflects the initial surface area estimate of each LIP. The + indicates the timing and absolute paleolatitude of the centroid of each LIP at the time of emplacement. Car.-Col. = Caribbean-Colombian. **B)** Total LIP area through time for the different post-emplacent scenarios. Only the 'no decay' scenario excludes pre-Phanerozoic LIPs. **C)** Tropical LIP area through time for the different post-emplacement scenarios. The arrows to the right indicate reconstructed tropical LIP area at the time of emplacement for the ca. 720 and 1109 Ma Franklin and Umkondo LIPs. The triangles show the paleogeographic reconstruction times in Fig. 1.5. **D)** Contour plot showing the latitudinal distribution of LIP area for one of the post-emplacement models. **E)** Latitudinal extent of land ice away from the poles (Macdonald et al., 2019) and compilation of pCO_2 proxies (Foster et al., 2017) (pCO_2 y-axis reversed, and in log-scale). Error bars indicate standardized uncertainties, and grey bands indicate 68 and 95% confidence intervals for Monte Carlo resampled LOESS fits to the pCO_2 proxy data (Foster et al., 2017). Note that there are pCO_2 proxy estimates <100 ppm that are cut off in this plot.

To evaluate the relationship between Earth's climate state and total and tropical LIP area, we compared these areas to a compilation of the latitudinal extent of continental ice sheets over the Phanerozoic (Macdonald et al., 2019; Fig. 1.4E). The goal in doing so is to evaluate the hypothesis that there is a correlation between LIP area in the tropics and Earth's long-term climate state. The land ice record is an imperfect tracker of climate as it is insensitive to changes in temperature during non-glacial intervals, is influenced by additional factors such as the physical geography of the continents during glacial intervals, and is potentially vulnerable to removal from the observable geologic record via erosion and burial. Furthermore, the threshold $p\mathrm{CO}_2$ for establishing a glacial climate is dependent on ocean circulation and changing solar luminosity (e.g. Shevenell, 2004; DeConto et al., 2008). Nevertheless, it forms a physical record of Earth's climate through time and delineates glacial and non-glacial climate states. We take two approaches for comparison between the LIP area reconstructions and the record of ice extent. The first is to calculate the Pearson correlation coefficient between LIP area and the extent of ice away from the pole. The second is to consider the degree of overlap between intervals of high LIP area (defined as LIP area >30% of the maximum in a given post-emplacement model) and intervals of glacial climate (defined as ice extent >10° from the poles). This overlap approach places less emphasis on the specific magnitudes of the peaks in the compiled ice extent and LIP area records.

Another approach would be to compare the LIP area reconstructions to proxy compilations of $p\mathrm{CO}_2$ (as done by Johansson et al., 2018) instead of the latitudinal extent of continental ice sheets. However, such $p\mathrm{CO}_2$ proxies are potentially problematic as they can be difficult to calibrate in deep time and can be affected by secondary alteration. Even when stringent quality criteria and the latest understanding of each of the $p\mathrm{CO}_2$ proxies have been applied to available $p\mathrm{CO}_2$ records (Foster et al., 2017), both significant uncertainty in the estimated $p\mathrm{CO}_2$ for any given data point as well as disagreement between techniques remain (Fig. 1.4E). For instance, in the Late Triassic (∼240-200 Ma), estimates of $p\mathrm{CO}_2$ span ∼3000 ppm. Even a probabilistic approach to a large $p\mathrm{CO}_2$ proxy data set can not constrain $p\mathrm{CO}_2$ at the 95% confidence level to within a few hundred ppm for any given time interval, especially when we look deeper in time than the Cenozoic (Foster et al., 2017; Fig. 1.4E). For the pedogenic carbonate $\delta^{13}\mathrm{C}$ proxy, which forms the majority of the pre-Cenozoic data in the compilation of Foster et al. (2017), such scatter could result from diagenesis (Michel et al., 2016) and the sensitivity of the $p\mathrm{CO}_2$ estimates on assumptions regarding soil-respired CO_2 (Montañez, 2013). Nevertheless, despite these shortcomings, the $p\mathrm{CO}_2$ proxy record is broadly consistent with the ice extent record (Fig. 1.4E) - $p\mathrm{CO}_2$ proxy data decreases ∼400-310 Ma as the Late Devonian glacial interval occurs and the Permo-Carboniferous glacial interval begins and waxes, $p\mathrm{CO}_2$ proxy data roughly increases ∼310-240 Ma as the Permo-Carboniferous glacial interval wanes and ends, $p\mathrm{CO}_2$ proxy data broadly remains relatively high ∼240-40 Ma when no glacial intervals are robustly documented, and $p\mathrm{CO}_2$ proxy data roughly decreases ∼40-0 Ma as the Cenozoic glacial interval begins. Given these considerations, we thus prefer to use the latitudinal extent of land ice to reflect Earth's overall climate state throughout the Phanerozoic, despite its own limitations.

1.4 Results

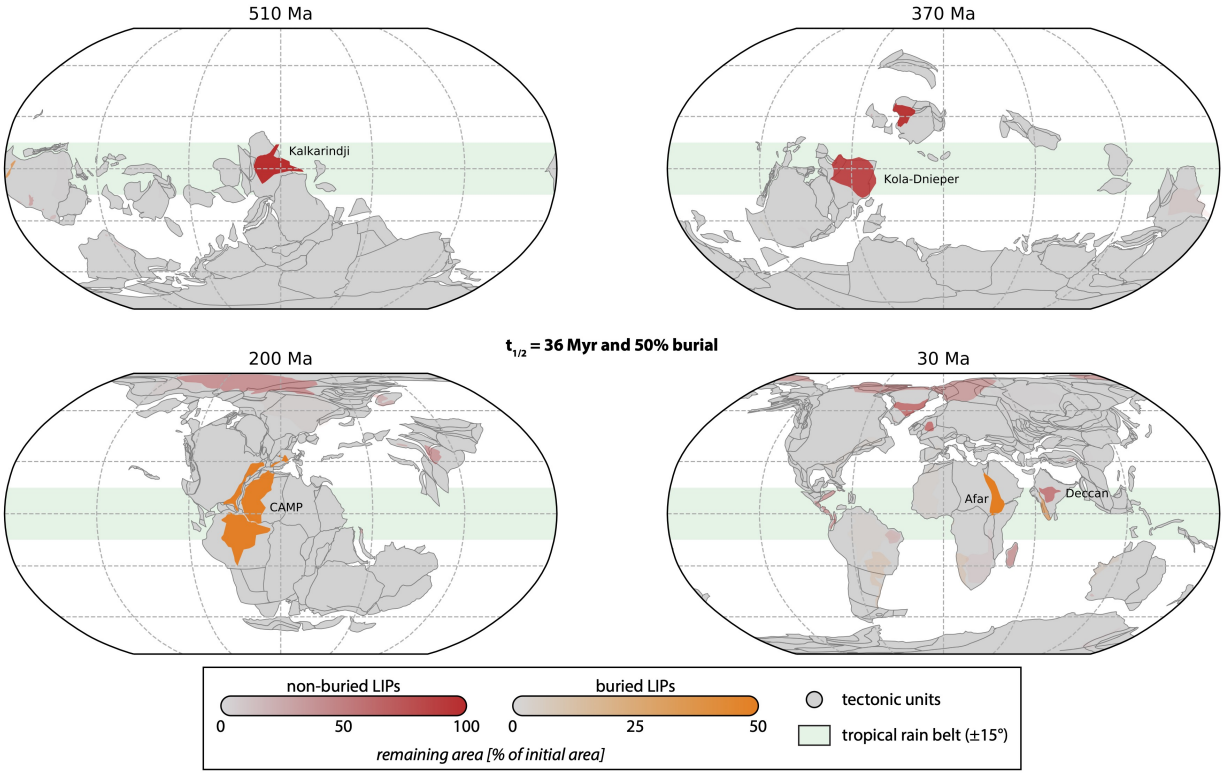

Figure 1.5: Paleogeographic reconstructions for times that correspond to peaks of LIP area in the tropics (Fig. 1.4C). The opacity of LIP polygons indicates their parameterized remaining area at the time of the reconstruction as a percentage of initial LIP area, under the preferred post-emplacement scenario of '$t_{1/2}$ = 36 Myr + 50% burial'.

In the '$t_{1/2}$ = 36 Myr' scenario, we observe four main peaks in the calculated LIP area within the tropics (Fig. 1.4C). The first peak ca. 510 Ma is associated with the emplacement of the Kalkarindji LIP, the second peak ca. 380 Ma is associated with the emplacement of the Kola-Dnieper LIP, the third peak ca. 200 Ma is associated with the emplacement of the Central Atlantic Magmatic Province (CAMP), and the fourth peak is associated with both the ca. 30 Ma emplacement of the Afar LIP as well as the earlier drift of the ca. 66 Ma Deccan LIP into the tropics (Figs. 1.4A and 1.5). When we account for burial ('$t_{1/2}$ = 36 Myr + 50% burial' and '$t_{1/2}$ = 36 Myr + 100% burial' scenarios), only the latter two of these four peaks are affected – the ca. 200 Ma peak is attenuated/removed due to the partial/complete burial of the CAMP, and the Cenozoic peak is attenuated due to the partial/complete burial of the Afar LIP. However, after accounting for burial, a minor area of LIPs remain in the tropics from ca. 130 Ma onwards, due to the Equatorial Atlantic

Magmatic Province (EQUAMP), Caribbean-Colombian, and Deccan LIPs. Using the longer decay half-life of 120 Myr (the '$t_{1/2}$ = 120 Myr + 100% burial' scenario) increases the area of LIPs in the tropics at any given time step, and has the effect of extending the duration of each peak.

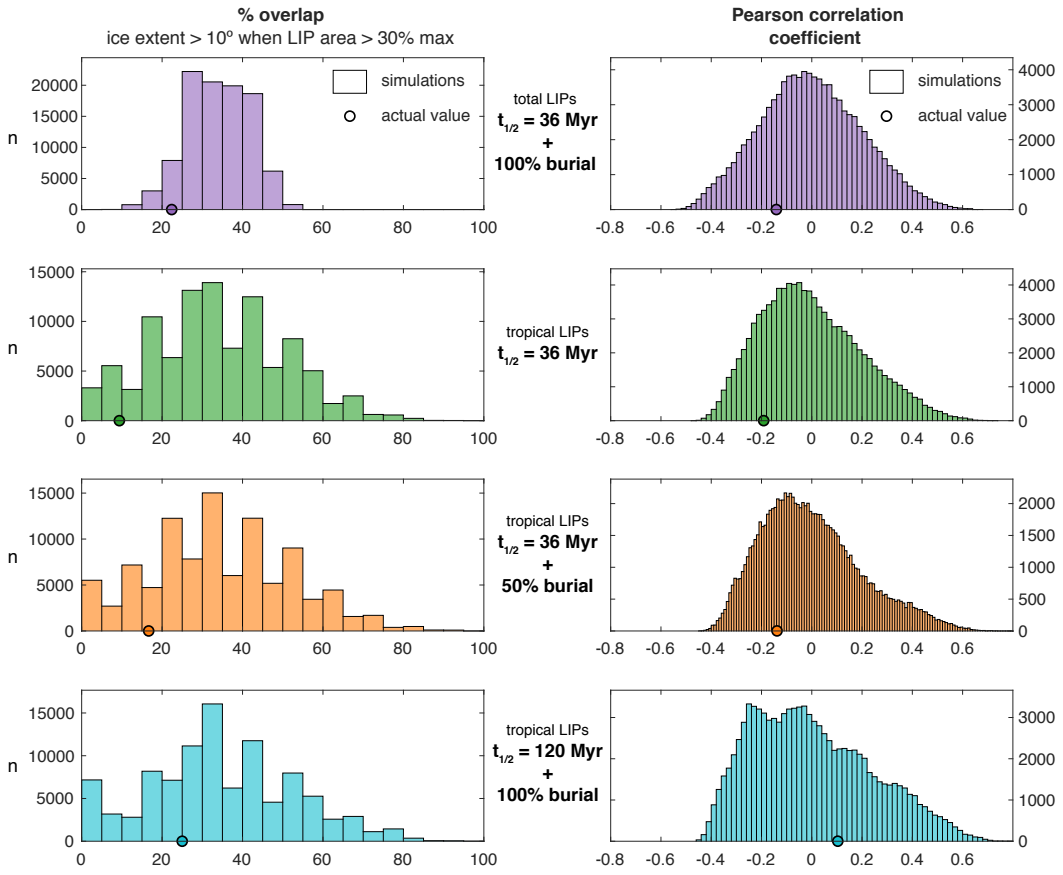

Figure 1.6: The % overlap and Pearson correlation coefficients between LIP area and the actual ice-extent record are shown with circles. These values are compared to histograms that show the range of values that arise when comparing the LIP area record to glacial intervals that have been shifted randomly in time 100,000 times. The fraction of randomly timed glacial interval simulations that correlate/overlap better with LIP area than the actual ice-extent record is the p-value shown in Table 1.2.

The only scenario which results in a non-negative Pearson correlation coefficient (0.10) between LIP area in the tropics (±15°; Fig. 1.4C) and the ice extent record (Fig. 1.4E) is the scenario with the slow decay rate and complete burial of LIPs associated with rifting (the '$t_{1/2}$ = 120 Myr + 100% burial' scenario; Fig. 1.6). All other scenarios (including both total LIP area and tropical LIP area) yield a near zero or weak negative correlation coefficient (Fig. 1.6). The weak positive correlation of the '$t_{1/2}$ = 120 Myr + 100% burial' scenario relative to the other scenarios can be primarily attributed to the complete removal of the

CAMP, which was emplaced during an extended interval of ice-free conditions, as well as the effect of the longer decay half-life extending the duration of the earlier two peaks, such that they overlap more with the Late Ordovician and Permo-Carboniferous glacial intervals.

To assess the statistical significance of the correlation implied by the Pearson correlation coefficients (or lack thereof), we applied the approach of Macdonald et al. (2019) and simulated the four glacial episodes (Fig. 1.4E) occurring at random times through the past 520 Myr, and recomputed the correlation coefficient and % overlap between the LIP area in the tropics and the randomly timed glacial intervals for each of these 100,000 simulations (Fig. 1.6). This approach accounts for the fact that spurious correlation can arise between auto-correlated data sets such as these, where each value is not independent, but is instead dependent on the previous state of the system. For the '$t_{1/2}$ = 120 Myr + 100% burial' scenario, 72% of the randomly timed glacial interval simulations correlate better with LIP area in the tropics than the actual ice extent record. With an associated p-value of 0.72, the null hypothesis that glacial intervals do not correlate to LIP area in the tropics cannot be rejected. Taking this approach, none of the positive or negative correlations that emerge between the LIP area scenarios and the ice extent record are statistically significant (Table 1.2).

1.5 Discussion

In the original models that proposed the 'Fire and Ice' hypothesis as an explanation for the onset of the Sturtian 'Snowball Earth' glaciation, chemical weathering was modeled as a function of temperature and runoff only (Donnadieu et al., 2004b). However, such an approach neglects the effects of soil shielding and regolith development in low-relief regions. Recent progress on understanding the relationships between landscapes, topography, and chemical weathering reveals that these effects are important (Gabet and Mudd, 2009; Hartmann et al., 2014; Maher and Chamberlain, 2014; Goddéris et al., 2017a). Soil shielding can lead to a transport-limited weathering regime in which the weathering rate of the underlying bedrock becomes insensitive to kinetic and equilibrium factors such as temperature and runoff - factors that would, in the absence of soil shielding, lead to relatively high weathering rates in the tropical rain belt. As a result, more recent modeling of chemical weathering incorporates such processes and highlights the importance of high-relief regions relative to low-relief ones for setting global weatherability (West, 2012; Goddéris et al., 2017a). LIPs are often emplaced in relatively low-relief areas, and as such, without active uplift, soil shielding from regolith development on these low-relief LIPs could significantly decrease the local weatherability of a LIP and mute its impact on global weatherability (as suggested in Kent and Muttoni, 2013). In this way, soil shielding could explain the lack of correlation between tropical LIP area and ice extent (Figs. 1.4 and 1.6). In contrast, processes that lead to continued exhumation of mafic lithologies and the creation of steep topography that minimizes soil shielding, particularly in tropical regions, may exert a strong control on global weatherability and long-term climate. This interpretation underlies the hypothesis

that arc-continent collisions in the tropics during the Ordovician (Swanson-Hysell and Macdonald, 2017) and the Cenozoic (Jagoutz et al., 2016) played a significant role in transitions into glacial climate states at those times - a correlation that appears robust throughout the Phanerozoic (Fig. 1.7; Macdonald et al., 2019).

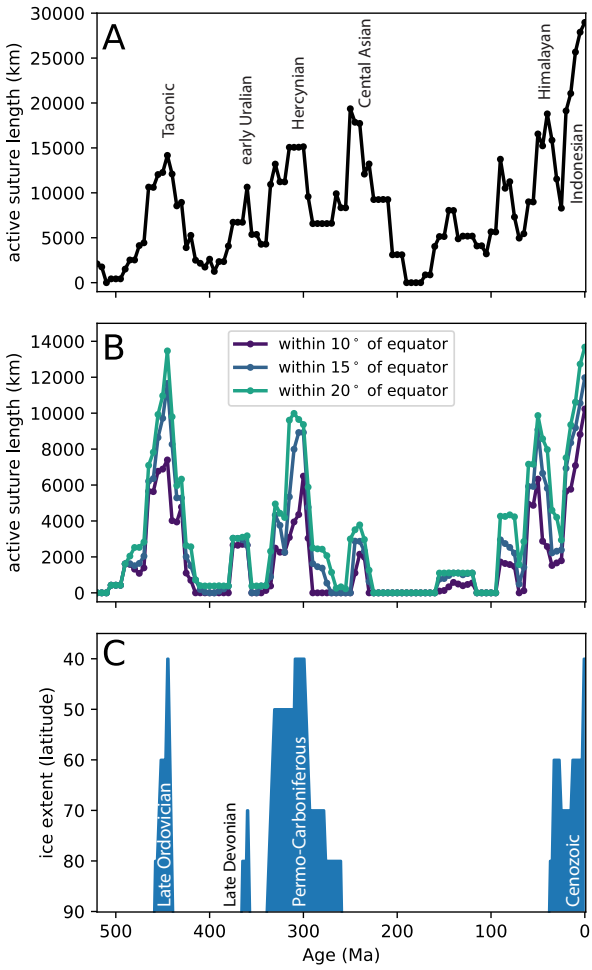

Figure 1.7: Phanerozoic suture length in the tropics compared to the latitudinal extent of land ice away from the poles, taken from Macdonald et al. (2019). **A)** Total active suture length at all latitudes. **B)** Active suture length that is reconstructed to be within 10°, 15°, and 20° of the equator over the past 520 m.y. **C)** Latitudinal extent of land ice away from the poles, as in Fig. 1.4E.

A complication with the interpretation of soil shielding and limited weathering of LIPs is the rapid area decay rate ($t_{1/2}$ = 36 Myr) inferred from the comparison of current LIP surface extent to estimated original surface extent (Fig. 1.2). A couple considerations are relevant with respect to this analysis: 1) the current surface extent of LIP exposure is reduced

in part by volcanics being covered by unconsolidated sediments (i.e. regolith development itself) in a number of the provinces; 2) the current surface extent of LIP exposure may be incomplete and an underestimate for some of the provinces; 3) the initial LIP surface extents are typically poorly constrained and are likely over-estimates which could be resulting in inflated interpreted decay rates; and 4) the relationship between LIP area and volume is poorly constrained. Future efforts that improve the LIP database, such as developing better-constrained estimates of original LIP surface extent, constraining burial and uplift histories, and refining the timing of eruptions associated with LIPs, will improve analyses that consider the LIP record in its entirety, such as that in this contribution.

We have focused this analysis on the Phanerozoic record given that well-constrained paleogeographic models are available for the past ∼520 Myr. The approach of seeking to evaluate correlation between LIP area and glaciation is further complicated for Neoproterozoic Snowball Earth events because ice-albedo runaway leads to persistent global glaciation on timescales of tens of millions of years without continued forcing through normal carbon cycle processes until sufficient CO_2 to drive deglaciation builds up in the absence of silicate weathering (Hoffman et al., 2017). Moreover, cooling past the critical threshold for rapid global glaciation may have occurred on a sub-million year timescale (e.g. Macdonald and Wordsworth, 2017). Nevertheless, evaluating the hypothesis of tropical LIP area associated with the ca. 720 Ma Franklin LIP increasing global weatherability and contributing to the onset of the Sturtian Snowball Earth is a major motivating driver behind conducting this analysis.

How does the tropical LIP area associated with the Franklin LIP compare to that observed in the Phanerozoic? Using the paleomagnetic pole of Denyszyn et al. (2009), we reconstruct the paleolatitude of the Franklin LIP at the time of emplacement, and find that ∼99.7% (or ∼2.6 Mm^2) of the LIP erupted within 15° of the equator. This Franklin LIP tropical area at the time of emplacement is approximately equivalent to the Cenozoic peak, and is smaller than the other Phanerozoic peaks (Fig. 1.4C). The ca. 1109 Ma Umkondo is another Precambrian LIP that is constrained to have erupted in the tropics, although it is not known to be associated with any glaciation (no glacial deposits are found within the contemporaneous Midcontinent Rift basin; Swanson-Hysell et al., 2019). We reconstruct the paleolatitude of the Umkondo LIP at the time of emplacement using the paleomagnetic pole of Swanson-Hysell et al. (2015a), and find that effectively all of the LIP (or ∼2.0 Mm^2) erupted within the tropics, an area that is slightly smaller than that estimated for the Franklin LIP (Fig. 1.4C).

Together, these results indicate that the Franklin LIP, when compared to Phanerozoic as well as other Precambrian LIPs, did not have a uniquely large area in the tropics. Given that similar (and larger) peaks in tropical LIP area are not associated with the onset of glacial periods, additional processes beyond an increase in weatherability due to LIP area in the tropics must have been at play in the initiation of the Sturtian Snowball Earth. One such process could have been unusually high planetary albedo associated with the low-latitude continental configuration of the supercontinent Rodinia (Kirschvink, 1992; Li et al., 2008). However, our analysis of zonal continental area reveals an almost invariant

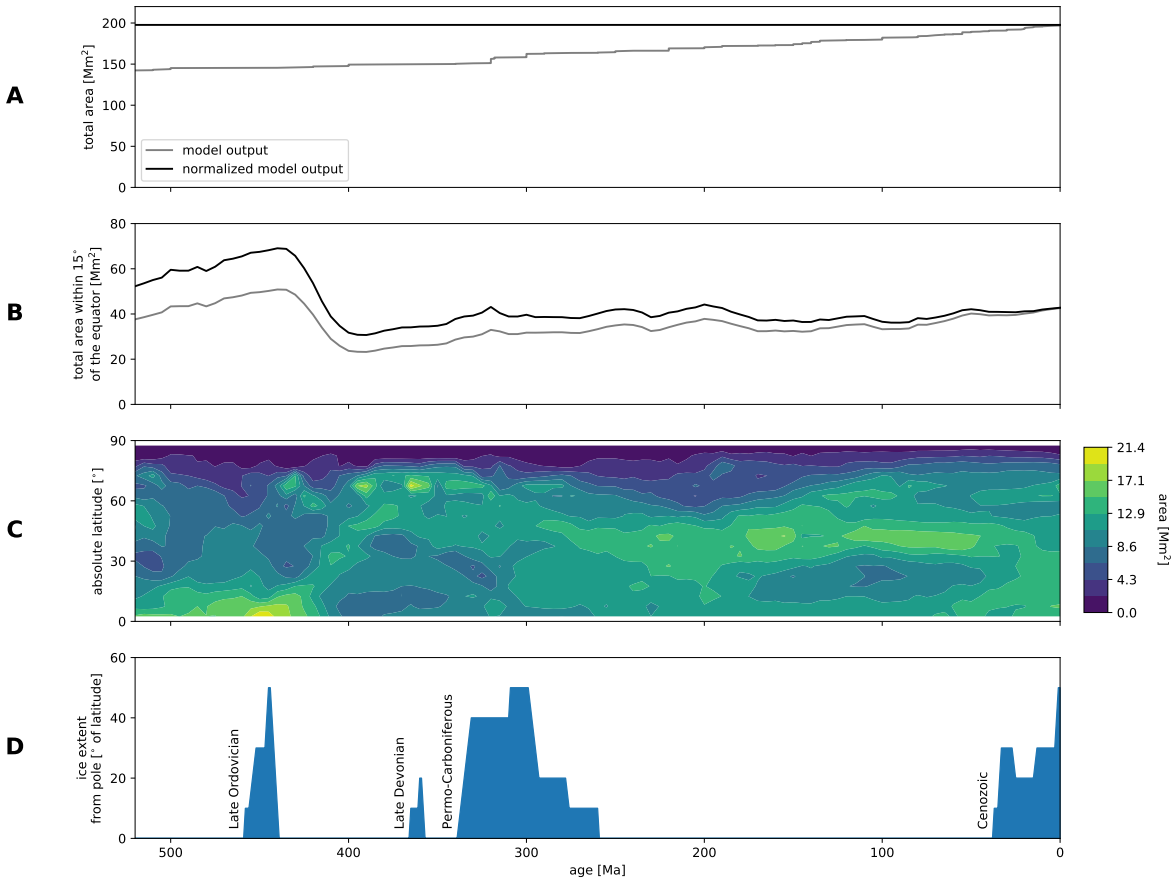

Figure 1.8: **A)** Total continental area through time. In the paleogeographic model used in this study, tectonic units (Torsvik and Cocks, 2016) are progressively added to the model, leading to a net increase in total continental area in the model of ∼33% over the Phanerozoic. However, estimates of continental crust growth (e.g. Pujol et al., 2013) suggest that continental area was roughly constant through the Phanerozoic. We therefore normalize the total continental area curve in our model by assuming a fixed continental area through the Phanerozoic. **B)** Tropical continental area through time. We normalize the tropical continental area curve using the normalization ratio implied in (A). **C)** Contour plot showing the latitudinal distribution of continental area. **D)** Latitudinal extent of land ice away from the poles (Macdonald et al., 2019).

tropical continental area from ∼400 Ma to the present (Fig. 1.8) and consequently no significant correlation between tropical continental area and the ice extent record in the Phanerozoic, although it is intriguing that there is a high and rising low-latitude continental area in the Ordovician. Similar to the LIP area analysis, this continental area analysis suggests that a low-latitude continental configuration can not be invoked as the sole driver of planetary cooling, although it could be a contributing factor. Another potential contributing process for Neoproterozoic cooling leading up to the Sturtian glaciation is an increase in global weatherability associated with the collision and accretion of arc terranes within the

present-day Arabian-Nubian Shield (Park et al., 2020b). Together, a low-latitude continental configuration and abundant arc-continent collisions in the tropics may have led to a cool background climate, and the emplacement of the Franklin LIP may have further increased global weatherability to the point where the ice-albedo runaway could take effect. However, tropical LIP area associated with the Franklin was not uniquely high, and therefore an associated increase in global weatherability was likely not the sole driver of Snowball Earth onset, consistent with the results of the Phanerozoic analysis.

The temporal overlap between Franklin LIP eruptions and the initiation of Sturtian glaciation remains compelling (Macdonald et al., 2010; MacLennan et al., 2018). This overlap could support arguments that other aspects of LIP emplacement, such as the injection of sulfur aerosols in the stratosphere (Macdonald and Wordsworth, 2017), played a role in the initiation of low-latitude glaciation. The temporary effect on albedo of such aerosols is maximized when they are injected into the atmosphere at low-latitudes into a cool background climate and their presence at high concentrations is pre-conditioned on eruption through sedimentary basins hosting evaporite deposits, as could have been the case for the Franklin LIP (Macdonald and Wordsworth, 2017). However, in the cases in which such aerosol-driven cooling does not result in ice-albedo runaway and a Snowball Earth, the climate would return to its background climate state within years (Macdonald and Wordsworth, 2017). A contrasting effect is that, on 1 kyr to 1 Myr timescales, LIP emplacement could instead cause transient warming associated with elevated CO_2 outgassing leading to transiently high pCO_2, as has been argued for the CAMP (Schaller et al., 2011, 2012).

The results from this analysis indicate that when the entire LIP database is considered in conjunction with a paleogeographic reconstruction and this parameterization of erosion, there is no significant relationship between total LIP area nor LIP area in the tropics and the extent of continental ice sheets. While this result need not imply that there is no increase in global weatherability from the emplacement of LIPs, it does suggest that changes in planetary weatherability associated with LIPs are not the fundamental control on whether Earth is in a glacial or non-glacial climate state.

1.6 Acknowledgements

Richard Ernst provided GIS compilations of LIP extent and present-day exposure that were essential to the analysis. The manuscript was improved by constructive reviews from Trond Torsvik, Dietmar Müller, and Dennis Kent. Discussions with Yves Goddéris made possible through the France-Berkeley Fund contributed valuably to aspects of the interpretation. Research was supported by NSF Grants EAR-1547434 and EAR-1925990.

Chapter 2

Emergence of the Southeast Asian islands as a driver for Neogene cooling

2.1 Abstract

Steep topography, a tropical climate, and mafic lithologies contribute to efficient chemical weathering and carbon sequestration in the Southeast Asian islands. Ongoing arc-continent collision between the Sunda-Banda arc system and Australia has increased the area of subaerially exposed land in the region since the mid-Miocene. Concurrently, Earth's climate has cooled since the Miocene Climatic Optimum, leading to growth of the Antarctic ice sheet and onset of Northern Hemisphere glaciation. We seek to evaluate the hypothesis that the emergence of the Southeast Asian islands played a significant role in driving this cooling trend through increasing global weatherability. To do so, we have compiled paleoshoreline data and incorporated them into GEOCLIM, which couples a global climate model to a silicate weathering model with spatially resolved lithology. We find that without the increase in area of the Southeast Asian islands over the Neogene, atmospheric pCO_2 would have been significantly higher than pre-industrial values, remaining above the levels necessary for initiating Northern Hemisphere ice sheets.

2.2 Introduction

The Southeast Asian islands (SEAIs) have an out-sized contribution to modern chemical weathering fluxes relative to its area. The confluence of steep topography, a warm and wet tropical climate, and the presence of mafic lithologies results in high fluxes of Ca and Mg cations in the dissolved load and associated CO_2 consumption (Gaillardet et al., 1999; Hartmann et al., 2009; Milliman and Farnsworth, 2013; Hartmann et al., 2014). There has been a significant increase in the area of subaerially exposed land within the region since the mid-Miocene associated with ongoing arc-continent collision between Australia and the Sunda-Banda arc system (Molnar and Cronin, 2015; Hall, 2017; Macdonald et al., 2019).

Concurrently, after the Miocene Climatic Optimum, a cooling trend began ca. 15 Ma and accelerated over the past 4 million years (m.y.) leading to the development of Northern Hemisphere ice sheets (Shackleton et al., 1984; Zachos et al., 2001). Many hypotheses have been proposed to explain this cooling trend including changes in ocean/atmosphere circulation (Haug and Tiedemann, 1998; Shevenell, 2004; Molnar and Cronin, 2015), a decrease in volcanic degassing (Berner et al., 1983), or uplift in the Himalaya (Raymo et al., 1988; Galy et al., 2007). Here we seek to evaluate the hypothesis that emergence of the SEAIs was a significant factor in driving long-term climatic cooling over the Neogene.

Over geologic time-scales, CO_2 enters Earth's ocean–atmosphere system primarily via volcanism and metamorphic degassing, and leaves primarily through the chemical weathering of silicate rocks and through organic carbon burial (Kump et al., 2000). Chemical weathering delivers alkalinity and cations to the ocean which drives carbon sequestration through carbonate precipitation. Steady-state pCO_2 is set at the pCO_2 level at which CO_2 sinks are equal to sources. As CO_2 sinks increase and pCO_2 falls, temperature decreases and the hydrological cycle is weakened, causing the efficiency of the silicate weathering sink to decrease until a new steady-state is achieved at lower pCO_2 (Kump and Arthur, 1997).

Topography, climate, and lithology all effect chemical weathering. High-relief regions generally lack extensive regolith development, and thus tend to have reaction-limited weathering regimes that are more prone to adjust when climate changes (Gabet and Mudd, 2009; West, 2012; Maher and Chamberlain, 2014). High physical erosion rates contribute to high chemical weathering fluxes in these high-relief regions (Goddéris et al., 2017a). In warm and wet regions, mineral dissolution kinetics are faster leading to enhanced chemical weathering (Lasaga et al., 1994; West, 2012). Mafic rocks have higher Ca and Mg concentrations and dissolution rates than felsic rocks, and thus have the potential to more efficiently sequester carbon through silicate weathering (Dessert et al., 2003). These factors have led to the proposal that arc-continent collisions, which create steep landscapes that include mafic lithologies, within the tropical rain belt have been important in enhancing global weatherability, lowering atmospheric pCO_2, and initiating glacial climate over the past 520 m.y. (Jagoutz et al., 2016; Swanson-Hysell and Macdonald, 2017; Macdonald et al., 2019) and perhaps in the Neoproterozoic as well (Park et al., 2020b).

Quantitatively estimating the magnitude of decrease in steady-state pCO_2 associated with the emergence of a region with a high carbon sequestration potential, such as the SEAIs, requires constraints on changing tectonic context and accounting of associated feedbacks. As this region emerges, the total global silicate weathering flux will transiently exceed the volcanic degassing flux, causing pCO_2 to initially decline until a new steady-state is established where the total magnitude of the CO_2 sinks is the same as before the change. However, the sensitivity of the silicate weathering flux in any particular location to this change in pCO_2 is variable and dependent on the specific topography, climate, and lithology at that location. Furthermore, how regional climate responds to this change in pCO_2 is itself spatially variable. Therefore, the magnitude of pCO_2 change that is required to balance the total global silicate weathering flux with the volcanic degassing flux will depend on the specific spatial distribution of topography, climate, and lithology at the time of emergence. As a result,

any attempt to meaningfully estimate the decrease in steady-state pCO_2 associated with emergence of the SEAIs must model spatially resolved climatology and silicate weathering fluxes in tandem and account for the spatial distribution of the factors that affect these inter-connected systems.

2.3 GEOCLIM Model

To estimate the decrease in steady-state pCO_2 associated with the increase of subaerially exposed land area in the SEAIs, we use the global spatially resolved GEOCLIM model (Goddéris and Donnadieu, 2017). GEOCLIM estimates changes in steady-state pCO_2 associated with coupled changes in erosion, chemical weathering, and climatology by linking a silicate weathering model to climate model runs at multiple pCO_2 levels.

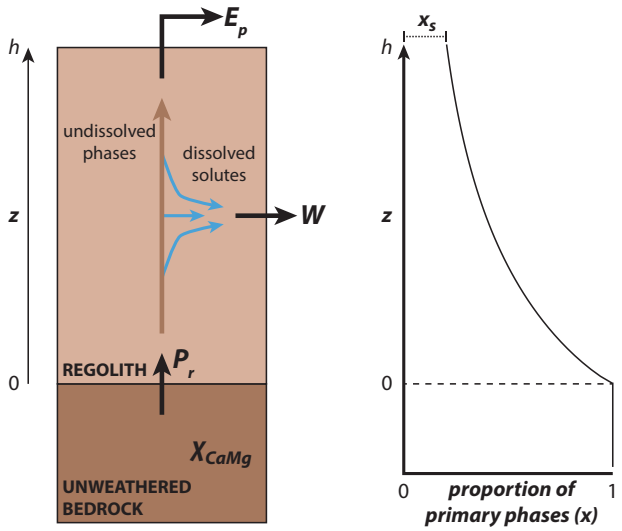

Figure 2.1: A schematic representation of the silicate weathering component of GEOCLIM in a single profile at steady-state. A rock particle leaves the unweathered bedrock with production rate P_r, and transits vertically through a regolith of height h. Regolith production and physical erosion (E_p) are equal at steady-state. As a particle transits upwards, some fraction of the primary phases (x) are chemically weathered (W), with the flux of dissolved Ca+Mg being W multiplied by the concentration of Ca+Mg in unweathered bedrock (χ_{CaMg}). Details of the formulation for the silicate weathering component of GEOCLIM can be found in *Materials and Methods*.

The silicate weathering component of GEOCLIM calculates CO_2 consumption resulting from silicate weathering for subaerially exposed land. We assume that Ca and Mg are the only cations that consume CO_2 over geologic time-scales, such that each mole of Ca or Mg that is dissolved by silicate weathering consumes one mole of CO_2. While reverse weathering is another potential sink for Ca or Mg (Michalopoulos and Aller, 1995), its parameterization

is unclear and it has been interpreted to be a relatively minor flux in the Cenozoic (Isson and Planavsky, 2018), and we do not include it in our model. In previous versions of the model, silicate weathering was a function of temperature and runoff only, and all bedrock was assigned identical chemical compositions (Goddéris and Donnadieu, 2017). More recent versions of GEOCLIM implement regolith development and soil shielding (Fig. 2.1), which introduces a dependence on erosion rate (and therefore topographic slope; Maffre et al., 2018). While this introduction of regolith development into GEOCLIM is important for assessing the impact of tropical arc-continent collisions on $p\mathrm{CO}_2$, the relatively high Ca+Mg concentration in arc rocks relative to other lithologies must also be considered.

We therefore implement variable bedrock Ca+Mg concentration into GEOCLIM (*Supporting Information*). The spatial distribution of lithologies is sourced from the Global Lithologic Map (GLiM; Hartmann and Moosdorf, 2012) and is represented by 6 categories: metamorphic, felsic, intermediate, mafic, carbonate, and siliciclastic sediment. Each land pixel is assigned these lithologic categories at a resolution of $0.1^\circ \times 0.1^\circ$. The Ca+Mg concentrations of felsic, intermediate, and mafic lithologies are assigned based on the mean of data of these lithologic categories compiled in EarthChem (www.earthchem.org/portal). Given that GLiM does not distinguish ultramafic lithologies, such rocks are grouped with mafic rocks. As a result, the Ca+Mg concentration is likely an underestimate in regions of obducted ophiolites, such that the estimated effect of these regions on changing steady-state $p\mathrm{CO}_2$ could be conservative (Schopka et al., 2011). The weathering of carbonate does not contribute to long-term CO_2 consumption and its Ca+Mg concentration is ignored. The Ca+Mg concentrations of metamorphic and siliciclastic sediment lithologies are more difficult to define, since their chemical composition is strongly dependent on protolith composition and, in the case of siliciclastic sediment, the degree of previous chemical depletion. We explore a range of feasible Ca+Mg concentrations for metamorphic rocks and siliciclastic sediment during calibration of the silicate weathering component of GEOCLIM.

Calibration

The values of four parameters within the silicate weathering component that modify the dependence of silicate weathering on temperature, runoff, erosion, and regolith thickness are poorly constrained. Rather than prescribing single values, we select multiple values for each of these four parameters along with the Ca+Mg concentration of metamorphic and siliciclastic lithologies from within reasonable ranges (*Supporting Information*; Table A.2). We then permute all possible combinations of these values for the six parameters, leading to 93,600 unique parameter combinations (i.e. permutations). For each combination, we compute spatially resolved long-term CO_2 consumption associated with Ca+Mg fluxes using present-day runoff, temperature, and slope. We sum computed CO_2 consumption over watersheds for which data-constrained estimates are available (Gaillardet et al., 1999; Moquet et al., 2018), then calculate the coefficient of determination (r^2) between computed and measured CO_2 consumption in each of these watersheds. After eliminating parameter combinations that result in low r^2, 573 parameter combinations remain (*Supporting Information*; Fig. A.3).

The resulting global CO_2 consumption of these filtered model runs all overlap with independently derived estimates of the global CO_2 degassing flux (Gerlach, 2011), as they should for a steady-state long-term carbon cycle (*Supporting Information*; Fig. A.3).

Climate Model Component

Having calibrated the silicate weathering component of GEOCLIM, we use it to estimate the decrease in steady-state pCO_2 associated with emergence of the SEAIs. For the climate model component, we use temperature and runoff from a subset of the GFDL CM2.0 experiments (*Supporting Information*; Delworth et al., 2006). These experiments are well-suited for this analysis because all non-CO_2 forcings are held constant at values representative of pre-industrial conditions, allowing the effect of changing pCO_2 on climatology to be isolated. Furthermore, the experiments were run long enough for the final system to approximate steady-state.

2.4 Paleoshorelines

To determine the position of paleoshorelines in the SEAIs over the past 15 m.y., we use terrestrial and marine sedimentary deposits (Fig. 2.2; *Supporting Information*). The paleoshoreline data indicate that the Sunda-Banda Arc and New Guinea are primarily responsible for the increase in area since 15 Ma. Exhumation of the modern Sunda-Banda Arc is the result of ongoing arc-continent collision with the Australian Plate (Harris, 2006). Most of Sumatra and Java along with the non-volcanic islands of the Outer Banda Arc were elevated above sea level after 5 Ma (Hall, 2013b). In New Guinea, emergence in the mid-Miocene is associated with collision between the Melanesian Arc and Australia's distal margin (Cloos et al., 2005), which drove exhumation of the Irian-Marum-April Ophiolite Belt. Exhumation accelerated over the past 4 m.y. in the New Guinea Central Range due to slab-breakoff and buoyant uplift, and in eastern New Guinea due to jamming of the north-dipping subduction zone (Cloos et al., 2005). We also include changes in areas of presently submerged continental shelves such as the Sunda Shelf that were previously exposed (*Supporting Information*; Fig. A.7). These tectonic drivers and others throughout the region led to progressive emergence over the past 15 m.y. that accelerated following 5 Ma (Fig. 2.2B). This trend mirrors broad cooling over the Neogene that resulted in the initiation of Northern Hemisphere ice sheets (Fig. 2.2C).

We use GEOCLIM to estimate pCO_2 associated with the reconstructed subaerial extent of the SEAIs at ca. 15, 10, and 5 Ma ("paleo-SEAIs" scenarios; Fig. 2.3). Because we use a climate model forced with modern geography, the position of the tectonic blocks remain fixed. Although there has been motion of these tectonic blocks since 15 Ma, they have remained within tropical latitudes such that this fixed scenario is a good approximation of the paleogeography (*Supporting Information*; Fig. A.10). We also test an end-member

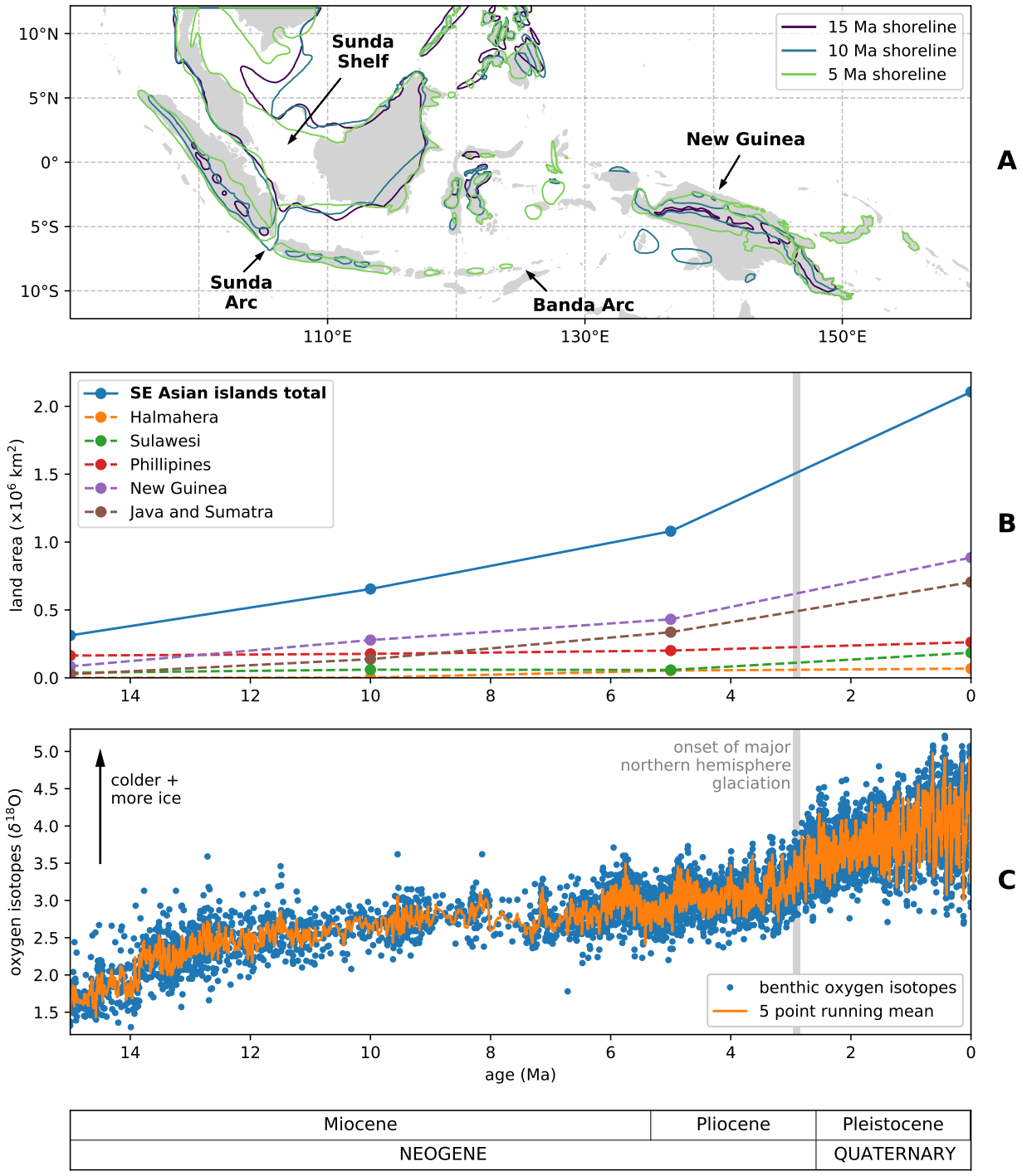

Figure 2.2: The emergence of the Southeast Asian islands (also referred to as the Maritime Continent in the climate science literature) from the mid-Miocene to present. Past shorelines at 5, 10, and 15 Ma are shown in **A** with associated land area summarized in **B**. A significant increase in area over the past 5 million years is coincident with cooling and the onset of Northern Hemisphere glaciation as reflected in the benthic oxygen isotope record (Zachos et al., 2008) shown in **C**.

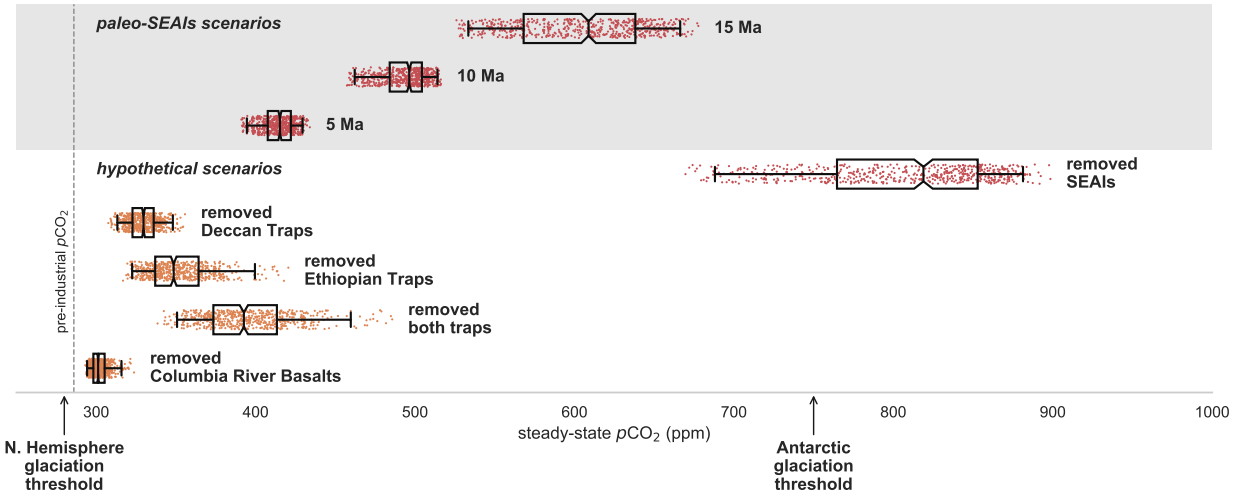

Figure 2.3: Steady-state $p\mathrm{CO}_2$ estimates from GEOCLIM for the various scenarios discussed in the text. For each of the seven scenarios, each point represents an estimate from one of the 573 unique parameter combinations that most closely matched estimates of present-day CO_2 consumption in 80 watersheds around the world (*Supporting Information*). The box encloses the middle 50% of the $p\mathrm{CO}_2$ estimates (i.e. the interquartile range), and the notch represents the median with its 95% confidence interval. The whiskers extend to the 2.5 and 97.5 percentile values. Glaciation thresholds (DeConto et al., 2008) are shown on the x-axis.

scenario, in which all islands associated with arc-continent collision in the region are removed ("removed SEAIs" scenario; Fig. 2.3).

2.5 $p\mathrm{CO}_2$ Estimates

Using the 573 unique parameter combinations, the paleo-SEAIs scenarios resulted in 526–678 ppm for 15 Ma, 457–516 ppm for 10 Ma, and 391–434 ppm $p\mathrm{CO}_2$ for 5 Ma (Fig. 2.3). These results indicate a progressive decrease in $p\mathrm{CO}_2$ over the Neogene associated with the emergence of the SEAIs, and suggest that without this emergence, pre-industrial $p\mathrm{CO}_2$ would have been ~526–678 ppm. These paleo-SEAIs scenarios do not account for Neogene changes outside of the SEAIs (e.g. changes in ocean/atmosphere circulation, volcanic degassing, and weathering fluxes elsewhere on Earth, discussed in *Alternative Mechanisms for Neogene Cooling*). Therefore, these results are not estimating $p\mathrm{CO}_2$ at 15 Ma, but rather are quantifying $p\mathrm{CO}_2$ change associated with emergence of the SEAIs.

Proxy-based estimates of the magnitude and trajectory of $p\mathrm{CO}_2$ change from the Miocene to the Pliocene are variable between techniques and associated assumptions underlying their interpretation (*Supporting Information*; Fig. A.11). The $p\mathrm{CO}_2$ values from the 5 Ma paleo-SEAIs scenario overlap with many proxy-based estimates (Foster et al., 2017) as well as

values that emerge from approaches that assimilate climate and ice sheet model output with benthic $\delta^{18}O$ data (van de Wal et al., 2011; Berends et al., 2020). The modeled pCO_2 values for 15 Ma resemble the higher end of proxy-based pCO_2 estimates for the early to mid-Miocene, indicating that the increase in subaerially exposed land area and tectonic topography of the SEAIs is sufficient to explain long-term cooling of Earth's climate over the Neogene. The pCO_2 threshold for Antarctic glaciation is estimated to be ∼750 ppm with that for Northern Hemisphere glaciation being significantly lower at ∼280 ppm (DeConto et al., 2008). These modeled values of decreasing pCO_2 associated with emergence of the SEAIs are therefore consistent with the record of Neogene climate with Miocene ice sheets on Antarctica (Sugden et al., 1995) followed by Northern Hemisphere ice sheets developing in the Pliocene (Haug et al., 2005) as pCO_2 subsequently decreased.

The results of our paleo-SEAIs scenarios highlight the importance of the combination of topography, runoff, and lithology in setting Earth's climate state. To independently explore the effect of the modern-day surface exposure of lower-relief basaltic lavas on steady-state pCO_2 (Kent and Muttoni, 2013), we replace mafic volcanics associated with the Deccan Traps, Ethiopian Traps, and Columbia River Basalts with the Ca+Mg concentration of bulk continental crust in GEOCLIM (Fig. 2.3). The resulting pCO_2 is ∼300–500 ppm, indicating that the presence of mafic rocks in these igneous provinces affects steady-state pCO_2 as has been suggested to be important for Paleogene cooling (Kent and Muttoni, 2013). However, the higher 526–678 ppm values for the 15 Ma paleo-SEAIs scenario illustrate that higher relief and a wet tropical climate significantly increase the efficiency of CO_2 consumption, especially when paired with high Ca+Mg lithologies. As such, arc-continent collisions in the tropics are likely more important for driving long-term changes in pCO_2 than the eruption of flood basalts (Macdonald et al., 2019; Park et al., 2019).

Previous work has estimated that the decrease in pCO_2 since 5 Ma associated with the emergence of the SEAIs and enhanced silicate weathering is ∼19 ppm (Molnar and Cronin, 2015), in which case their emergence would be a relatively minor contributor to Neogene cooling. This 19 ppm estimate was obtained using an equation that assumes a direct linear relationship between mean global temperature and changes in weathering-rate-weighted land area, scaled by a factor that is intended to account for the influence of both runoff and temperature. pCO_2 was then estimated from the calculated temperature using a simple energy balance equation. However, the relationship between mean global temperature (or pCO_2) and weathering-rate-weighted land area is not linear. Furthermore, this simple linear relationship ignores spatial variability in topography and climatology, and only crudely accounts for spatial variability in lithology. In fact, the 19 ppm estimate is closer in magnitude to the decrease in pCO_2 that we estimate if mafic volcanics associated with the Deccan Traps (a relatively flat area outside of the warm and wet tropics) are replaced with the Ca+Mg concentration of bulk continental crust (22–70 ppm; Fig. 2.3). The significant difference in steady-state pCO_2 estimated between the "removed Deccan Traps" scenario and the paleo-SEAIs scenarios (Fig. 2.3) demonstrates that considering changes in the spatial distribution of lithologies alone is not adequate for estimating changes in steady-state pCO_2. Instead, spatially varying topography and climatology significantly modulates silicate weathering rates,

and must be accounted for when estimating pCO_2 change associated with paleogeographic change.

An important caveat for these estimates of pCO_2 is that our modeling is determining the climatology in the GFDL CM2.0 model at which steady-state is achieved – a climatology that has an associated pCO_2 value in the model. However, climate models are variable in their response to changes in pCO_2. One way to summarize this variability is through the equilibrium climate sensitivity value – the steady-state change in global mean surface air temperature associated with a doubling of pCO_2. A range of 1.5 to 4.5°C per pCO_2 doubling was proposed in the landmark Charney report (Charney et al., 1979) and this range was considered to be the credible interval (>66% likelihood) in the last IPCC report (Stocker et al., 2013). Integrating constraints both from understanding of climate feedback processes and the climate record, a recent comprehensive review estimates the 66% probability range of climate sensitivity to be 2.6 to 3.9°C per pCO_2 doubling with a 5 to 95% range of 2.3 to 4.7°C per pCO_2 doubling (Sherwood et al., 2020). The equilibrium climate sensitivity associated with the CM2.0 climate models is 2.9°C per pCO_2 doubling, which falls within these ranges although these ranges remain broad. An alternative way to consider the results from our analysis would be that an estimate of 572 ppm (2× pre-industrial pCO_2) for the 15 Ma paleo-SEAIs scenario is implying that Earth would be ∼2.9°C warmer. If Earth's climate sensitivity is at the higher end of the probable range and higher than in the CM2.0 model, as it is in some climate models, this same amount of Neogene cooling resulting from the emergence of the SEAIs could have been driven by a smaller change in pCO_2.

2.6 Alternative Mechanisms for Neogene Cooling

Ocean/Atmosphere Circulation

Some hypotheses to explain ice sheet growth over the Neogene invoke changes in ocean/atmosphere circulation including: further climatic isolation of Antarctica due to strengthening of the circumpolar current (Shevenell, 2004); increased atmospheric moisture in the Northern Hemisphere due to intensified thermohaline circulation following Panama Isthmus emergence (Haug and Tiedemann, 1998); and cooling of North America resulting from a strengthened Walker Circulation associated with emergence of the SEAIs (Molnar and Cronin, 2015). Such changes in ocean/atmosphere circulation are likely to modulate pCO_2 thresholds for glacial initiation and ice sheet growth (DeConto et al., 2008). However, the prolonged time-scale of the cooling trend since 15 Ma (Fig. 2.2C) is most readily attributable to decreasing pCO_2 associated with evolving geological sources and sinks of carbon, modulated by the silicate weathering feedback (Walker et al., 1981; Raymo, 1991; Berner and Caldeira, 1997; Kump and Arthur, 1997; Berner, 2001).

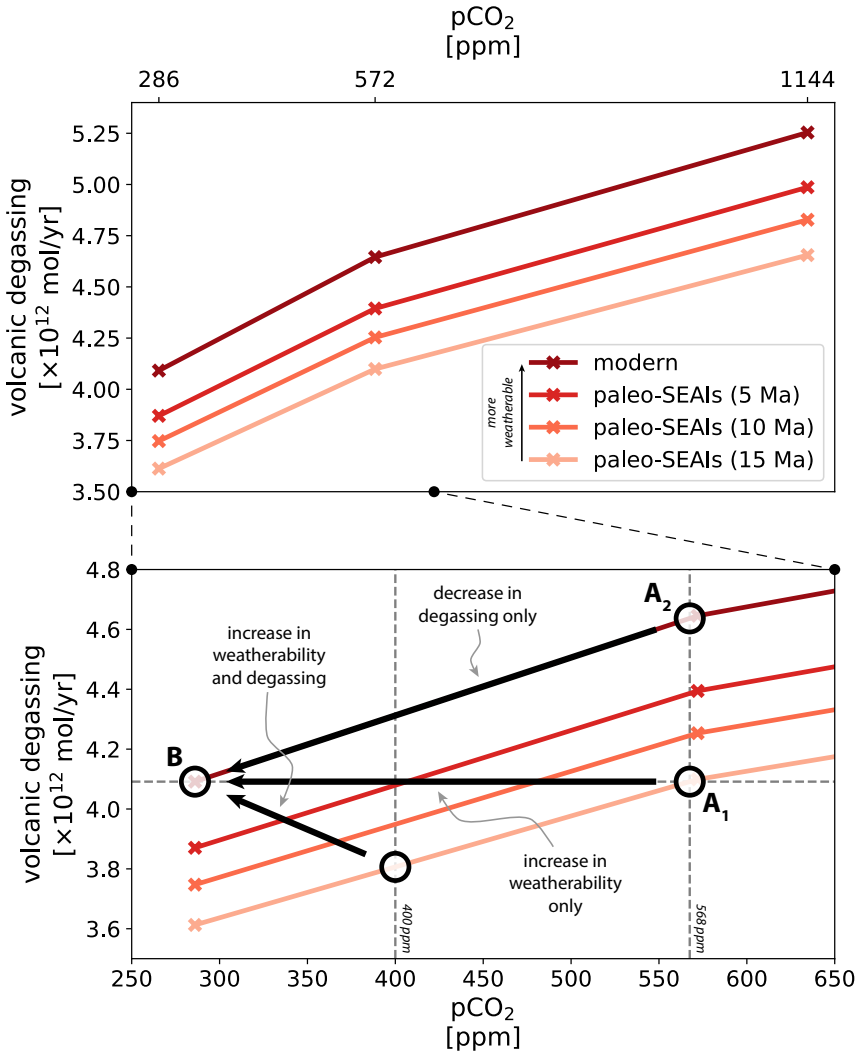

Figure 2.4: Weatherability curves for the modern and paleo-SEAIs scenarios shown in Figure 2.3. The lower panel expands the lower pCO_2 range (x-axis) of the upper panel. Details on how these curves were generated are described in *Materials and Methods*. Each of the 4 curves represent a different tectonic boundary condition (i.e. the reconstructed paleoshorelines of the SEAIs; Fig. 2.2A) and therefore a different global weatherability. The curves show the resulting pCO_2 for a given volcanic degassing flux such that the input flux is balanced by the silicate weathering output flux. Point B represents the pre-industrial, in which pCO_2 is 286 ppm. The arrow from Point A_1 to B represents the "increase in weatherability only" scenario, in which global weatherability increases as the SEAIs emerge, but the volcanic degassing flux does not change over the past 15 m.y. In this scenario, the pCO_2 decreases from the value dictated by the 15 Ma paleo-SEAIs weatherability curve (568 ppm). The arrow from Point A_2 to B instead represents the "decrease in degassing only" scenario, in which global weatherability remains the same as the pre-industrial, but the same change in pCO_2 as the "increase in weatherability only" scenario is achieved by decreasing the volcanic degassing flux from a value ~13% greater than the pre-industrial. The arrow from Point A_3 to B represents the "increase in weatherability and degassing" scenario, in which a change in pCO_2 from 400 ppm to 286 ppm is achieved by increasing both global weatherability from our 15 Ma tectonic boundary condition as well as the volcanic degassing flux from a value ~7% smaller than the pre-industrial flux.

Volcanic Degassing

A decrease in volcanic degassing (Berner et al., 1983) has also been proposed as a driver for Neogene cooling. However, proxy-based estimates of the evolution of volcanic degassing fluxes throughout the Neogene are inconsistent with each other, such that not even the sign of the change in volcanic degassing over the past ∼15 m.y. is without ambiguity (Goddéris and Donnadieu, 2017). For example, it has both been estimated that the volcanic degassing flux was ∼25% lower (Cogné and Humler, 2006) and ∼10% higher (Van Der Meer et al., 2014) at 15 Ma relative to the present day.

Our model framework provides an opportunity to estimate the decrease in volcanic degassing flux necessary to achieve the same change in $p\mathrm{CO}_2$ predicted for the increase in global weatherability associated with the emergence of the SEAIs over the past 15 m.y. If we use the parameter combination that had the highest r^2 between computed and measured CO_2 consumption in watersheds around the world during calibration (*Calibration* and *Supporting Information*; Fig. A.4), GEOCLIM estimates a pre-industrial volcanic degassing flux of 4.1×10^{12} mol/yr to balance the silicate weathering flux at 286 ppm $p\mathrm{CO}_2$. If we then assume that this volcanic degassing flux did not change over the past 15 m.y., then GEOCLIM estimates that the increase in global weatherability associated with the emergence of the SEAIs led to a change in $p\mathrm{CO}_2$ of ∼280 ppm ("increase in weatherability only" scenario in Fig. 2.4). If we instead assume that global weatherability did not change over the past 15 m.y., then we estimate that the volcanic degassing flux needs to have been ∼13% greater at 15 Ma relative to the pre-industrial to drive the same ∼280 ppm change in $p\mathrm{CO}_2$ ("decrease in degassing only" scenario in Fig. 2.4). This ∼13% value is higher than 10%, the highest current estimate for the volcanic degassing flux at 15 Ma relative to the present day (Van Der Meer et al., 2014).

However, changes in the volcanic degassing flux would have modulated changes in $p\mathrm{CO}_2$ associated with changes in global weatherability. For example, some proxy-based approaches as well as some model-data assimilation approaches estimate that mid-Miocene $p\mathrm{CO}_2$ was lower than 568 ppm (*Supporting Information*; Fig. A.11). Take a scenario in which $p\mathrm{CO}_2$ was 400 ppm at 15 Ma. If we assume that the $p\mathrm{CO}_2$ decrease to the pre-industrial value of 286 ppm was driven by the increase in global weatherability associated with emergence of the SEAIs in conjunction with an increase in volcanic degassing which counteracts cooling by increasing the flux of CO_2 to the atmosphere ("increase in weatherability and degassing" scenario in Fig. 2.4), the volcanic degassing flux would have had to have been ∼7% smaller than the pre-industrial. More robust constraints on $p\mathrm{CO}_2$ (*Supporting Information*; Fig. A.11) and/or volcanic degassing rates over the past 20 m.y. are needed to constrain which of the "increase in weatherability only" or "increase in weatherability and degassing" scenarios (Fig. 2.4) is more representative of the mechanisms driving Neogene cooling.

Himalayan Uplift

Marine $^{87}Sr/^{86}Sr$ has overall been increasing since ca. 35 Ma (McArthur et al., 2012). The traditional explanation for this trend is that it reflects increased weathering of radiogenic (i.e. high $^{87}Sr/^{86}Sr$) silicate rocks (Raymo et al., 1988; Edmond, 1992). Associated with this explanation is the proposal that increasing weathering of radiogenic silicate rocks in the Himalayas was the primary driver of Neogene cooling (Raymo and Ruddiman, 1992). It could be argued that increasing marine $^{87}Sr/^{86}Sr$ is inconsistent with the hypothesis that increasing weathering of juvenile (i.e. low $^{87}Sr/^{86}Sr$) silicate rocks in the SEAIs was an important driver of Neogene cooling. However, the globally averaged ratio of silicate weathering fluxes from radiogenic cratonic rocks versus juvenile arc lithologies can be at least partially decoupled from marine $^{87}Sr/^{86}Sr$ via the regional weathering of isotopically unique lithologies. For example, in addition to highly radiogenic granites and gneisses (Edmond, 1992), unusually radiogenic carbonates are abundant in Himalayan strata, and it is estimated that $\sim$75% of Sr coming from the Himalayas can be attributed to carbonate rather than silicate weathering (Jacobson et al., 2002; Quade et al., 2003; Oliver et al., 2003). As such, there are challenges in interpreting the marine $^{87}Sr/^{86}Sr$ record as a direct proxy for silicate weathering fluxes. Nevertheless, steadily increasing marine $^{87}Sr/^{86}Sr$ is interrupted ca. 16 Ma when the slope of the $^{87}Sr/^{86}Sr$ curve decreases (McArthur et al., 2012). This decrease in slope has been attributed to coincident exhumation of relatively low $^{87}Sr/^{86}Sr$ Outer Lesser Himalaya carbonates (Myrow et al., 2015; Colleps et al., 2018), but could also be at least partially driven by the emergence of low $^{87}Sr/^{86}Sr$ lithologies in the SEAIs during arc-continent collision. Increasing seawater Mg/Ca since ca. 15 Ma (Higgins and Schrag, 2012) is consistent with an increasing proportion of the global silicate weathering flux being derived from mafic and ultramafic sources.

Himalayan uplift would have affected geological carbon sinks, either via increased weathering of silicate rocks (Raymo and Ruddiman, 1992) or enhanced burial of organic matter in the Bengal Fan (Galy et al., 2007). Increased weathering of the emerging SEAIs would have occurred in tandem with such changes in the Himalaya, such that the effects of these paleogeographic changes on geochemical proxy records, like marine $^{87}Sr/^{86}Sr$, become difficult to disentangle. In addition, given the large uncertainty associated with changes in regional climatology across Asia due to Himalayan orogeny, developing quantitative estimates of the evolution of global silicate weathering fluxes associated with Himalayan orogeny remains a major challenge.

2.7 The Geologic Carbon Cycle

If geological carbon sources remain approximately constant, global alkalinity delivery from silicate weathering needs to be approximately constant as well to keep the long-term carbon cycle in steady-state (Kump and Arthur, 1997). Enhanced silicate weathering in a region such as the SEAIs is compensated by a decrease in silicate weathering elsewhere. Global

alkalinity delivery from silicate weathering does not change, but occurs more efficiently and thereby at lower $p\mathrm{CO}_2$. Given that carbonate weathering is disconnected from the long-term carbon-cycle mass balance, changes in carbonate accumulation through time (Si and Rosenthal, 2019) could be driven by changes in carbonate weathering.

The long-term carbon-cycle mass balance can be perturbed via mechanisms that are disconnected from changes in volcanic degassing and silicate weathering rates. For example, sulphide oxidation coupled to carbonate dissolution could act as a source of CO_2 on million year time-scales (Torres et al., 2014). Similarly, the weathering of sedimentary organic matter could serve as a source of CO_2 (Hilton et al., 2014). On the other hand, enhanced burial of organic matter enabled by higher sediment and nutrient delivery could be an important sink of CO_2, as has been suggested in the Bengal Fan (Galy et al., 2007) and Taiwan (Kao et al., 2014). The fluxes of CO_2 represented by these processes are not accounted for in our model framework, and could have been affected by emergence of the SEAIs and/or Himalayan orogeny. $p\mathrm{CO}_2$ changes that result from these processes would be superimposed on $p\mathrm{CO}_2$ changes associated with evolving silicate weathering fluxes. However, our coupled weathering-climate model indicates that the $p\mathrm{CO}_2$ change associated with increased global weatherability driven by emergence of the SEAIs is sufficient to explain the majority of Neogene cooling (Fig. 2.3). Without this emergence, $p\mathrm{CO}_2$ would have remained above the level necessary for the growth of Northern Hemisphere ice sheets.

2.8 Conclusions

Coupled geological constraints and modeling experiments demonstrate that the SEAIs have been a growing hot spot for carbon sequestration due to silicate weathering from the Miocene to present. Changes in volcanic degassing and paleogeography elsewhere on Earth, particularly in the Himalaya and Central America, would have also affected geological carbon sources and sinks. Yet, not only does the history of emergence of the SEAIs coincide with Neogene cooling and the onset of Northern Hemisphere glaciation, but our coupled weathering-climate model also indicates that the associated steady-state $p\mathrm{CO}_2$ change is sufficient to explain much of this cooling. These results highlight that the Earth's climate state is particularly sensitive to changes in tropical geography.

2.9 Materials and Methods

The code for the GEOCLIM model used in this study can be found at: https://github.com/piermafrost/GEOCLIM-dynsoil-steady-state/releases/tag/v1.0. The code that generated the inputs and analyzed the output of the GEOCLIM model can be found at: https://github.com/Swanson-Hysell-Group/GEOCLIM_Modern.

GEOCLIM Silicate Weathering Component

The silicate weathering component of the GEOCLIM model has been modified from the previously published version (Goddéris et al., 2017a). The new component implements the model of Gabet and Mudd (2009) for the development of a chemically weathered profile. We refer to this chemically weathered profile as regolith where the base of the regolith is unweathered bedrock. In the model of Gabet and Mudd (2009), material enters the regolith and leaves either as a solute through chemical weathering of the material during its travel from the bedrock towards the surface, or as a physically weathered particle once it reaches the top. We use the DynSoil implementation of the Gabet and Mudd (2009) model, which integrates chemical weathering within the regolith (West, 2012). The transient time-varying version of this regolith model is described by three equations:

$$\frac{dh}{dt} = P_r - E_p \tag{2.1}$$

$$\frac{\partial x}{\partial t} = -P_r \frac{\partial x}{\partial z} - K\tau^{\sigma} x \tag{2.2}$$

$$\frac{\partial \tau}{\partial t} = -P_r \frac{\partial \tau}{\partial z} + 1 \tag{2.3}$$

Equation 2.1 is a statement of material conservation, where h is the total height of the regolith (m), t is the model time (yr), P_r is the regolith production rate (m/yr), and E_p is the physical erosion rate (m/yr). Equation 2.2 describes how the residual fraction of weatherable phases (x, unitless) changes as a function of time (t, yr) and depth (z, m). $K\tau^{\sigma}$ is the dissolution rate constant, which depends on the local climate (captured by K, $\mathrm{yr}^{-1-\sigma}$) and the time that a given rock particle has spent in the regolith (τ, yr) to some power σ (unitless) which implements a time-dependence. Equation 2.3 describes how the time that a given rock particle has spent in the regolith changes as time in the model progresses.

The net weathering rate in the regolith column (W, m/yr) can then be calculated with:

$$W = \int_0^h K\tau^{\sigma} x \, dz \tag{2.4}$$

The regolith production rate can be expressed as the product of the optimal production rate (P_0) and a soil production function ($f(h)$):

$$P_r = P_0 \, f(h) \tag{2.5}$$

$$P_0 = k_{rp} \, q \, e^{-\frac{E_a}{R}\left(\frac{1}{T} - \frac{1}{T_0}\right)} \tag{2.6}$$

$$f(h) = e^{\frac{-h}{d_0}} \tag{2.7}$$

P_0 is the 'optimal' regolith production rate (m/yr), which is defined to be the regolith production rate when there is no overlying regolith. In Equation 2.6, where k_{rp} is a proportionality constant (unitless), q is the runoff (m/yr), E_a is the activation energy (J/K/mol), R is the ideal gas constant (J/mol), T is the temperature (K), and T_0 is the reference temperature (K), we parameterize the 'optimal' regolith production rate (Carretier et al., 2014). $f(h)$ is the soil production function (unitless), which describes how regolith production decreases as the thickness of the regolith increases. It takes an exponential form as is commonly applied in the literature (Gabet and Mudd, 2009). In Equation 2.7, d_0 is a reference regolith thickness (m) (Heimsath et al., 1997).

Our implementation of the erosion rate is parameterized based on runoff and slope (s; m/m):

$$E_p = k_e \, q^m \, s^n \tag{2.8}$$

k_e is a proportionality constant ($(\mathrm{m/yr})^{1-m}$) and m and n are adjustable exponents that are kept as 0.5 and 1 (Maffre et al., 2018). This formulation is directly inspired by the stream power law (Davy and Crave, 2000). This formulation and these exponent values are supported by compilations, but variability in the proportionality constant is difficult to capture at a global scale (Lague, 2013).

The K in the dissolution rate constant in Equation 2.2 describes the dependence of the chemical weathering on climate:

$$K = k_d \left(1 - e^{-k_w q}\right) e^{-\frac{E_a}{R}\left(\frac{1}{T} - \frac{1}{T_0}\right)} \tag{2.9}$$

Equation 2.9 is an empirical simplification of mineral dissolution rates derived from kinetic theory and laboratory experiments (West, 2012), where k_d is a proportionality constant that modifies the dependence of dissolution rate on runoff and temperature ($\mathrm{yr}^{-1-\sigma}$), and k_w is a proportionality constant that modifies the dependence of dissolution rate on runoff (yr/m).

In this study, we are interested in obtaining the steady-state solution rather than the transient time-varying solution. The steady-state solution for DynSoil can be calculated analytically by setting the time derivatives equal to zero resulting in the following set of equations:

$$h = \max\left(0,\ d_0 \log\left(\frac{P_0}{E_p}\right)\right) \tag{2.10}$$

$$x(z) = \exp\left(-\frac{K}{\sigma + 1}\left(\frac{z}{E_p}\right)^{\sigma+1}\right) \tag{2.11}$$

$$W = E_p(1 - x(h)) = E_p(1 - x_s) \tag{2.12}$$

$x(z)$ is the abundance profile of primary phases inside the regolith, varying with height upward from the base of the regolith as shown in Figure 2.1. Setting z equal to the regolith

thickness (h) gives x_s which is the proportion of primary phases remaining at the top of the regolith column.

Weatherability Curves

To create the 15 Ma paleo-SEAIs curve shown in Figure 2.4, we use the reconstructed paleoshorelines of the SEAIs at 15 Ma (Fig. 2.2A). We then select the parameter combination that had the highest r^2 between computed and measured CO_2 consumption in watersheds around the world during calibration (*Calibration* and *Supporting Information*; Fig. A.4), and fix pCO_2 at the 3 pCO_2 levels at which the GFDL CM2.0 climate model experiments were computed (*Supporting Information*). We then run GEOCLIM at each of these pCO_2 levels until steady state is achieved (i.e. until the volcanic degassing flux is equal to the silicate weathering flux). We then repeat this process for the 10 and 5 Ma paleo-SEAIs paleoshorelines and the present day shorelines to generate the 3 other weatherability curves. Each estimated pCO_2 in Figure 2.3 is the result of underlying weatherability curves that change with the different chemical weathering parameters.

Supporting Information

A detailed description of the implementation of lithology into the silicate weathering component of GEOCLIM, the calibration of the silicate weathering component of GEOCLIM, the GFDL CM2.0 climate model, and the paleoshoreline reconstructions can be found in the *Supporting Information*.

2.10 Acknowledgements

Collaborative research between N.L.S.-H. and Y.G. was initially supported by a grant from the France-Berkeley Fund. Project research was supported by NSF FRES grants #1926001 and #1925990. We thank Alec Brenner, Sam Lo Bianco, Mariana Lin, and Judy Pu for their data compilation contributions to the paleoshoreline reconstructions.

Chapter 3

The lead-up to the Sturtian Snowball Earth: Neoproterozoic chemostratigraphy time-calibrated by the Tambien Group of Ethiopia

3.1 Abstract

The Tonian-Cryogenian Tambien Group of northern Ethiopia is a mixed carbonate-siliciclastic sequence that culminates in glacial deposits associated with the first of the Cryogenian glaciations - the Sturtian 'Snowball Earth.' Tambien Group deposition occurred atop arc volcanics and volcaniclastics of the Tsaliet Group. New U-Pb isotope dilution thermal ionization mass spectrometry (ID-TIMS) dates demonstrate that the transition between the Tsaliet and Tambien groups occurred at ca. 820 Ma in western exposures and ca. 795 Ma in eastern exposures, which is consistent with west to east arc migration and deposition in an evolving back-arc basin. The presence of intercalated tuffs suitable for high-precision geochronology within the Tambien Group enable temporal constraints on stratigraphic datasets of the interval preceding, and leading into, the Sturtian Glaciation. Recently discovered exposures of Sturtian glacial deposits and underlying Tambien Group strata in the Samre Fold-Thrust Belt present the opportunity to further utilize this unique association of tuffs and carbonate lithofacies. U-Pb ID-TIMS ages from zircons indicate that Tambien Group carbonates were deposited from ca. 820 Ma until 0 to 2 Myr before the onset of the Sturtian Glaciation, making the group host to a relatively complete carbonate stratigraphy leading into this glaciation. New $\delta^{13}C$ and $^{87}Sr/^{86}Sr$ data and U-Pb ID-TIMS ages from the Tambien Group are used in conjunction with previously published isotopic and geochronologic data to construct newly time-calibrated composite Tonian carbon and strontium isotope curves. Tambien Group $\delta^{13}C$ data and U-Pb ID-TIMS ages reveal that a pre-Sturtian sharp negative $\delta^{13}C$ excursion (referred to as the Islay anomaly in the literature) precedes the Sturtian

Glaciation by ∼18 Myr, is synchronous in at least two separate basins, and is followed by a prolonged interval of positive $\delta^{13}C$ values. The composite Tonian $^{87}Sr/^{86}Sr$ curve shows that, following an extended interval of low and relatively invariant values, inferred seawater $^{87}Sr/^{86}Sr$ rose ca. 880-770 Ma, and then decreased to the ca. 717 Ma initiation of the Sturtian Glaciation. These data, when combined with a simple global weathering model and analyses of the timing and paleolatitude of large igneous province eruptions and arc accretion events, suggest that the $^{87}Sr/^{86}Sr$ increase was influenced by increased subaerial weathering of radiogenic lithologies as Rodinia rifted apart at low latitudes. The following $^{87}Sr/^{86}Sr$ decrease is consistent with enhanced subaerial weathering of arc lithologies accreting in the tropics over tens of millions of years, lowering pCO_2 and contributing to the initiation of the Sturtian Glaciation.

3.2 Introduction

Life and climate evolved dramatically during the Tonian Period (1000-717 Ma). Sedimentary rocks from this period record the diversification of eukaryotic life (e.g. Knoll et al., 2006; Butterfield, 2015), large-scale fluctuations of the carbon cycle as recorded by the $\delta^{13}C$ of shallow marine carbonates (e.g. Halverson et al., 2005), and major changes to paleogeography (e.g. Li et al., 2008, 2013; Merdith et al., 2017) during the lead-up to severe Cryogenian glaciations. Understanding global change leading up to these glaciations is critical for interpreting the boundary conditions that allowed these extreme environmental conditions to occur, especially since no ice sheets are known to have existed for ∼1.5 Gyr between ca. 2.2 Ga Paleoproterozoic glaciation (Evans et al., 1997) and the ca. 717 Ma start of the Cryogenian glaciations (Macdonald et al., 2010; MacLennan et al., 2018).

The Tonian-Cryogenian Tambien Group of the Tigray region of northern Ethiopia is a mixed carbonate-siliciclastic sequence deposited in an arc-proximal basin that culminates in glacial deposits associated with the first of the Cryogenian glaciations - the Sturtian 'Snowball Earth' (Beyth et al., 2003; Miller et al., 2003; Swanson-Hysell et al., 2015b; MacLennan et al., 2018). The presence of intercalated tuffs suitable for high-precision U-Pb isotope dilution thermal ionization mass spectrometry (ID-TIMS) geochronology leading into the glaciation makes the Tambien Group a target for temporally constraining stratigraphic and isotopic datasets of the interval preceding, and leading into, the Sturtian Glaciation. For example, large-scale carbon isotopic change ca. 810-790 Ma (the Bitter Springs stage) was inferred to be globally synchronous on the basis of U-Pb ID-TIMS dates from western exposures of lower Tambien Group rocks in Ethiopia (Swanson-Hysell et al., 2015b) in conjunction with U-Pb ID-TIMS dates from Fifteenmile Group rocks in Canada (Macdonald et al., 2010). Swanson-Hysell et al. (2015b) also developed a lithostratigraphic framework for the Tambien Group that built on the prior work of Beyth (1972), Hailu (1975), and Garland (1980), and proposed that upper Tambien Group formations only had been documented in the core of the Negash Syncline at that time. However, a lack of geochronology from these strata limited the potential to test this proposed framework and develop time-calibrated

stratigraphic records.

Subsequent fieldwork led to the discovery of abundant previously unstudied exposures of upper Tambien Group stratigraphy, including Sturtian glacial deposits, in the Samre Fold-Thrust Belt (Figs. 3.1 and 3.2). These exposures provide the opportunity to produce lithostratigraphic, geochronologic, and chemostratigraphic data from the interval immediately preceding the Sturtian Glaciation. Geochronologic and δ^{13}C data from these Samre Fold-Thrust Belt exposures provide evidence for the global synchronicity of both a large-scale carbon isotopic excursion ca. 735 Ma (often referred to as the Islay anomaly in the literature, although Fairchild et al., 2018 proposed that the term should be deprecated), and separately the initiation of the Sturtian Glaciation (MacLennan et al., 2018). Tambien Group carbonates were deposited from ca. 820 Ma until 0 to 2 Myr before the onset of the Sturtian Glaciation, making the group host to what may be the most demonstrably complete carbonate stratigraphy leading into this glaciation reported to date from anywhere in the world (MacLennan et al., 2018).

This study presents new lithostratigraphic and chemostratigraphic (δ^{13}C, δ^{18}O, and ^{87}Sr/^{86}Sr) data, and additional U-Pb ID-TIMS dates from zircons, from the lower Tambien Group in the Mai Kenetal Syncline and the upper Tambien Group in the Negash Syncline and the newly mapped Samre Fold-Thrust Belt. With these data, we construct the most complete and temporally well-constrained pre-Sturtian chemostratigraphic composite record to date, which we use to assess the nature of pre-glacial carbon isotope anomalies and the role of changing global weathering fluxes on the initiation of the Sturtian Glaciation.

3.3 Geological Setting

The Arabian-Nubian Shield is a region of Neoproterozoic juvenile crust with an area of $\sim 2.7 \times 10^6$ km^2 that makes up the northern portion of the East African Orogen (Fig. 3.1; Johnson, 2014). Its construction began with arc and back-arc volcanism generating juvenile crust starting at ca. 858 $\pm$ 7 Ma (sensitive high-resolution ion microprobe (SHRIMP) U-Pb date on zircons from a gneiss of oceanic arc affinity; Küster et al., 2008) and continuing through the Tonian into the Cryogenian until final terrane accretion in the Ediacaran at ca. 620 Ma (closure of basin constrained by inductively coupled plasma mass spectrometry (ICP-MS) U-Pb dates on detrital zircons and felsic magmatism intruding ophiolites; Cox et al., 2012; Johnson, 2014; Cox et al., 2018a). The paleogeographic setting in which arc volcanism began is poorly constrained, although it has been proposed that the ocean basin in which this volcanism occurred (known as the Mozambique Ocean) formed as the result of rifting between the Indian, Saharan, and Congo-Tanzanian cratons (Johnson et al., 2011). However, it is well constrained that this juvenile crust amalgamated as East Gondwana (Indian craton) and West Gondwana (Saharan and Congo-Tanzanian cratons) collided in the Ediacaran resulting in the East African Orogeny (Stern, 1994; Fritz et al., 2013).

The East African Orogeny spanned over 6000 km from the Middle East to Madagascar (Collins and Windley, 2002; Johnson, 2014). In general, metamorphic grade in the Arabian-

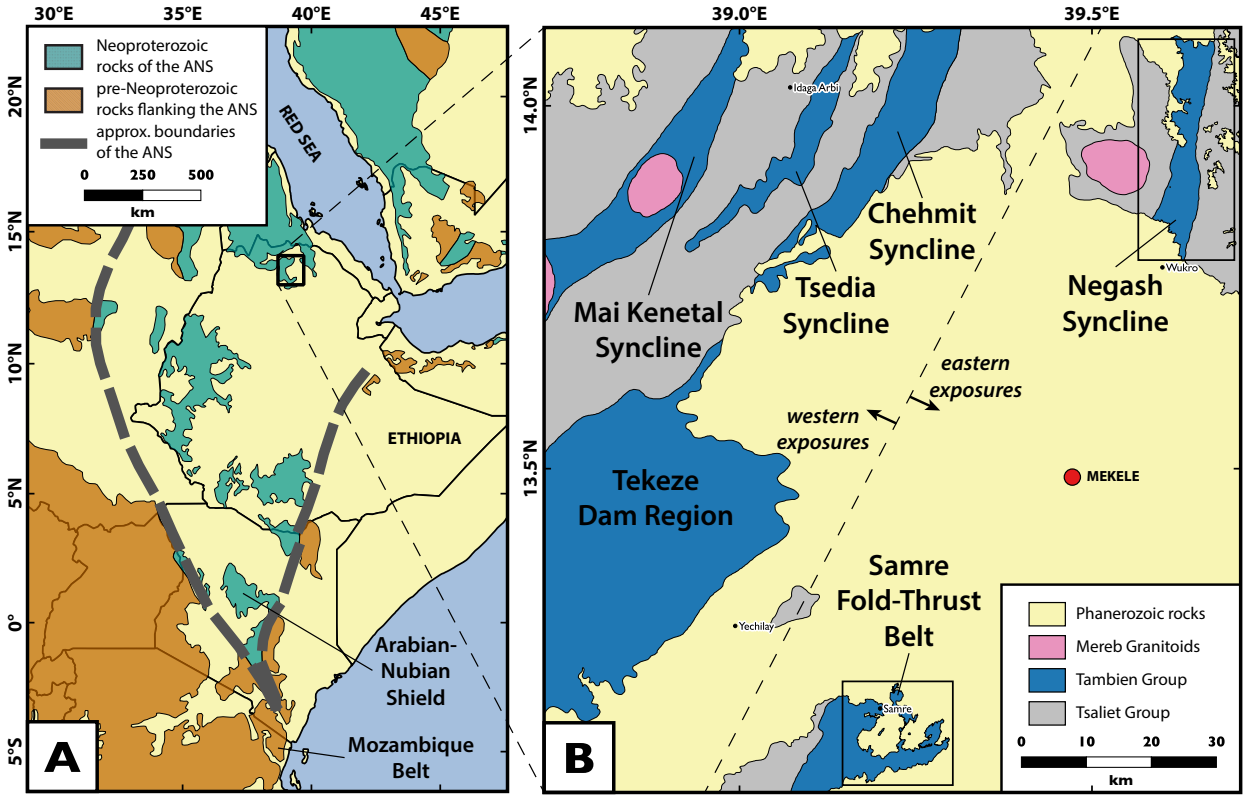

Figure 3.1: **A)** Overview geologic map of exposures of the Arabian-Nubian Shield (ANS) and adjacent Archean rocks (simplified from Johnson, 2014). **B)** Overview geologic map of Tambien Group exposures in northern Ethiopia. Inset boxes show the locations of detailed geological maps of the Negash Syncline and Samre Fold-Thrust Belt (Fig. 3.2), where sedimentary rocks interpreted to be glacigenic of the Negash Formation have been identified. The dashed line separates what we define as the western and eastern Neoproterozoic exposures in this study.

Nubian Shield increases from sub-greenschist and greenschist facies in the north to granulite facies in the south, where the Arabian-Nubian Shield transitions into higher grade metamorphic rocks of continental affinity known as the Mozambique Belt (Fig. 3.1; Johnson et al., 2011). This overall northward decrease in metamorphic grade allows for the preservation of primary sedimentary structures and geochemical signals in the Arabian-Nubian Shield. As a result, sedimentary rocks in this area are a viable target for reconstructing surface processes and environments at the time of deposition.

The Tambien Group (Fig. 3.1) is a Tonian-Cryogenian (ca. 820-700 Ma) sequence of carbonate and siliciclastic sedimentary rocks that culminates in a diamictite that has been interpreted to correlate with the ca. 717-660 Ma Sturtian Glaciation (Beyth et al., 2003; Alene et al., 2006; Miller et al., 2009; Swanson-Hysell et al., 2015b; MacLennan et al., 2018). This sequence was deposited on top of the Tsaliet Group, which consists of volcanic and

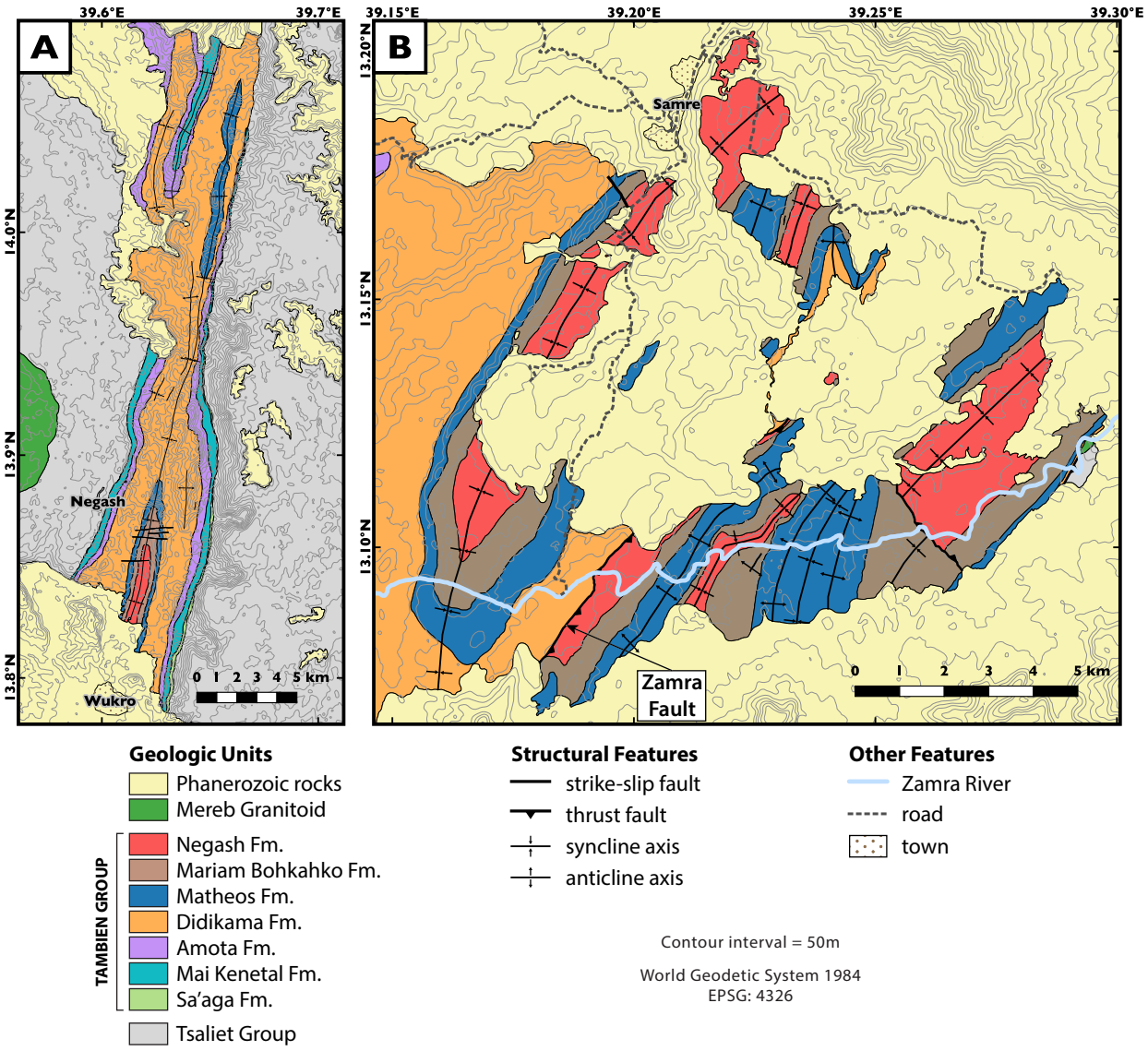

Figure 3.2: Geologic maps of the upper Tambien Group corresponding to inset boxes in Figure 3.1. **A)** Negash Syncline geologic map synthesized from Beyth et al. (2003) and new mapping. **B)** Samre Fold-Thrust Belt geologic map based on new mapping. There are notable differences in lithostratigraphy across the major NE-striking thrust fault, which we refer to as the Zamra Fault.

volcaniclastic lithologies correlated with 854 ± 3 Ma Eritrean volcanics (Pb-Pb evaporation date; Teklay, 1997) that are associated with Arabian-Nubian Shield island arc volcanism. A maximum depositional age near the top of the Tsaliet Group (within 75 m of the Tsaliet-Tambien group contact) of 821.2 ± 1.5 Ma, and an eruptive age near the base of the Tambien Group (∼150 m above the Tsaliet-Tambien group contact) of 815.29 ± 0.32 Ma (U-Pb ID-

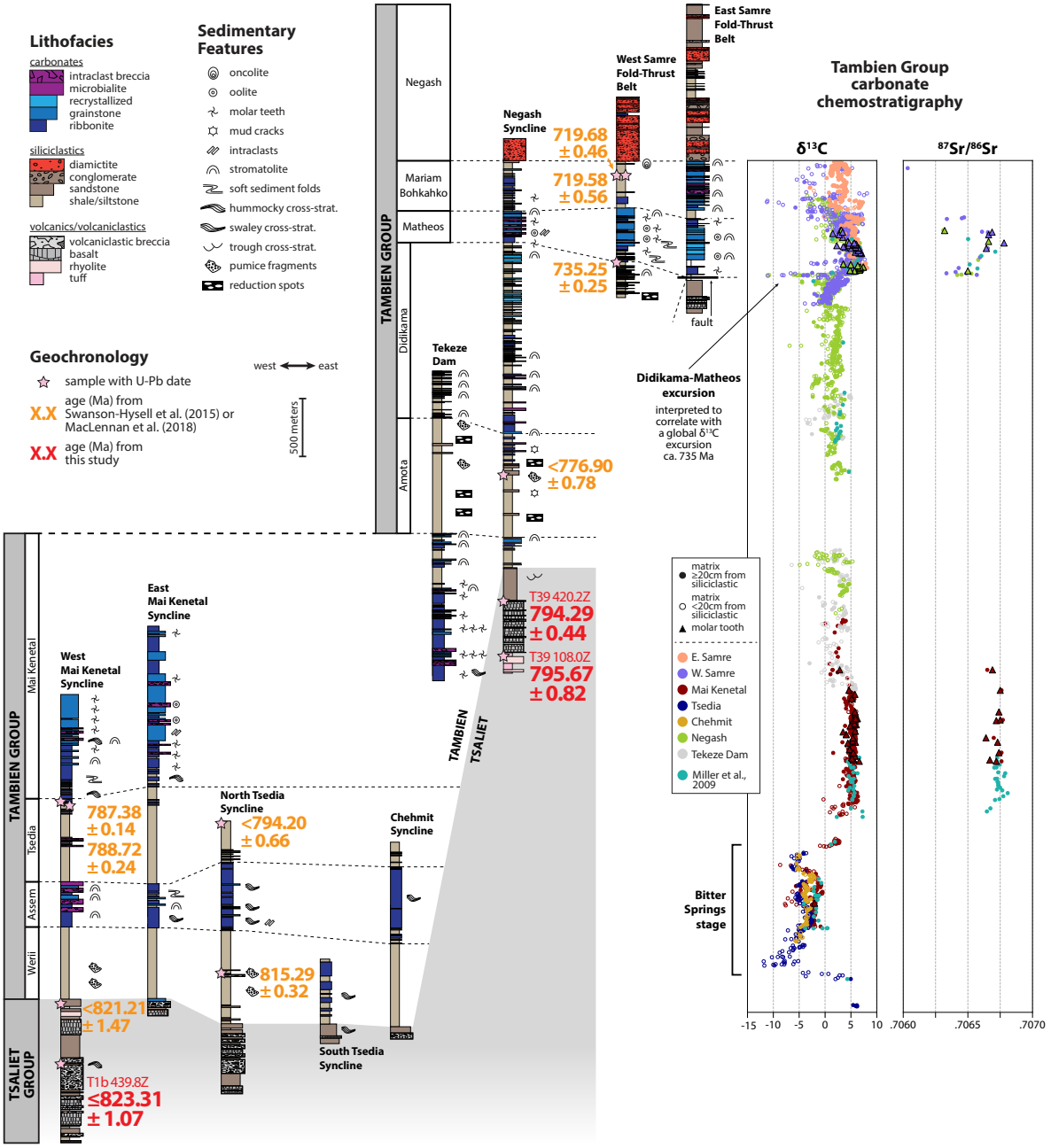

Figure 3.3: Representative simplified stratigraphy and $\delta^{13}C$ and $^{87}Sr/^{86}Sr$ chemostratigraphy of the Tambien Group. For the $\delta^{13}C$ chemostratigraphy, open circles denote samples that are <20 cm from the closest siliciclastic unit. Data from the Tsedia Syncline resolve the onset of the Bitter Springs stage in Ethiopia, and data from the Samre Fold-Thrust Belt and the Negash Syncline resolve the recovery from the nadir of a large negative $\delta^{13}C$ excursion (the Didikama-Matheos excursion, detailed in Fig. 3.8). U-Pb ID-TIMS dates are in units of Ma with uncertainties corresponding to the analytical uncertainty, which can be used for comparison between these dates since they were developed using the same tracer. Orange dates are from Swanson-Hysell et al. (2015b) or MacLennan et al. (2018), and red dates are from this study. These dates show that the transition from the volcanism of the Tsaliet Group to the sedimentation of the Tambien Group occurred significantly later in the Negash Syncline than in exposures further to the west.

TIMS on zircon; Swanson-Hysell et al., 2015b) constrains the age of the Tsaliet-Tambien group transition in the west (Fig. 3.3). U-Pb ID-TIMS dates of 719.58 ± 0.56 and 719.68 ± 0.46 Ma from tuffs ∼80 m below the Negash Formation glacial deposits provide the best available maximum age constraints on those deposits and are consistent with a ca. 717 Ma onset of glaciation in the basin (Fig. 3.3; MacLennan et al., 2018). The strata subsequently were folded into a series of synclines with fold axes oriented NNE-SSW (Fig. 3.1B) during the East African Orogeny (Stern, 1994), with maximum metamorphic temperatures estimated to have reached <250°C based on chlorite thermometry (Alene, 1998). Synchronous with and following this deformation was the emplacement of granitoid plutons, known as the Mereb Granitoids, into the Tambien Group (Fig. 3.1) with dates of ca. 610 Ma (U-Pb SHRIMP and Pb-Pb evaporation; Miller et al., 2003; Avigad et al., 2007).

3.4 Methods

Field Methods

Tambien Group rocks near the town of Samre in the Tigray region of northern Ethiopia previously were mapped as 'undifferentiated Neoproterozoic sedimentary rocks' (Arkin et al., 1971), and no Neoproterozoic diamictite from the region was reported in the literature, with the notable exception of a brief mention in Bussert (2010). Our geologic mapping of this area has revealed extensive exposures of upper Tambien Group strata including large areas of diamictite within a series of folds (Fig. 3.2). We refer to this area as the Samre Fold-Thrust Belt, and differentiate units within it based on the stratigraphic framework developed in the Negash Syncline (Swanson-Hysell et al., 2015b) since the lithostratigraphy of the strata correlates well between the two areas (Fig. 3.3). Stratigraphic sections with good exposure were identified and measured using a Jacob's staff in both the Negash Syncline and the Samre Fold-Thrust Belt. During the measurement of these sections, carbonate samples with minimal visible alteration were collected for geochemical analyses at a resolution of ∼0.5-5 m (depending on proximity to other measured sections) where the stratigraphy is carbonate dominated, and wherever possible where the stratigraphy is siliciclastic dominated.

Geochemical Analyses

Carbonate samples were cut perpendicular to bedding to expose a fresh surface before micro-drilling. Visibly altered zones of the fresh surface, such as those exhibiting veins and/or fractures, were avoided. The subsequent analyses described here were performed on aliquots of these micro-drilled powders.

Previous work has determined that molar tooth structures typically consist of high purity microspar calcite relative to the surrounding micrite host (Smith, 1968; Fairchild et al., 1997; Pratt, 1998). These structures appear as subvertical dual-tapered carbonate-cement-filled cracks that are generally <1 cm wide, and historically their plan view was interpreted

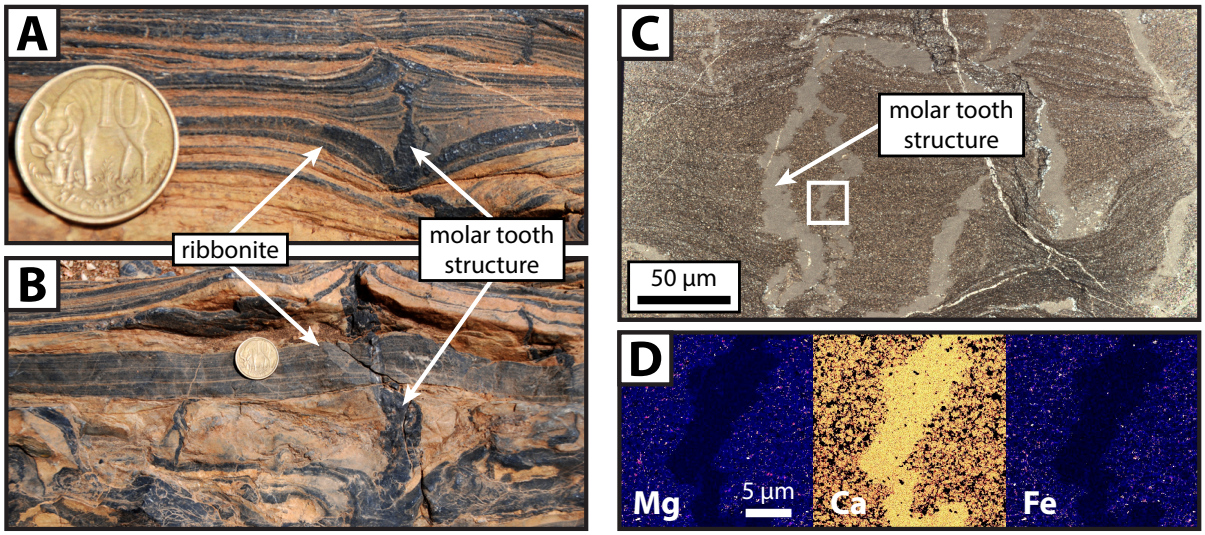

Figure 3.4: Molar tooth structures from the Tambien Group. **A)** and **B)** Photographs in cross-section view of molar tooth structures from the Mai Kenetal Formation, showing differential compaction of carbonate ribbonite around the structures. The 10 cent of Ethiopian birr coin used for scale has a diameter of 23 mm. **C)** Photomicrograph in cross-section view of molar tooth structures within ribbonite of the Mariam Bohkahko Formation from the Negash Syncline taken using cross-polarized light. Inset box shows field of analysis for D. **D)** Wavelength-dispersive x-ray spectroscopy elemental maps of a molar tooth structure, with warmer colours indicating higher concentration. The maps show the high purity of the microspar calcite in the molar tooth structures relative to the surrounding micrite matrix. Low Mg and high Ca suggests undolomitized calcite, and low Fe suggests a lack of a clay component or Fe-rich carbonate.

to resemble the upper surface of elephant molar teeth (Fig. 3.4; Bauerman, 1884; Daly, 1912). The differential compaction of sediment around molar tooth structures, which typically are crumpled perpendicular to bedding planes, requires that molar tooth structures formed prior to or during compaction and dewatering of the sediment. Hypotheses of molar tooth structure crack formation are varied and include subaqueous shrinkage cracks (Smith, 1968), the expansion of gas from organic decay (Pollock et al., 2006), wave-induced cracking due to heaving of sediment (Bishop and Sumner, 2006), or microbial conversion of smectite to illite coupled with wave loading (Hodgskiss et al., 2018). Regardless of the mode of crack formation, precipitation of calcite cement within the cracks requires significant throughput of seawater prior to or during dewatering and lithification of the host carbonate mud.

Molar tooth structures occur in a number of formations in the Tambien Group (Fig. 3.3), often in ribbonite (thinly bedded wavy- to parallel-laminated fine-grained limestone) that can exhibit swaley cross-stratification. Petrographic analysis shows that these structures consist of high purity calcite microspar, whereas the surrounding micrite can have a clay component (Fig. 3.4). Furthermore, in samples where the surrounding micrite is partially dolomitized,

molar tooth structures are not (Fig. 3.4), suggesting that the structures are more resistant to dolomitization. Therefore, wherever possible, molar tooth structure microspar calcite was targeted for geochemical analyses along with the host bulk carbonate matrix.

δ^{13}C and δ^{18}O

Carbonate powders were weighed out to 1 mg and heated to 110°C to remove any residual water. Samples then were reacted with 250 μL of H_3PO_4 at 75°C. The resulting CO_2 gas was extracted using a GasBench II auto-sampler and analyzed on a SerCon Callisto continuous-flow isotope ratio mass spectrometry (CF-IRMS) system at Princeton University to obtain δ^{13}C and δ^{18}O values. Powders of NBS-19 (δ^{13}C = 1.95‰ and δ^{18}O = -2.20‰) and an internally calibrated standard (δ^{13}C = -1.48 ± 0.1‰ and δ^{18}O = -8.54 ± 0.1‰) also were analyzed once every 10 samples to calibrate the sample measurements. Typical measured precision was σ = 0.1‰ for δ^{13}C and σ = 0.2‰ for δ^{18}O.

Elemental Analysis

Carbonate powders were weighed out to 10 mg and then reacted with 10.0 mL of pH = 4.9 buffered acetic acid solution (3 mL of glacial acetic acid and 3 mL of ammonium hydroxide for every 497 mL of water) for 4-5 hours in a 25°C sonicator. Samples then were centrifuged, and 0.8 mL of the solution was extracted and mixed with 7.2 mL of 2% HNO_3. These diluted samples were simultaneously analyzed for Al, Ca, Fe, Mg, Mn, K, Na, and Sr on a Perkin Elmer 5300 DV inductively coupled plasma optical emission spectrometer (ICP-OES) in the College of Natural Resources at UC Berkeley. Raw measurements were transformed into concentrations using 6 internal standards of known concentration with 2% HNO_3 matrix (diluted from a commercial standard of known concentration). Standard concentrations bracketed the concentrations observed in samples. When the known concentrations were plotted against measured intensity, linear fits through these 6 standards produced R^2>0.98 for Al and K, R^2>0.999 for Ca, Mg, and Na, and R^2>0.9999 for Fe, Mn, and Sr.

^{87}Sr/^{86}Sr

Carbonate powders were weighed out to ∼30 mg and washed 3 times in a 1.0 mL 1:1 methanol:water solution to encourage the suspension of clays (McArthur et al., 2006). The samples then were reacted in an ultrasonic bath 3 times with 1.0 mL of 0.2 M ammonium acetate to remove loosely bound Sr cations and rinsed in an ultrasonic bath 3 times with ultrapure water to remove residual ammonium and clay. These cleaned samples then were reacted with 1.0 mL of 0.5 M acetic acid, and any insoluble residue was removed via a centrifuge. The sample solutions then were dried down using heating lamps in a nitrogen atmosphere and then reacted with 250 μL of 6 M HNO_3. Sr was isolated via standard column chemistry techniques using 100-150 μm Sr-spec resin, dried down again with 3 drops of 15 M HNO_3, and then loaded onto single rhenium filaments in H_3PO_4 with a $TaCl_5$ activator. Strontium isotopes were measured on a ThermoFisher Triton thermal ionization

mass spectrometer (TIMS) at the Center for Isotope Geochemistry at UC Berkeley using a static multicollection routine. Mass discrimination was corrected to $^{86}Sr/^{88}Sr = 0.11940$. A minor correction ratio of <1.00003 also was applied to the raw data to match the $^{87}Sr/^{86}Sr$ of blanks with NBS-987 ($^{87}Sr/^{86}Sr = 0.710245$), which was analyzed alongside the samples.

U-Pb Geochronology

Zircons were extracted from rock samples at Princeton University by crushing using a jaw crusher and disc mill followed by magnetic and gravimetric separation. The zircon separates were annealed in quartz crucibles at 900°C for 48 to 60 hours. Individual zircons were photographed and transferred to microcapsules, after which 100 μg of 29 M HF and 15 μg of 30% HNO_3 were added. The microcapsules were put into a Parr bomb and placed in an oven at 195°C for 12 hours to chemically abrade the zircons, preferentially targeting metamict and damaged parts of the zircon that have undergone Pb loss. After chemical abrasion, the zircon grains were rinsed in ten steps of alternating distilled 6 N HCl, 30% HNO_3 and MQ water. Distilled HF and HNO_3 were again added, as well as the EARTHTIME ET535 tracer solution (Condon et al., 2015; McLean et al., 2015), before total dissolution at 210°C for 48 hours. After total dissolution, the solutions were dried down and converted to chlorides. U and Pb separation was performed using ion exchange resin (Eichrom 200-400 mesh chloride form).

The U and Pb cut was dried down with a microdrop of dilute H_3PO_4. The dried U-Pb fraction was redissolved in a silica gel emitter, and deposited onto outgassed zone-refined Re filaments. U and Pb isotopic measurements were made using an IsotopX PhoeniX-62 TIMS at Princeton University. Pb analyses were performed in peak hopping mode on a Daly photomultiplier ion counting detector. Depending on the signal intensity, U measurements were made either on the Daly photomultiplier in peak hopping mode or as a static measurement on the Faraday cups connected to 10^{12} ohm resistor boards. U was measured as an oxide. The Pb and U deadtime characteristics of the Daly photomultiplier were monitored by running NBS982 and CRM U500 on a weekly basis. The NBS982 runs also were used to quantify Pb mass-dependent fractionation. Unless stated otherwise, all U-Pb uncertainties reported in this manuscript are the internal (analytical) uncertainties in the absence of all external or systematic errors, with these additional uncertainties reported in Table 3.1.

3.5 Lithostratigraphy

From oldest to youngest, nine formations within the Tambien Group have been differentiated: the Werii, Assem, Tsedia, Mai Kenetal, Amota, Didikama, Matheos, Mariam Bohkahko, and Negash formations (Figs. 3.2 and 3.3; Swanson-Hysell et al., 2015b). In the Negash Syncline, the Negash Formation is limited in aerial extent to ~3 km^2 and is more penetratively foliated than most of the Tambien Group since it is only exposed in the southern-most core of the syncline (Fig. 3.2). Our team's mapping now has differentiated extensive exposures of

Table 3.1: Summary of CA-ID-TIMS $^{206}Pb/^{238}U$ dates from the Tsaliet and Tambien groups.

Sample	Description and Formation/Group	Latitude Longitude	$^{206}Pb/^{238}U$ Date (Ma)	Type	Reference
T1-12.3	volcaniclastic unit upper Tsaliet Grp.	14.0444°N 38.9554°E	<821.2 ±1.5	maximum depositional age from youngest concordant single crystal	Swanson-Hysell et al., 2015b
TS22	tuff Werii Fm.	14.0382°N 39.1079°E	815.29 ±0.32/0.46/0.99	eruptive age from weighted mean (MSWD=0.52, n=5)	Swanson-Hysell et al., 2015b
TS23	siltstone Tsedia Fm.	14.0379°N 39.1298°E	<794.20 ±0.66	maximum depositional age from youngest concordant single crystal	Swanson-Hysell et al., 2015b
T2	tuff upper Tsedia Fm.	14.0437°N 38.9733°E	788.72 ±0.24/0.40/0.94	eruptive age from weighted mean (MSWD=1.2, n=6)	Swanson-Hysell et al., 2015b
T1-1202	tuff upper Tsedia Fm.	14.0482°N 38.9757°E	787.38 ±0.14/0.35/0.91	eruptive age from weighted mean (MSWD=18, n=7)	Swanson-Hysell et al., 2015b
T22-453	volcaniclastic unit Amota Fm.	13.8436°N 39.6397°E	<776.90 ±0.78	maximum depositional age from youngest concordant single crystal	Swanson-Hysell et al., 2015b
T46-102.2Z	tuff lower Matheos Fm.	13.1588°N 39.2512°E	735.35 ±0.25/0.39/0.88	eruptive age from weighted mean (MSWD=0.36, n=5)	MacLennan et al., 2018
SAM-ET-04	tuff upper Mariam Bohkahko Fm.	13.1398°N 39.1763°E	719.68 ±0.46/0.54/0.94	eruptive age from weighted mean (MSWD=1.3, n=8)	MacLennan et al., 2018
SAM-ET-03	tuff upper Mariam Bohkahko Fm.	13.1398°N 39.1761°E	719.58 ±0.56/0.64/1.0	eruptive age from weighted mean (MSWD=0.54, n=3)	MacLennan et al., 2018
T1b-439.8Z	lava flow Tsaliet Grp.	14.0445°N 38.9522°E	<823.3 ±1.1	maximum eruptive age from youngest concordant single crystal	this study
T39-108.0Z	ignimbrite Tsaliet Grp.	13.8488°N 39.6523°E	795.67 ±0.82/0.89/1.2	eruptive age from weighted mean (MSWD=0.084, n=3)	this study
T39-420.2Z	tuff Sa'aga Fm. of the Tsaliet Grp.	13.8509°N 39.6499°E	794.29 ±0.44/0.51/0.99	eruptive age from weighted mean (MSWD=0.21, n=5)	this study

Notes:
2σ uncertainties are reported in the format ± X/Y/Z, where X is the internal (analytical) uncertainty in the absence of all external or systematic errors, Y is the uncertainty incorporating the U-Pb tracer calibration error, and Z is the uncertainty including X and Y, as well as the uranium decay constant uncertainty; MSWD = mean square of weighted deviates; n = number of zircon analyses included in the calculated date.

the Negash Formation, along with further exposures of the underlying strata, in the Samre Fold-Thrust Belt (Figs. 3.1 and 3.2).

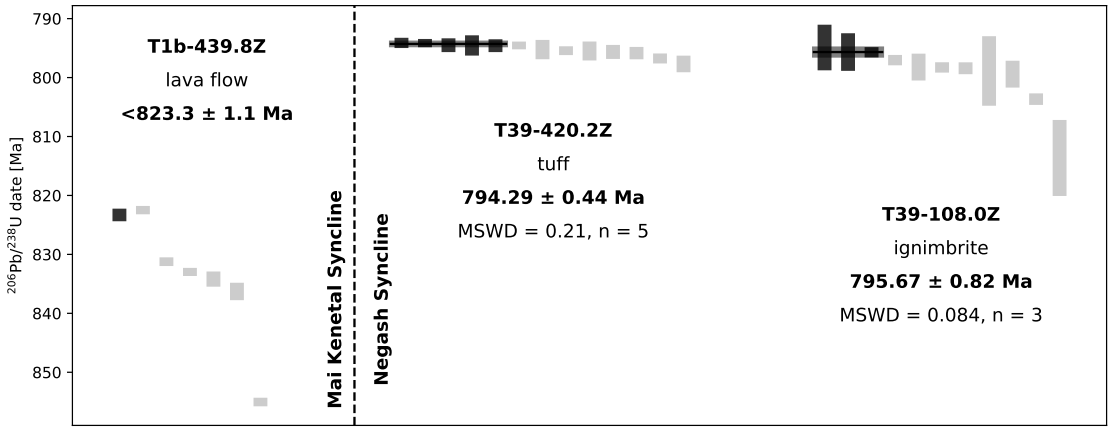

Figure 3.5: U-Pb ID-TIMS analyses for individual zircon grains. T1b-439.8Z is from the Tsaliet Group in the Mai Kenetal Syncline, and T39-420.2Z and T39-108.0Z are from the Tsaliet Group in the Negash Syncline (Fig. 3.3). Vertical bars represent the 2σ uncertainty for the $^{206}Pb/^{238}U$ date of each zircon. Black vertical bars represent zircons included in the calculation of the weighted mean. Reversely discordant zircons are not shown. Horizontal lines and grey bars represent the calculated weighted means and 2σ uncertainties respectively. MSWD = mean square of weighted deviates; n = number of zircon analyses included in the calculated date. Concordia diagrams, data tables, and sample photos are included in the *Supporting Information*.

Western Exposures

In broad terms, mapping of the Tambien Group to date has revealed that older formations are exposed in the western synclines and younger formations are exposed in the eastern synclines, with the Tekeze Dam Region in the southwest exposing stratigraphy that links the two areas (Swanson-Hysell et al., 2015b, building upon the work of Beyth, 1972, Hailu, 1975, and Garland, 1980). We define western Neoproterozoic exposures as the Mai Kenetal Syncline, Tsedia Syncline, Chehmit Syncline, and Tekeze Dam Region (Fig. 3.1). Lithostratigraphic correlation between these four areas is relatively straightforward, although there is notable lateral variability (Fig. 3.3). The lithostratigraphic framework of these western exposures, as well as $\delta^{13}C$ and geochronologic data from these areas, were developed by Swanson-Hysell et al. (2015b). This study adds to this previous work by describing in detail the lithostratigraphy of the western exposures, adding an age constraint to the upper Tsaliet Group in the Mai Kenetal Syncline, developing new $\delta^{13}C$ data from previously unreported limestone ribbonite horizons within the Werii Formation in the southwestern Tsedia Syncline,

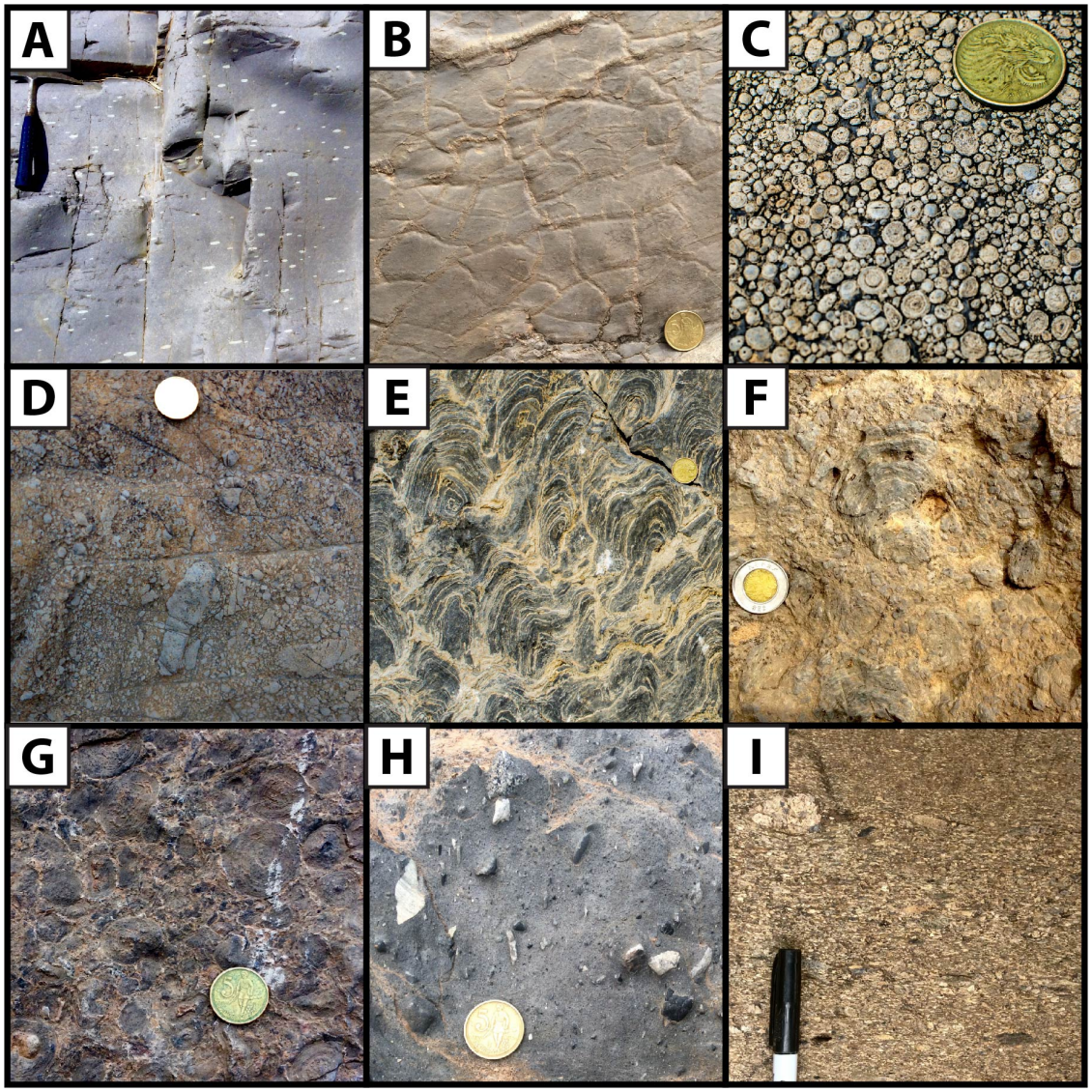

Figure 3.6: Photos of key lithofacies of the Tambien Group. **A)** Reduction spots within siltstones of the Amota Formation in the Negash Syncline. **B)** Mud cracks within siltstones of the Amota Formation in the Negash Syncline. **C)** Oolite within the Matheos Formation in the Samre Fold-Thrust Belt. **D)** Limestone intraclast breccia within the Matheos Formation in the Samre Fold-Thrust Belt. **E)** Stromatolites at the base of the Mariam Bohkahko Formation in the western Samre Fold-Thrust Belt. **F)** Carbonate breccia containing stromatolites from the Mariam Bohkahko Formation in the eastern Samre Fold-Thrust Belt. **G)** Oncolite from near the top of the Mariam Bohkahko Formation in the Samre Fold-Thrust Belt. **H)** Diamictite of the Negash Formation in the Samre Fold-Thrust Belt. **I)** Lithic arkose coarse sandstone with sparse pebbles of the Negash Formation in the Samre Fold-Thrust Belt. The hammer used for scale in A has a length of 33 cm. The 5 cent of Ethiopian birr coin used for scale in B, C, D, E, G and H has a diameter of 20 mm. The 1 Ethiopian birr coin used for scale in F has a diameter of 27 mm. The pen used for scale in I has a width of 1 cm. All photos are in cross-section views except B, which is of a bedding plane.

and developing new $^{87}Sr/^{86}Sr$ data from the Mai Kenetal Formation (Fig. 3.3). These $^{87}Sr/^{86}Sr$ data add to those developed in Miller et al. (2009).

Tsaliet Group

The Tsaliet Group comprises basaltic to intermediate lava flows, volcaniclastic breccias, and ignimbrites (Fig. 3.3). The lava flows can have vesiculated flow tops and are sometimes porphyritic with cm-scale tabular plagioclase phenocrysts. The volcaniclastic breccias have clasts as large as boulders and dominate portions of the group where there are few flows. The presence of flows and the ubiquity of large volcanic clasts in the breccias suggest that deposition of the Tsaliet Group would have happened on, or adjacent to, an active arc.

A maximum depositional age of 821.2 ± 1.5 Ma (youngest concordant zircon U-Pb ID-TIMS date) from a volcaniclastic unit in the Mai Kenetal Syncline within 75 m of the top of the Tsaliet Group (Swanson-Hysell et al., 2015b) was the best available constraint on the start of Tambien Group deposition. In this study, we report a U-Pb ID-TIMS date of 823.3 ± 1.1 Ma from the youngest concordant zircon grain analyzed within a lava flow ∼250 m below the top of the Tsaliet Group of the western limb of the Mai Kenetal Syncline. This result constrains the flow to be this age or younger, since no consistent age population of multiple zircons was identified in the analyzed sample (Figs. 3.3 and 3.5; Table 3.1).

Werii Formation

The Werii Formation is a ∼400-500 m thick sequence of siltstones and very fine sandstones exposed in the Mai Kenetal, Chehmit, and Tsedia synclines, except in the southwestern Tsedia Syncline where previously unreported limestone ribbonite horizons are interbedded within siltstones (Fig. 3.3). The transition from the Tsaliet Group to the Werii Formation appears conformable where observed with decreasing volcaniclastics up stratigraphy. An eruptive U-Pb ID-TIMS age of 815.29 ± 0.32 Ma from a welded volcanic tuff with pumice fragments 150 m above the base of the Werii Formation in the Tsedia Syncline (Swanson-Hysell et al., 2015b) is consistent with this interpretation of conformable deposition when compared to the age constraints within the upper Tsaliet Group.

The strata contains large (up to 50 cm) hyper-vesiculated scoria bombs in the proximity of the tuff that yields the 815.29 ± 0.32 Ma age. The presence of these bombs indicates that arc volcanism remained nearby and active during the deposition of the Werii Formation, but was more distal than during the deposition of flows and volcaniclastic breccias of the Tsaliet Group.

Assem Formation

A transition into carbonate-dominated stratigraphy marks the beginning of the Assem Formation, which is ∼200-300 m thick and exposed in the Mai Kenetal, Chehmit, and Tsedia synclines (Fig. 3.3). There is significant west-east lateral facies variability in the Assem Formation. In the Mai Kenetal Syncline, ribbonite dominates at the base of the formation,

and transitions upwards into microbialaminite, stromatolite, and intraclast breccia horizons. This sequence of lithofacies suggests shallowing through the deposition of the Assem Formation such that the upper part of the formation was deposited in a high energy environment within the photic zone. To the east, in the Tsedia and Chehmit synclines, the formation is dominated by ribbonite with swaley cross-stratification likely developed by the combined flow of storm waves. This west-east variability suggests transportation of carbonate mud from a shallow-water microbial carbonate factory in the west out to greater depths to the east.

Tsedia Formation

The Tsedia Formation is ∼500 m thick and characterized by siltstones interbedded with cm-scale carbonates. The formation is exposed in the Mai Kenetal, Chehmit, and Tsedia synclines, and has a transitional contact with the underlying carbonate-dominated Assem Formation (Fig. 3.3). The full thickness of the Tsedia Formation only is known to be exposed within the Mai Kenetal Syncline, as the formation is the highest level of the stratigraphy exposed in the other places it has been mapped (Tsedia and Chehmit synclines). However, exposure of the Tsedia Formation is poor throughout the Mai Kenetal Syncline, with the best exposures as it transitions into the overlying Mai Kenetal Formation.

U-Pb ID-TIMS dates within the Tsedia Formation constrain its age: from the Tsedia Syncline there is a maximum depositional age constraint of 794.20 ± 0.66 Ma from detrital zircons within a siltstone near the base of the formation, and from the Mai Kenetal Syncline there are eruptive ages of 788.72 ± 0.24 and 787.38 ± 0.14 Ma (Swanson-Hysell et al., 2015b). These latter two eruptive dates are from tuffs with feldspar phenocrysts ∼25 m below the base of the Mai Kenetal Formation.

Mai Kenetal Formation

Similar to the Werii-Assem formation contact, the Tsedia-Mai Kenetal formation contact is marked by a transition into the carbonate-dominated stratigraphy of the ∼1400 m thick Mai Kenetal Formation. In the western exposures, the formation is exposed in the Mai Kenetal Syncline and Tekeze Dam Region (Fig. 3.3). The lower part of the formation consists of ribbonite carbonate with abundant hummocky and swaley cross-stratification occasionally interbedded with siltstones, suggesting deposition at intermediate depths that commonly experienced combined waves and currents below fair weather base. These strata transition into a series of <10 m thick shallowing-upward parasequences defined by siltstone, ribbonite, grainstone, and intraclast breccia. Well-developed molar tooth structures (Figs. 3.4 and 3.6) are abundant throughout the formation. This formation represents the youngest rocks of the Tambien Group known to be exposed in the Mai Kenetal Syncline.

Amota Formation

The Amota Formation is a ∼500 m thick siliciclastic unit exposed in the Tekeze Dam Region and the Negash Syncline of the eastern exposures (Fig. 3.3). The formation's base is transitional and marked by the last carbonate horizon before hundreds of meters of fine-grained siliciclastic lithofacies. Reduction spots (flattened green ellipsoids ∼1-3 cm long) frequently contrast against the purple of the siltstones within this formation (Fig. 3.6). In some cases, the reduction spots are cored with recrystallized minerals, including chlorite, that may have originated as pumice that sank into the depositional environment of the siltstone. In the Tekeze Dam Region, the formation comprises relatively homogenous purple siltstones with rare sandstone interbeds.

Didikama Formation

Like the Amota Formation, the only documented exposure of the Didikama Formation in the western exposures is in the Tekeze Dam Region (Fig. 3.3). The formation represents the highest exposed stratigraphy of the Tambien Group currently recognized in the western exposures. The formation's base is marked by the initial appearance of carbonates, which often are extensively dolomitized and recrystallized resulting in pale brown carbonate beds interbedded with siltstones. Primary features within the carbonates of the formation can be obscured by the recrystallization associated with dolomitization, but in places primary ribbonites and grainstones can be identified. Stromatolites also are found in the formation at the top of shallowing-upward parasequences comprised of ribbonites, grainstones, and siltstones. Taken together, these lithofacies are indicative of deposition in a generally shallow-water environment.

Eastern Exposures

For the purposes of this discussion, we define eastern Neoproterozoic exposures as the Negash Syncline and the Samre Fold-Thrust Belt (Figs. 3.1 and 3.2). Stratigraphy between these two regions is broadly similar, although there is important lateral variability.

The Werii, Assem, Tsedia, Mai Kenetal, Amota, and Didikima formations in the western exposures can be stratigraphically linked to the Mai Kenetal, Amota, Didikama, Matheos, Mariam Bohkahko, and Negash formations in the eastern exposures by Mai Kenetal, Amota, and Didikama formation stratigraphy exposed in the Tekeze Dam Region (Fig. 3.3; Swanson-Hysell et al., 2015b). The lithostratigraphic framework of the Negash Syncline, as well as δ^{13}C data and one age constraint from that area, were developed previously by Swanson-Hysell et al. (2015b). MacLennan et al. (2018) added to this work by presenting initial δ^{13}C and geochronologic data from the Samre Fold-Thrust Belt. This study presents the first geologic map of the Samre Fold-Thrust Belt, describes the lithostratigraphy of the eastern exposures in detail, adds two age constraints to the upper Tsaliet Group in the Negash Syncline, develops additional δ^{13}C data from the Negash Syncline and Samre Fold-Thrust

Belt, and presents $^{87}Sr/^{86}Sr$ data from the Negash Syncline and Samre Fold-Thrust Belt (Fig. 3.3).

Tsaliet Group

Similar to the exposures in the west, the Tsaliet Group in the eastern exposures in the proximity of the Tambien Group comprises basaltic to intermediate lava flows, volcaniclastic breccias, and ignimbrites. However, its contact with the Tambien Group in the eastern exposures is different from that in the west. Where this contact is exposed in the Negash Syncline, the top ∼150 m of the Tsaliet Group comprises immature sandstone dominated by basaltic lithic clasts (the Sa'aga Formation; Fig. 3.3). The Sa'aga Formation sandstone contains large dune-scale cross-beds with faint pinstripe laminations and coset thicknesses of up to 2 m, suggesting an aeolian depositional environment. This lithofacies indicates subaerial deposition on weathering arc volcanics as the basin transitioned from Tsaliet Group volcanics into Tambien Group marine sediments. We present eruptive ages of 794.29 ± 0.44 Ma from a 30 cm thick rhyolitic tuff near the base of the immature sandstone, and 795.67 ± 0.82 Ma from an ignimbrite ∼300 m below the rhyolitic tuff within the volcanic succession (U-Pb ID-TIMS on zircon; Figs. 3.3 and 3.5; Table 3.1). These ages are ∼25 Myr younger than the contact between the Tsaliet and Tambien groups in the western exposures, which is constrained to be between 821.2 ± 1.5 and 815.29 ± 0.32 Ma (Fig. 3.3). Previous correlation schemes of the Tambien Group interpreted the Didikama Formation in the Negash Syncline to correlate with the Assem Formation in the west, and the Matheos Formation in the Negash Syncline to correlate with the Mai Kenetal Formation in the west (Alene et al., 2006; Miller et al., 2009). These dates indicate that Tambien Group deposition was not occurring in the east at the time that Tambien Group deposition began in the west, and that the Didikama Formation does not correlate to the Assem Formation. Rather, the Tsaliet-Tambien group contact is significantly diachronous across the region, with local volcanism continuing to generate the lava flows of the Tsaliet Group in the east while Tambien Group sediment deposition had already begun in the west. Sedimentation across the eastern region was ongoing by ca. 793 Ma.

In the Samre Fold-Thrust Belt, the Tsaliet Group only has been mapped in a small area at the eastern limit of Neoproterozoic exposure in this locality (Fig. 3.2). In that area, basaltic to intermediate lava flows are overlain by immature sandstone, similar to what is observed at the top of the Tsaliet Group in the Negash Syncline. However, the immature sandstone in the Samre Fold-Thrust Belt lacks cross-stratification and pinstripe laminations - instead, it is largely massive, with parallel laminations only being observed in a few outcrops. Furthermore, in the Samre Fold-Thrust Belt, the contact between the Tsaliet Group and the overlying Tambien Group only has been mapped where the two are in fault contact.

Mai Kenetal Formation

In the Negash Syncline, the base of the Tambien Group comprises siltstones interbedded with dolomitized carbonates (Fig. 3.3). Rare cm-scale horizons of calcite pseudomorphs after gypsum can be found within the siltstones. We tentatively correlate this sequence of lithofacies with the Mai Kenetal Formation in the western exposures based on two observations. First, these sediments underlie lithofacies that are suggestive of the Amota Formation in the western exposures. Second, as discussed above, deposition of the Mai Kenetal Formation began ca. 787 Ma in the western exposures. This age is younger, but similar, to the age of 794.29 ± 0.44 Ma developed from the base of the immature sandstone in the Tsaliet Group of the Negash Syncline.

However, there are significant differences between what we are considering the Mai Kenetal Formation in the east relative to the formation in the west. The carbonates of the formation are more extensively dolomitized and the overall ratio of carbonate to siliciclastics is much lower in the Negash Syncline. Molar tooth structures and ooids that are abundant in the formation within the western exposures are not present in the formation within the Negash Syncline. Furthermore, the lithofacies with calcite pseudomorphs after gypsum in the Negash exposures are not found in the western exposures. These differences likely are associated with deposition of the Mai Kenetal Formation in the Negash Syncline occurring more proximal to the arc than in the western exposures, which could have led to periodic restriction and evaporite mineral precipitation at Negash, but not further west.

Amota Formation

The Amota Formation is exposed in the Negash Syncline in the eastern exposures, and is similar to that in the western exposures (Fig. 3.3). The disappearance of carbonate lithofacies for hundreds of meters of stratigraphy marks the base of the formation. Relatively homogenous purple siltstones with green reduction spots dominate the formation, with less frequent sandstone interbeds. Deposition of the Amota Formation in the Negash Syncline occurred in shallow waters: coarse sandstones and pebble to cobble conglomerates are relatively abundant, very fine sandstones and siltstones often are ripple cross-stratified, and there are horizons of mud cracks (Fig. 3.6). These lithofacies indicate that the Amota Formation was deposited in shallower waters in the eastern exposures relative to the west, where mud cracks and lithologies coarser than fine sandstone have not been observed.

Didikama Formation

At present, the Didikama Formation is the lowest Tambien Group formation unambiguously identified in the Samre Fold-Thrust Belt. Preliminary reconnaissance mapping identified lithofacies that may be correlative with the Amota Formation in the westernmost portion of the currently mapped Samre Fold-Thrust Belt area (Fig. 3.2). However, further work is required to substantiate this correlation.

The Didikama Formation exposures in the east are similar to those in the west, with the transitional appearance of carbonate lithofacies marking the base of the formation. Pale brown dolomitized and recrystallized carbonate beds are interbedded with siltstones, and primary sedimentary structures often are obscured by dolomitization. Stromatolites are found near both the top and bottom of the formation. An interval of black shale is present at two locations near the top of the formation on the eastern limb of the Negash Syncline.

The full thickness of the Didikama Formation only has been documented in the Negash Syncline. However, parasitic folds (∼10-100 m in scale) within the larger Negash Syncline structure are concentrated within the Didikama Formation, making it difficult to accurately estimate the true stratigraphic thickness of the formation. Nevertheless, our mapping and stratigraphic measurements suggest that the formation is <1200 m thick (Fig. 3.3).

Matheos Formation

The Matheos Formation is dominated by limestone and has a thickness ∼150-350 m in the Negash Syncline and the Samre Fold-Thrust Belt (Figs. 3.3 and 3.7). In both localities, the blue-grey limestones of the formation form distinctive topographic ridges that are readily identified both in the field and from satellite imagery. In contrast to the Didikama Formation, primary textures are well-preserved.

In the Negash Syncline and west of the major NE-striking thrust fault in the Samre Fold-Thrust Belt (the Zamra Fault; Fig. 3.2), the formation begins with grey ribbonite limestone with horizons of molar tooth structures and transitions into grainstone with abundant oolite, intraclast breccia, and molar tooth structures (Fig. 3.6). These lithofacies indicate a shallowing upwards trend with deposition occurring in an energetic shallow-water environment. East of the fault, although the formation begins with the same grey ribbonite limestone with horizons of molar tooth structures that is seen in the other areas, oolite and stromatolitic carbonates are the dominant lithofacies (Fig. 3.7). Deposition of the Matheos Formation to the east of the Zamra Fault also occurred in a shallow-water environment, but one dominated by stromatolites.

Mariam Bohkahko Formation

The Mariam Bohkahko Formation is exposed in the Negash Syncline and the Samre Fold-Thrust Belt (Fig. 3.3). The beginning of the formation is marked by the end of the distinctive blue-grey limestone facies of the Matheos Formation.

In the Negash Syncline and west of the Zamra Fault in the Samre Fold-Thrust Belt, the base of the Mariam Bohkahko Formation consistently is marked by partially dolomitized stromatolitic carbonate (Figs. 3.6 and 3.7). These stromatolites are followed by mixed siliciclastic-carbonate sedimentary rocks that are dominated by siltstone. The carbonate beds that are interbedded with the siltstones often are boudined and dolomitized, likely due to their proximity to the core of the large-scale synclines. Some horizons of coarser-grained siliciclastics (up to very fine sandstone) are present toward the top of the formation,

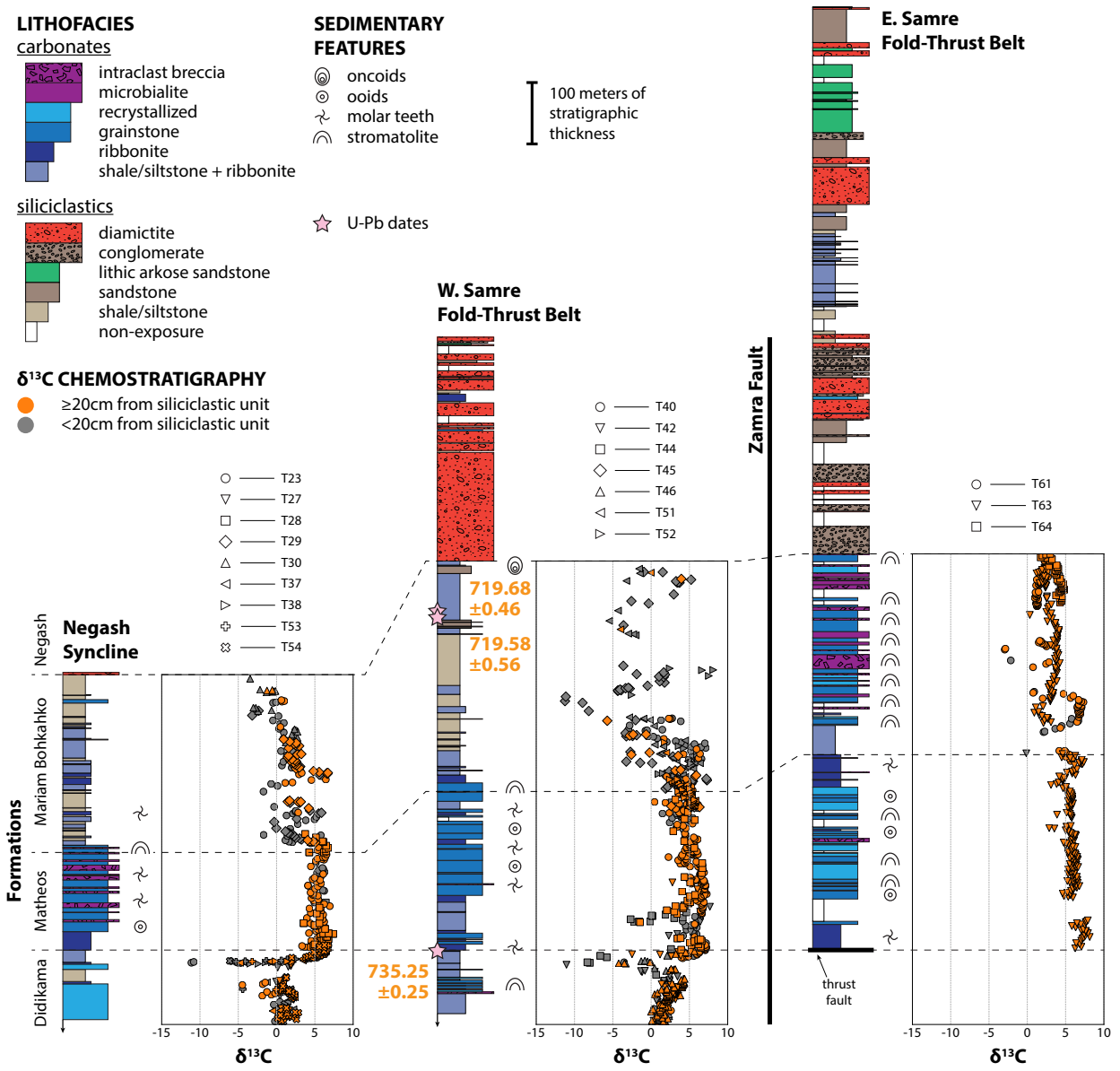

Figure 3.7: Lithostratigraphy and δ^{13}C chemostratigraphy of upper Tambien Group exposures in the Negash Syncline and Samre Fold-Thrust Belt (west and east of the Zamra Fault). The stratigraphic sections are representative composites of individually measured sections in each locality with the data within the δ^{13}C composite keyed out to each individual section. δ^{13}C data are colored based on their stratigraphic distance from the closest siliciclastic unit. U-Pb dates are in units of Ma, and are from MacLennan et al. (2018). A more detailed depiction of the contact between the Mariam Bohkahko and Negash formations in the Samre Fold-Thrust Belt is shown in Figure 3.13.

some of which are cross-stratified. In some areas, climbing ripples, oolitic grainstones, and oncolites are observed within ∼30 m of the top of the Mariam Bohkahko Formation before the contact with the overlying Negash Formation, with carbonate grainstone beds within 1 m of the contact. Overall, these lithofacies suggest deposition in a shallow-water environment.

East of the Zamra Fault, the base of the Mariam Bohkahko Formation consists of siltstones with interbedded ribbonites (Fig. 3.7). The rest of the formation in this area comprises almost entirely of partially dolomitized carbonates, including stromatolites, oncolites, oolitic grainstone, ribbonite, and intraclast breccia, with only rare siliciclastic intervals. Toward the top of the formation, the stratigraphy often comprises *in situ* stromatolites, intraclast breccia with clasts of stromatolites, and minor microbialaminite (Figs. 3.6 and 3.7). Again, overall, these lithofacies suggest deposition in a shallow-water environment.

These differences in the stratigraphy of the Mariam Bohkahko Formation across the Zamra Fault indicate different sediment sources and/or depositional environments and potentially significant offset across the fault. To the east, the dominance of carbonate facies (including stromatolites, oncolites, oolites, and microbialaminite) in the Mariam Bohkahko Formation suggest deposition in a shallow-water tropical carbonate belt within the photic zone that lacks significant siliciclastic sediment input. Tidal bypass channels could be transporting silt through this carbonate belt to an outer detrital belt to the west, where minor carbonate beds are interbedded in strata dominated by siltstone. Carbonate interbeds to the west likely represent redeposition of the carbonate sediment being generated in the shallow-water carbonate factory to the east.

Given the importance of the nature of the contact between the Mariam Bohkahko and Negash formations, it is discussed separately in *Onset of the Sturtian Snowball.*

Negash Formation

The Negash Formation is exposed in the Negash Syncline and the Samre Fold-Thrust Belt (Fig. 3.3). In the Negash Syncline and west of the Zamra Fault in the Samre Fold-Thrust Belt, the formation mostly comprises massive diamictite with a silt matrix (Figs. 3.6 and 3.7). Clast sizes within the diamictite are variable between pebble and boulder. Clast density also is variable, with clast-poor versus clast-rich horizons. Clasts within the diamictite include carbonate lithologies, some of which retain primary textures allowing them to be identified as ribbonites, grainstone, and ooilitic grainstone. Although not uniquely diagnostic, the facies as well as the carbon isotope composition of these carbonate clasts (see *Diagenetic Considerations*) are consistent with the interpretation that they were derived from the Tambien Group and point to an intra-basinal source. In addition to carbonate clasts, clasts of sandstone, vein quartz, rhyolite, meta-basalt, volcaniclastic breccia, aplite, and granite are present. Detrital zircon geochronology (U-Pb SHRIMP) conducted on matrix combined with clasts of the Negash Formation collected in the Negash Syncline reveal dates dominantly between 850 and 750 Ma with a minor population between 1050 and 950 Ma (Avigad et al., 2007). Many of these lithologies, as well as the 850 to 750 Ma zircons, could have been sourced from rocks associated with the Arabian-Nubian arcs, some of which had

collided and amalgamated by that time (Johnson, 2014). However, the 1050 to 950 Ma zircons, as well as the granitoid clasts, are likely of extra-basinal origin, which is consistent with the interpretation that the diamictite is glacigenic. A minor portion of the Negash Formation in these areas comprises facies that are distinct from the massive diamictite with silt matrix, including: diamictite with a coarse sand matrix, pebble to cobble conglomerates with carbonate and/or metavolcanic clasts, thin beds of limestone ribbonite, fine to coarse lithic arkose sandstones (likely sourced from the proximal arc) with rare pebbles/cobbles, and clast-free sandstone and siltstone (Fig. 3.7).

The Negash Formation frequently is foliated in the core of the Negash Syncline, but also in some outcrops in the Samre Fold-Thrust Belt. This foliation can make it difficult to confidently identify glacigenic sedimentary textures, such as deformation of layers associated with dropstones, and to liberate clasts for the observation of striations. Nevertheless, MacLennan et al. (2018) and Miller et al. (2003) identified grooves on cobbles that were interpreted as striations of glacial origin.

East of the Zamra Fault, the Negash Formation is significantly more variable than that west of the fault and in the Negash Syncline, with a smaller proportion of the stratigraphy comprising massive diamictite (Fig. 3.7). The base of the formation in this area can either be massive diamictite, or a clast-supported conglomerate with a dolomitized carbonate matrix and sub-angular carbonate clasts that have facies that are identical to those found in the underlying Mariam Bohkahko (stromatolite and stromatolite breccia) and Matheos (oolite) formations (Fig. 3.6; discussed further in *Onset of the Sturtian Snowball*). In the most representative and continuous Negash Formation section measured in this area, this carbonate breccia is overlain by cm-scale fining upward beds of very fine to fine sandstone. These beds transition into massive diamictite interbedded with medium to coarse sandstones and the carbonate breccia described previously, followed by an interval of siltstones interbedded with cm-scale carbonate ribbonites and occasional horizons of cm-scale coarse poorly sorted sandstones that consist of limestone and lithic fragments. The ribbonites from within this interval are likely the fine-grained products of redeposition of eroded underlying Tambien Group carbonates, given that carbonate precipitation is expected to be thermodynamically inhibited in the cold waters of a global glaciation. Diamictite above and below this interval are almost identical, and the cm-scale carbonate beds are distinct from the thick Sturtian cap carbonate sequences observed in other localities (Kennedy et al., 1998; Hoffman et al., 2011). To date, no tuffs have been observed in the Negash Formation, preventing the development of direct geochronologic constraints on the formation. The stratigraphically highest observed exposures of the Negash Formation in this eastern Samre Fold-Thrust Belt consist of intervals of massive diamictite with a fine to coarse sand matrix and fine to coarse lithic arkose sandstones with rare pebbles/cobbles.

West of the Zamra Fault, the dominance of massive diamictite may suggest glaciomarine deposition near the grounding line of the local glacier. On the other hand, the relative lack of massive diamictite east of the Zamra Fault could represent proximity to subglacial meltwater channels and/or deposition in an outwash plain slightly more distal from the grounding line of the glacier. Similar to the Mariam Bohkahko Formation, this difference in the stratigraphy

of the Negash Formation across the Zamra Fault could be explained by movement along the fault. The Zamra Fault could have initially been a syn-depositional normal growth fault that later got reactivated as a thrust fault during the East African Orogeny, juxtaposing two locales that were once further apart. However, more study of the lithofacies of the Negash Formation is warranted.

Basin Development

Deposition in a back-arc basin is consistent with the geologic context of the Tambien Group. Other sedimentary sequences overlying ca. 850-800 Ma volcanics in western Eritrea and northern Ethiopia have been interpreted as being deposited in back-arc basins on the basis of the trace-element composition of the volcanics and field relationships between the sedimentary sequences and adjacent oceanic-arc rocks (Tadesse et al., 1999; Teklay et al., 2003; Teklay, 2006). Furthermore, mapping within the Arabian-Nubian Shield of Ethiopia, Sudan, and Eritrea has identified several ophiolites within roughly north-south trending suture zones (Berhe, 1990), U-Pb crystallization ages from Arabian-Nubian Shield volcanic and plutonic rocks are dominantly Tonian to Cryogenian in age (Johnson, 2014), Sm-Nd isotopes indicate derivation from juvenile mantle sources, and Nd model ages are dominantly Tonian to Cryogenian (Johnson, 2014). Together, these data support a model wherein the Arabian-Nubian Shield formed through the amalgamation of multiple arcs and associated arc-related basins.

The transition from volcanic and volcaniclastic lithologies of the Tsaliet Group to the mixed carbonate-siliciclastic sediments of the Tambien Group could be associated with slab rollback that caused the arc to migrate away from the initial site of eruption and volcaniclastic deposition, resulting in extensional and flexural accommodation space followed by thermal-isostatic subsidence. The ages of 795.67 $\pm$ 0.82 and 794.29 $\pm$ 0.44 Ma from within and above the lava flows of the Tsaliet Group in the Negash Syncline of the eastern exposures are considerably younger than the eruptive age of 815.29 $\pm$ 0.32 Ma from a tuff within siltstones in the basal Tambien Group in the Tsedia Syncline of the western exposures (Swanson-Hysell et al., 2015b), which indicates that local volcanism continued to generate lava flows in the Negash Syncline while Tambien Group deposition already had begun in the western exposures. This diachronous timing of the transition from volcanism to sedimentation from west to east supports a back-arc basin setting, with the locus of volcanism (recorded by the lava flows in the Tsaliet Group) migrating eastward in present day coordinates. Slab rollback has been well-documented in the the more recent geologic record as a process causing arc migration and accommodating back-arc basin development (e.g. Uyeda and Kanamori, 1979; Kastens et al., 1988; Schellart et al., 2006). For example, over the past $\sim$80 Myr, the rollback for the Pacific plate has accommodated the opening of multiple back-arc basins north of New Zealand and has proceeded at rates between $\sim$40-0 km/Myr (Schellart et al., 2006). Mean rates of trench retreat globally are on the order of 10 km/Myr (Schellart et al., 2008). Based on the present-day distance in northern Ethiopia that does not account for shortening, the minimum average eastward migration rate of the Tsaliet-Tambien group boundary between the Tsedia Syncline ($\sim$820 Ma) and the Negash Syncline ($\sim$790 Ma) is

~2 km/Myr. This value is well within the range of average slab rollback rates estimated at the Australian-Pacific plate boundary, even if the shortening in the Tsaliet and Tambien groups approaches that estimated for the Himalayan fold-thrust belt (75%; Long et al., 2011). Furthermore, the broad similarity of the stratigraphy between the Negash Syncline and the Samre Fold-Thrust Belt (a present day lateral distance of ~100 km, which has likely changed little since the time of deposition since the axis of compression during the East African Orogeny was oriented approximately perpendicular to the axis that spans these two locations; Stern, 1994) suggests that the Tambien basin was elongate along the present day NNE-SSW direction. This geometry is consistent with structural inversion of a back-arc basin from an extensional to a compressional regime, since the major structural features (synclines, anticlines, and thrust faults) also have NNE-SSW orientations. Tuffs near the base of the Tambien Group also have pumice fiamme in the eastern exposures, and are associated with cobble- to boulder-sized scoria bombs in the western exposures, indicating proximity to an active arc (Swanson-Hysell et al., 2015b). In contrast, tuffs higher in the Tambien Group do not have such associations and are more consistent with having formed through air-fall ash sourced from active arcs further from the basin. Lithofacies of the upper Tsaliet Group and Mai Kenetal and Amota formations also suggest shallower deposition in the eastern exposures relative to the lithofacies of these formations in the west (see *Lithostratigraphy*), which again supports eastward migration of volcanism and associated transgression in this basin. We note, however, that the presence of facies that suggest deposition above wave base throughout the Tambien Group indicates that deposition of the siliciclastic and carbonate sediments overall kept pace with subsidence. The lithologic difference between carbonate-dominated and siliciclastic-dominated portions of the stratigraphy likely is dominantly controlled by time and spatially varying siliciclastic sedimentary input into that particular portion of the basin. The lifespan of Tambien Group deposition (>100 Myr) also is similar to that of other identified back-arc basins in the geologic record (Woodcock, 2004).

3.6 Tambien Group Chemostratigraphy

Stratigraphic sections across the Tambien Group are correlated to one another by using the geochronologic constraints and aligning both the characteristic lithofacies of the formations and the $\delta^{13}C$ curve to create a composite Tambien Group $\delta^{13}C$ and $^{87}Sr/^{86}Sr$ chemostratigraphic record (Fig. 3.3). All geochemical data and the Python code used to assess the degree of alteration of each sample and develop the composite Tambien Group chemostratigraphy are included in the *Supporting Information*. $\delta^{13}C$ and $^{87}Sr/^{86}Sr$ data developed by Miller et al. (2009) also are incorporated into our Tambien Group composite. Given that the data from Miller et al. (2009) were collected from surface transects rather than measured stratigraphic sections, integration into our chemostratigraphic dataset was made based on: A) correlation of sampling localities (shown on maps in Miller et al., 2009) to our geological maps; B) correlation of sample heights and formations (shown approximately in fence diagrams in Miller et al., 2009) to our measured sections; and C) correlation of $\delta^{13}C$ values.

Chemostratigraphic Results

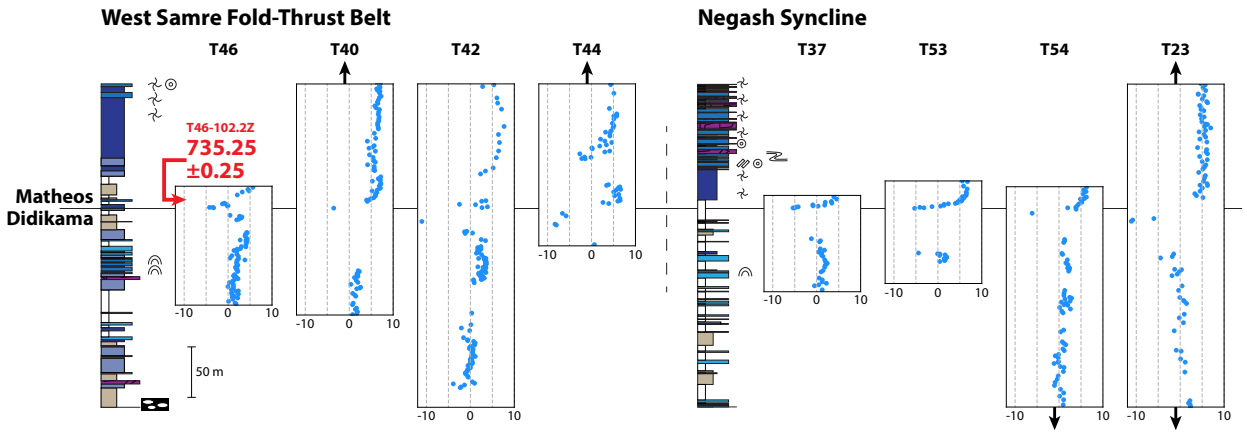

Figure 3.8: Summary lithostratigraphy and δ^{13}C data from sections that capture the Didikama-Matheos excursion from the Samre Fold-Thrust Belt and Negash Syncline. The symbology for the lithofacies and sedimentary structures is the same as that used in Figure 3.7. Black arrows indicate that lithostratigraphic and δ^{13}C data continues upwards/downwards for that section, but are not shown.

Paired δ^{13}C data and U-Pb dates from the lower Tambien Group have led to the interpretation that the negative δ^{13}C values within the Assem Formation correlate with the ca. 810-790 Ma Bitter Springs stage (Swanson-Hysell et al., 2015b). However, samples that resolved the onset of the stage (i.e. the descent from ∼5‰ to ∼-4‰) had not been identified, due to a lack of carbonate horizons in the lower Tambien Group. New δ^{13}C data from carbonates within the lower Werii Formation in the southwestern Tsedia Syncline begin at values of ∼5‰ and fall sharply to <-5‰, with values of ∼-5‰ for the rest of the Werii Formation, similar to those in the overlying Assem Formation (Fig. 3.3). We interpret these δ^{13}C data to reflect the onset of the Bitter Springs stage, which further supports the hypothesis that the stage has a rapid onset leading into a prolonged global perturbation to the carbon cycle (Maloof et al., 2006; Swanson-Hysell et al., 2015b). After the recovery from the Bitter Springs stage, δ^{13}C values are sustained at ∼5‰, before the stratigraphy transitions from the carbonate-dominated Mai Kenetal Formation to the mixed carbonate-siliciclastic Amota and Didikama formations. δ^{13}C values from carbonates within these mixed carbonate-siliciclastic parts of the stratigraphy are more scattered than those in carbonate-dominated parts of the stratigraphy. Nevertheless, the majority of the data through the Amota and Didikama formations lie between 0 and 5‰, and no major excursions are observed. Near the contact between the Didikama and Matheos formations, a large δ^{13}C excursion to ∼-12‰ is observed, which we will refer to as the Didikama-Matheos excursion (see *Diagenetic Considerations* and *δ^{13}C Excursions*; Swanson-Hysell et al., 2015b; MacLennan et al., 2018). This δ^{13}C excursion now is reproduced in eight sections across the basin (Fig. 3.8). Fol-

lowing this excursion, δ^{13}C values are steady at ∼5‰, before the stratigraphy transitions from the Matheos Formation to the Mariam Bohkahko Formation, which has more variable δ^{13}C values. However, we attribute the majority of this scatter within the Mariam Bohkahko Formation to alteration processes that drive δ^{13}C to more negative values (see *Diagenetic Considerations* and *$\delta^{13}C$ Excursions*), and thus we interpret the primary δ^{13}C values to be broadly declining from ∼5 to ∼2‰ in the interval between the Didikama-Matheos excursion and the onset of the Sturtian Glaciation (Fig. 3.7).

$^{87}Sr/^{86}Sr$ data that we interpret to be primary (see *Diagenetic Considerations*) have relatively stable values of ∼0.7067 in the Mai Kenetal Formation (Fig. 3.3). These data are followed by a large gap before values of ∼0.7063 at the base of the Matheos Formation (Fig. 3.3). Through the Matheos Formation, $^{87}Sr/^{86}Sr$ rises to ∼0.7067, before declining to ∼0.7063 in the middle of the Mariam Bohkahko Formation. One sample within 25 m of the contact between the Mariam Bohkahko and Negash formations is interpreted to retain primary $^{87}Sr/^{86}Sr$ = ∼0.70603. However, this sample ([Sr] = 1408 ppm and Mn/Sr = 0.34) barely passes our filtering thresholds used to assess alteration. Although the $^{87}Sr/^{86}Sr$ of this sample seems to lie on the projected trajectory of declining $^{87}Sr/^{86}Sr$ in the upper Mariam Bohkahko Formation (Fig. 3.3), more data from the time interval immediately preceding the onset of the Sturtian Glaciation is required to test whether our interpretation of the primary nature of the $^{87}Sr/^{86}Sr$ of this sample is robust.

Diagenetic Considerations

Sample Proximity to Siliciclastic Units

Some of the proposed mechanisms for cooling and the initiation of the Sturtian Snowball Earth have invoked connections between global glaciation and a negative δ^{13}C excursion leading into the glaciation. Therefore, constraining the carbon isotopic composition of marine dissolved inorganic carbon during the lead-up to the Sturtian Snowball Earth is particularly important for testing these hypotheses.

There is substantial variability (up to ∼10‰) in the carbon isotopic composition of stratigraphically equivalent Mariam Bohkahko Formation carbonates immediately beneath the Negash Formation (Fig. 3.7). This variability is most pronounced in the Negash Syncline and west of the Zamra Fault in the Samre Fold-Thrust Belt, where the Mariam Bohkahko Formation stratigraphy comprises mixed siliciclastic-carbonate sedimentary rocks that are dominated by siltstone (Fig. 3.7). In contrast, δ^{13}C variability is minimal east of the Zamra Fault where the lithofacies of the formation are dominated by carbonate, and δ^{13}C values broadly decrease from ∼5 to ∼2‰ (Fig. 3.7). Given that siliciclastics do not provide a carbonate buffer against altering fluids, it is plausible that carbonate samples collected closer to siliciclastic horizons are less likely to preserve primary δ^{13}C and other geochemical signals leading to the higher variability in δ^{13}C values observed in the siltstone-rich sections.

To assess whether the proximity of each carbonate sample to the closest siliciclastic unit (d) is a reasonable predictor of δ^{13}C alteration, we perform a principal components analysis

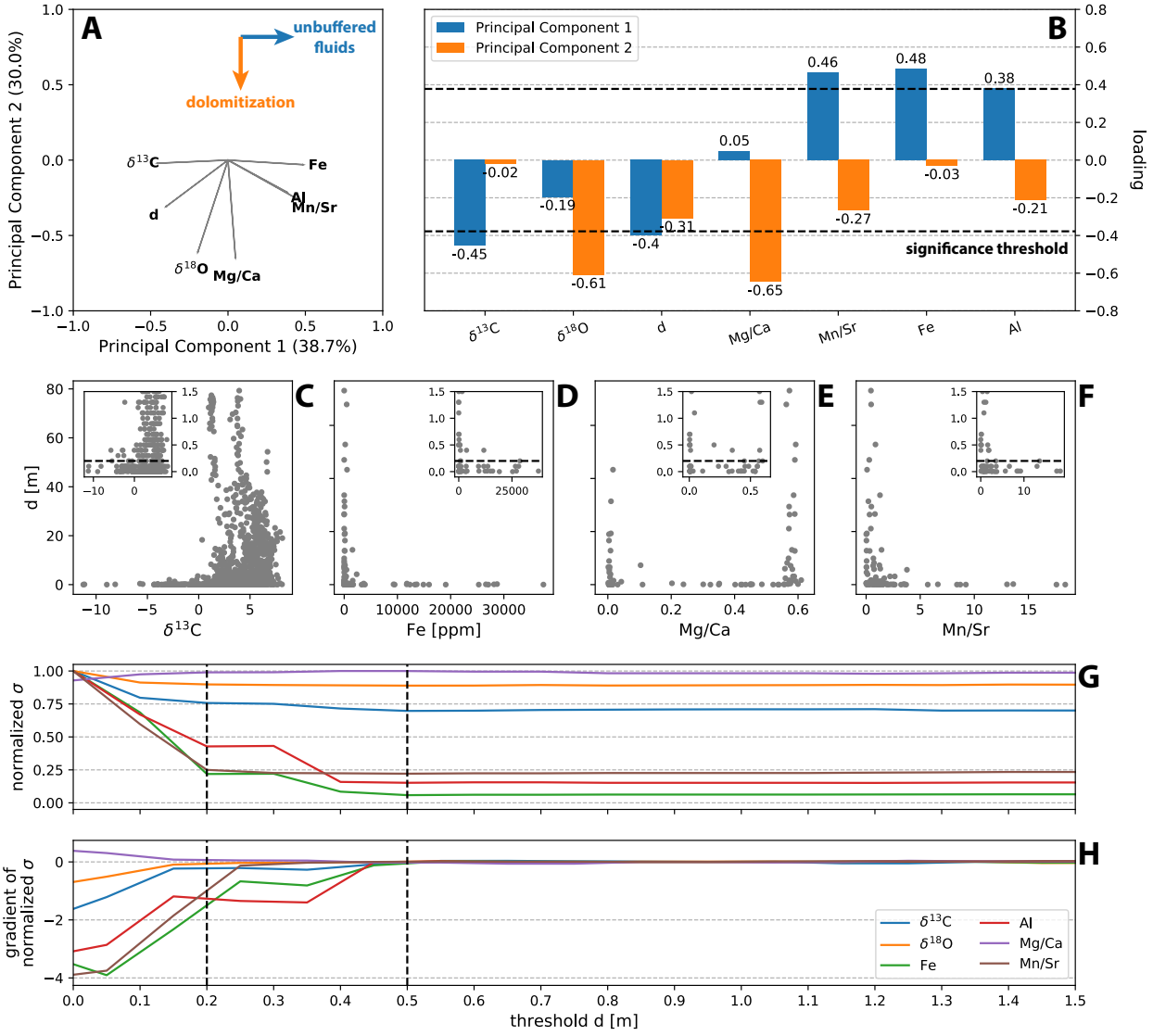

Figure 3.9: A) Loadings plot from a principal components analysis (PCA) on all samples with element concentration data above the Didikama-Matheos excursion. The analysis reveals two main alteration pathways, associated with the first two principal components. δ^{13}C and d (the proximity of each carbonate sample to the closest siliciclastic unit) are anti-correlated with the first alteration pathway, which we interpret to be via 'unbuffered (with respect to carbonate) fluids.' **B)** Histogram of loadings/eigenvalues on the first two principal components. The significance threshold is defined as $\sqrt{\frac{1}{\text{number of variables}}}$. **C-F)** Scatter plots of samples above the Didikama-Matheos excursion. Inset plots have the same x-axes as their parent plots, but have y-axes zoomed in to d 0-1.5 m. The dashed line in the inset plots shows the selected d threshold of 0.2 m. The variance for δ^{13}C, Fe, Al, and Mn/Sr increase considerably at low d. **G)** Standard deviation (σ) of the remaining data as samples below a given d (x-axis) are removed, normalized to the σ when no samples are removed (i.e. all the data). The dashed line at $d = 0.2$ m denotes where σ for δ^{13}C falls to background levels, and the dashed line at $d = 0.5$ m denotes where σ for Fe, Al, and Mn/Sr fall to background levels. **H)** The corresponding gradient of G.

(PCA) on the samples for which we developed elemental concentration (Al, Fe, Mn, Sr, Mg, Ca) as well as isotope (δ^{13}C and δ^{18}O) data. A PCA simplifies the complexity in a high-dimensional dataset by geometrically projecting the dataset onto principal components (or eigenvectors), each of which are a linear combination of the original variables in the dataset. The first principal component accounts for as much of the variability in the data as possible, and each following component accounts for as much of the remaining variability as possible. Ultimately, the goal of a PCA is to reduce the dimensionality of the dataset by accounting for the maximum portion of variance present in the dataset using as few principal components as possible. While the lithology of covered intervals without exposure is not known, for determining d we make the conservative assumption that covered units are recessive, fine-grained siliciclastic units. We also exclude samples below and within the Didikama-Matheos excursion, so that we can eliminate the complication of potentially primary fluctuations in the δ^{13}C chemostratigraphy increasing the variance in the data. Element concentration data and d are log-transformed to transform these variables into near-normal distributions, then all variables are centered and standardized.

As shown in Figure 3.9A and B, we interpret that the PCA reveals two main alteration pathways corresponding to the first two principal components, which together explain 68.7% of the variance in the dataset (see *Supporting Information* for a discussion on the selection of these two components). The first pathway (principal component 1) shows high positive loadings on Fe, Al, and Mn/Sr, consistent with alteration via a fluid that has had significant interaction with siliciclastic units prior to interacting with the carbonate samples. The second pathway (principal component 2) shows high negative loadings on Mg/Ca, which is consistent with alteration via dolomitization. Mg/Ca is positively correlated with δ^{18}O, which suggests that dolomitization occurred early during the diagenetic history of the carbonates, locking in high δ^{18}O values that were later less susceptible to overprinting via warm and/or meteoric low δ^{18}O fluids due to the lower reactivity of dolomites relative to limestones. Most importantly, however, the PCA reveals that δ^{13}C and d are anti-correlated with the first of these alteration pathways - in other words, high Fe, Al, and Mn/Sr often are associated with low δ^{13}C and small stratigraphic distance from a siliciclastic unit (low d) in our carbonate samples. This result suggests that many of the low δ^{13}C values in this portion of the stratigraphy where δ^{13}C values are scattered are likely a result of alteration via fluids that are unbuffered with respect to carbonate (which we term 'unbuffered fluids') that likely have interacted with low δ^{13}C organic matter during transit through siliciclastic units. Whether this alteration via unbuffered fluids occurred soon or much after deposition is not constrained by the PCA. At greater distances from the nearest siliciclastic unit (higher d), fluids would have spent more time transiting through carbonates prior to interaction with a sampled horizon, and these carbonate-buffered fluids are not expected to significantly change δ^{13}C, Fe, Al, and Mn/Sr.

The results of the PCA are corroborated by the scatter plots shown in Figure 3.9C-F – at the lowest distances from the closest siliciclastic unit (d), the variation in δ^{13}C, Fe, Al, and Mn/Sr jumps dramatically. On the other hand, Mg/Ca is bimodally distributed except at low d where intermediate Mg/Ca values are observed. This result suggests that the unbuffered fluids associated with this alteration pathway can cause partial dolomitization,

but are not responsible for the vast majority of the dolomitization in the Tambien Group.

To constrain the degree to which these unbuffered fluids have penetrated into the carbonate horizons in the Tambien Group and potentially altered primary $\delta^{13}C$, we compute the standard deviation of each of the geochemical variables as samples below a given d are removed (Fig. 3.9G and H). The variability in $\delta^{13}C$ falls to background values at ∼0.2 m, and for Fe, Al, and Mn/Sr between ∼0.2 and 0.5 m. These results suggest that the characteristic length scale of alteration of Tambien Group carbonates by unbuffered fluids is ∼0.5 m, with alteration of $\delta^{13}C$ being most significant up to ∼0.2 m. This difference in overprinting length scales of $\delta^{13}C$ vs. Fe, Al, and Mn/Sr can be explained by the ability of carbonates to buffer against changes in C more effectively than trace elements.

The results of filtering out samples below various values of d on the $\delta^{13}C$ composite chemostratigraphy of the Tambien Group are shown in the *Supporting Information*. As suggested by the analysis of the standard deviations above (Fig. 3.9G and H), most large inconsistencies in $\delta^{13}C$ at any given composite stratigraphic height are removed using the $d = 0.2$ m threshold, and increasing the threshold beyond that value, in general, simply removes all data in intervals of the composite chemostratigraphy where carbonate horizons are relatively thin.

Notably, data that resolve the Didikama-Matheos excursion as well as the descent into and recovery out of the Bitter Springs stage (but not the prolonged interval of negative values that define the Bitter Springs stage) are partially removed under the $d = 0.2$ m threshold (Fig. 3.3), and completely removed by $d = 0.5$ m (see *Supporting Information*). Furthermore, the Didikama-Matheos excursion coincides with a major facies transition from siliciclastic-dominated strata to carbonate-dominated strata that defines the Didikama-Matheos formation boundary (Fig. 3.8). The difference in permeability associated with this facies boundary may have created a significant conduit for fluid flow at this stratigraphic horizon, driving $\delta^{13}C$ to more negative values than elsewhere in the Tambien Group. Together, these two observations could support an interpretation that the sharp negative $\delta^{13}C$ excursion at the Didikama-Matheos formation boundary is a product of secondary alteration. It is important to note, however, that several samples within the Didikama-Matheos excursion that record $\delta^{13}C$ as low as -5‰, significantly below the >0‰ values before and after the excursion, are not culled on the basis of the $d = 0.2$ m threshold. Furthermore, it is important to consider the limitations of this $\delta^{13}C$ filter based on d. First, the filter is likely not useful at d significantly beyond the characteristic length scale of alteration of Tambien Group carbonates by unbuffered fluids (i.e. ∼0.2 m for carbon) - selecting a d threshold significantly above this value would arbitrarily remove $\delta^{13}C$ data that have not been altered by these fluids. Second, heterogeneity in the distance to which these unbuffered fluids penetrated into Tambien Group carbonates is expected. This method does not account for such spatial heterogeneity, and so samples that fall below the threshold d may or may not have been altered by the unbuffered fluids. Indeed, we find that some samples that we have high confidence are recording primary $\delta^{13}C$ based on the consistency in $\delta^{13}C$ values of samples within and between measured sections (e.g. samples with $\delta^{13}C$ ∼5‰ in the Mai Kenetal Formation; Fig. 3.3) are removed using this approach. On the other hand, we can have relatively high confidence

that the δ^{13}C values of samples above the threshold d have not been altered by unbuffered fluids. Third, this method takes the conservative approach and assumes that intervals of no outcrop within measured sections are siliciclastic units. Since siliciclastic units (especially fissile siltstones, which dominate the siliciclastic portions of Tambien Group stratigraphy) often are less resilient to weathering than carbonates, the probability that this assumption holds is high within some sections. Nevertheless, the possibility remains that some of these covered intervals are actually carbonates that have been buried by colluvium.

There are several other observations that argue for the primary nature of the Didikama-Matheos excursion. First, high-precision age constraints from zircons in tuffs demonstrate that this δ^{13}C excursion occurs at the same time as negative δ^{13}C values interpreted as a ca. 735 Ma δ^{13}C anomaly observed in other basins around the world (Fig. 3.12, and $\delta^{13}C$ *Excursions*). Second, the Didikama-Matheos excursion is consistently reproduced across the >100 km distance between the Samre Fold-Thrust Belt and Negash Syncline (Fig. 3.8), and wherever samples were collected across the Didikama-Matheos formation boundary, a sharp δ^{13}C excursion has been observed. Third, although the driver for the ca. 735 Ma δ^{13}C anomaly is not known, it is likely that a perturbation to the carbon cycle of the magnitude required to create such an excursion would be associated with major environmental change and an associated change in lithofacies. Fourth, the samples that record low δ^{13}C values in the Didikama-Matheos excursion generally exhibit lower Fe, Al, and Mn/Sr than samples with low δ^{13}C above the Didikama-Matheos excursion, suggesting that low δ^{13}C Didikama-Matheos excursion samples have been less altered by the unbuffered fluids than low δ^{13}C post-Didikama-Matheos excursion samples (see *Supporting Information*).

Given the balance of evidence for and against the primary nature of the Didikama-Matheos excursion, and given the inherent limitations of the δ^{13}C filter based on d, we interpret the excursion to be a primary feature of the record. If these carbonates have been altered by unbuffered fluids, the effect may have been to 'deepen' the excursion, rather than creating it from an otherwise stable δ^{13}C chemostratigraphy. We find that the primary utility of the filter as described here is to assess which δ^{13}C values are primary in intervals of the stratigraphy where time-equivalent carbonates produce inconsistent results (e.g. in the Mariam Bohkahko Formation). Nevertheless, we acknowledge the possibility that the sharp negative δ^{13}C excursion at the Didikama-Matheos formation boundary is instead a product of secondary alteration.

Isotope Conglomerate Test

We perform an isotope conglomerate test on carbonate clasts within the diamictite of the Negash Formation of both the Negash Syncline (n = 17) and the Samre Fold-Thrust Belt (n = 61) (Fig. 3.10). In such a test, carbonate clasts are sampled to test whether carbon and oxygen isotopes within the clasts were reset to similar δ^{13}C and δ^{18}O values through either meteoric or burial diagenesis (Husson et al., 2012, 2015b). If the clasts show substantial variability in their isotopic composition, we infer that their isotopic values were acquired prior to deposition in the clastic unit and were not fully reset through burial diagenesis.

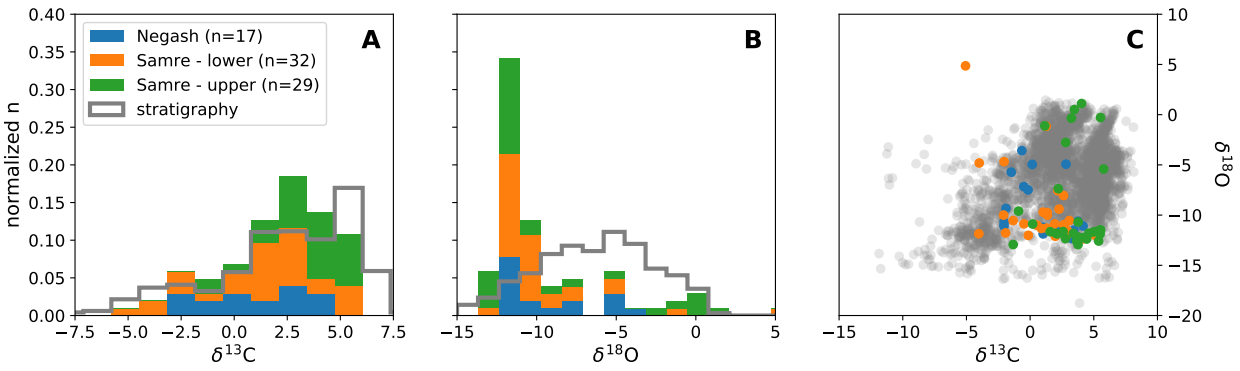

Figure 3.10: **A)** and **B)** Histograms of δ^{13}C and δ^{18}O values of carbonate clasts within the diamictite of the Negash Formation from the Negash Syncline and Samre Fold-Thrust Belt. Clasts from the Negash Syncline (n = 17) were sampled from a single horizon. Clasts from the Samre Fold-Thrust Belt (n = 61) were sampled from two horizons (lower and upper) ~100 m stratigraphically apart. **C)** Cross plot of δ^{13}C vs δ^{18}O values of the carbonate clasts. In all panels, grey data represent all carbonate samples taken from below the diamictite in the Tambien Group (i.e. from the *in situ* stratigraphy).

The isotope conglomerate test in the Negash Syncline reveals a ~7‰ range in δ^{13}C values, and in the Samre Fold-Thrust Belt there is a slightly greater range of ~10‰. These values are consistent with the carbonate clasts being sourced from the underlying stratigraphy (Fig. 3.10). However, the δ^{18}O values of the clasts in both areas cluster at ~-12‰, which may indicate that the δ^{18}O values of the clasts, unlike the δ^{13}C values, largely were reset after the deposition of the Negash Formation. However, the δ^{13}C and δ^{18}O of the clasts do not appear to be correlated, which supports the interpretation that the clasts preserve near primary δ^{13}C even for clasts where the δ^{18}O was altered. This indication of preferential preservation of primary δ^{13}C over δ^{18}O is consistent with carbon being more rock-buffered against altering fluids than oxygen (Banner and Hanson, 1990).

Sr Isotopes

Relative to C isotopes, Sr isotopes in carbonates are more vulnerable to secondary alteration (e.g. Banner and Hanson, 1990). Trace element geochemistry can be used to assess the degree of such alteration. Mn/Sr values are a commonly-used indicator of alteration, since interaction with secondary fluids tend to increase [Mn] and decrease [Sr] (Brand and Veizer, 1980; Banner and Hanson, 1990; Jacobsen and Kaufman, 1999). Furthermore, low [Sr] makes $^{87}Sr/^{86}Sr$ more susceptible to overprinting since less exchange is required to alter the original strontium isotopic ratio (Brand and Veizer, 1980; Veizer, 1989; Banner and Hanson, 1990). As in other studies (e.g. Halverson et al., 2007a), we apply a filter based on minimum [Sr] and maximum Mn/Sr in order to exclude $^{87}Sr/^{86}Sr$ values from samples that are more likely to be altered. To select appropriate [Sr] and Mn/Sr thresholds for our samples, we take advantage

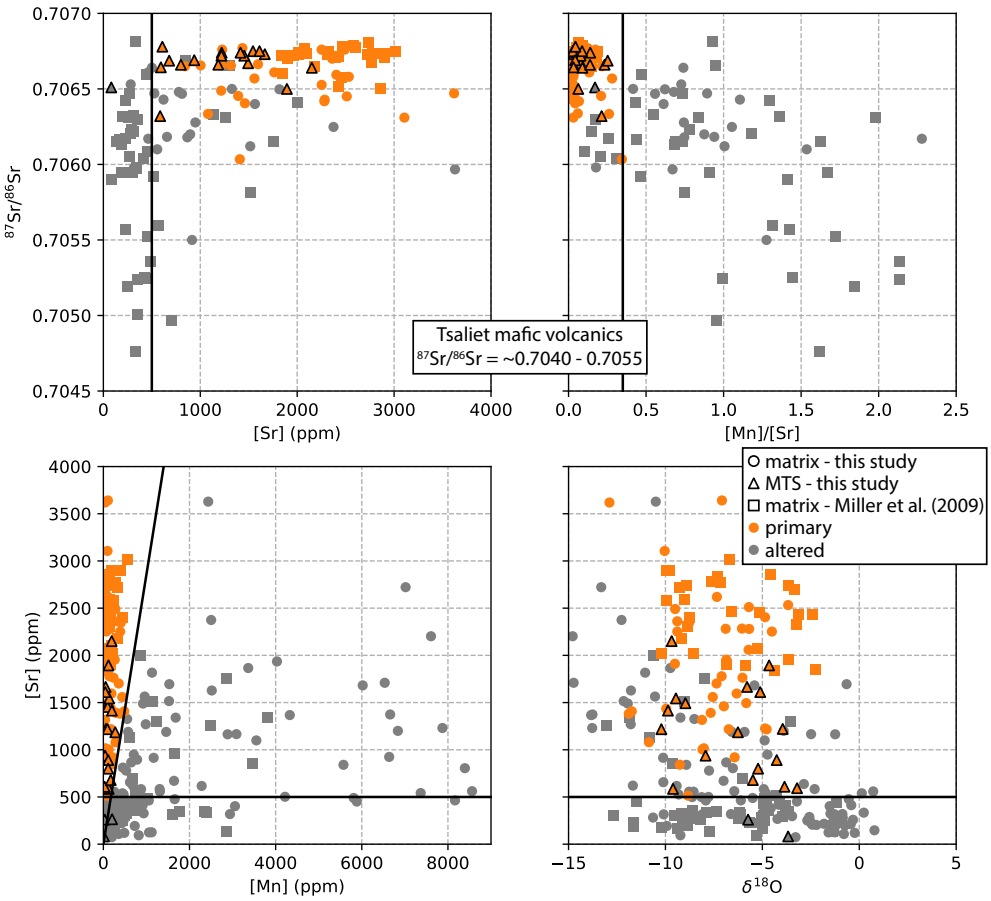

Figure 3.11: Cross plots of [Sr] and Mn/Sr against $^{87}Sr/^{86}Sr$, and [Mn] and $\delta^{18}O$ against [Sr] for data presented in this study and Miller et al. (2009). Black lines illustrate the thresholds used to interpret primary versus altered $^{87}Sr/^{86}Sr$ ([Sr]>500 ppm and Mn/Sr<0.35). MTS = molar tooth structure.

of the presence of molar tooth structures in the Tambien Group, since these structures consist of high purity calcite that precipitated from seawater within the host carbonate mud prior to dewatering and lithification. As a result, these structures are more likely to record primary geochemical signals relative to the surrounding micrite due to a lack of Rb-containing clay and more limited recystallization (Fig. 3.4). Given that all molar tooth structure samples cluster at Mn/Sr<0.35, and all molar tooth structure samples except one have [Sr]>500 ppm, these values are used as filtering thresholds to generate a record that is more likely to be reflective of primary $^{87}Sr/^{86}Sr$ (Fig. 3.11). We find that the $\delta^{13}C$ and $^{87}Sr/^{86}Sr$ values from molar tooth structures are similar to that of immediately adjacent micrite that pass the elemental thresholds (see *Supporting Information*). This similarity suggests that micritic samples from the Tambien Group (provided that they pass the elemental thresholds set above) also are capable of preserving primary geochemical signals, and supports their use

alongside calcite from molar tooth structures in reconstructing Tonian marine $^{87}Sr/^{86}Sr$.

Fluid-rock geochemical models generally predict that overprinting results in a sharp increase in $^{87}Sr/^{86}Sr$ below a threshold [Sr] (Banner and Hanson, 1990; Jacobsen and Kaufman, 1999). These models assume that the altering fluid has high $^{87}Sr/^{86}Sr$ resulting from interaction with radiogenic rocks with high $^{87}Sr/^{86}Sr$ prior to interacting with the carbonates. However, as discussed by Miller et al. (2009), the altering fluids that are responsible for overprinting in the Tambien Group would have had significant interaction with juvenile arc volcanics and volcaniclastics with low $^{87}Sr/^{86}Sr$ before interacting with the carbonates, since the Tambien Group was deposited atop of the arc volcanics and volcaniclastics of the Tsaliet Group. Two samples of mafic volcanics of the Tsaliet Group in the proximity of the Tsedia Syncline have $^{87}Sr/^{86}Sr$ values of 0.704047 and 0.705406, which confirms these expected low values. As a result, we do not expect to see a sharp increase in $^{87}Sr/^{86}Sr$ below the threshold [Sr]. Instead, we expect to see a decrease in $^{87}Sr/^{86}Sr$ at low [Sr] due to the altering fluid containing Sr sourced from juvenile arc material. This latter relationship is observed in the data (Fig. 3.11). We note that the majority of the low [Sr] and high Mn/Sr samples that have low (and excluded) $^{87}Sr/^{86}Sr$ values come from Miller et al. (2009); many of the data developed in this study are from samples that were screened for [Sr] and Mn/Sr prior to $^{87}Sr/^{86}Sr$ analysis.

3.7 Tonian-Cryogenian Chemostratigraphic Composite

Combined with U-Pb ID-TIMS dates on zircons from Swanson-Hysell et al. (2015b) (815.29 $\pm$ 0.32, 788.72 $\pm$ 0.24, and 787.38 $\pm$ 0.14 Ma), MacLennan et al. (2018) (735.25 $\pm$ 0.25, 719.58 $\pm$ 0.56, and 719.68 $\pm$ 0.46 Ma), and this study (Table 3.1), $\delta^{13}C$ and $^{87}Sr/^{86}Sr$ data from the Tambien Group (Miller et al., 2009; Swanson-Hysell et al., 2015b; this study) now comprise the most temporally well-constrained pre-Sturtian chemostratigraphic dataset to date. These data are combined with other chemostratigraphic and geochronologic datasets from Neoproterozoic sedimentary rocks in other localities around the world to generate an updated composite Tonian chemostratigraphy (Fig. 3.12). We use the Tambien Group $\delta^{13}C$ curve as the backbone for making correlations with other datasets. Tonian $\delta^{13}C$ and $^{87}Sr/^{86}Sr$ data within the composite come from the Akademikerbreen Group of Svalbard (Halverson et al., 2007a,b), the Eleanore Bay Supergroup of East Greenland (Cox et al., 2016), the Bitter Springs Group of Australia (Swanson-Hysell et al., 2010; Cox et al., 2016), the Fifteenmile Group of Canada (Macdonald et al., 2010; Cox et al., 2016), the Little Dal Group of Canada (Halverson, 2006; Halverson et al., 2007a), the Coates Lake Group of Canada (Halverson, 2006; Halverson et al., 2007a; Rooney et al., 2014), the Shaler Supergroup of Canada (Asmerom et al., 1991; Jones et al., 2010), the Dalradian Supergroup of Scotland (Sawaki et al., 2010), Proterozoic carbonates of the Uchur–Maya and Turukhansk regions of Siberia (Bartley et al., 2001; Cox et al., 2016), and the Karatau Group of the Urals

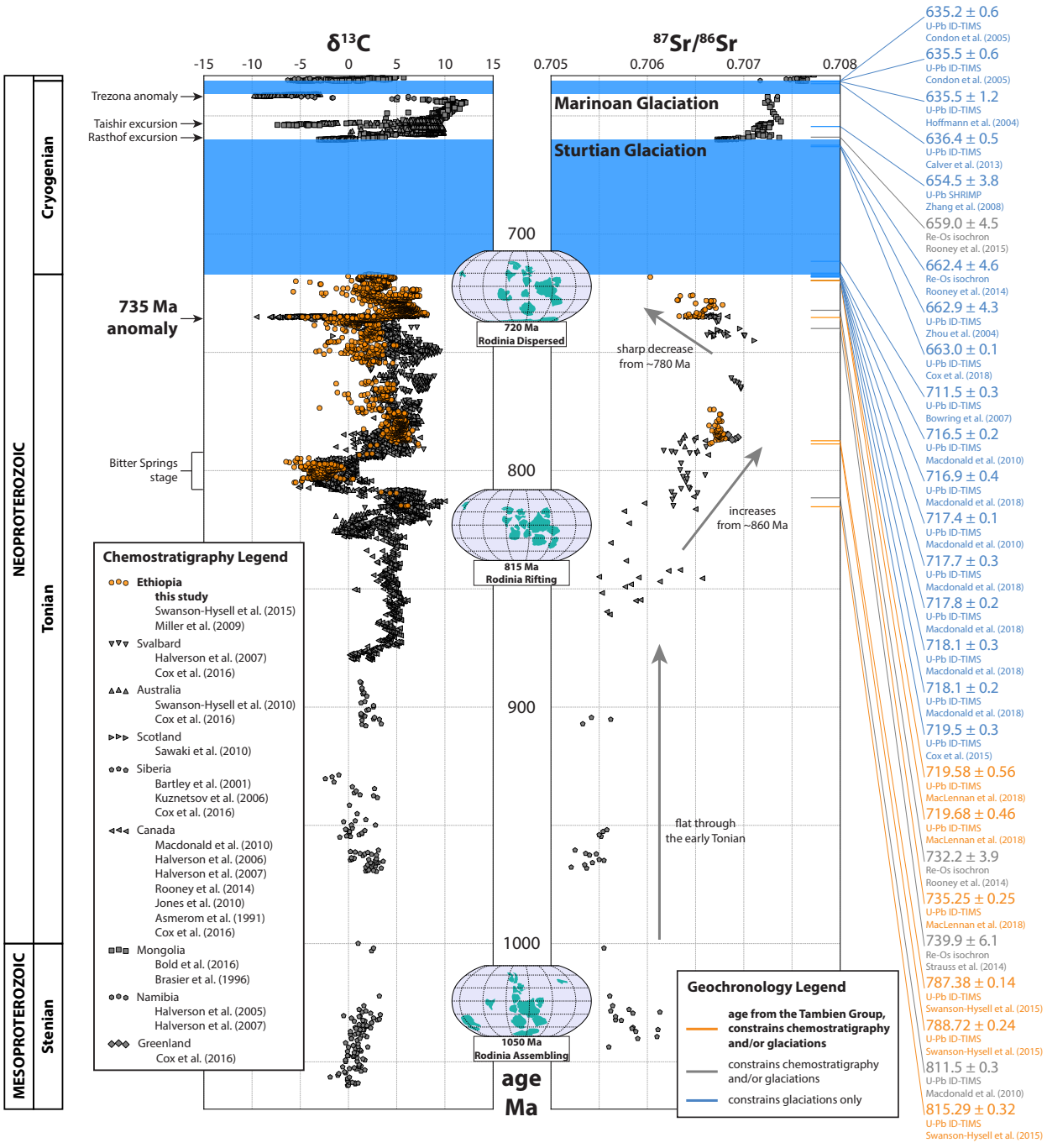

Figure 3.12: Tonian-Cryogenian $\delta^{13}C$ and $^{87}Sr/^{86}Sr$ chemostratigraphic composite. The paleogeographic reconstructions are included to illustrate the approximate geometry of Rodinia (assembled vs. dispersed) through the Tonian.

(Kuznetsov et al., 2006; Cox et al., 2016). Cryogenian $\delta^{13}C$ and $^{87}Sr/^{86}Sr$ data within the composite come from the Tsagaan-Olam Group of Mongolia (Brasier et al., 1996; Bold et al., 2016), the Hay Creek Group of Canada (Rooney et al., 2014), the Adelaide Rift Complex of South Australia (Swanson-Hysell et al., 2010; Rose et al., 2012), and the Otavi Group of Namibia (Halverson et al., 2005, 2007a).

Correlations between datasets are made using absolute age constraints where possible - otherwise, the characteristic negative $\delta^{13}C$ anomalies of the ca. 800 Ma Bitter Springs stage and the ca. 735 Ma anomaly that is referred to in the literature as the Islay anomaly (although this name is potentially problematic; Fairchild et al., 2018) are used to align datasets. The same criteria for assessing altered $^{87}Sr/^{86}Sr$ values that were used in the original publications are applied here, unless our analysis of $^{87}Sr/^{86}Sr$ vs. [Sr] and $^{87}Sr/^{86}Sr$ vs. Mn/Sr suggested a different criteria for alteration. However, even when different criteria are applied for a particular dataset, the resulting $^{87}Sr/^{86}Sr$ curve is similar to that presented in the original study with little difference for the large-scale $^{87}Sr/^{86}Sr$ trends through the Tonian. The details of the methodology, details regarding the compiled data, and a link to the Python code used to develop the Tonian-Cryogenian chemostratigraphic composite are included in the *Supporting Information*.

3.8 Discussion

Onset of the Sturtian Snowball

Geochronology

Energy balance models of Snowball Earth initiation propose that, once ice sheets reach ∼30° latitude, the ice-albedo positive feedback overwhelms negative feedbacks on temperature, causing Earth's surface temperature to plummet and ice to advance to the equator on the time scale of less than a few thousand years (Baum and Crowley, 2001; Hoffman and Schrag, 2002; Pollard and Kasting, 2005). In other words, energy balance models predict that, at the resolution of U-Pb ID-TIMS dating, all low-latitude areas were covered by ice at the same time. While this hypothesis is supported by climate models of varying complexity, a direct field test for the synchronous onset of any of the Snowball Earth episodes has not been made. In order to perform such a test, high-precision ages from as close as possible to the onset of glacigenic deposits in as many different basins as possible is required. However, despite the fact that glacigenic deposits associated with the Sturtian Snowball Earth have been identified in numerous basins around the world (Hoffman and Li, 2009), very few of these basins have direct geochronologic data that precisely constrains the onset of the glacigenic deposits in their respective basins.

Prior to data from the Tambien Group, the best age constraints on the start of the Sturtian Glaciation came from northwestern Canada where U-Pb ID-TIMS on zircons from a volcanic tuff within glacial diamictite and from a rhyolite underlying this diamictite yielded weighted mean ages of 716.9 ± 0.4 and 717.43 ± 0.14 Ma respectively (Macdonald et al., 2010,

2018). Given that thick volcanic units have the potential to obscure sedimentary evidence of glaciation, the 717.43 ± 0.14 Ma age from the rhyolite cannot be interpreted to be pre-glacial in this basin without ambiguity. Age constraints for the onset of Sturtian glacigenic deposits also come from other basins around the world, but provide looser constraints than the dates from northwestern Canada. U-Pb ID-TIMS on detrital zircons from a volcaniclastic unit underlying Sturtian diamictite in Arctic Alaska yielded a maximum depositional age of 719.47 ± 0.29 Ma (Cox et al., 2015). These data cannot rule out that the onset of continental ice in Arctic Alaska significantly post-dated 719.47 ± 0.29 Ma, especially since an unconformity separates the volcaniclastic unit from the diamictite. U-Pb ID-TIMS on zircons from a tuffaceous graywacke within a Sturtian diamictite in Oman yielded an age of 711.52 ± 0.31 Ma (Brasier et al., 2000; Bowring et al., 2007). This minimum age constraint on the onset of continental ice in Oman is consistent with the data from northwestern Canada, but is too young to reliably test the rapid onset of low-latitude glaciation. U-Pb secondary-ion mass spectrometry (SIMS) dates on zircons from tuffaceous slates underlying Sturtian diamictite in South China yielded ages of 715.9 ± 2.8 and 716.1 ± 3.4 Ma, also consistent with dates from northwestern Canada. However, zircons from these tuffaceous slates range in age from 705 to 827 Ma (Lan et al., 2014) with large uncertainty on individual dates, and the *in situ* methods used on these samples do not chemically abrade the zircon prior to analysis, which combined with lower precision makes it difficult to identify Pb-loss compared to dates developed using ID-TIMS.

An estimated age of the base of the glacial deposits in the Tambien Group is between 718.0 and 716.4 Ma at the 95% confidence level (MacLennan et al., 2018). This constraint is too imprecise to conclude that low-latitude glaciation was as globally synchronous as energy balance models predict. Nevertheless, this result is consistent with synchronous onset of deposition of the Negash Formation and the glacigenic deposits in northwestern Canada.

Lithostratigraphy

In addition to the geochronologic constraints consistent with synchronous onset of low-latitude glaciation, the evolution of the depositional environment as recorded by the sedimentary lithofacies leading into the Sturtian Glaciation can add insight into the nature of glacial onset. West of the Zamra Fault in the Samre Fold-Thrust Belt (Fig. 3.2), the upper ∼50 m of the Mariam Bohkahko Formation consists of siltstones and very fine sandstones interbedded with minor carbonates (Figs. 3.7 and 3.13). These carbonates are mostly grainstone beds that are generally <50 cm thick, and in many places are within a few meters of or in direct contact with the basal diamictite of the Negash Formation. Trough cross-stratification and scour surfaces are common sedimentary features in these strata, as well as carbonate rip-up clasts and ooid grains within the grainstones. In two measured sections, a 60-70 cm oncolite horizon (Fig. 3.6) is observed 7.0 and 23.2 m below the basal diamictite respectively. Together, these lithofacies suggest deposition in or near a shallow-water environment with significant siliciclastic sediment input, proximal to a warm shallow-water carbonate factory that occasionally delivered carbonate sediment to this part of the basin

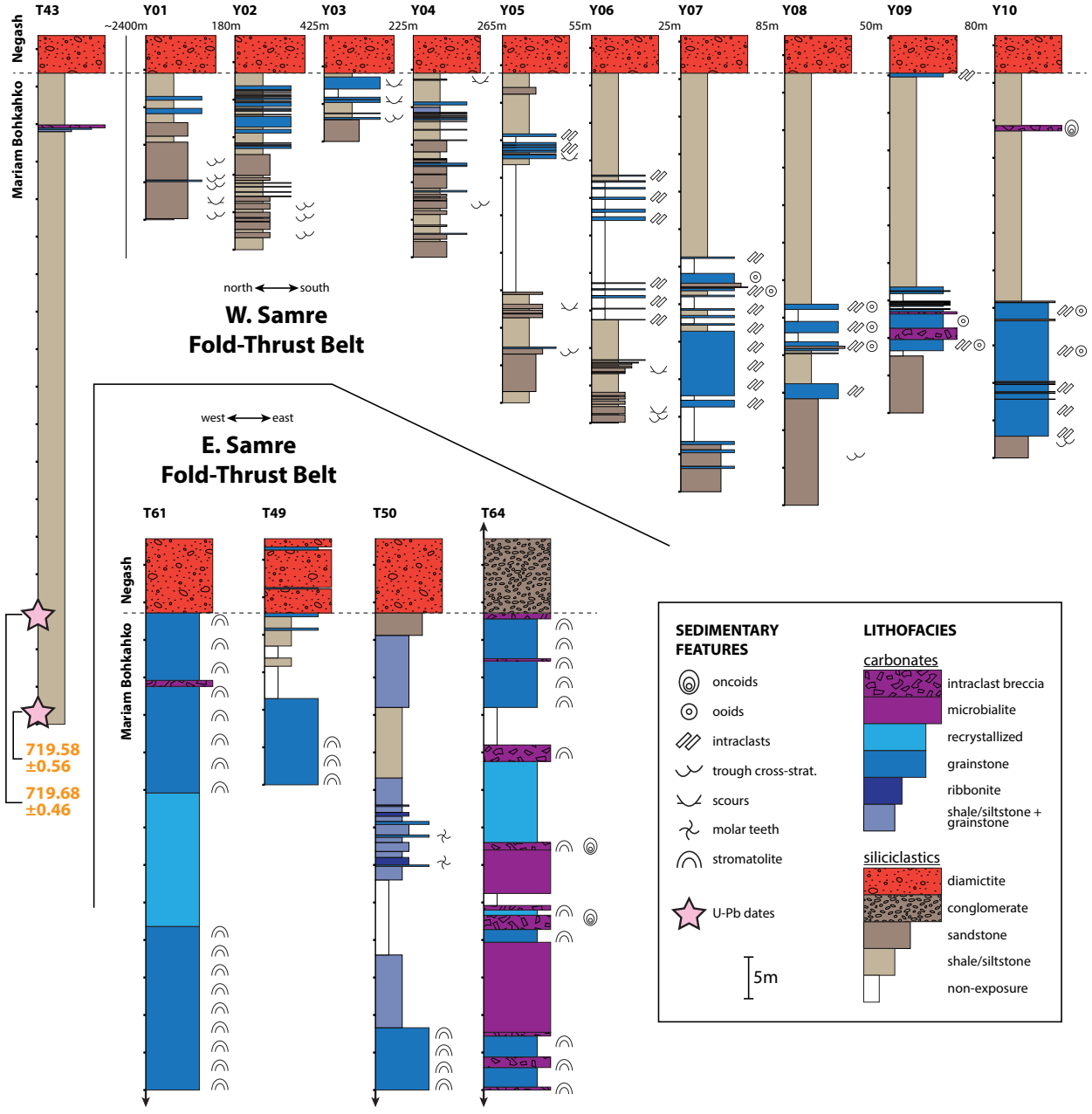

Figure 3.13: Lithostratigraphy near the contact between the Mariam Bohkahko and Negash formations in the Samre Fold-Thrust Belt. In the western Samre Fold-Thrust Belt, sections shown here were measured from north to south along the eastern limb of the major syncline west of the Zamra Fault, except for T43 which was measured along the western limb (Fig. 3.2). These sections are representative of the nature of this contact in that area. Meter values above the stratigraphic columns indicate the distance along bedding strike between each of the measured sections. In the eastern Samre Fold-Thrust Belt, sections shown here were measured in three different synclines east of the Zamra Fault near the Zamra River (Fig. 3.2), and are organized from west to east. Black arrows indicate that lithostratigraphic data continues upwards/downwards for that section, but are not shown. Tick marks to the left of each stratigraphic column represent 5 m intervals.

during storms. Notably, we do not observe any change in this depositional environment leading up to the basal diamictite, nor do we observe any outcrop-scale erosional unconformities between the Mariam Bohkahko and Negash formations. Instead, this contact is characterized by the sudden appearance of pebble-sized clasts within previously clast-free siltstones, making it look like a conformable contact. Although accumulation rates are expected to vary significantly between lithofacies, especially on short time scales, MacLennan et al. (2018) estimated an average long-term accumulation rate of the Matheos and Mariam Bohkahko formations between 2.8-3.5 cm/kyr at the 95% confidence level. Given that the exact contact (within a few centimeters) between the Mariam Bohkahko and Negash formations is often poorly exposed, if we assume that this accumulation rate estimate holds to first-order for the uppermost Mariam Bohkahko Formation, the fact that we do not observe any change in the warm tropical shallow-water depositional environment leading up to the basal diamictite is consistent with energy balance models that predict that ice advanced to the equator on the time scale of less than a few thousand years (Baum and Crowley, 2001; Hoffman and Schrag, 2002; Pollard and Kasting, 2005). While the contact appears planar at the outcrop scale, it is possible that there is an erosional unconformity between the two formations. Such an unconformity, for instance via glacial scouring, could be called upon to explain the northward thinning of the uppermost siltstone unit in Figure 3.13, as well as the northward thinning of the Mariam Bohkahko Formation as a whole near the southern nose of the syncline just west of the Zamra Fault (Fig. 3.2). Lateral variability in the sequence of lithofacies between measured sections in the uppermost Mariam Bohkahko Formation west of the Zamra Fault could instead reflect lateral variability in basin topography and/or flow patterns during storm events, and the northward thinning of the Mariam Bohkahko Formation as a whole could be explained by structural thickening via isoclinal folds close to the nose of the syncline just west of the Zamra Fault and/or structural thinning via increased boudinaging of carbonate beds moving northward away from the nose of this syncline (see *Lithostratigraphy*). In any case, zircons in volcanic tuffs within the Mariam Bohkahko Formation 73.6 and 85.3 m below the base of the Negash Formation in this area yield U-Pb ID-TIMS ages of 719.68 ± 0.46 and 719.58 ± 0.56 Ma respectively (Fig. 3.13; MacLennan et al., 2018). Given that the geochronologic constraints from northwestern Canada suggest that global glaciation was ongoing by 716.9 ± 0.4 Ma (Macdonald et al., 2018), that energy balance models predict that ice advanced to the equator on the time scale of less than a few thousand years (Baum and Crowley, 2001; Hoffman and Schrag, 2002; Pollard and Kasting, 2005), and that tens of meters of sediments continued to be deposited between the eruption of these two tuffs and the first occurrence of diamictite in the Tambien Group, the ages from the Mariam Bohkahko Formation indicate minimal (if any) erosion of the Mariam Bohkahko Formation west of the Zamra Fault.

East of the Zamra Fault in the Samre Fold-Thrust Belt (Fig. 3.2), the nature of the contact between the Mariam Bohkahko and Negash formations is more variable than to the west (Figs. 3.7 and 3.13). Stromatolites are ubiquitous in the carbonates of the Mariam Bohkahko Formation in this area, and in some cases lie directly in contact with the basal diamictite of the Negash Formation. However, in other cases, siltstones and very fine sand-

stones interbedded with minor grainstones and ribbonites lie between these stromatolites and the basal diamictite. These siliciclastics with carbonate interbeds could represent a change in water depth or a transition to siliciclastic sediment input into this part of the basin. In the eastern-most syncline of the Samre Fold-Thrust Belt (Fig. 3.2), the uppermost Mariam Bohkahko Formation consists of stromatolites, microbialites, and intraclast breccias with stromatolite and oncoid clasts (Fig. 3.6), suggesting deposition in a very shallow warm tropical environment that was conducive to the formation of microbial mats. The base of the Negash Formation in this syncline consists of a distinctive >45 m thick clast-supported conglomerate composed of sub-angular carbonate clasts within a dolomitized carbonate matrix (Fig. 3.13), instead of the massive diamictite with a silt matrix observed in all other areas. The origin of this carbonate conglomerate is enigmatic, but it could represent a subglacial fan at the mouth of a subglacial channel, a terminal moraine, an olistolith (e.g. Le Heron et al., 2014), or a subglacial channel conglomerate. It is therefore plausible that the contact between the Mariam Bohkahko and Negash formations is unconformable in this eastern-most syncline, especially since no geochronologic data for strata in this area have been developed. However, we do not observe any indication of an erosional unconformity between the Mariam Bohkahko and Negash formations further to the west, and therefore the juxtaposition of marine carbonates, especially stromatolites, with the basal diamictite lends further support to the hypothesis of rapid cooling immediately prior to the glaciation and sudden advance of ice toward the equator.

δ^{13}C Excursions

The mechanism(s) behind the exceptionally large negative δ^{13}C excursions in the Neoproterozoic remain(s) a mystery. Proposed mechanisms for the excursions include: a decrease in the ratio of organic to inorganic carbon burial resulting from colder conditions suppressing organic productivity (Kaufman et al., 1997; Hoffman et al., 1998), oxidation of a large dissolved organic carbon pool (Rothman et al., 2003), enhanced export of organic matter from the upper ocean into anoxic deep water where dissolved and particulate organic carbon is remineralized (Tziperman et al., 2011), precipitation of authigenic carbonate during early diagenesis (Schrag et al., 2013), interactions of hydrocarbon-influenced fluids with carbonates during diagenesis (Derry, 2010), and meteoric diagenesis in response to sea level fall (Swart and Kennedy, 2012). Some of these proposed mechanisms for large negative δ^{13}C excursions imply that the excursions are global in nature, and therefore synchronous between basins, while others imply local processes that would not necessarily lead to the excursions being recorded in the same age rocks between basins (but see Swart, 2008). Furthermore, some of these proposed mechanisms draw connections between large negative δ^{13}C excursions and the onset of glaciation.

Data from the Tambien Group add new constraints to this debate. A volcanic tuff (sample T46-102.2Z) adjacent to carbonates with δ^{13}C = ~0‰ was identified ~4 m above the ~-12‰ nadir of the large negative excursion near the Didikama-Matheos formation boundary (Fig. 3.8). Zircons from this tuff yield a weighted mean age of 735.25 ± 0.88 Ma

(including all external uncertainties; MacLennan et al., 2018) using U-Pb ID-TIMS. This age is consistent with geochronologic constraints from within a similar large negative $\delta^{13}C$ excursion in the Windermere Supergroup of northwestern Canada (referred to as the Islay anomaly in the literature): Rooney et al. (2014) obtained a Re-Os age of 732.2 ± 3.9 Ma (including all external uncertainties) from black shales adjacent to carbonates with $\delta^{13}C$ = ∼0‰ and ∼200 m above the nadir of the excursion, and Strauss et al. (2014) obtained a Re-Os age of 739.9 ± 6.1 Ma (including all external uncertainties) from black shales adjacent to carbonates with $\delta^{13}C$ = ∼-4‰ and ∼5 m below the nadir of the excursion. These three dates suggest that the Didikama-Matheos excursion records the same perturbation to the carbon cycle as that in the Windermere Supergroup. Furthermore, although no direct reliable age constraints have been developed, sharp negative $\delta^{13}C$ excursions interpreted to be correlative to this ca. 735 Ma anomaly in the Windermere Supergroup also have been observed in the Dalradian Supergroup of Scotland (Sawaki et al., 2010), the Akademikerbreen Group of northeastern Svalbard (Halverson et al., 2007b; Hoffman et al., 2012), and the Windermere Supergroup (Coates Lake Group) of northwestern Canada (Halverson, 2006). Together, these data suggest that a large negative $\delta^{13}C$ excursion occurs synchronously at ca. 735 Ma in at least two separate basins and potentially globally, and that it precedes the Sturtian Glaciation by ∼18 Myr (MacLennan et al., 2018). We refer to this excursion, which we interpret to be global, as the '735 Ma anomaly.'

Most Tonian stratigraphic sequences either do not host carbonates in the interval immediately preceding the onset of the Sturtian Glaciation, or have missing time associated with an unconformity. Carbonate stratigraphy from northwestern Canada (Halverson, 2006; Macdonald et al., 2010; Rooney et al., 2014) and northeastern Svalbard (Halverson et al., 2007b) are interpreted to end at or soon after the 735 Ma anomaly (Fig. 3.12). The Coppercap Formation of the Coates Lake Group of northwestern Canada preserves carbonate stratigraphy that records $\delta^{13}C$ values >5‰ after the nadir of the 735 Ma anomaly (Halverson, 2006; Rooney et al., 2014), but if the duration of the 735 Ma anomaly (from the initiation of the downturn in $\delta^{13}C$ values through to the full recovery) is ∼1 Myr (MacLennan et al., 2018) and sediment accumulation rates in the Coates Lake Group are constant, the top of this succession would have an age >730 Ma. However, the Dalradian Supergroup of Scotland may preserve carbonates significantly younger than 735 Ma. $\delta^{13}C$ values in carbonates of the Garbh Eilach Formation of the Dalradian Supergroup are sustained at ∼-5‰ for ∼50 m of stratigraphy before gradually increasing to values of ∼1‰ over ∼10 m of stratigraphy (Fairchild et al., 2018). These negative $\delta^{13}C$ values are referred to as the Garvellach anomaly. The weakly positive values are then sustained through the ∼10 m of stratigraphy that are interpreted by Fairchild et al. (2018) to represent a conformable transition into the Sturtian glacial deposits of the Port Askaig Formation. However this interpretation is not without ambiguity, since no direct geochronologic constraints exist for the Garbh Eilach Formation, and the $^{87}Sr/^{86}Sr$ data from the carbonates within this formation (Fairchild et al., 2018) are too scattered to use for nuanced chronostratigraphic intepretation. Therefore, it is possible that the intermittent subaerial exposure suggested by the sedimentary features in the upper Garbh Eilach Formation (such as gypsum pseudomorphs; Fairchild et al., 2018) obscures a

significant unconformity, and that the Garvellach anomaly may be correlative to the 735 Ma anomaly. Furthermore, the intermittent subaerial exposure could have exposed Garbh Eilach Formation carbonates to meteoric alteration, or created a depositional environment with limited connection to the open ocean. If so, the low $\delta^{13}C$ values of the Garvellach anomaly could be a result of local processes that do not reflect global marine $\delta^{13}C$ at the time of deposition.

On the other hand, our analysis of the geochemical data indicates that $\delta^{13}C$ values are sustained at ∼5‰ following the recovery from the 735 Ma anomaly in the Tambien Group, then remain at positive values with a broad decrease to values of ∼2‰ through the Mariam Bohkahko Formation up to the contact with the Negash Formation, with low $\delta^{13}C$ values in the Mariam Bohkahko Formation being a result of secondary alteration via unbuffered fluids (see *Diagenetic Considerations*; Fig. 3.7). Furthermore, geochronologic constraints demonstrate that carbonate stratigraphy from the Tambien Group continues well past the 735 Ma anomaly until at least ca. 719.6 Ma - at most only a few million years before the onset of Sturtian Glaciation (Fig. 3.7). This makes the Tambien Group host to the most demonstrably complete pre-Sturtian (from ca. 820 Ma until 0 to 2 Myr before the onset of global glaciation) carbonate stratigraphy studied to date, and suggests that no large negative $\delta^{13}C$ excursion was associated with the onset of the Sturtian Glaciation. However, if further work demonstrates that the Garbh Eilach Formation is conformable with Sturtian glacial deposits and that the low $\delta^{13}C$ values in that formation reflect global marine $\delta^{13}C$ at the time of deposition, then the Garvellach anomaly must be between ∼719-717 Ma and not recorded in the Tambien Group, and could be associated with the onset of the Sturtian Glaciation.

Other sharp high-amplitude Neoproterozoic $\delta^{13}C$ excursions have been interpreted to be global signals that are temporally disconnected from low-latitude glaciation, such as the Cryogenian inter-glacial Taishir excursion (Fig. 3.12; Bold et al., 2016) and the Ediacaran Shuram-Wonoka excursion (Husson et al., 2015b). Together, these conclusions suggest that proposed mechanisms to explain at least some of these sharp high-amplitude $\delta^{13}C$ excursions: 1) do not have to be consistent with low pCO_2 and the onset of low-latitude glaciation; and 2) should have the capacity to explain synchronicity in at least a number of basins around the world.

Pre-Sturtian $^{87}Sr/^{86}Sr$ and the Drivers of Planetary Cooling

Large Igneous Provinces

One of the most prominent proposed mechanisms for the initiation of the Sturtian Snowball Earth argues that the emplacement of large igneous provinces (LIPs) at low latitudes contributed to the onset of the snowball climate state by enhancing planetary weatherability, leading to a lower atmospheric CO_2 concentration (the 'Fire and Ice' hypothesis; Goddéris et al., 2003; Cox et al., 2016). Central to this hypothesis is the fact that mafic lithologies have high weathering rates as well as high concentrations of Ca and Mg that are liberated through chemical weathering and ultimately sequester carbon through carbonate precipitation (Dessert et al., 2001). Furthermore, there is an apparent increase in the area and

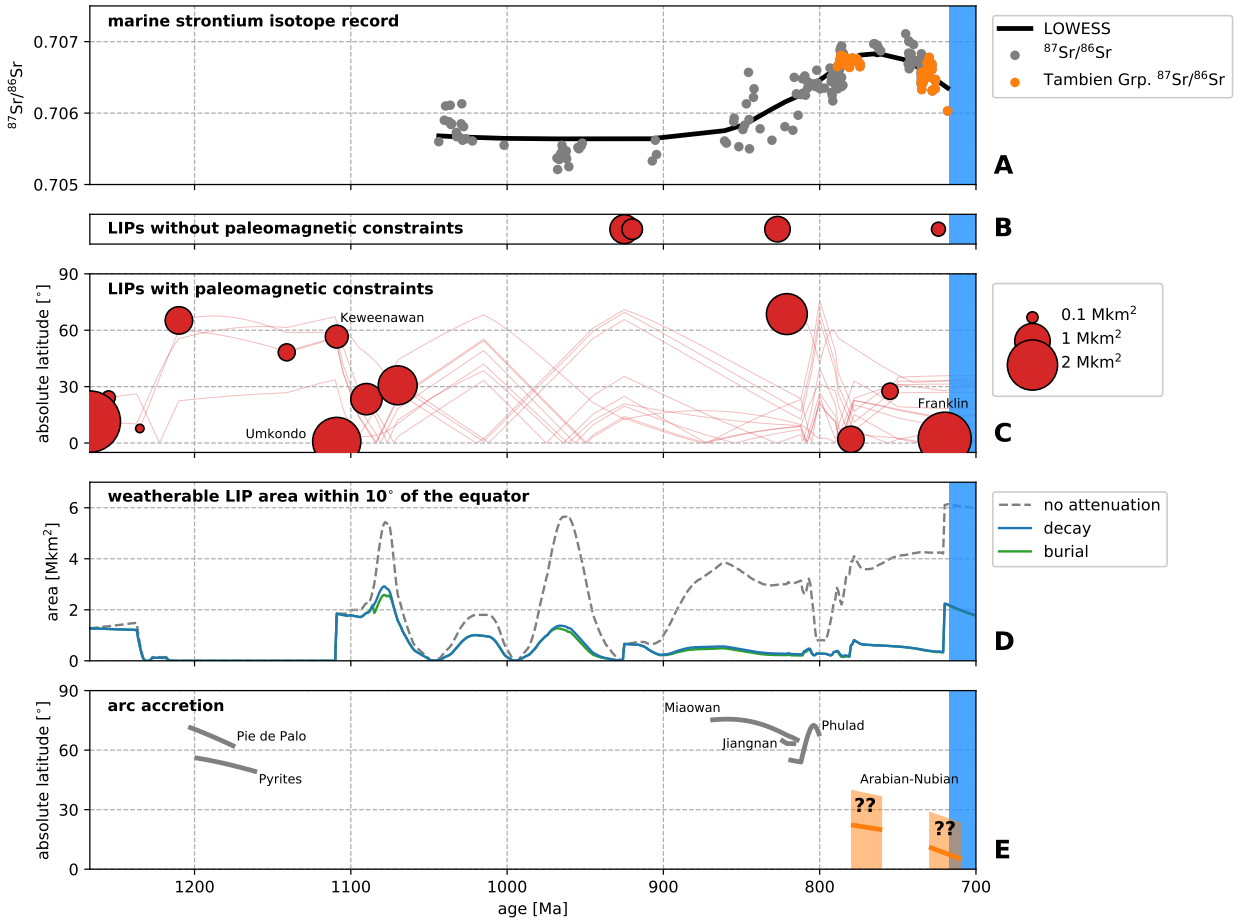

Figure 3.14: **A)** Composite $^{87}Sr/^{86}Sr$. The black line is a locally weighted scatterplot smoothing (LOWESS) line - using 45% of the data when estimating each y-value resulted in a line that neither over- nor under-represented major trends in the $^{87}Sr/^{86}Sr$ data. **B)** Emplacement timing and area of LIPs (adapted from Ernst and Youbi, 2017) without paleomagnetic constraints. **C)** Emplacement timing, area, and latitude of LIPs (adapted from Ernst and Youbi, 2017) with paleomagnetic constraints. The lines represent the tracks of the centroids of each LIP after emplacement, obtained from a paleogeographic model (Swanson-Hysell et al., 2019) which incorporates a pair of true polar wander events ca. 810 and 790 Ma (Maloof et al., 2010; Swanson-Hysell et al., 2012). **D)** Weatherable LIP area within 10° of the equator. The three lines represent three different treatments of LIPs after emplacement (see *Pre-Sturtian $^{87}Sr/^{86}Sr$ and the Drivers of Planetary Cooling*). **E)** Centroids of arc accretion events. The paleolatitude of the Arabian-Nubian accretion events are poorly constrained. The shaded orange region represents the approximate range of latitudes that Arabian-Nubian arc accretion could have occurred at, based on the paleolatitude of India and the African cratons. The orange line represents a single model position for Arabian-Nubian arc accretion that is consistent with existing constraints. In all panels, the blue bar represents the Sturtian Glaciation.

frequency of continental flood basalts from ca. 860 Ma onward (Cox et al., 2016), culminating in the eruption of the 2.225×10^6 km^2 Franklin LIP (Fig. 3.14; Ernst et al., 2008) around

the time of Sturtian Glaciation initiation. At this time, paleogeographic reconstructions (e.g. Li et al., 2008) place the Franklin LIP at low latitudes where chemical weathering rates are expected to be highest due to relatively high temperatures and runoff rates. We assess these arguments below through the lens of the newly temporally-calibrated composite $^{87}Sr/^{86}Sr$ curve.

The strontium isotopic composition of the oceans is sensitive to the relative weathering flux from different lithologies, and thus provides a record that could give insight into the 'Fire and Ice' hypothesis. Sr enters the ocean from a number of distinct sources: weathering of continental lithologies, hydrothermal interaction with mid-ocean ridges, and weathering of island arcs and oceanic island basalts (Richter et al., 1992). Continental lithologies can be divided into the broad categories of carbonates, juvenile igneous rocks (such as basalt), and older cratonic rocks (such as gneiss and granite). Importantly, each of these lithologies have different weatherabilities, Sr concentrations, and Sr isotopic compositions (Allègre et al., 2010). In particular, juvenile volcanic lithologies have relatively low $^{87}Sr/^{86}Sr$ and are readily weathered, whereas older cratonic lithologies have relatively high $^{87}Sr/^{86}Sr$ and are less readily weathered (Dessert et al., 2003). The higher $^{87}Sr/^{86}Sr$ in cratonic lithologies arises as a result of higher concentrations of Rb in differentiated crust where ^{87}Rb decays to ^{87}Sr. ^{87}Sr also is able to accumulate for a long time in ancient cratonic rocks. Sr leaves the ocean primarily through the formation of carbonate minerals (aragonite/calcite/dolomite), which record the $^{87}Sr/^{86}Sr$ of ocean water at the time of formation (Brand, 2004). The Sr isotopic composition of the ocean is effectively homogenous at any given time, since the residence time of strontium in the oceans (∼3-5 Myr) is much longer than the mixing time of the ocean (∼1000 yr) (Broecker and Peng, 1982). Thus, the $^{87}Sr/^{86}Sr$ of the oceans, and therefore unaltered marine carbonates, commonly is interpreted as a proxy for the relative globally averaged fluxes coming from each of the four sources (subaerial weathering of continental carbonates, subaerial weathering of continental radiogenic lithologies, subaerial weathering of continental and oceanic juvenile lithologies, and hydrothermal interaction with mid-ocean ridges) at any given point in time. Therefore, if there was a large increase in the weathering of juvenile material associated with low-latitude LIP emplacement immediately prior to the Sturtian Snowball Earth as the 'Fire and Ice' hypothesis argues, the $^{87}Sr/^{86}Sr$ of the oceans is expected to respond by significantly decreasing.

The global composite Tonian $^{87}Sr/^{86}Sr$ curve is flat at low values of ∼0.7055 until ca. 860 Ma when there is an increase up to $^{87}Sr/^{86}Sr$ values of ∼0.7070 by ca. 770 Ma (Figs. 3.12 and 3.14). There is a subsequent decrease back down to values of ∼0.7060 leading up to the initiation of the Sturtian Glaciation ca. 717 Ma. This decrease in $^{87}Sr/^{86}Sr$ interrupts the otherwise increasing $^{87}Sr/^{86}Sr$ values from ca. 880 Ma onwards that culminates in values ∼0.7090 by 600 Ma (Halverson et al., 2007b). There may be additional shorter time scale trends in the global composite Tonian $^{87}Sr/^{86}Sr$ curve, but given the scatter in the data at any given time interval, the uncertainty in the precise correlation of the curves between some basins, and the susceptibility of the strontium isotopic composition of carbonates to diagenetic alteration, we choose to focus on interpreting the broader and more robust trends described above.

In Figure 3.14, the $^{87}Sr/^{86}Sr$ curve is plotted along with the emplacement timing, area, and latitude of LIPs in order to evaluate proposed connections between the two. Estimates of original emplacement extents are adapted from Ernst and Youbi (2017), which were drawn to include the full surface extent of all presently-exposed dikes, sills, and volcanics interpreted to be associated with each LIP. For some LIPs, this approach may over-estimate the original surface extent, given that subsurface intrusions could extend over a broader area than the surface volcanics. The polygons also assume complete surface coverage between wide-spread remnants, which could also lead to an over-estimate of the original surface extent. On the other hand, the original extent outlines could also under-estimate the surface area for some LIPs where flows have been eroded and feeder dikes are not exposed or poorly documented. The movements of LIPs after emplacement are determined using a paleogeographic model that incorporates available paleomagnetic constraints. In addition to paleolatitude, the post-emplacement tectonic and erosional history of each LIP is important for considering the effect that a LIP will have on planetary weatherability. For example, without active uplift, soil shielding from regolith development on low-relief LIPs could significantly decrease the local weatherability of a LIP (Gabet and Mudd, 2009; Hartmann et al., 2014; Goddéris et al., 2017a). Furthermore, the thickness of this regolith is dependent on the local climate (Norton et al., 2014). Ultimately, all LIPs will cease weathering at some point, either through burial or complete erosion. As in Park et al. (2019), we construct simplified post-emplacement models for LIPS and plot how these scenarios impact the total weatherable area of LIPs within the tropics in Figure 3.14D. We define the tropics to be within 10° of the equator based on the modern zonal-average distributions of temperature and precipitation, which appear to have been stable through time (Evans, 2006). In the 'no attenuation' model, weatherable LIP areas are held constant from the time of emplacement (i.e. no post-emplacement processes are accounted for). This model is intended as an end-member reference as LIPs do not persist indefinitely for the reasons described above. In the 'decay' model, the weatherable area of each LIP undergoes exponential decay from the time of emplacement, with a half-life of 100 Myr. This model follows the approach of Goddéris et al. (2017b) and the implemented 100 Myr half-life is within the range of observed values for younger, better-constrained LIPs. The 'burial' model is identical to the 'decay' model, except that we account for burial of the ca. 1109 Ma Keweenawan LIP at ca. 1085 Ma by removing it from the model at that time, given that this region thermally subsided and the volcanics were buried by sediment (White, 1997; Ojakangas et al., 2001; Swanson-Hysell et al., 2019). We note that accounting for the burial of the Keweenawan LIP in the 'burial' model does not significantly affect the area of weatherable LIPs in the tropics in our post-emplacement models since the LIP has a relatively small area confined to a continental rift. It is important to note that, while broadly representative, these three models are an oversimplification of the true post-emplacement histories for several reasons. For instance, all LIPs (with the exception of the Keweenawan LIP) are treated identically, when instead they may have experienced very different tectonic histories that could result in very different weathering histories. Furthermore, global and local climate would have been sensitive to the paleogeography and paleotopography at any given time step, which together may have created different temperature and runoff conditions

at each LIP. For example, the topography of the Himalaya-Tibetan plateau is linked to the Asian monsoons, which introduces significantly higher precipitation in affected areas compared to the zonal average for that latitude (Zhisheng et al., 2001). Nevertheless, the 'decay' and 'burial' models are likely much closer to the true post-emplacement histories and associated LIP area in the tropics than the 'no attenuation' model.

Between ca. 1270 and 1110 Ma, LIP emplacement is relatively frequent (Fig. 3.14C). However, these LIPs are either emplaced at mid- to high latitudes, or drift there soon after emplacement, resulting in a minimal area within the tropics (Fig. 3.14D). At ca. 1110 Ma, the Umkondo LIP (Kalahari craton) is emplaced at low latitudes, followed closely by the Keweenawan (Laurentia craton), SW Laurentia, and Warakurna (Australia craton) LIPs at mid-latitudes, leading to a significant increase in LIP area within the tropics (Fig. 3.14D). After the emplacement of these four LIPs, there are no identified LIP emplacement events over the next ∼150 Myr until ca. 920 Ma, but several Mesoproterozoic LIPs drift through the tropics during this time. As described above, it is unclear whether each of these LIPs were still exposed well enough to increase global weatherability when they drifted through the tropics, but, if the post-emplacement models (Fig. 3.14D) reasonably approximate the effect of the true post-emplacement histories, then relatively large areas of weatherable LIPs pass through the tropics between ca. 1100 and 920 Ma. The weathering of these LIPs in the tropics could lead to a relatively high contribution to the global weathering flux coming from juvenile rocks passing through the warm and wet tropics and provide an explanation for the low $^{87}Sr/^{86}Sr$ values observed throughout this period (Fig. 3.14A). The Dashigou (North China craton) and Gangil-Mayumbia (Congo craton) LIPs are next emplaced ca. 920 Ma (Fig. 3.14B). However, no direct paleomagnetic constraints exist for these two LIPs, and their paleolatitudes at the time of emplacement are uncertain. In the paleogeographic model, the Gangil-Mayumbia LIP is at low latitudes at the time of emplacement, but this position is poorly constrained. Nevertheless, given its relatively small area, its contribution to global weatherability is likely to be small, even if emplaced within the tropics. Between ca. 880 and 780 Ma, Mesoproterozoic LIPs continue to transit through the tropics. However, our post-emplacement models predict that the weatherable area of these >∼200 Myr old LIPs has decayed to small values by this time, which would make them ineffective at contributing to the global weathering flux despite being in the tropics. These models therefore are consistent with a decreasing relative contribution of juvenile rocks to the global weathering flux, driving $^{87}Sr/^{86}Sr$ to higher values as is observed over this period. Notably, the large SWCUC LIP (South China craton) is emplaced at high, rather than low, latitudes at ca. 820 Ma during this interval of increasing $^{87}Sr/^{86}Sr$ ca. 880-770 Ma. The Willouran-Gairdner LIP (Australia craton) also is emplaced ca. 830 Ma, and although robust paleomagnetic constraints do not exist for this LIP, the paleogeographic model places it at mid-latitudes. The emplacement of both of these LIPs, which were potentially associated with the break-up of the supercontinent Rodinia (Ernst et al., 2008), do not appear to have any significant impact on the trend of increasing $^{87}Sr/^{86}Sr$, which is consistent with the climate at the latitudes of their emplacement not being conducive to a high weathering rate. At ca. 780 Ma, the Gunbarrel LIP is emplaced in the tropics, which roughly coincides with the inflection in

$^{87}Sr/^{86}Sr$ ca. 770 Ma, when $^{87}Sr/^{86}Sr$ begins decreasing leading into the ca. 717 Ma Sturtian Glaciation. Notably, however, none of the three post-emplacement models in Figure 3.14D predict any significant difference in the contribution of juvenile rocks to the global weathering flux between ca. 880-770 Ma when $^{87}Sr/^{86}Sr$ is observed to be increasing and ca. 770-717 Ma when $^{87}Sr/^{86}Sr$ is observed to be decreasing. In other words, all three models place a roughly stable area of weatherable LIPs in the tropics between ca. 880 and 717 Ma, with the notable exception of the Franklin LIP causing an increase ca. 720 Ma (Denyszyn et al., 2009).

Global Weathering Model

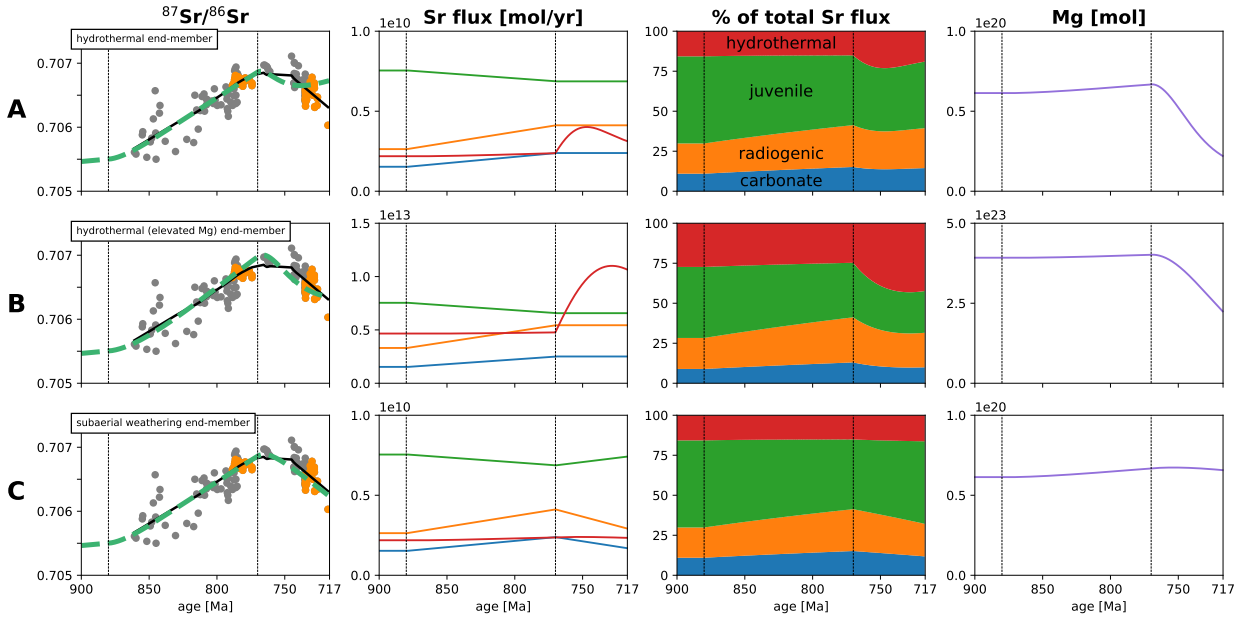

Figure 3.15: Global weathering model results. Each row represents a different weathering flux scenario. In the first column, the black curves are the LOWESS fits from Figure 3.14, and the dashed green curves are the model outputs. Vertical black lines represent times when changes in weathering flux are forced in the model. Each model run has the same weathering flux trajectories from 880 to 770 Ma with varying scenarios between 770 Ma and the onset of Sturtian Glaciation. **A)** Change in hydrothermal flux only end-member scenario. **B)** Change in hydrothermal flux only with elevated ocean [Mg] end-member scenario. **C)** Change in subaerial weathering fluxes only end-member scenario. Note that in the second and fourth columns, scenario B uses different y-axis scales than that used in scenarios A and B.

The lack of a clear correlation between the LIP record and the ca. 770-717 Ma descent in $^{87}Sr/^{86}Sr$ suggests that there are other factors that are driving at least some of the major trends observed in the Tonian $^{87}Sr/^{86}Sr$ record. In order to explore these factors, we constructed a simple global weathering model that tracks calcium, magnesium, and strontium

fluxes into and out of the ocean. This model is modified from Maloof et al. (2010) and the Python code that implements it is available in the *Supporting Information*. The core of the model is based around three equations:

$$\frac{dCa}{dt} = W_{Ca-carb} + W_{Ca-rad} + W_{Ca-juv} + H_{Ca-basalt} - P_{Ca-carb} \tag{3.1}$$

$$\frac{dMg}{dt} = W_{Mg-carb} + W_{Mg-rad} + W_{Mg-juv} - H_{Mg-clays} - P_{Mg-carb} \tag{3.2}$$

$$\frac{dSr}{dt} = W_{^nSr-carb} + W_{^nSr-rad} + W_{^nSr-juv} + H_{^nSr-basalt} - P_{^nSr-carb} \tag{3.3}$$

W_{X-carb}, W_{X-rad}, and W_{X-juv} are the inputs of Ca, Mg, and Sr coming from subaerial weathering of carbonate (*carb*), radiogenic (*rad*) lithologies, and juvenile (*juv*) lithologies respectively. Each of these terms can be broken down into:

$$W_{X-lithology} = W_{lithology} \times [X]_{lithology} \tag{3.4}$$

$W_{lithology}$ is the total (all elements) weathering flux coming from the given lithology, and $[X]_{lithology}$ is the average concentration of Ca, Mg, and Sr in the given lithology. $H_{Mg-clays}$ is the loss of Mg in seawater due to the precipitation of clay minerals, $H_{X-basalt}$ is the input of Ca and Sr associated with the weathering of ocean crust during hydrothermal circulation on or near mid-ocean ridges, and P_{X-carb} is the Mg, Ca, and Sr sink associated with the formation of carbonate minerals. n refers to each isotope of Sr (^{88}Sr, ^{87}Sr, ^{86}Sr). The values of variables used in our model are listed in the *Supporting Information*. We note that the simple global weathering model used here does not account for changes in seawater chemistry due to dolomitization, which may have acted as a quantitatively significant input/output flux for Mg, Ca, and Sr (Fantle and Higgins, 2014).

We first spin up the model to steady state over 500 Myr, choosing total Mg, total Ca, k, W_{carb}, W_{rad}, and W_{juv} such that, at the model start age of 880 Ma, Mg/Ca = 10 (based on fluid inclusion data from Spear et al., 2014) and ^{87}Sr/^{86}Sr = 0.7055 (to match the ^{87}Sr/^{86}Sr of the time; Fig. 3.12). As a percentage of the total Sr input into the ocean, this model yields hydrothermal = ∼15%, carbonate = ∼10%, radiogenic lithologies = ∼20%, and juvenile lithologies = ∼55% (Fig. 3.15A and B). These initial steady-state Sr fluxes are not a unique solution, and are different than Sr fluxes estimated for the present (hydrothermal = ∼10%, carbonate = ∼35%, radiogenic lithologies = ∼25%, and juvenile lithologies = ∼30%, from Allègre et al., 2010). However, given that modern seawater has a much higher ^{87}Sr/^{86}Sr (∼0.7091; Allègre et al., 2010) than is estimated for 880 Ma, and Sr fluxes are unconstrained for the Tonian, it is expected, reasonable, and plausible that our initial steady-state Sr fluxes have a higher contribution from juvenile sources (both subaerial weathering of juvenile lithologies and hydrothermal exchange) than is estimated for the present. Furthermore, given that modern seawater has a much lower Mg/Ca (5.2; Lowenstein, 2001) than is estimated for the Tonian, it is also expected and reasonable that our initial steady-state Sr fluxes have a

lower contribution from carbonate sources than is estimated for the present. After initial spin up to steady state, total silicate (radiogenic and juvenile lithologies) Mg + Ca weathering is held constant throughout the model runs to avoid untenable variations in pCO_2 over million-year time scales (Berner and Caldeira, 1997). We also make the simplifying assumption that carbonate lithologies are distributed homogenously over the globe wherever radiogenic lithologies exist, and thus also hold the ratio of W_{rad} to W_{carb} constant throughout the model runs. We do not expect changes in the carbonate weathering flux to be strongly coupled to changes in the subaerial weathering flux from juvenile lithologies, since carbonate lithologies are not commonly associated with juvenile volcanic rocks erupted as part of a large igneous province. However, these two fluxes may be coupled in the case where basins associated with island arcs have a significant sedimentary carbonate component, and these basins are uplifted and weathered in association with arc amalgamation or arc-continent collision. Our model does not account for this potential coupling, which is a limitation.

From these initial conditions, we sought to explore scenarios that would result in the observed pre-Sturtian Glaciation $^{87}Sr/^{86}Sr$ curve. We find that forcing a linear increase in the proportion of the subaerial weathering flux from both the radiogenic lithologies and carbonates (W_{rad} and W_{carb}) from ∼20% and ∼10% respectively at 880 Ma to ∼25% and ∼15% respectively at 770 Ma, while decreasing the proportion of the subaerial weathering flux from juvenile lithologies (W_{juv}) from ∼55% to ∼45%, produces the increase in $^{87}Sr/^{86}Sr$ from ca. 880 Ma (Fig. 3.15A and C). This solution represents a feasible tectonic scenario for this time interval - Rodinia had begun to rift apart at low latitudes during this time (Li et al., 2008), which would have brought ocean basins in proximity to previously landlocked continental interiors, resulting in as much as an order of magnitude increase in runoff in these areas (Goddéris et al., 2017b). The increased runoff in previously arid continental interiors, combined with the generally high runoff and temperature at low latitudes, could have increased the relative weathering flux from radiogenic continental interiors and driven up marine $^{87}Sr/^{86}Sr$ between ca. 880-770 Ma, as proposed by Halverson et al. (2007a). In addition, as discussed above, the 'decay' and 'weathering' models both predict a small weatherable area of LIPs in the tropics ca. 880-770 Ma relative to the preceding ∼230 Myr (Fig. 3.14D). This tectonic scenario also could have contributed to driving $^{87}Sr/^{86}Sr$ to higher values by decreasing the weathering flux from juvenile sources. Since increases or decreases in W_{rad} must be matched by decreases or increases in W_{juv} in order to keep total silicate Mg + Ca weathering constant, the combination of Rodinia rifting apart at low latitudes and a decreasing weatherable area of LIPs within the tropics could have driven $^{87}Sr/^{86}Sr$ to higher values. However, significant uncertainty associated with these Tonian paleogeographic reconstructions remain, and this modeled solution is non-unique. Nevertheless, there needs to be an increase in the Sr flux from radiogenic sources relative to juvenile ones to produce the observed increase in $^{87}Sr/^{86}Sr$ ca. 880-770 Ma. We note that the rifting of a supercontinent may be associated with an increase in the length of mid-ocean ridges, and therefore an increase in the low $^{87}Sr/^{86}Sr$ flux coming from hydrothermal systems (as has been proposed for the opening of the Iapetus Ocean in the Early Cambrian; Maloof et al., 2010). However, since the majority of oceanic crust preserved today is younger than the beginning of the break

up of the most recent supercontinent Pangea (Müller et al., 2008), the effect of supercontinent break up on total mid-ocean ridge length is poorly constrained. Nevertheless, even if the low $^{87}Sr/^{86}Sr$ flux coming from hydrothermal systems increased during Rodinia break up, it must have been overwhelmed by the increase in the Sr flux from radiogenic sources in order to drive $^{87}Sr/^{86}Sr$ to higher values during this time.

To explain the fall in $^{87}Sr/^{86}Sr$ leading into the Sturtian Glaciation, we consider two end-member scenarios. In the first scenario, the absolute flux of H_2O in hydrothermal systems (k) increases, which could represent an increasing length of mid-ocean ridges. In the second scenario, the relative flux coming from the subaerial weathering of juvenile vs. radiogenic lithologies increases, which could represent either an increase in the weatherable area of subaerially exposed LIPs and arcs, a movement/emplacement of LIPs and arcs into higher runoff areas, a movement of radiogenic continental crust into lower runoff areas, or a combination of these forcings.

To replicate the first end-member scenario, we try forcing a 4-fold linear increase in the absolute flux of H_2O in hydrothermal systems from 770 to 717 Ma (Fig. 3.15A). While this forcing produces a $^{87}Sr/^{86}Sr$ curve that matches the initial observed downturn starting at 770 Ma, it later deviates from the observed $^{87}Sr/^{86}Sr$ curve and begins rising at ca. 740 Ma. This change in the modeled $^{87}Sr/^{86}Sr$ trajectory is a result of depleting seawater of Mg due to the increasing flux of H_2O in hydrothermal systems. This Mg-depletion reduces hydrothermal Mg-Ca exchange, which in turn reduces the Sr flux coming from hydrothermal alteration (Berndt et al., 1988). However, since the absolute concentration of ions in seawater is poorly constrained during the Neoproterozoic, we tried to circumvent the problem of depleting [Mg] by changing the initial steady-state conditions such that [Mg] was ∼3 orders of magnitude higher than that used in the first model (Fig. 3.15B). Even with this unrealistically large increase in [Mg] (which requires increasing the initial steady-state subaerial weathering flux from juvenile, radiogenic, and carbonate lithologies by 3 orders of magnitude relative to the initial steady-state conditions used in the first model in order to maintain initial Mg/Ca = 10), a ∼4-fold increase in the absolute flux of H_2O in hydrothermal systems from 770 to 717 Ma is still required to match the observed $^{87}Sr/^{86}Sr$ curve. As discussed above, it is unclear how supercontinent break up effects the total length of mid-ocean ridges, but a 4-fold increase in this length should be unrealistically large, especially when we consider that mid-ocean ridges outside of Rodinia existed independent of the break-up of the supercontinent. The Arabian-Nubian Shield itself comprises at least 10 distinct tectonostratigraphic island arc terranes that accreted onto the periphery of Rodinia (Johnson, 2014) resulting from active seafloor spreading. Furthermore, if the hypothesis that rifting played an important role in increasing the Sr flux coming from radiogenic lithologies ca. 880-770 Ma is correct, the associated possible increase in the length of mid-ocean ridges would have preceded the decline in $^{87}Sr/^{86}Sr$ going into the glaciation.

To replicate the second end-member scenario, we found that forcing a linear increase in the subaerial weathering flux from juvenile lithologies from ∼45% at 770 Ma to ∼55% at 717 Ma (while keeping total silicate Mg + Ca weathering constant) produces the decrease in $^{87}Sr/^{86}Sr$ from ca. 770 Ma leading into the Sturtian Glaciation (Fig. 3.15C).

Together, these three global weathering model scenarios (Fig. 3.15) suggest that the primary driver of decreasing $^{87}Sr/^{86}Sr$ leading into the Sturtian Glaciation was the second end-member scenario – an increasing relative flux coming from the subaerial weathering of juvenile lithologies, rather than an increase in the absolute flux of H_2O in hydrothermal systems. However, as discussed above, all three post-emplacement models in Figure 3.14D place a roughly stable area of weatherable LIPs in the tropics ca. 880-720 Ma. Therefore, an increase in the weathering flux from LIPs is likely not the primary driver for increasing the relative flux coming from the weathering of juvenile lithologies starting ca. 770 Ma. Furthermore, current paleogeographic reconstructions overall suggest that Rodinia continued to rift apart at low latitudes ca. 770-717 Ma (e.g. Li et al., 2008) in a manner similar to that described above for ca. 880-770 Ma. Such plate motions would not lead to any significant increase of 'continentality' or movement of continental crust into higher latitudes ca. 770-717 Ma, and therefore an associated decrease in the weathering flux from radiogenic continental crust as a result of these processes is not expected.

Arc Accretion

A potential driver of the ca. 770 Ma inflection in the $^{87}Sr/^{86}Sr$ record is the first episode of Arabian-Nubian arc accretion along the Bi'r Umq-Nakasib Suture – estimated to have occurred ca. 780-760 Ma based on the ages of terrane protoliths and of syn- and post-tectonic intrusions (Pallister et al., 1988; Johnson et al., 2003; Johnson and Woldehaimanot, 2003; Johnson, 2014; Fig. 3.14E). This accretion event represents a difference between ca. 880-770 Ma and ca. 770-720 Ma, and was followed by accretion along the Allaqi-Heiani-Yanbu Suture – estimated to have occurred ca. 730-710 Ma based on the ages of terrane protoliths and post-tectonic intrusions (Ali et al., 2010; Johnson, 2014; Kozdrój et al., 2017). The paleolatitude of this accretion and associated exhumation is poorly constrained. However, the record of Arabian-Nubian arc accretion during the late Neoproterozoic assembly of Gondwana suggests that the Arabian-Nubian arc terranes were situated between India and the Congo + Saharan cratons (Li et al., 2008; Hoffman and Li, 2009; Merdith et al., 2017). This position leads to a low to mid-latitude position at the time of the ca. 780-760 Ma accretion event within paleogeographic models (e.g. Li et al., 2008; Merdith et al., 2017; Fig. 3.14E). A tropical position of proto-Arabian-Nubian Shield arc terranes is consistent with the interpreted depositional environment of the Tambien Group, given the abundance of carbonate lithofacies such as oolite which are indicative of warm waters that are supersaturated with respect to calcium carbonate (Fig. 3.3). Exhumation associated with arc terrane collision would have led to the development of steep topography and high rates of physical erosion and chemical weathering (Gabet and Mudd, 2009). The high concentrations of Ca and Mg in the uplifted rocks make it so they would have had high carbon sequestration potential. The development of topography also generates a physical barrier that forces air masses to rise and cool, which should result in an increase in the local precipitation, supplementing the already high precipitation in the tropics. Together, these factors could have substantially increased the weathering flux coming from these juvenile island arcs. Given that the LIP analysis

(Fig. 3.14D) suggests that an increase in the weathering flux from LIPs ca. 880-720 Ma is unlikely, this episode of Arabian-Nubian arc accretion stands as a strong candidate for the primary driver for falling $^{87}Sr/^{86}Sr$ starting ca. 770 Ma.

Other major ca. 1300-700 Ma arc accretion events that can be identified in the geological record (Fig. 3.14E) include: the ca. 1204-1174 Ma accretion of the Pie de Palo Complex (Vujovich and Kay, 1998; Vujovich et al., 2004) and the ca. 1200-1160 Ma accretion of the Pyrites Ophiolite Complex (McLelland et al., 2013) onto Laurentia during the Shawinigan Orogeny, the ca. 870-813 Ma accretion of the Miaowan Ophiolite onto the northern margin of the Yangtze block of South China (Peng et al., 2012), the ca. 825-815 Ma Jiangnan Orogen associated with the closure of the ocean basin between the terranes of the Yangtze and Cathaysia blocks that make up South China (Zhao, 2015), and the ca. 820-800 Ma closure of the ocean basin between the Greater India landmass and the Marwar craton (Volpe and Douglas Macdougall, 1990; Chatterjee et al., 2017). However, paleomagnetic poles place Laurentia (Palmer et al., 1977; Buchan et al., 2000), South China (Li et al., 2004; Niu et al., 2016), and India (Meert et al., 2013) outside of the tropics at or near the time of these accretion events, indicating that exhumation of associated mafic lithologies would have occurred at mid- to high latitudes with a correspondingly muted influence on global weathering and $^{87}Sr/^{86}Sr$ values compared to the Arabian-Nubian events (Fig. 3.14). We note, however, that this compilation of ca. 1300-700 Ma arc accretion events (Fig. 3.14E) is limited to the current literature on ophiolite-bearing sutures. Additional arc accretion events associated with the late Mesoproterozoic-early Neoproterozoic assembly of Rodinia (Cawood et al., 2016), may not be preserved due to exhumation and erosion. Therefore, while it is possible that Arabian-Nubian arc accretion is unique in terms of a low-latitude position in this time interval, such a conclusion would be premature.

By appreciating that arc accretion, especially in the tropics, has the potential to contribute sufficient solutes to the global weathering flux to alter global marine $^{87}Sr/^{86}Sr$ for tens of millions of years, we can examine the factors that contributed to the ca. 717 Ma initiation of the Sturtian Glaciation from a fresh perspective. Age constraints on the emplacement of the Franklin LIP into the tropics (Fig. 3.14C and D) cluster at ca. 720 Ma, but range from ca. 723 Ma to ca. 712 Ma (Heaman et al., 1992; Pehrsson and Buchan, 1999; Denyszyn et al., 2009). Without tighter age constraints on the timing of this emplacement, interpreting its precise relationship to the ca. 717 Ma initiation of the Sturtian Glaciation is difficult. If the emplacement precisely coincided with the initiation of the Sturtian Glaciation, then its primary contribution to initiating Snowball Earth could have been through cooling associated with the injection of sulfur aerosols into the stratosphere (Macdonald and Wordsworth, 2017). On the other hand, if the emplacement preceded the initiation by $\sim$1 Myr or more, then its contribution to it would have been to enhance planetary weatherability (Goddéris et al., 2003; Rooney et al., 2014; Cox et al., 2016), since the residence time of sulfur aerosols in the stratosphere is less than a few years (McCormick et al., 1995). Regardless of the precise nature of this relationship, our LIP area analysis (Fig. 3.14C and D) indicates that the Franklin LIP does not correspond to a uniquely large LIP area in the tropics. While it is one of the two highest peaks of tropical LIP area in the 1300-700 Ma interval, a larger area of

weatherable LIP is reconstructed to have existed both globally and within the tropics at ca. 1100 Ma due to the Umkondo LIP, comparable in size to the Franklin LIP, being emplaced in the tropics ca. 1110 Ma, as well as the migration of the SW Laurentia LIP into the tropics at this time. Furthermore, larger areas of weatherable LIP than both the Umkondo and Franklin LIPs have been reconstructed to exist within the tropics several more times in the Phanerozoic (Park et al., 2019). Given that there were no Snowball Earth glaciations ca. 1100 Ma or in the Phanerozoic despite there being larger areas of weatherable LIPs emplaced within the tropics than ca. 717 Ma, it is difficult to explain the initiation of the Sturtian Glaciation with the Franklin LIP alone.

However, what may differentiate the interval preceding the Sturtian Glaciation and ca. 1100 Ma are the pair of Arabian-Nubian arc accretion events that potentially occured in the tropics (Fig. 3.14E). Within this context, the Franklin LIP was not solely responsible for cooling Earth to the threshold required to initiate global glaciation. Rather, as suggested by the $^{87}Sr/^{86}Sr$ record, we propose that Arabian-Nubian arc accretion in the tropics enhanced planetary weatherability and lowered atmospheric CO_2 concentration over the $\sim$50 Myr prior to the initiation of the Sturtian Glaciation. The Franklin LIP then was emplaced in the tropics into an already cool planet, and its additional cooling effect, either through CO_2 consumption via silicate weathering and/or cooling associated with the injection of sulfur aerosols, may have tipped the climate over the threshold required for the ice-albedo positive feedback to overwhelm negative feedbacks on cooling and initiate global glaciation. Therefore, Arabian-Nubian arc accretion may have worked together with LIP emplacement to allow global glaciation to occur, and that without this arc exhumation, the Sturtian Glaciation may not have occurred. Subsequent arc accretion events within the Arabian Shield in the Cryogenian (Johnson, 2014) may have played a role in elevating planetary weatherability and contributing to the onset of the Marinoan Glaciation as well. Other studies also have argued that tropical arc accretion events contributed to global cooling in the Eocene, Cretaceous (Jagoutz et al., 2016), and Ordovician (Swanson-Hysell and Macdonald, 2017) - a correlation that appears robust throughout the Phanerozoic (Macdonald et al., 2019). Crucially, this hypothesis hinges on the paleogeographic position of these Arabian-Nubian arc accretion events to sufficiently increase planetary weatherability. Direct paleomagnetic data that provides such constraints should be a priority for future research. Furthermore, the LIP and arc accretion analysis presented here is limited to ca. 1300-700 Ma, and extending this analysis to the rest of Earth history is necessary to further evaluate the uniqueness of the combination of tropical LIPs, tropical arc accretion events, and global cooling.

3.9 Conclusions

The Tambien Group was deposited for over 100 million years of Tonian Earth history leading into the Sturtian Glaciation. The presence of carbonates and tuffs throughout the strata enable the generation of temporally well-constrained chemostratigraphic data leading into the first of the Cryogenian glaciations. U-Pb ID-TIMS ages indicate that Tambien Group

carbonates were deposited from ca. 820 Ma until 0 to 2 Myr before the onset of the Sturtian Glaciation, making the group host to the most complete carbonate stratigraphy leading into this glaciation that has been constrained with geochronology. We have used new $\delta^{13}C$ and $^{87}Sr/^{86}Sr$ data and U-Pb ID-TIMS ages from the Tambien Group to construct the most temporally well-constrained Tonian composite chemostratigraphic dataset to date, and used it to show: 1) that the 735 Ma anomaly is synchronous in at least two separate basins, precedes the Sturtian Glaciation by ∼18 Myr, and is followed by a prolonged interval of positive $\delta^{13}C$ values; 2) low-latitude glaciation was likely rapid leading into the Sturtian Glaciation, as predicted by energy balance models; and 3) enhanced subaerial weathering of juvenile lithologies, and an associated increase in weatherability that would have lowered CO_2, began ∼50 Myr prior to the initiation of the Sturtian Glaciation. The accretion of Arabian-Nubian Shield volcanic arcs in the tropics during this time likely played an important role in increasing global weatherability, contributing to the initiation of the first Neoproterozoic Snowball Earth.

3.10 Acknowledgements

Research funding came from the U.S. National Science Foundation grants EAR-1325230 (Swanson-Hysell) and EAR-1323158 (Maloof). Tremblay was supported by an U.S. National Science Foundation Graduate Research Fellowship. Sr isotope data were collected in the Center for Isotope Geochemistry at UC Berkeley directed by Don DePaolo, which is supported by the Director, Office of Science, Office of Basic Energy Sciences, of the U.S. Department of Energy under contract number DE-AC02-05CH11231. Acknowledgement and thanks go to Shaun Brown and Thomas Owens for assisting with the development of Sr isotope data, to Wenbo Yang for assisting with the development of element concentration data, Samantha Gwizd, Sergey Oleynik, and Disha Okhai for assisting with the development of C and O isotope data, and Sara Beroff for assisting with the development of the molar tooth structure petrographic data with support from the Cal NERDS program. Gawen Jenkin helped introduce Swanson-Hysell and Maloof to the Tambien Group. Daniel Condon was instrumental in generating previous U-Pb dates on the Tambien Group that was built-upon in the current work.

Chapter 4

Tonian paleomagnetism from South China permits an inclusive Rodinia or Bitter Springs Stage true polar wander, but not both

4.1 Abstract

The Tonian supercontinent Rodinia is hypothesized to have included almost all Proterozoic continental blocks. Competing models variably place South China at the core or periphery of Rodinia, or separated from it entirely. Tonian paleogeographic models also vary in whether they incorporate proposed large and rapid oscillatory true polar wander associated with the ca. 810–795 Ma Bitter Springs Stage. Here we develop new paleomagnetic data paired with U-Pb chemical abrasion isotope dilution thermal ionization mass spectrometry (CA-ID-TIMS) zircon geochronology from the Tonian Xiajiang Group in South China to establish the craton's position and test the Bitter Springs Stage true polar wander hypothesis. The Xiajiang Group comprises fine-grained siliciclastic rocks with interbedded volcanic ashes and unconformably overlies folds associated with the Jiangnan Orogeny, which united the Yangtze and Cathaysia blocks of South China. A U-Pb CA-ID-TIMS zircon date of 815.73±0.18 Ma from a tuff near the base of the Xiajiang Group brackets regional folding associated with the Jiangnan Orogeny to have occurred between ca. 830 and 816 Ma. Paleomagnetic data from stratigraphic units near the dated horizons constrain South China to high latitudes ca. 813 Ma. These data indicate a relatively stable high-latitude position from the time of the ca. 821 Ma Xiaofeng dikes pole to the ca. 805 Ma Madiyi Formation pole. These high-latitude constraints either connect the craton to Rodinia along its periphery, or disconnect it from the (super)continent entirely. The difference in pole position between the pre-Bitter Springs Stage Xiajiang Group pole and the syn-Bitter Springs Stage Madiyi Formation pole is significantly less than that predicted for the Bitter Springs Stage true polar wander

hypothesis. If this pole difference is interpreted as true polar wander superimposed upon differential plate motion, it requires South China to have been separate from Rodinia.

4.2 Introduction

Earth's lithosphere moves through two fundamental mechanisms. The more familiar of these mechanisms are tectonic motions — that is, differential movement between lithospheric plates. The second mechanism is the rotation of the entire silicate Earth in order to maintain rotational equilibrium. On any rotating planetary body, changes in the distribution of mass on (e.g. the melting of ice sheets; Mitrovica et al., 2005; Matsuyama et al., 2010; Cambiotti et al., 2010) or within (e.g. mantle convection; Spada et al., 1992) can cause reorientation of the planetary surface relative to the rotational axis (Evans, 2003; Matsuyama et al., 2014). Such reorientation causes all of Earth's tectonic plates, as well as the underlying mantle, to rotate in unison relative to the spin axis and the core. To an observer on Earth's surface, it would appear that the pole is changing position and the process is therefore referred to as true polar wander (TPW). Differential plate tectonics and TPW are operating today and were in Earth's past. Both processes are built into paleogeographic models over the past 400 million years (m.y.), with an overall dominance of differential plate tectonics (Steinberger and Torsvik, 2008; Torsvik et al., 2012).

Plate kinematic reconstructions indicate that the median plate velocity over the past 200 m.y., during which a seafloor spreading record is preserved, is ∼4 cm/yr (Zahirovic et al., 2015). Although plate velocities have been observed to significantly exceed this median value, such as during the rapid northward motion of India toward Eurasia ca. 55 Ma when its velocity was as high as 19 cm/yr (van Hinsbergen et al., 2011; Zahirovic et al., 2012), such motions are short-lived (up to ∼10 m.y.; Zahirovic et al., 2015). Based on these plate kinematic reconstructions, it has been argued that plate velocities rarely exceed ∼20 cm/yr (Meert et al., 1993; Zahirovic et al., 2015).

Over the past 300 m.y., there has been near continuous TPW at rates of 1–10 cm/yr attributed to advection of mass heterogeneities in the mantle (Steinberger and Torsvik, 2008; Torsvik et al., 2012), with the possibility of more rapid TPW in the Jurassic (Kent et al., 2015). These rates are comparable to rates of differential plate motion, which can make TPW difficult to distinguish in the record. The possibility of TPW occurring at rates exceeding those of typical plate tectonics has been discussed as a theoretical possibility in the geophysical literature (Gold, 1955; Fisher, 1974; Steinberger and O'Connell, 1997; Evans, 2003), and has been proposed as an explanation for large shifts in paleomagnetic poles in the geological record (e.g. Kirschvink, 1997). The rate at which true polar wander can occur is a function of the magnitude of the perturbation to Earth's moment of inertia tensor, the timescale over which that perturbation is applied, and the timescale for viscoelastic adjustment of Earth's rotational bulge, which is itself largely a function of mantle viscosity (Tsai and Stevenson, 2007; Steinberger and Torsvik, 2010; Creveling et al., 2012). Additionally, stabilization is thought to result from TPW-induced stresses in the lithosphere that can form

a remanent bulge (Ricard et al., 1993; Chan et al., 2014). Numerical models have suggested that velocities due to TPW motion can be higher than ∼150 cm/yr (Spada et al., 1992), although other treatments have argued that TPW exceeding ∼25 cm/yr is unlikely (Tsai and Stevenson, 2007). Ultimately, however, the rate at which TPW has proceeded at different periods of Earth history is a question for geologic and paleomagnetic records.

A pair of oscillatory TPW events ca. 810 and 795 Ma have been proposed to have occurred during the Tonian Period of the Neoproterozoic Era (Maloof et al., 2006). This hypothesis is based on paleomagnetic, isotopic, and stratigraphic data from carbonate strata in the Akademikerbreen Group of East Svalbard — a terrane that was part of Laurentia in the Tonian (Maloof et al., 2006). Two >50° shifts in paleomagnetic direction from East Svalbard, with associated plate velocities implied to be >50 cm/yr based on an interpretation that the directions are primary, were observed to be coincident with abrupt shifts in δ^{13}C (referred to as the Bitter Springs Stage; Maloof et al., 2006). These poles are from carbonate units that are separated by unconformities that were interpreted to reflect the transient changes in local relative sea level predicted to occur given the differential response of the fluid and solid Earth (Mound et al., 1999; Maloof et al., 2006). These shifts were interpreted as 'there and back again' TPW rotations in which the entire solid Earth (and therefore all of Rodinia) rotated 50° about an equatorial axis and then returned to near its prior position (Maloof et al., 2006). Further geochronologic constraints on δ^{13}C records correlated to the Bitter Springs Stage, and therefore the proposed oscillatory TPW, constrain it to have started after 811.51±0.25 Ma (U-Pb CA-ID-TIMS zircon from a tuff ∼50 m below carbonates that record the first abrupt shift to negative δ^{13}C values in the Fifteenmile Group of northwest Canada; Macdonald et al., 2010) and to have ended by 788.72±0.24 Ma (U-Pb CA-ID-TIMS zircon from a tuff ∼250 m above carbonates that record the second abrupt shift to positive δ^{13}C values in the Tambien Group of northern Ethiopia; Swanson-Hysell et al., 2015b; Park et al., 2020b). Interpolation using these and other geochronologic constraints suggest that the Bitter Springs Stage started before 807.9±0.2 Ma and ended after 800.6±0.2 Ma (Swanson-Hysell et al., 2015b). However, no direct geochronologic constraints exist on the Akademikerbreen Group stratigraphy, and therefore the ages of these paleomagnetic poles for Svalbard are reliant on carbon and strontium isotope chemostratigraphic correlations (Halverson et al., 2007b).

Given that TPW results in rotation of the entire lithosphere around the spin axis, it should manifest in the paleomagnetic record as simultaneous and identical motion of paleomagnetic poles across all continents, once standard differential plate tectonic motion has been subtracted out (Evans, 2003). Efforts to test the Bitter Springs Stage TPW hypothesis within the Bitter Springs Group of central Australia led to distinct paleomagnetic pole positions from syn-Bitter Springs Stage and post-Bitter Springs Stage sedimentary rocks (Swanson-Hysell et al., 2012). The post-Bitter Springs Stage pole was developed from a hematite remanence held in Johnny's Creek Formation siltstone and is included as a constraint for Australia in models of Rodinia (e.g. Merdith et al., 2017). The syn-Bitter Springs Stage pole from Love's Creek Formation carbonate overlaps with the Cambrian apparent polar wander path of Australia, raising the possibility that the difference in position between

the Love's Creek and Johnny's Creek poles is the result of remagnetization, leaving ambiguity in using these data to test the TPW hypothesis (Swanson-Hysell et al., 2012). The paleomagnetic remanence of carbonate rocks can be challenging to interpret as they are prone to remagnetization (Voo and Torsvik, 2012; Jackson and Swanson-Hysell, 2012). Carbonate remagnetization can be particularly vexing as it can result from chemical alteration at low temperatures such as the conversion of smectite to illite. This process can lead to the authigenic formation of magnetite at temperatures as low as 70°C (Katz et al., 1998; Tohver et al., 2008). This mechanism may explain the magnetization obtained from carbonates of the Love's Creek Formation of the Bitter Springs Group as a Cambrian overprint from authigenic magnetite formation during burial (Swanson-Hysell et al., 2012). This clay transformation mechanism, or other processes associated with fluid flow, have been invoked to explain widespread remagnetization of carbonates particularly at time periods of regional orogenesis (Voo and Torsvik, 2012). For example, at the time of the Alleghenian orogeny, North American carbonates both proximal to the orogen and hundreds of kilometers away were remagnetized through the precipitation of authigenic magnetite (McCabe and Elmore, 1989; Voo and Torsvik, 2012).

Of potential relevance to the data upon which the Bitter Springs Stage TPW hypothesis was formulated, Michalski et al. (2011) developed paleomagnetic data from metasedimentary rocks from the central terrane of Svalbard that were metamorphosed and remagnetized ca. 430 Ma during the Caledonian orogeny. The remagnetization direction in these rocks has a similar position to the pre-Bitter Springs Stage pole of the Akademikerbreen Group (lGfm from Maloof et al., 2006), leading Michalski et al. (2011) to suggest that the pole does not record a primary magnetization, and is instead the result of remagnetization at the time of the Caledonian orogeny that effected both Central and East Svalbard. However, the post-Bitter Springs Stage pole from the Akademikerbreen Group (S4fm) passes a syn-sedimentary fold test which provides strong support for a primary remanence held by magnetite for that pole. These constraints seemingly require variable remagnetization in different units of the Akademikerbreen Group for the interpretation of Michalski et al. (2011) to be correct.

These potential complexities associated with the specter of carbonate remagnetization highlight the importance of testing the Bitter Springs Stage TPW hypothesis using other lithologies such as detrital hematite-bearing siliciclastics and igneous rocks. Tonian deposition in the Nanhua Basin of South China includes reds beds and volcanic tuffs. These units potentially span the Bitter Spring Stage and provide an opportunity to develop high quality paleomagnetic data paired with precise geochronology to test both the Bitter Springs Stage TPW hypothesis and models of the configuration of the Neoproterozoic supercontinent Rodinia.

4.3 Paleogeographic Setting

Many Proterozoic continental blocks are hypothesized to have come together to form the supercontinent Rodinia during the latest Mesoproterozoic to Neoproterozoic (Hoffman, 1991;

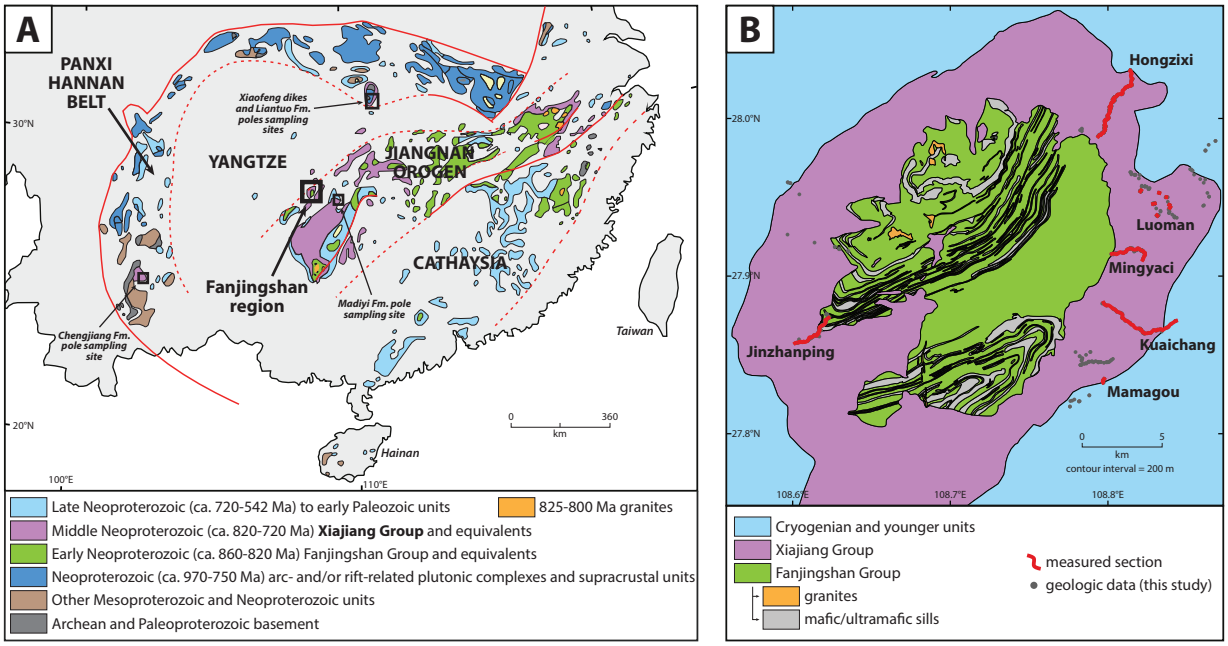

Figure 4.1: A) Summary geologic map of South China, adapted from Cawood et al. (2017), showing the Fanjingshan region from where the Xiajiang Group pole is developed in this study, as well as the localities where other Neoproterozoic poles are developed (Table 4.3). **B)** Geologic map of the Fanjingshan region. The distribution of volcanic units within the Fanjingshan Group and the contact between the Fanjingshan and Xiajiang groups were adapted from Wang et al. (2016a). Both the sedimentary and volcanic units of the Fanjingshan Group were folded, uplifted, and eroded prior to Xiajiang Group deposition. The contact between the Xiajiang Group and the overlying Cryogenian units was adapted from Zhao et al. (2011). Unit boundaries were adjusted to be consistent with our geologic data where available. Red lines show the location of the measured stratigraphic sections in Figure 4.2. Note that the Luoman section consists of seven individually measured sections that were correlated to each other based on local bedding and elevation measurements.

Li et al., 2008). However, geochronologic, geologic, and paleomagnetic research continues to refine the configuration of these blocks as well as the timing of their assembly and breakup. At the center of debates regarding the configuration of Rodinia is the South China craton (Fig. 4.1). For many years, the most widely-used paleogeographic models for the Neoproterozoic adopted the Missing Link model (Li et al., 1995, 2008), which places South China at the core of Rodinia between Australia-East Antarctica and Laurentia. This hypothesis was originally based on the interpretation that the Jiangnan Orogen between the Yangtze and Cathaysia blocks that comprise the South China craton was of similar age to the Grenvillian Orogen of Laurentia (ca. 1.1-1.0 Ga; Li et al., 1995). In this model, the Yangtze block (along with Australia) collides with the Cathaysia block and Laurentia ca. 1.0 Ga (Li et al., 1995).

Recent geologic, geochemical, and geochronological data have instead interpreted the Jiangnan Orogen to record ongoing accretionary orogenesis of magmatic arc and back arc

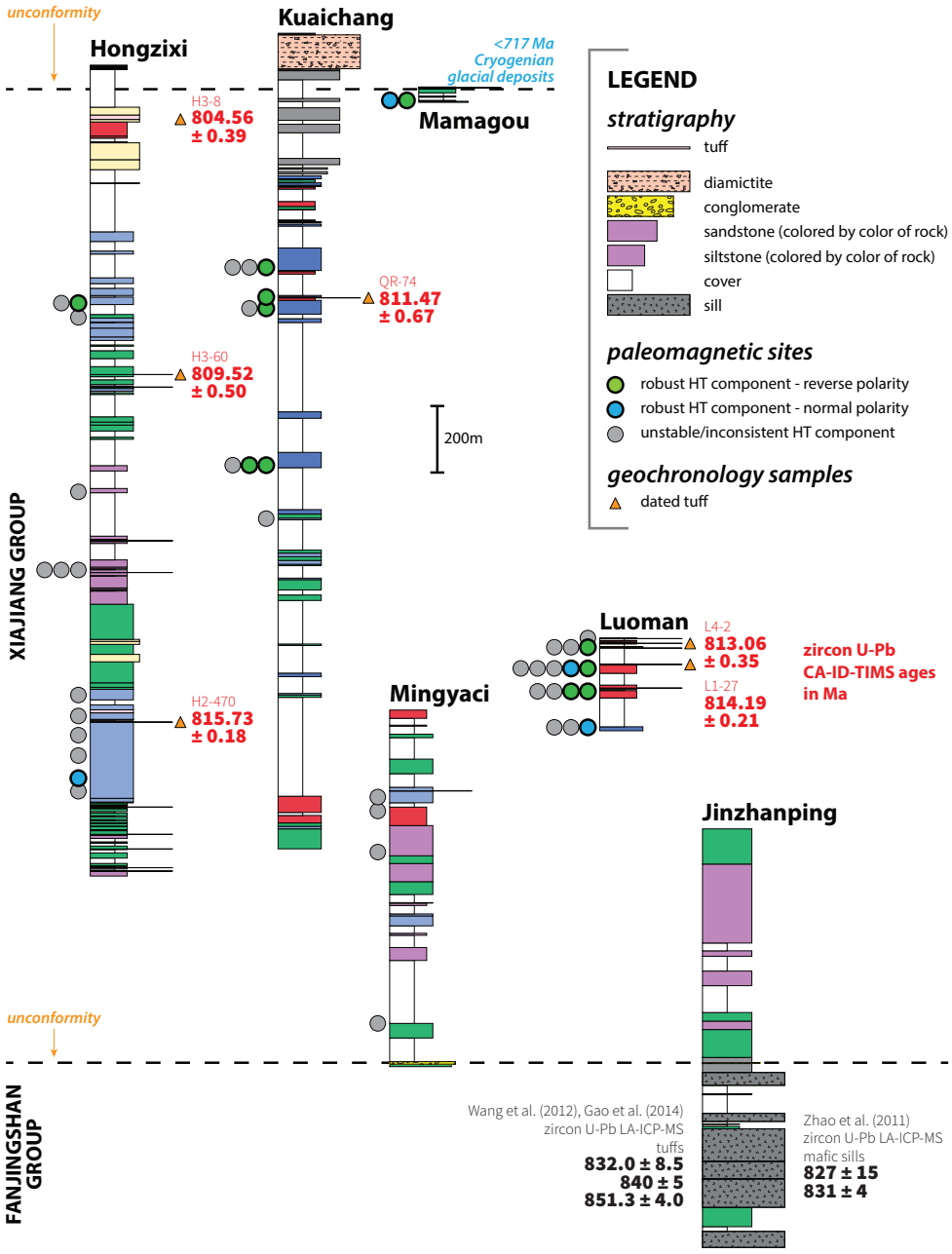

Figure 4.2: Stratigraphic sections measured in the Fanjingshan region. Locations of measured sections are shown in Figure 4.1. The colors are associated with the color of the sedimentary rocks. U-Pb CA-ID-TIMS dates from the Xiajiang Group are from this study and are shown at the stratigraphic levels where the tuffs were collected. The dates from the Fanjingshan Group are not from the section shown, but are from other studies of the rocks elsewhere in the region.

assemblages along the southeast margin of the Yangtze block in the Tonian up until <830 Ma terminal collision with Cathaysia (Cawood et al., 2017; Yan et al., 2019). In addition to this record of later Tonian magmatism and orogenesis between the Yangtze and Cathaysia blocks, there was accretionary orogenesis and continental arc volcanism along the Panxi-Hannan Belt of the northwest Yangtze block (Cawood et al., 2017). This record includes both the obduction of ca. 800 Ma ophiolites (Zhao et al., 2017) and ca. 870-706 Ma arc-related magmatism (Dong et al., 2012). These data indicate that South China was surrounded by active margins with subduction zones through much of the Tonian. This record is difficult to reconcile with a position in the interior of a stable supercontinent. Instead, these data suggest that South China was on the periphery of Rodinia (Cawood et al., 2017), or disconnected from it entirely (Merdith et al., 2017). Nevertheless, the Missing Link position for South China, as implemented in Li et al. (2008), remains the default in many depictions of Neoproterozoic paleogeography motivating the need for further development of paleogeographic constraints.

4.4 Geologic Setting

This study presents paleomagnetic and U-Pb chemical abrasion isotope dilution thermal ionization mass spectrometry (CA-ID-TIMS) zircon geochronologic data from the Xiajiang Group in the Fanjingshan region of Guizhou province, China (Fig. 4.1A). The Fanjingshan region lies within the Jiangnan orogenic belt that separates the Yangtze and Cathaysia blocks of the South China craton, and is characterized by a regional anticline that developed in the Mesozoic (Fig. 4.1B; Li et al., 2016b; Ma et al., 2019). At the core of the anticline is the Fanjingshan Group, dominantly composed of sandstones intruded by intermediate to ultramafic sills (Fig. 4.1B; Wang et al., 2014). These sills are interpreted to have formed in a subduction-related environment just prior to amalgamation of the Yangtze and Cathaysia blocks (Wang et al., 2014).

Both the sedimentary rocks and the intrusive sills of the Fanjingshan Group are folded, and are separated from the overlying Xiajiang Group by an angular unconformity (Fig. 4.1B). Tuffs of the Fanjingshan Group in the Fanjingshan region have yielded U-Pb laser ablation inductively coupled plasma mass spectrometry (LA-ICP-MS) zircon dates of 851.3±4.0 Ma, 840±5 Ma, and 832.0±8.5 Ma (Wang et al., 2012; Gao et al., 2014). U-Pb LA-ICP-MS zircon dates for the mafic sills are 831±4 Ma and 827±15 Ma (Zhao et al., 2011), and U-Pb LA-ICP-MS detrital zircon dates within the sediments are as young as 849±6.5 Ma (Zhao et al., 2011). These dates constrain the exposure, folding, and erosion of the Fanjingshan Group to have been after ca. 830 Ma. A cobble to boulder conglomerate is often the lowest unit of the Xiajiang Group, before the stratigraphy transitions into hundreds of meters of red, purple, green, and grey-blue graded beds of siltstone and fine-grained sandstone interbedded with volcanic ashes (Fig. 4.2). The fine-grained sandstone-siltstone interbeds locally exhibit ripple cross-stratification, which are interpreted to have formed as Bouma-C beds associated with distal turbidity currents. The presence of ∼1–5 cm volcanic ashes throughout the

stratigraphy without lithic fragments indicate the presence of a nearby, but not immediately adjacent, volcanic arc. Existing U-Pb LA-ICP-MS zircon dates for tuffs of the Xiajiang Group in the Fanjingshan region of 814.0±6.3 Ma and 813.5±9.6 Ma (Gao et al., 2010, 2014) suggest deposition of Xiajiang Group began by ca. 815 Ma. Unconformably overlying the Xiajiang Group in the Fanjingshan region are glacial deposits correlated with the Cryogenian Sturtian 'Snowball Earth' glaciation (referred to locally as the Tiesi'ao Formation; Xiong et al., 2014). Geochronologic constraints from South China, Laurentia, Oman, and the Arabian-Nubian Shield indicate that onset of the Sturtian glaciation was rapid and globally synchronous within the available precision of the geochronology (Bowring et al., 2007; Macdonald et al., 2010; MacLennan et al., 2018; Lan et al., 2020). These constraints on the Sturtian glaciation constrain Xiajiang Group deposition to have ended prior to ca. 717 Ma. No continuous individual section was identified that captures both the Fanjingshan-Xiajiang Group contact and the contact between the Xiajiang Group and the Sturtian glacial deposits (Fig. 4.2). However, correlation of individually measured sections based on aligning the bounding unconformities of the Xiajiang Group and the geochronologic results suggests that the Xiajiang Group is ∼3000 m thick in this region (Fig. 4.2).

We note that the nomenclature of pre-Sturtian Neoproterozoic strata in South China varies in the literature. In some publications, the term the 'Banxi Group' is used to refer to any ca. 815–717 Ma sediments in South China, including those in our study area (e.g. Zhao et al., 2011; Zhang et al., 2019). In other publications, the term the 'Banxi Group' is used to refer exclusively to ca. 815–717 Ma sediments in the Hunan province, and equivalent strata in our study area in the Guizhou province is referred to as the 'Xiajiang Group' (e.g. Bureau of Geology and Mineral Resources of Guizhou Province, 1984; Wang et al., 2014; Xiong et al., 2014; Geng, 2015; Li et al., 2016c; Wang et al., 2016a; Yan et al., 2019). Further to the southeast, sedimentary rocks interpreted to correlate with the Banxi and Xiajiang Groups are referred to as the 'Danzhou Group' (Yan et al., 2019). There are similar regional nomenclature differences for the older Fanjingshan Group, which is referred to as the 'Fanjingshan Group' in our study area and is correlated with units known as the 'Lengjiaxi Group' and the 'Sibao Group' elsewhere, and the younger Tiesi'ao Formation, which is referred to as the 'Tiesi'ao Formation' in our study area and is correlated with units known as the 'Chang'an Formation' elsewhere. In this study, we follow the nomenclature most widely used for the Guizhou province, using the term Fanjingshan Group, and referring to the sediments unconformably bounded by the Fanjingshan Group and Sturtian glacial deposits in the Fanjingshan region as the Xiajiang Group.

4.5 Methods

Paleomagnetism

Where exposure of the stratigraphy was good, sections were measured using a Jacob's staff. In cases where vegetation obscured the stratigraphy for hundreds of meters, the thickness of

covered stratigraphy was estimated based on GPS measurements and local bedding orientations, leading to the covered intervals shown in Figure 4.2.

Cores from the studied sedimentary rocks were collected using a gas-powered drill and a Pomeroy orienting device. Sun compass data were used for sample orientations when possible, and magnetic compass orientations were used when necessitated by cloud cover. Sample collection was organized into 'sites,' where each site consists of a set of samples that were obtained from within a few meters of stratigraphy. This grouping provides a useful organizational framework although it does not correspond to the definition of a site within the framework of the MagIC database wherein every sample in a site should be expected to record a direction from the same moment in time. In most cases, cores were collected from the least foliated purple/red siltstone of the Xiajiang Group, but when no such lithologies were present, green/grey-blue siltstones were also collected.

Thermal demagnetization and magnetic remanence measurements were conducted at UC Berkeley and the China University of Geosciences, Beijing. At the UC Berkeley Paleomagnetism Laboratory, measurements were made using a 2G Enterprises DC-SQUID superconducting rock magnetometer equipped with an automated pick-and-place sample changer system (Kirschvink et al., 2008). The magnetometer is housed in a magnetostatic shield with magnetic fields <500 nT. A quartz glass sample rod brings the samples into the measurement region and is typically measured at $\sim 5 \times 10^{-12}$ Am^2. After measurement of the natural remanent magnetization (NRM), the samples were progressively step-heated and thermally demagnetized in an ASC thermal specimen demagnetizer (residual fields <10 nT).

At the China University of Geosciences, Beijing, paleomagnetic analyses were conducted in a magnetically shielded room with a residual field of <300 nT in the Laboratory of Paleomagnetism and Environmental Magnetism. Magnetic remanence was measured using a 2G 755-4 K three-axis cryogenic magnetometer, and stepwise thermal demagnetizations were carried out with an ASC TD-48 or MMTDSC furnace, both of which have an internal residual field of <10 nT.

All paleomagnetic data to the measurements level, as well as interpreted fits made using the PmagPy software package (Tauxe et al., 2016), are available in the MagIC database (https://earthref.org/MagIC/doi/).

Geochronology

Tuffs collected for U-Pb geochronology typically appear as ∼1–5 cm horizons within the Xiajiang Group of the Fanjingshan region. Their tan/white color is distinguishable from the purple/red/green/grey-blue of the adjacent siltstone and fine sandstone. In some cases, the exposed surface of the tuffs have weathered into a clay-rich unlithified mud, likely due to the weathering of the volcanic ash to clays (e.g. bentonite). In these cases, the mud was removed before sampling of the lithified tuff. All samples were scrubbed with steel brushes to remove any recent detritus prior to further analysis.

Zircon grains were isolated from the bulk rock by standard mineral separation techniques. All zircon grains analyzed in this study employed the protocols and data reduction outlined in

Meyers et al. (2012). Prior to dissolution, zircon grains were subjected to a modified chemical abrasion in order to remove radiation-damaged zones of the zircon and minimize the effects of Pb loss (Mattinson, 2005). The accuracy of the $^{238}U/^{206}Pb$ dates presented herein is controlled by the gravimetric calibration of the EARTHTIME U-Pb tracer employed in this study and the determination of the ^{238}U decay constant (Jaffey et al., 1971; Condon et al., 2015). Unless stated otherwise, uncertainties on U-Pb dates reported in this manuscript are the internal (analytical) uncertainties in the absence of external or systematic errors, with these additional uncertainties reported in Table 4.2.

4.6 Results

Paleomagnetism

Table 4.1: Paleomagnetic results for individual sites with stable and consistent high temperature components in the Xiajiang Group of the Fanjingshan region.

site	section	lab	site lat.	site lon.	n	$\mathbf{dec}_{1.0}$	$\mathbf{inc}_{1.0}$	$\mathbf{dec}_{0.6}$	$\mathbf{inc}_{0.6}$	α_{95}	polarity
TR007	Hongzixi	Beijing	27.991	108.797	13	14.1	64.4	14.1	73.9	8.9	N
TR014	Hongzixi	Berkeley	28.014	108.805	12	150.2	-66.8	330.2	75.6	12.1	R
TR018	Kuaichang	Berkeley	27.867	108.820	14	208.3	-64.0	28.3	73.7	14.2	R
TR020	Kuaichang	Berkeley	27.866	108.821	10	111.6	-76.9	291.6	82.1	11.2	R
TR021	Kuaichang	Beijing	27.864	108.822	9	208.0	-71.5	28.0	78.6	17.0	R
TR024	Kuaichang	Berkeley	27.872	108.811	9	124.9	-63.5	304.9	73.3	18.2	R
TR026	Kuaichang	Berkeley	27.872	108.811	9	150.3	-85.7	330.3	87.4	16.0	R
TR004a	Mamagou	Berkeley	27.835	108.797	10	334.8	71.4	334.8	78.6	8.2	N
TR004b	Mamagou	Berkeley	27.835	108.797	5	106.4	-75.9	286.4	81.4	12.6	R
TR031	Luoman	Beijing	27.938	108.831	8	337.6	65.2	337.6	74.5	14.5	N
TR034	Luoman	Beijing	27.939	108.831	11	291.6	-75.9	111.6	81.5	13.0	R
TR035	Luoman	Berkeley	27.954	108.821	19	42.4	68.4	42.4	76.6	14.9	N
TR037	Luoman	Beijing	27.946	108.829	17	202.1	-86.3	22.1	87.8	17.2	R
TR039	Luoman	Beijing	27.946	108.829	9	136.8	-78.1	316.8	82.8	21.2	R
TR042	Luoman	Berkeley	27.943	108.839	14	131.5	-71.9	311.5	78.9	11.5	R

Notes:
(1) All directions are for the high temperature component.
(2) $\mathbf{dec}_{1.0}$ and $\mathbf{inc}_{1.0}$ refer to the declination and inclination of the mean tilt-corrected direction, without correcting for polarity or inclination shallowing.
(3) $\mathbf{dec}_{0.6}$ and $\mathbf{inc}_{0.6}$ refer to the declination and inclination of the mean tilt-corrected direction, after correcting for polarity and inclination shallowing using a flattening factor of 0.6.
(4) For the **polarity**, we interpret the mean directions with a positive inclination as normal polarity (N), and the mean directions with a negative inclination as reverse polarity (R).

Thermal demagnetization data from siltstones of the Xiajiang Group in the Fanjingshan region show variable behaviour from site to site. A component removed during initial thermal demagnetization steps (<300°C) is present in most samples and typically yields a

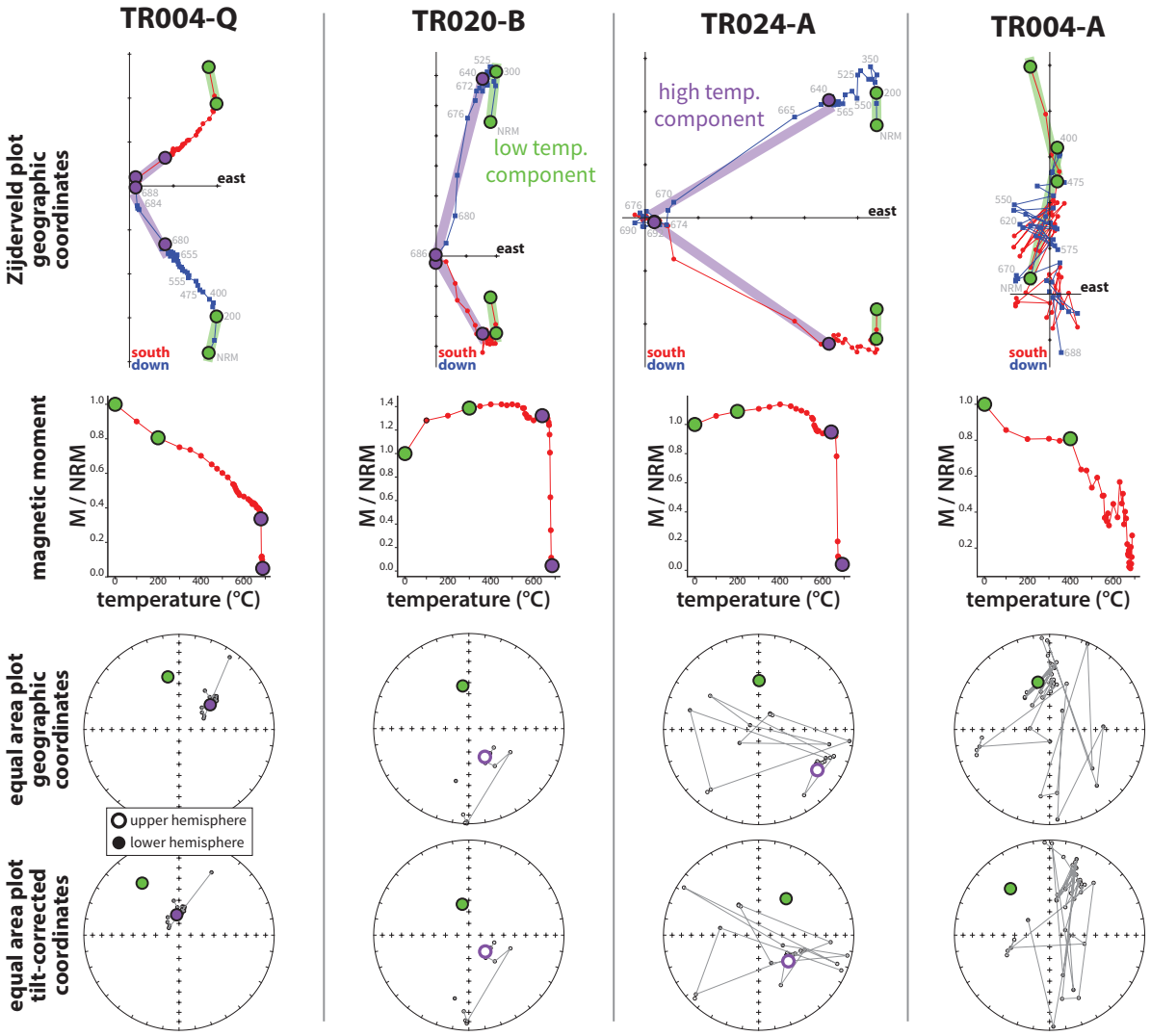

Figure 4.3: Thermal demagnetization results. Specimens TR004-Q, TR020-B, and TR024-A exhibit magnetic behaviour typical of specimens that yield a stable and consistent high temperature component. Specimen TR004-Q exhibits magnetic behaviour typical of specimens that do not yield a stable high temperature component. In the Zijderveld plots, the specimen magnetizations at a given thermal demagnetization step (grey numbers) are shown (NRM = natural remanent magnetization). Fits to the low and high temperature components are shown in green and purple respectively. Note that the Zijderveld plots and the upper equal area plots are in geographic coordinates, whereas the lower equal area plot is in tilt-corrected coordinates.

direction that is consistent with a present local field overprint acquired via viscous remanent magnetization (Fig. 4.3). Samples within 29 of the 44 sites yield either unstable or inconsistent behaviour at temperatures >300°C. However, the remaining 15 sites yield stable and consistent behaviour at high temperatures. This high-temperature component is well-fit by least-squares lines that intersect the origin on a Zijderveld plot between ∼650 and

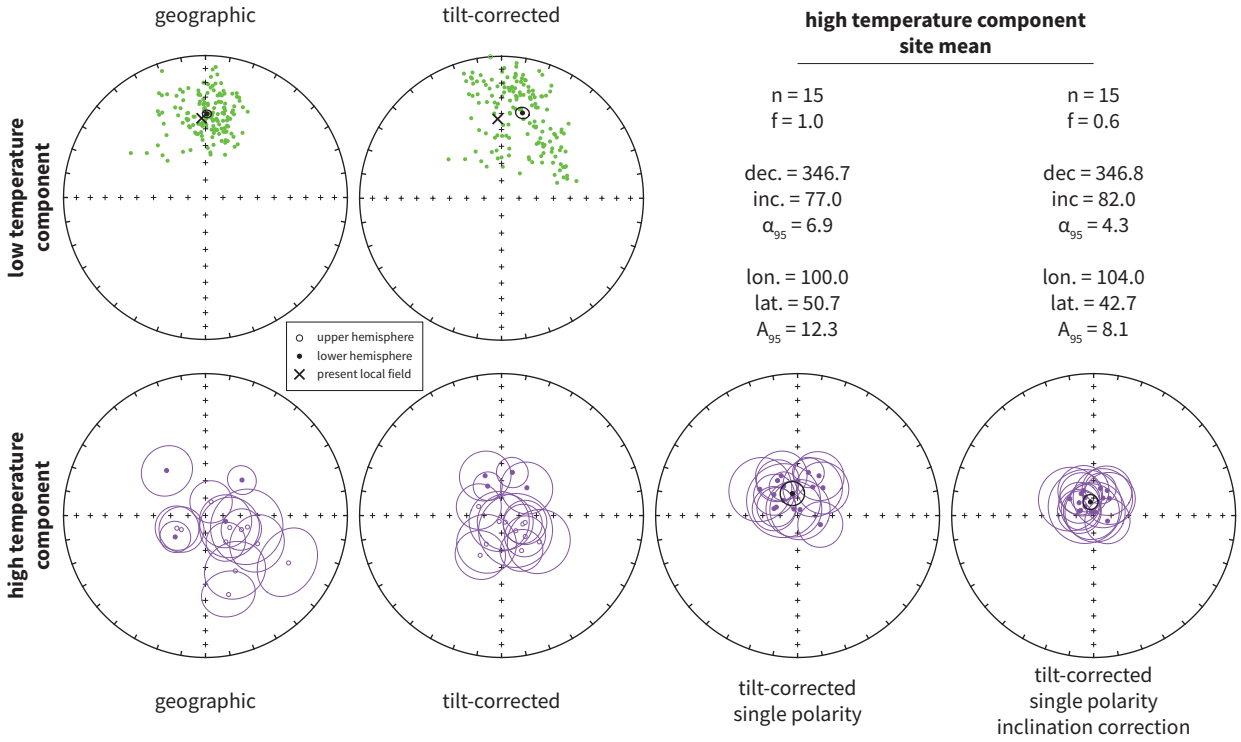

Figure 4.4: Paleomagnetic results for sites that yielded specimens with stable and consistent high temperature components in the Xiajiang Group of the Fanjingshan region (Table 4.1). For the low temperature component, each point represents an individual specimen. For the high temperature component, each point and associated uncertainty ellipse represents the specimen mean for individual sites. The reported site means are the means of these specimen means.

∼690°C (Fig. 4.3). These high unblocking temperatures are close to the Néel temperature of >500 nm hematite, and are therefore consistent with the high-temperature component being dominantly held by primary detrital hematite rather than finer-grained authigenic pigmentary hematite (Dunlop and Özdemir, 2001; Jiang et al., 2015; Swanson-Hysell et al., 2019).

Two polarities are recorded by the high-temperature component. Of the 15 successful sites, 4 sites yield normal polarity (positive inclination) directions, while the other 11 sites yield reversed polarity (negative inclination) directions (Figs. 4.2 and 4.4; Table 4.1). We interpret positive inclinations to correspond to normal geomagnetic polarity, although we recognize that a correlation of positive inclination to reversed geomagnetic polarity could be permissible in alternative paleogeographic reconstructions. When all sites are converted into a single polarity, the null hypothesis that the specimen mean directions of the normal and reversed polarity sites were drawn from distributions that share a common mean direction can not be rejected at the 95% confidence level (in the Watson V test, $V = 4.9$ and $V_{crit} = 7.4$). Since $V < V_{crit}$, the two polarities recorded by the high-temperature component pass a

reversal test after tilt corrections are applied to the high-temperature component site mean directions.

A bootstrap fold test (Tauxe and Watson, 1994) finds that the tightest grouping of site mean directions is obtained between 68 and 103% unfolding at the 95% confidence level (Fig. S1). Since this range of unfolding encompasses 100%, the high temperature component passes a fold test, thereby constraining the high-temperature component to have been acquired prior to Mesozoic folding of the Xiajiang Group (Li et al., 2016b; Ma et al., 2019).

Based on the high unblocking temperatures characteristic of detrital hematite, the positive reversal test, and the positive fold test, we interpret the high temperature component (Fig. 4.4) as being primary and acquired at the time of deposition.

Deposition and burial compaction can result in detrital hematite magnetization being shallower in inclination than the local magnetic field direction at the time of deposition (Tauxe, 2005; Bilardello, 2016). The degree to which the inclination (I) has been shallowed can be expressed by the flattening factor (f) in the equation $\tan(I_{observed}) = f \tan(I_{original})$, where $f = 1$ indicates no inclination shallowing and $f = 0$ indicates a completely flattened direction (King, 1955). Although the flattening factor in any given sedimentary unit depends on a variety of factors such as the composition of the sediment, values of f obtained from empirical studies of detrital hematite-bearing rocks can be reasonably well-explained by a normal distribution about a mean of $\sim$0.6 (Tauxe and Kent, 1984; Bilardello, 2016). We therefore apply this empirically-derived inclination correction ($f = 0.6$) to the specimen means obtained from individual sites (Fig. 4.4), and interpret the resulting direction as approximating the direction of the geomagnetic field at the time of deposition. Directions and poles calculated with and without this inclination correction are shown in Figures 4.4 and 4.6.

Geochronology

U-Pb zircon secondary ion mass spectrometry (SIMS) and laser ablation inductively coupled plasma mass spectrometry (LA-ICP-MS) analyses can be conducted relatively rapidly and are often utilized to determine the age of tuff samples. However, U-Pb determinations using SIMS are significantly less precise than that measured using CA-ID-TIMS and are subject to an U-Pb calibration correction that contributes additional uncertainty. This single data point imprecision makes it difficult to recognize real age variation within a sampled population (due to either analyses of domains with Pb loss and/or older zircon). As a result, isotope ratios measured using SIMS can be affected by Pb loss that cannot be identified at the precision of SIMS, which can bias SIMS-derived weighted mean dates toward younger ages. Conversely, deriving a weighted mean from a non-single age population (with variation not resolvable by the single data point analyses) can bias the interpreted age towards being too old. An additional issue in the interpretation of microbeam U-Pb geochronology is that there are dates in the literature where the youngest dates are deconvolved from a larger age population to derive a weighted mean that approximates the ages of eruption. Calculating a weighted mean from the 'young tail' for a distribution of imprecise dates could result in a date that

Table 4.2: Summary of CA-ID-TIMS $^{206}Pb/^{238}U$ dates from tuffs developed in this study.

sample	**latitude °N**	**longitude °E**	**section**	**stratigraphic height (m)**	**$^{206}Pb/^{238}U$ date (Ma)**	**error (2σ) X**	**Y**	**Z**	**MSWD**	**n**	**N**
Xiajiang Group of the Fanjingshan region (Guizhou province)											
H2-470	27.99396	108.79792	Hongzixi	1586.2	815.73	0.18	0.28	0.92	1.6	6	16
L1-27	27.93856	108.83107	Luoman	1752.3	814.19	0.21	0.31	0.92	1.7	5	9
L4-2	27.94335	108.83931	Luoman	1815.5	813.06	0.35	0.48	1.0	1.8	3	4
H3-60	28.01002	108.80240	Hongzixi	2622.4	809.52	0.50	0.62	1.1	1.9	6	10
QR-74	27.86578	108.82076	Kuaichang	2850.3	811.47	0.67	0.77	1.2	1.9	3	6
H3-8	28.02468	108.81506	Hongzixi	3389.3	804.56	0.39	0.52	1.0	0.6	3	4
Madiyi Formation in the Zhijiang region (Hunan province)											
ZJ-B	27.5	109.6	-	-	804.90	0.36	0.49	0.99	0.9	5	6
Liantuo Formation in the Three Gorges region (Hubei province)											
FDM14-1	30.8527	111.1512	-	-	779.52	0.26	0.38	0.92	2.0	8	16

Notes:
(1) **stratigraphic height** is the estimated composite stratigraphic height derived from correlation of individually measured sections based on aligning the bounding unconformities of the Xiajiang Group and the geochronologic results.
(2) For the **errors**, **X** is the internal (analytical) uncertainty in the absence of external or systematic errors, **Y** is the uncertainty incorporating the U-Pb tracer calibration error, and **Z** is the uncertainty including X and Y, as well as ^{238}U decay constant uncertainty (0.108%; Jaffey et al., 1971). This Z error needs to be utilized when comparing to dates developed using other decay systems (e.g., $^{40}Ar/^{39}Ar$, ^{187}Re-^{187}Os).
(3) **MSWD** is the mean square of weighted deviates
(4) **n** is the number of individual zircon dates included in the calculated weighted sample mean date.
(5) **N** is the total number of individual zircons analyzed.
(6) Data for individual zircons are provided in the Supporting Information.

is too young either due to Pb loss in these grains or simply through arbitrary grouping of the youngest dates in a low precision normal distribution of dates. Such a bias could explain calculated SIMS dates from pre-Sturtian strata that are younger than ca. 717 Ma in South China (e.g. Lan et al., 2015) and in practice requires other independent information to defend the interpretation. In addition to the issues surrounding age interpretations, microbeam U-Pb dates require consideration of the U/Pb calibration uncertainty that is typically 1–2% and is a limiting uncertainty.

The chemical abrasion step of the CA-ID-TIMS method has been developed to effectively remove (i.e. leach) the analyses of radiation-damaged zones of zircon grains, which are most likely to suffer Pb loss, prior to analysis (Mattinson, 2005). This technique is not perfect – depending on the nature of the material being analysed (U content, zonation patterns), for some samples a proportion of analyses suffering Pb-loss may still persist. The higher-precision of the CA-ID-TIMS single data points often reveals age complexity with excess variance ascribed to geological age variation and residual Pb-loss.

Evaluating a hypothesis such as the Bitter Springs Stage TPW hypothesis requires precise age constraints on poles. The SIMS dates prevalent in the literature could have true age

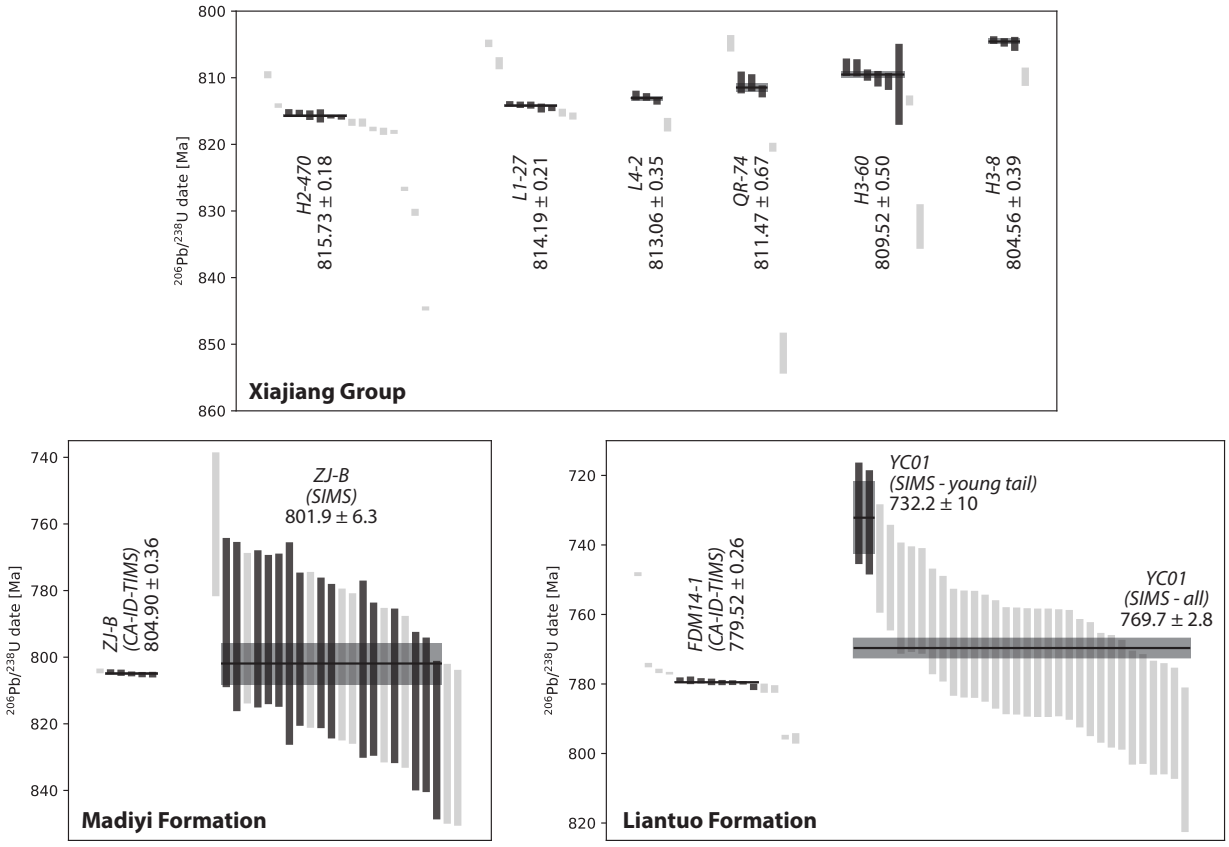

Figure 4.5: 2σ uncertainty of CA-ID-TIMS U-Pb dates for zircons analyzed in this study. The previously reported SIMS dates for sample ZJ-B of the Madiyi Formation (Xian et al., 2020) and sample YC01 of the Liantuo Formation (Lan et al., 2015) are also shown. For sample YC01, we show the weighted mean dates that result from isolating the two youngest zircons (as is preferred in Lan et al., 2015) and from including all of the zircons. Solid vertical bars indicate zircons that are included in the calculation of the weighted mean date. Faded vertical bars indicate zircons interpreted to have been inherited or affected by Pb or U loss, and are excluded in the calculation of the weighted mean date. Measurement data are and concordia diagrams are shown in the Supporting Information.

uncertainty well beyond the weighted mean uncertainty, particularly if the assumptions made are incorrect (i.e. a single age population, no Pb-loss) in addition to the calibration uncertainty. As a result, it is essential to develop CA-ID-TIMS dates in order to have high-precision age constraints on paleomagnetic poles.

We developed U-Pb CA-ID-TIMS ages from zircon for six tuff samples collected from the Xiajiang Group in the Fanjingshan region (Figs. 4.2 and 4.5; Table 4.2). For each of these ash layers we make a subjective age interpretation based upon the U-Pb zircon data combined with information about the general nature of the materials. Five tuffs from the lower and middle Xiajiang Group yield dates ca. 816–810 Ma, and one tuff from near the top

of the Xiajiang Group in the Hongzixi section yields a younger date of ca. 805 Ma. Within ∼100 m of this youngest tuff, a major unconformity separates ca. 805 Ma sediments of the Xiajiang Group with <717 Ma Sturtian Snowball Earth glacial deposits (Bowring et al., 2007; Macdonald et al., 2010; MacLennan et al., 2018; Lan et al., 2020).

Prior to this study, age constraints on Tonian paleomagnetic poles from the Madiyi and Liantuo formations were based on U-Pb SIMS analyses. In order to improve the precision of these age constraints, as well as evaluate whether they might be biased toward younger ages, we developed new age constraints for these poles using U-Pb CA-ID-TIMS. These new CA-ID-TIMS age constraints supersede the previous SIMS age constraints.

The tuff associated with the paleomagnetic pole for the Madiyi Formation in the Hunan province (sample ZJ-B of Xian et al., 2020) is within the 12 m thick succession of the Madiyi Formation from which the paleomagnetic data were developed. A U-Pb zircon SIMS date of 801.9±6.3 Ma was reported for the tuff in Xian et al. (2020). The new CA-ID-TIMS data from five zircons result in a weighted mean $^{206}Pb/^{238}U$ date of 804.90±0.36 Ma (Fig. 4.5); Table 4.2). This date overlaps with the SIMS date of Xian et al. (2020) within uncertainty and constrains the timing of the Madiyi Formation pole to higher precision.

The tuff associated with the paleomagnetic pole for the Liantuo Formation (Evans et al., 2000; Jing et al., 2015) lies ∼15 m below the base of the stratigraphic interval which was sampled for paleomagnetic analysis in Evans et al. (2000), and is in the vicinity of a tuff that was previously dated at 748±12 Ma using SIMS (Fig. S5; Ma et al., 1984). The new CA-ID-TIMS data from eight zircons result in a weighted mean $^{206}Pb/^{238}U$ date of 779.52±0.26 Ma – ∼20 m.y. older than the maximum reported uncertainty of the SIMS-derived date (Fig. 4.5; Table 4.2).

4.7 Discussion

Tectonic Setting

The South China craton consists of two distinct tectonic blocks, the Yangtze and Cathaysia blocks, separated by the Jiangnan Orogen (Fig. 4.1). However, the depositional setting of sedimentary units in the Jiangnan Orogen as well as the tectonic context of the intrusive units and deformation found throughout the orogen continues to be debated in the literature. A widely-adopted model proposed that the Fanjingshan Group (and equivalent strata) was deposited in a Grenvillian (ca. 1.3–0.9 Ga) arc-related basin on the Yangtze block as the oceanic crust formerly separating the Yangtze and Cathaysia blocks subducted under the Yangtze block (e.g. Li et al., 2002, 2009). In this model, deformation of the Fanjingshan Group was interpreted to reflect collision of the Yangtze and Cathaysia blocks as the supercontinent Rodinia came together around South China ca. 1.0–0.9 Ga, with Laurentia on the Cathaysia-side of South China and Australia on the Yangtze-side (i.e. the Missing Link model, as shown in Figure 4.8). The model then proposes that later Tonian (ca. 850–750 Ma) magmatism in the Jiangnan Orogen is associated with a mantle superplume that initiated

the break up of Rodinia (e.g. Li et al., 2003, 2009). In this scenario, the Xiajiang Group (and equivalent strata) is interpreted to have been deposited within a failed intra-continental rift basin between the Yangtze and Cathaysia blocks as Australia, South China, and Laurentia rifted apart.

Geochronologic and geochemical data initially appeared to support this Missing Link model (e.g. Li et al., 2002, 2003, 2009), and consequently many Neoproterozoic paleogeographic models adopted it (e.g. Li et al., 2008). However, subsequent geochronologic, geochemical, and paleomagnetic data introduce new constraints that are difficult to reconcile with this model.

The timing of Yangtze and Cathaysia block collision represented by the Jiangnan Orogen can no longer be considered to be coeval with the ca. 1080 to 980 Ma Grenvillian Orogen. U-Pb LA-ICP-MS geochronologic constraints from the tuffs, sedimentary rocks, and sills of the Fanjingshan Group (Zhao et al., 2011; Wang et al., 2012; Gao et al., 2014) indicate that deformation of the group occurred after ca. 830 Ma. Our new U-Pb CA-ID-TIMS results constrain initiation of Xiajiang Group deposition, and therefore termination of Fanjingshan Group deformation, to have occurred by 815.73±0.18 Ma (Fig. 4.2). The interpretation that the Jiangnan Orogeny, and the associated deformation of the Fanjingshan Group, was the result of collision between the Yangtze and Cathaysia blocks gains support from the geochemistry and geochronology of the igneous rocks of the Jiangnan Orogen that are indicative of a supra-subduction, volcanic arc setting (Cawood et al., 2013, 2017).

The Fanjingshan Group is dominated by siliciclastic sediments and also contains horizons of volcanic rocks including pillow basalts (Zhou et al., 2009). These units were intruded by ca. 830 Ma mafic sills with geochemical signatures consistent with subduction-related magmatism (Wang et al., 2014) as well as 835±5 Ma (U-Pb SIMS) felsic intrusive rocks (Fig. 4.1B; Gao et al., 2011). Both fore-arc (Zhao et al., 2011) and retro/back-arc (Lin et al., 2016; Yao et al., 2019) settings have been interpreted for the Fanjingshan Group deposition. However, fore-arc settings are typically cold and amagmatic, and consequently we prefer a syn-collisional retro-arc foreland model with ultramafic magmatism associated with slab-breakoff. In either model, the Fanjingshan Group is deposited and intruded in an arc-related basin as the oceanic crust formerly separating the Yangtze and Cathaysia blocks subducted under the Yangtze block (Lin et al., 2016). As Yangtze and Cathaysia (or at least a portion of Cathaysia) collided between ca. 830 Ma and 815.73±0.18 Ma, sedimentary rocks of the Fanjingshan Group were folded, uplifted, and eroded. Following this deformation and the development of an erosional unconformity, subsidence enabled deposition of the overlying Xiajiang Group. Taken together, these data constrain the collision of the Yangtze and Cathaysia blocks to have occurred between ca. 830 Ma and 815.73±0.18 Ma, not ca. 1000 to 900 Ma as is proposed in the Missing Link model implemented in Li et al. (2008).

In addition to this evidence of Tonian convergence between the Yangtze and Cathaysia blocks, the record of the northwest Yangtze block indicates a convergent tectonic setting in the Tonian that extended into the Cryogenian. Geochronologic and geochemical constraints from the Panxi-Hannan Belt (Fig. 4.1) indicate that arc-related magmatism was occurring in that belt ca. 870–706 Ma (Dong et al., 2012), and therefore that the northwestern margin

of the Yangtze block was an active margin throughout the time that Rodinia is hypothesized to have been a coherent supercontinent. This arc-related magmatic activity associated with subduction along the northwestern margin of the Yangtze block is the likely source for the ashes that formed the tuffs within the Xiajiang Group that we have targeted for geochronology (Fig. 4.2).

Finally, paleomagnetic constraints indicate that South China was at high latitudes throughout the late Tonian (discussed further in *Tonian APWP of South China*) rather than at low-latitudes as would be required by the Missing Link model (discussed further in *South China and Rodinia*; Fig. 4.8). Additionally, the paleomagnetic data suggests that the Panxi-Hannan Belt lay from the east to the north relative to the Fanjingshan region in reconstructed coordinates during the time of Xiajiang Group deposition (ca. 815–800 Ma; Fig. 4.6). At these high latitudes, the prevailing winds are polar easterlies, which is consistent with the idea that the ashes that formed the tuffs within the Xiajiang Group were transported from the Panxi-Hannan Belt (Hildebrand, 1988).

Together, these constraints are inconsistent with South China being within the interior of a stable supercontinent during the Tonian. Instead, they indicate a convergent setting with the northwestern margin of the Yangtze block being an active margin into the Cryogenian rather than being juxtaposed against a conjugate continent. Therefore, the data are more compatible with South China on the periphery of Rodinia or disconnected from it entirely (Fig. 4.8).

The tectonic setting of the basin in which the Xiajiang Group (and equivalent strata) was deposited is commonly interpreted as a failed intra-continental rift basin (Zhang et al., 2019), potentially associated with the hypothesized mantle superplume that initiated the break up of Rodinia (Li et al., 2003, 2009). However, this basin development framework is rooted in a tectonic setting interpretation that would have South China within the interior of a supercontinent undergoing break-up — a setting that is inconsistent with available constraints. Rather, any basin development model needs to honor the following:

- There was a geologically short interval (ca. 15 m.y.) between the orogenesis that deformed the Fanjingshan Group and the subsidence that enabled deposition of the Xiajiang Group.
- There was an active margin along the northwestern margin of the Yangtze block at the time of Xiajiang Group subsidence. This margin is the likely source of the tuffs throughout the Xiajiang Group stratigraphy.
- The site of Xiajiang Group deposition must have been folded, uplifted, and eroded prior to subsidence.
- Subsidence rates were initially quite high as evidenced by the rapid sediment accumulation rates in the Xiajiang Group. These high subsidence rates led to the deep-water setting of the Xiajiang Group sediments.

- While some strata could be missing through glacial erosion, the duration of missing time (∼90 m.y.) in the ca. 805 and 717 Ma pre-Sturtian unconformity suggests limited sediment accumulation in the pre-Sturtian interval relative to the thick ca. 815 to 805 Ma succession.

The Nanhua Basin into which the Xiajiang Group was deposited formed inland from the Panxi-Hannan Belt (Cawood et al., 2017). Based on the interpretation that the Panxi-Hannan Belt was an active arc at the time of Xiajiang Group deposition, Qi et al. (2019) argued that Nanhua Basin formation was the result of back-arc extension. Importantly, the timing of deposition of the Xiajiang Group coincides with the initiation of back-arc extension in the Panxi-Hannan arc (Dong et al., 2012). Back-arc extension provides a mechanism to explain regional extension and subsidence in the region of the Jiangnan suture. Furthermore, given that back-arc basin formation is the result of the combined driving mechanisms of surface kinematics and dynamic mantle flow (Sdrolias and Müller, 2006), it can lead to both rapid and transient subsidence. Geologic observations in more recent back-arcs have been interpreted to indicate significant back-arc extension in regions where lithosphere has been thickened through orogenesis (Göğüş, 2015). Numerical modeling has shown that post-orogenic lithosphere removal (such as that occurring as a result of delamination) in continental back-arc settings can lead to large-scale subsidence (Göğüş, 2015). This mechanism could explain the transition at the site of Xiajiang Group deposition from folding, uplift, and erosion in the Jiangnan Orogen as Yangtze collided with Cathaysia between ca. 830 Ma and 815.73±0.18 Ma, to Nanhua Basin subsidence as a back-arc basin formed. The Nanhua Basin is therefore best interpreted as a polyphase basin wherein this Tonian subsidence was followed by Cryogenian and Ediacaran subsidence potentially as the result of other mechanisms. The tuffs found throughout the Xiajiang Group stratigraphy are the result of the arc on the northwestern margin of the Yangtze block that was active throughout deposition, both driving subsidence through back-arc extension and contributing ashes via the prevailing polar easterly winds that enable us to develop geochronologic constraints.

Tonian APWP of South China

With the exception of the highest ash sample in the Hongzixi section, all dated ash samples from the Xiajiang Group of the Fanjingshan region yield an age of ca. 816–810 Ma (Fig. 4.2). Furthermore, the high temperature components in all sites record similar directions (Fig. 4.4). We therefore take the parsimonious interpretation that variability in the high temperature component between specimens/sites is largely recording short time-scale secular variation in the magnetic field, and therefore develop a single paleomagnetic pole from the mean direction of the high temperature component from all sites (Fig. 4.4). Based on the geochronologic constraints (Fig. 4.2), we assign a nominal age to this pole of 813±3 Ma. However, we discuss the possibility of multiple poles being recorded in the Xiajiang Group below.

Table 4.3: Neoproterozoic paleomagnetic poles for South China.

pole	nominal age (Ma)	age method	site lat.	site lon.	pole lat.	pole lon.	A_{95}	f	pole ref.	age ref.	note
Yanbian dikes	824±6	SIMS	26.9	101.5	45.1	130.4	19.0	1.0	Niu et al. (2016)	Niu et al. (2016)	(2)
Xiaofeng dikes	821.64±0.2	CA-ID-TIMS	31.0	111.2	26.1	82.1	14.6	1.0	Jing et al. (2019)	Wang et al. (2016b)	(3)
Xiajiang Group	816–810	CA-ID-TIMS	27.9	108.8	42.7	104.0	8.1	0.6	this study	this study	-
Madiyi Formation	804.90±0.99	CA-ID-TIMS	27.5	109.6	34.7	82.0	6.7	0.6	Xian et al. (2020)	this study	(4)
Chengjiang Formation	799.5±8.4	SIMS	25.1	102.4	29.7	75.3	7.9	0.6	Jing et al. (2019)	Jing et al. (2019)	(5)
Liantuo Formation	≤779.52±0.92	CA-ID-TIMS	30.8	111.1	19.6	144.4	4.2	0.6	Jing et al. (2015)	this study	(5)

Notes:
(1) **f** is the flattening factor, where f=1 indicates no inclination shallowing and f=0 indicates a completely flattened direction.
(2) Located within mobile belt.
(3) Pole recalculated after Li et al. (2004).
(4) Pole converted from specimen to site mean in this study.
(5) Pole converted from specimen to site mean and inclination correction applied in this study.

This new pole can be combined with existing Neoproterozoic paleomagnetic poles for South China (summarized in Table 4.3) to develop an apparent polar wander path (APWP). There are complications associated with the interpretation of these poles and their assigned ages and we will discuss each in turn.

The Yanbian dikes pole (Niu et al., 2016) was obtained from a deformed region on the western-most margin of the South China craton that experienced vertical axis rotation during the Cenozoic collision of India with Asia. The magnitude of this vertical axis rotation was estimated to be 5.3±3.0° based on paleomagnetic data from Pliocene sedimentary rocks in the region (Zhu et al., 2008), and Niu et al. (2016) applied a 5° vertical axis rotation correction to their Yanbian dikes pole. However, the vertical axis rotation correction may be as little as 2.3° or as high as 8.3° at the 95% confidence level (Zhu et al., 2008). The Yanbian dikes may also have experienced pre-Pliocene vertical axis rotation. Furthermore, no tilt-correction was applied to the majority of the directions obtained from the Yanbian dikes, despite observations that the dikes exhibit dips that range from 43° to vertical (Niu et al., 2016). Finally, the Yanbian dikes pole is inconsistent with the Xiaofeng dikes pole (Fig. 4.6A) despite the similar age of these two poles. Given these complications, we exclude the Yanbian dikes pole as a constraint in our preferred Tonian South China APWP (Fig. 4.6C).

The Xiaofeng dikes pole has had both its direction and age revised since its initial publication in Li et al. (2004). Jing et al. (2019) recognized that a subset of the dikes that were used to obtain the Xiaofeng dikes pole are located between two faults and have paleomagnetic directions that may have been rotated relative to the rest of the dikes. Therefore, to account for the possibility of vertical axis rotation affecting this subset of dikes, Jing et al. (2019) recalculated the Xiaofeng dikes pole by excluding them. The resulting pole is closer to the other ca. 820-800 Ma poles for South China (Fig. 4.6), although further work is needed to substantiate whether this difference in pole position is robust. In addition, the Xiaofeng dikes were originally dated to 802±10 Ma based on U-Pb SIMS analyses on zircon from the

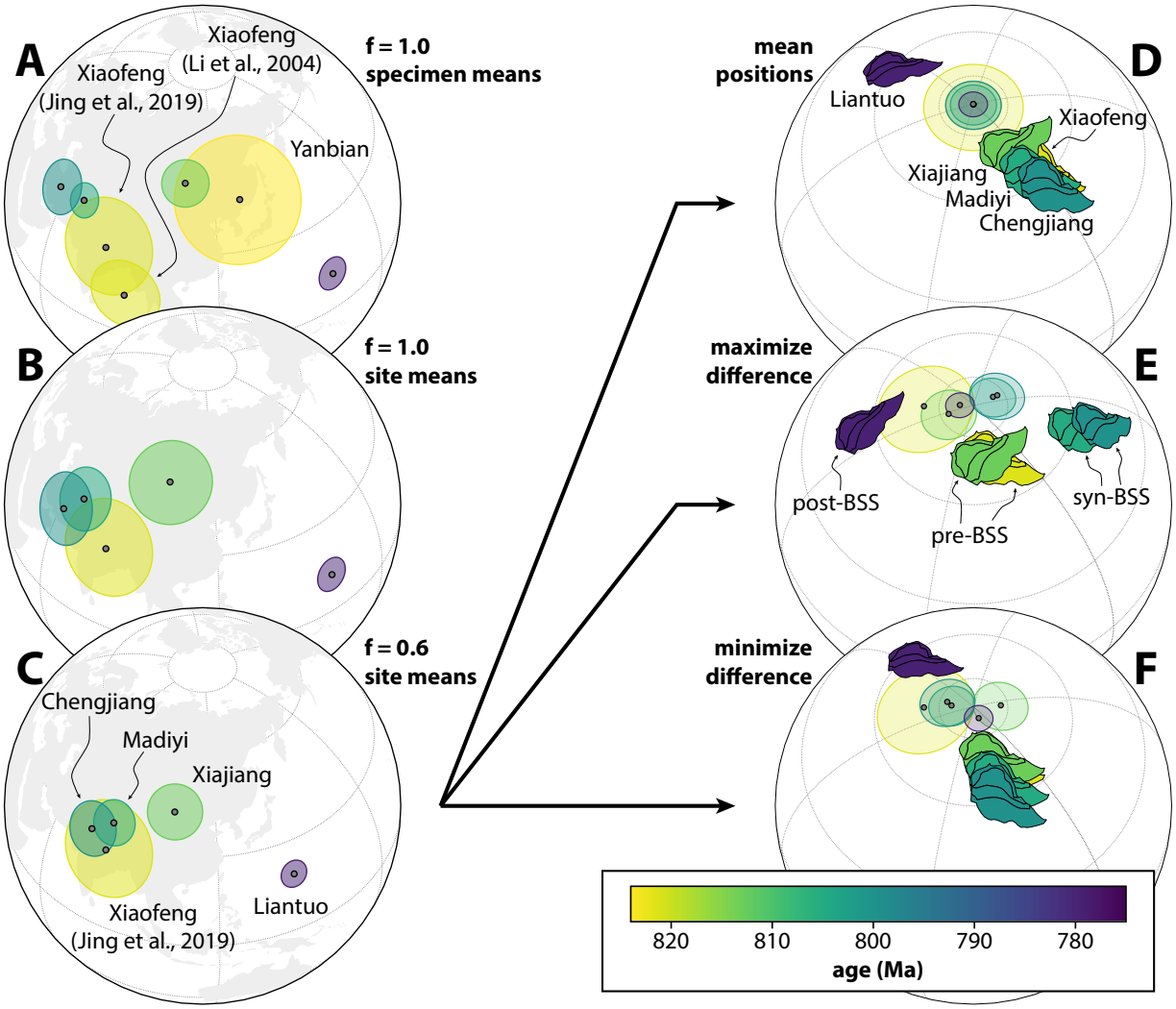

Figure 4.6: Tonian apparent polar wander paths (APWPs) and paleogeographic models for South China. **A)** APWP using all available paleomagnetic poles. Both the original (Li et al., 2004) and recalculated (Jing et al., 2019) Xiaofeng dikes poles are shown. Poles derived from sedimentary rocks are shown as specimen means without an inclination correction (Table 4.3). **B)** APWP excluding the Yanbian dikes and original Xiaofeng dikes poles. Poles derived from sedimentary rocks are shown as site means without an inclination correction. **C)** Our preferred APWP excluding the Yanbian dikes and original Xiaofeng dikes poles, and using site mean poles from sedimentary rocks with an inclination correction ($f = 0.6$). **D)** Paleogeographic model based on the preferred APWP in C. South China is reconstructed using the means of the poles. **E)** Paleogeographic model based on the preferred APWP with South China reconstructed to maximize the difference in position between the pre-, syn-, and post-Bitter Springs Stage (BSS) poles as permitted by the A_{95} uncertainties. **F)** Paleogeographic model based on the preferred APWP with South China reconstructed to minimize the difference in position permitted by the A_{95} uncertainties of all poles.

dikes (Li et al., 2004). When zircon from these dikes were reanalyzed at higher precision using CA-ID-TIMS, their age was revealed to be significantly older (821.64±0.2 Ma; Wang et al., 2016b). This revised age constraint for the Xiaofeng dikes pole is utilized here (Table 4.3; Fig. 4.6).

The previous age constraint on the Madiyi Formation pole of 801.9±6.3 Ma was also developed using U-Pb SIMS measurements on zircon from a tuff within the section where the paleomagnetic data were developed (Xian et al., 2020). Our new CA-ID-TIMS date of 804.90±0.36 Ma is within the uncertainty of this SIMS date and provides a higher precision age constraint on the age of the pole (Fig. 4.5) which supersedes the previous age and is utilized here (Table 4.3; Fig. 4.6).

The paleomagnetic pole for the upper Liantuo Formation has long been an important constraint for the Neoproterozoic paleogeography of South China (Evans et al., 2000). The Liantuo Formation unconformably overlies the Huangling granite suite for which U-Pb SIMS dates of 863±9, 844±10, and 842±10 Ma have been developed (Wei et al., 2012). These granites are intruded by the 821.64±0.2 Ma Xiaofeng dikes (Wang et al., 2016b). The Liantuo Formation is unconformably overlain by Cryogenian glacial deposits. The age assigned to the Liantuo Formation pole has varied in the literature. When a paleomagnetic pole from the formation was first reported in Evans et al. (2000), it was assigned an age of 748±12 Ma based on an U-Pb SIMS date on a tuff ∼15 m below the base of the stratigraphic interval that was sampled for paleomagnetic analysis (Ma et al., 1984; Fig. S5). When this paleomagnetic pole was updated in Jing et al. (2015) with the addition of paleomagnetic data from additional sites to the southwest of the stratigraphic section sampled in Evans et al. (2000), its age was interpreted to be ca. 720 Ma based on U-Pb SIMS dates on tuffs within the upper 20 m of the Liantuo Formation across the Three Gorges Area (Lan et al., 2015). A challenge with these U-Pb SIMS dates is that there is a distribution of dated grains around a peak of ca. 780 to 770 Ma that includes sparse younger dates (Fig. 4.5; Lan et al., 2015). In Lan et al. (2015), these younger dates are interpreted as the eruptive age of the tuffs, but it is possible that these grains are biased young. Ambiguity associated with correlation of the Liantuo Formation with possibly equivalent stratigraphy adds further complexity to the interpretation of geochronologic constraints on the Liantuo Formation. For example, zircons from a tuffaceous siltstone ∼25 m below Sturtian glacial deposits in the Gongdong Formation of northern Guangxi, which is often interpreted to be a deeper water equivalent to the Liantuo Formation (Wang and Li, 2003; Pi and Jiang, 2016), yield a weighted mean CA-ID-IRMS date of 720.16±1.40 Ma (Lan et al., 2020). If this interpretation that the Gongdong Formation correlates to the Liantuo Formation is correct, it suggests that, at least in some parts of the Nanhua Basin, sediments as young as ca. 720 Ma are preserved. On the other hand, if the two formations are not correlative, then the CA-ID-IRMS date of 720.16±1.40 Ma (Lan et al., 2020) does not place any geochronologic constraints on the Liantuo Formation.

We have developed a new CA-ID-TIMS date of 779.52±0.26 Ma for a tuff in the Liantuo Formation at the same location studied by Ma et al. (1984) close to the section sampled for paleomagnetic analyses by Evans et al. (2000). Similar to the updated Xiaofeng dikes

geochronology, this date is appreciably older than interpretations based on the previous SIMS U-Pb dates. It is possible that some or all of the zircons included in the calculation of the weighted mean date may be detrital and not representative of the eruptive age of the tuff. However, the consistency of the zircon dates (Fig. 4.5) suggests that the weighted mean date likely represents an eruptive age. Furthermore, while the ∼15 m of stratigraphy between the tuff and the paleomagnetic data of Evans et al. (2000) could represent significant time, the similar lithologies throughout the interval (fine to medium sandstone interbedded with siltstone; Fig. S5) suggests conformable deposition. Therefore, the age of the tuff is likely to be similar in age to the sedimentary rocks from which the paleomagnetic data were derived and unlikely to be tens of millions of years older. However, without further high-precision geochronologic constraints from the Liantuo Formation at or above the stratigraphy from which the paleomagnetic pole was derived, the possibility remains that the Liantuo Formation paleomagnetic pole post-dates 779.52±0.26 Ma. We prefer the interpretation that the age of the Liantuo Formation and its pole is close to 780 Ma and that the Liantuo Formation is not correlative to the ca. 720 Ma Gongdong Formation, which is preserved conformably below Cryogenian glacial deposits in a deeper-water setting (Lan et al., 2020).

The existing date of 799.5±8.4 Ma for the Chengjiang Formation pole was also developed using SIMS (Table 4.3). As evidenced for the Xiaofeng dikes and the Liantuo Formation, when SIMS-derived ages are re-investigated through CA-ID-TIMS, the result can be a significantly different date. Therefore, the accuracy of the SIMS-derived dates for the Chengjiang Formation pole remains uncertain.

The Xiajiang Group paleomagnetic pole developed in this study is calculated as a site mean (i.e. the mean of the means of specimen directions for each site; Fig. 4.4). However, the Chengjiang and Madiyi poles are reported in Jing et al. (2019) and Xian et al. (2020) as specimen means (i.e. the mean of specimen directions across all sites). While both methods can be justified for sedimentary rocks, the specimen mean direction leads to paleomagnetic poles with smaller A_{95} uncertainty ellipses due to the larger number of directions used to obtain the mean which has the potential to underestimate the uncertainty. We recalculate the paleomagnetic poles for the Chengjiang and Madiyi formations as site means, to be consistent with the methodology used to develop our Xiajiang Group pole (Figs. 4.6B and 4.6C).

An inclination correction has been applied to the paleomagnetic pole obtained from the Xiajiang Group in this study. Similarly, an inclination correction was applied to the pole obtained from the Madiyi Formation (Xian et al., 2020). Given that the poles from the Chengjiang and Liantuo formations are also derived from the hematite-held magnetization of similar siliciclastic sedimentary rocks, we apply the same inclination correction ($f = 0.6$) to these poles as that applied to the Xiajiang Group and Madiyi Formation poles (Fig. 4.6C). Given potential variability in inclination shallowing, the flattening could vary from this value which is an additional source of uncertainty.

The Xiaofeng dikes and the inclination-corrected Madiyi and Chengjiang poles all overlap within uncertainty, and the Xiajiang Group records a distinct, but similar, position as well (Fig. 4.6). Together, these poles constrain South China to have been in a roughly stable

position at high latitudes ($\gtrsim$60°) ca. 820–800 Ma (Figs. 4.6 and 4.7). The Liantuo Formation pole also constrains South China to be at high latitudes, although with a different orientation to the ca. 820–800 Ma position (Figs. 4.6 and 4.7). The poles constrain South China to be at high latitudes in the latter half of the Tonian, likely drifting across the pole after ca. 805 Ma (Fig. 4.6).

South China and Rodinia

Table 4.4: 900-700 Ma paleomagnetic poles for cratons proximal to South China.

pole	nominal age (Ma)	site lat.	site lon.	pole lat.	pole lon.	A_{95}	ref.	grade
Laurentia								
Gunbarrel dikes	778^{+2}_{-2}	44.8	248.7	9.1	138.2	12.0	Eyster et al. (2019)	B
Uinta Mountain Group	760^{+6}_{-10}	40.8	250.7	0.8	161.3	4.7	Weil et al. (2006)	B
Carbon Canyon	757^{+7}_{-7}	36.1	248.2	-0.5	166	9.7	Eyster et al. (2019)	NR
Carbon Butte/Awatubi	751^{+8}_{-8}	35.2	248.5	14.2	163.8	3.5	Eyster et al. (2019)	NR
Franklin event grand mean	724^{+3}_{-3}	73.0	275.4	6.7	162.1	3.0	Denyszyn et al. (2009)	A
Svalbard								
Lower Grusdievbreen Formation	815^{+5}_{-5}	79.0	18.0	19.6	204.9	10.9	Maloof et al. (2006)	B
Upper Grusdievbreen Formation	802^{+8}_{-7}	78.9	18.2	-1.1	252.6	6.2	Maloof et al. (2006)	B
Svanbergfjellet Formation	785^{+5}_{-5}	78.5	18.0	25.9	226.8	5.8	Maloof et al. (2006)	B
Siberia								
Kitoi Cryogenian dikes	758^{+4}_{-4}	52.3	102.8	1.1	21.8	5.6	Pisarevsky et al. (2013)	A
Australia								
Browne Formation	855^{+45}_{-45}	-25.0	123.8	44.5	141.7	6.8	Pisarevsky et al. (2007)	B
Johnny's Creek siltstones	760^{+30}_{-30}	-24.0	133.5	15.8	83.0	13.5	Swanson-Hysell et al. (2012)	B
Mundine Well dikes combined	755^{+3}_{-3}	-25.5	115.0	45.3	135.4	4.1	Wingate and Giddings (2000)	A
India								
Malani Igneous Suite combined	752^{+18}_{-18}	25.3	72.6	69.4	78.6	6.0	Meert et al. (2013)	A

Notes:
(1) **grade** is the quality of the pole as assessed by the Nordic Paleomagnetism Workshops (Evans et al., 2021). 'A' refers to poles that are considered to provide essential constraints given their high quality. 'B' refers to poles that are likely high quality, but retain some ambiguity about their age or direction. 'NR' refers to poles that were not rated at the Nordic Paleomagnetism Workshops.

Connections between Siberia (Ernst et al., 2016; Evans et al., 2016), Australia-East Antarctica (Veevers and Eittreim, 1988; Duebendorfer, 2002; Goodge et al., 2008; Goodge and Fanning, 2010; Li and Evans, 2011; Swanson-Hysell et al., 2012; Eyster et al., 2019), and the western margin of Laurentia are reasonably well-established for the late Tonian (Fig. 4.8). Paleomagnetic poles from India ca. 1070 and 750 Ma permit a connection with northwest Australia through the Tonian (Swanson-Hysell et al., 2012), although it has also been suggested that India was disconnected from Rodinia during this time (Merdith et al., 2017). Within this paleogeographic context of northern Rodinia, three models of South China's relationship with Rodinia have been proposed, which we refer to as the "Missing Link," "Periphery," and "Separate" models (Fig. 4.8). The Missing Link model proposes

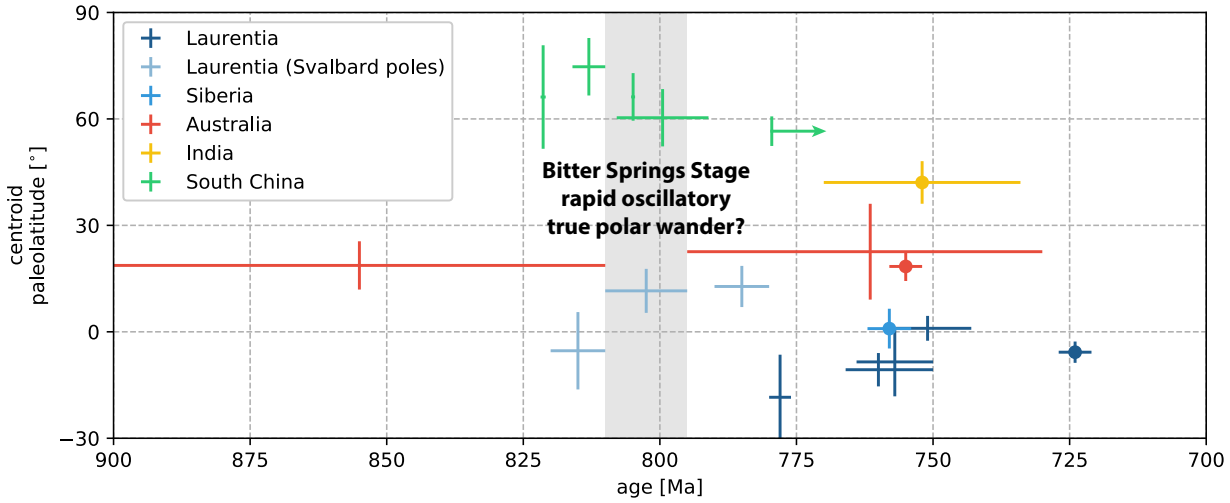

Figure 4.7: Paleolatitudes of points in the center of South China and other cratons implied by available paleomagnetic poles shown with age and paleolatitude uncertainty (Tables 4.3 and 4.4). The light blue 'Laurentia (Svalbard poles)' are for the centroid of Laurentia reconstructed using Svalbard poles with Svalbard rotated back to Laurentia. Points with a circle in the center indicate paleomagnetic poles that were given an 'A' rating by the Nordic Paleomagnetism Workshops. The grey bar indicates the timing of the ca. 810-795 Ma Bitter Springs Stage which is hypothesized to have been bracketed by rapid true polar wander rotations.

that the supercontinent Rodinia came together around South China ca. 1.0–0.9 Ga, with Laurentia on the Cathaysia-side of South China and Australia on the Yangtze-side (Fig. 4.8). The model was initially proposed to reconcile mismatches in the Mesoproterozoic geology of Australia-East Antarctica and Laurentia (Li et al., 1995). However, paleomagnetic data from South China constrain it to be at high latitudes from ca. 821 Ma to at least 780 Ma (*Tonian APWP of South China*, Fig. 4.6), whereas paleomagnetic data from Australia, Laurentia, and Siberia all constrain Rodinia to be on or near the equator ca. 775 Ma (Figs. 4.7 and 4.8). Furthermore, as previously discussed, the tectonic context of South China, with collision between the Yangtze and Cathaysia blocks between ca. 830 Ma and 815.73±0.18 Ma and subduction along northwestern Yangtze ca. 870-706 Ma (*Tectonic Setting*), cannot be reconciled with a position of South China within the interior of a stable supercontinent anytime in the Tonian Period.

On the other hand, the Periphery model (Fig. 4.8) is consistent with both the paleomagnetic constraints as well as our current understanding of the tectonic context of South China. In our Periphery model configuration, South China is at high latitudes, connected to Rodinia via northwestern India. Yangtze is free to have travelled across an open ocean to collide with Cathaysia between ca. 830 Ma and 815.73±0.18 Ma. Northwestern Yangtze faces this open ocean, allowing for subduction along that margin in the Tonian and into the Cryogenian. Tonian volcanism in northwest India shares geochemical characteristics

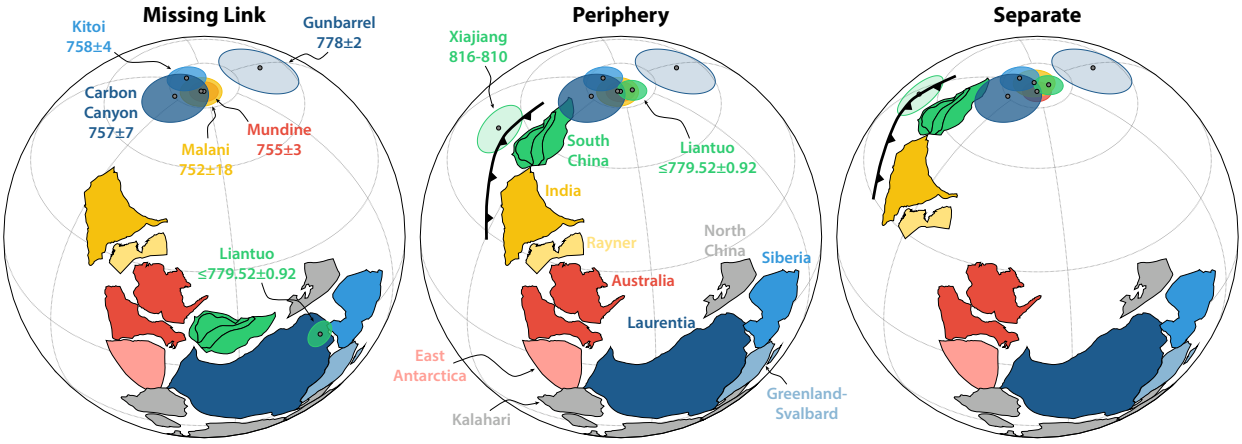

Figure 4.8: Paleogeographic reconstructions for Rodinia at 755 Ma. The Missing Link model places South China at low latitudes between Australia and Laurentia, which is inconsistent with both the paleomagnetic data as well as the tectonic context of South China. The Periphery model instead places South China at high latitudes connected to India, which satisfies the ca. 755 Ma and 780 Ma paleomagnetic data and allows for an active margin along the Panxi-Hannan Belt at this time. In order to satisfy ca. 821-805 Ma paleomagnetic data from South China, anticlockwise rotation of the entire Rodinia supercontinent from ca. 821-805 Ma to ca. 780 Ma is required in this Periphery model. The Separate model disconnects South China-India-Rayner from Rodinia. The Euler rotation parameters for South China relative to India in the Periphery and Separate models are (6.72° N, 77.69° E, 67.96°). Blocks that are not directly relevant to the relationship between South China and Rodinia are shown in grey.

with arc magmatism in the Panxi-Hannan Belt (Ashwal et al., 2013; Cawood et al., 2017), which has been interpreted as the result of a continuous subduction zone along northwestern Yangtze and western India and consistent with a connection between western South China and northwestern India. Detrital zircon spectra of Cryogenian sediments in South China also appear similar to that observed in northwestern India, further supporting this connection (Cawood et al., 2017; Qi et al., 2020). However, the ca. 755 Ma paleomagnetic poles result in a Periphery model configuration that differs from the paleogeographic models proposed in the literature that also place South China along the periphery of Rodinia. For example, it has been proposed that India-South China was connected to Rodinia, but further south along the western margin of Rodinia such that eastern India was juxtaposed against western East Antarctica and eastern South China was juxtaposed against western Australia (Cawood et al., 2017). However, ca. 755 Ma paleomagnetic poles from South China, India, and Australia are inconsistent with this alternative position.

It has also been proposed that India-South China was disconnected from Rodinia entirely (Merdith et al., 2017). In this Separate model, the Rayner province is also interpreted to be a terrane disconnected from Rodinia that amalgamated with India ca. 900 Ma resulting in the Eastern Ghats Orogen in eastern India, with subduction continuing along Rayner's margin until India-Rayner collides with East Antarctica near the Precambrian-Cambrian boundary (Merdith et al., 2017). In contrast, other models of Rodinia interpret Rayner to have been

part of Rodinia by 900 Ma, and that the Eastern Ghats Orogen records amalgamation of India with Rodinia (Li et al., 2008). Current geologic constraints from Rayner do not differentiate between these two scenarios.

Importantly, paleomagnetic data indicate that South China drifted across the pole after ca. 800 Ma (Fig. 4.6). In order to satisfy these paleomagnetic constraints, the Periphery model in which South China is in a constant position relative to the core of Rodinia would need to call upon anticlockwise vertical axis rotation of the entire Rodinia supercontinent(Fig. 4.8). Furthermore, the Periphery model would imply that the Lower and Upper Grusdievbreen Formation poles from Svalbard are inconsistent with the paleomagnetic data from South China, and therefore require that the Svalbard poles cannot be interpreted as robust ca. 800 Ma paleomagnetic constraints on the configuration and orientation of Rodinia. On the other hand, the Separate model does not require rotation of Rodinia to satisfy the paleomagnetic constraints from South China, and could allow the Svalbard poles to be reconciled with the South China poles.

Bitter Springs Stage True Polar Wander

TPW should result in the same change in paleomagnetic pole positions for all continents. As a result, the Bitter Springs Stage TPW hypothesis predicts a $\sim 50^{\circ}$ change in pole position between pre-Bitter Springs Stage poles (>ca. 810 Ma) and syn-Bitter Springs Stage poles (ca. 810 to 795 Ma), with a similar angular difference between syn-Bitter Springs Stage poles and post-Bitter Springs Stage poles (<ca. 795 Ma).

Paleomagnetic data from the Xiajiang Group of the Fanjingshan region have the potential to test this hypothesis. Our U-Pb dates demonstrate that there are Xiajiang Group sedimentary rocks that are both older and younger than the onset of the Bitter Springs Stage (ca. 810 Ma) preserved in at least some parts of the Fanjingshan region (Fig. 4.2). The bulk of the high temperature component paleomagnetic data (11 of 15 sites) were developed from strata below tuffs that are dated to be >810 Ma, and are therefore unambiguously constrained to have been deposited prior to the Bitter Springs Stage. However, the remaining 4 sites could have been deposited during the Bitter Springs Stage. One site that yielded a stable and consistent high temperature component in the Hongzixi section is bracketed by tuffs that constrain it to be between 809.52±0.50 Ma and 804.56±0.39 Ma (Fig. 4.2). However, this site cannot be interpreted to have been deposited during the Bitter Springs Stage, since the onset of the Bitter Springs Stage can only be constrained to have occurred after 811.51±0.25 Ma (based on CA-ID-TIMS on a tuff ∼50 m below carbonates that record the first abrupt shift to negative δ^{13}C values in the Fifteenmile Group of northwest Canada; Macdonald et al., 2010) and before ca. 807.9±0.2 Ma (based on interpolation between geochronologic constraints paired to the δ^{13}C record; Swanson-Hysell et al., 2015b). Paleomagnetic data were not developed from sediments in the Hongzixi section in the proximity of the tuff that yielded the 804.56±0.39 Ma date, because these coarser-grained sediments were judged in the field to be not as amenable for preserving a primary magnetic remanence and were not sampled. Another site in the Kuaichang section is above a tuff dated at 811.47±0.67 Ma (Fig. 4.2).

However, the age of this site may be very close to 811.47±0.67 Ma, and therefore also cannot be unambiguously interpreted to have been deposited during the Bitter Springs Stage. Stable dual-polarity paleomagnetic data were developed from the uppermost Xiajiang Group at two sites in the Mamagou section ∼35 m below the unconformity with the overlying Cryogenian glacial sediments (Fig. 4.2). If this unconformity is assumed to be time-correlative between the Hongzixi and Mamagou sections, then these Mamagou sites approximately correlate to the 804.56±0.39 Ma tuff in the Hongzixi section, suggesting that they are syn-Bitter Springs Stage in age. However, the Mamagou section lies ∼20 km to the south of the Hongzixi section, and along-strike variability of the erosional unconformity at the top of the Xiajiang Group could have resulted in the Mamagou section not being syn-Bitter Springs Stage in age.

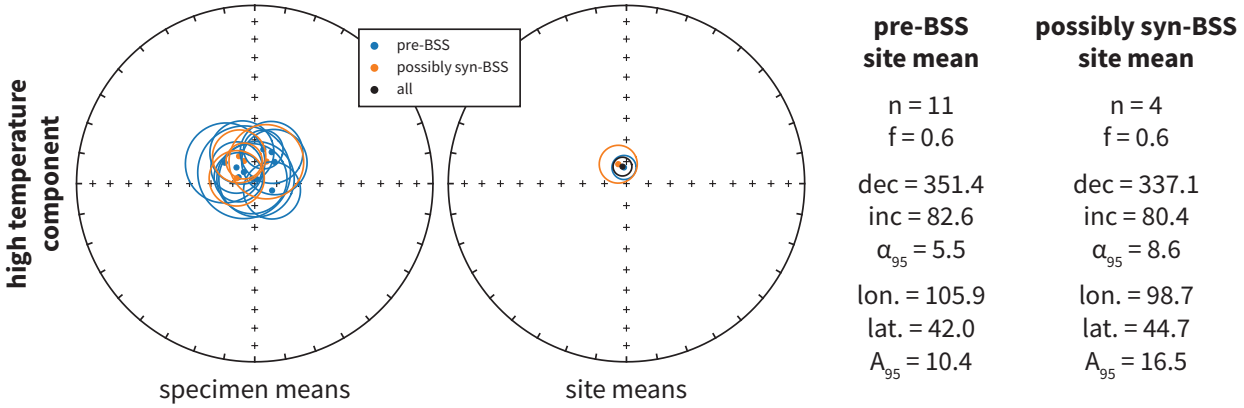

Figure 4.9: Comparison of the high temperature component from sites that are unambiguously constrained by the geochronology to be pre-Bitter Springs Stage and sites that could be syn-Bitter Springs Stage (Fig. 4.2). The angular difference between the two site mean directions is 3.0°.

We compare the high temperature components obtained from the 11 sites that are unambiguously pre-Bitter Springs Stage, with the high temperature components obtained from the four sites that could be syn-Bitter Springs Stage. After converting all sites into a single polarity and applying a tilt and inclination correction, the two site mean directions have an angular difference of 3.0°, and a common mean test cannot reject the null hypothesis at the 95% confidence level that the specimen mean directions were drawn from distributions that share a common mean direction (in the Watson V test, $V = 0.8$ and $V_{crit} = 6.9$; Fig. 4.9). This angular difference is much less than would be expected for Bitter Springs Stage TPW, indicating that the Nanhua Basin was in a similar position throughout Xiajiang Group deposition and that the sites can be grouped into a single paleomagnetic pole. However, ambiguity surrounding the age of the 4 sites that could be syn-Bitter Springs Stage hinders the ability to draw firm conclusions regarding TPW using the Xiajiang Group data alone. To gain more robust insight, we can assess the Xiajiang Group data in the context of the other Tonian South China poles.

The new 813±3 Ma Xiajiang Group pole and the new 804.9±0.4 Ma date on the Madiyi Formation pole provide paleomagnetic constraints on the position of South China before and during the Bitter Springs Stage. Additionally, the 821.6±0.2 Ma date on the Xiaofeng dikes pole constrains it to be pre-Bitter Springs Stage (although prior interpretations have taken the Xiaofeng dikes pole to represent a syn-Bitter Springs Stage position of South China using its previously assigned age of 802±10 Ma; Maloof et al., 2006; Jing et al., 2019). The pre-Bitter Springs Stage Xiaofeng dikes pole and the syn-Bitter Springs Stage Madiyi Formation pole share a common mean (Fig. 4.6). Interpreting these two poles alone would suggest that South China was in a stable position between ca. 821 and 805 Ma in contrast to the prediction of the TPW hypothesis.

However, the pre-Bitter Springs Stage Xiajiang Group pole has a distinct position from the syn-Bitter Springs Stage Madiyi Formation pole, with an angular difference of 19° between the means of the poles (Fig. 4.6). In order to assess this angular difference in comparison to the poles from Svalbard while accounting for the uncertainty on the pole positions and ages, we take a Monte Carlo approach in which 10,000 random draws are taken from Fisherian distributions for the pole positions and from Gaussian distributions for the pole ages (Figs. 4.10A and 4.10B; Swanson-Hysell et al., 2014). Taking this approach, the angular difference between the Xiajiang Group and Madiyi Formation poles is 11–27° at the 95% confidence level, whereas the angular difference between the Lower and Upper Grusdievbreen Formation poles is much higher at 41–62° at the 95% confidence level (Fig. 4.10C). In fact, the probability that a Xiajiang Group–Madiyi Formation pole pair has an equal or larger angular difference than a Lower–Upper Grusdievbreen Formation pole pair is only 8.5×10^{-5}% (calculated using the means and standard deviations of the normal distributions in Fig. 4.10C). As such, the angular difference between the pre- and syn-Bitter Springs Stage poles is significantly less than predicted by the hypothesis that the Svalbard paleomagnetic poles are primary and that their differing positions is the result of TPW. Therefore, this Monte Carlo analysis suggests that the angular difference between the pole pairs from South China and Svalbard can not be straight-forwardly interpreted to be associated with a single TPW rotation.

The velocity of South China implied by the Xiajiang Group and Madiyi Formation poles is also slower than that implied for Svalbard by the Lower and Upper Grusdievbreen Formation poles, being 14–48 cm/yr rather than 60–284 cm/yr at the 95% confidence level, if the Upper Grusdievbreen Formation pole is taken to be 1 to 10 m.y. younger than the Lower Grusdievbreen Formation pole (Maloof et al., 2006; Fig. 4.10D). In contrast to the very rapid rates implied by the Svalbard poles, the rate for South China's motion is at the upper end of the range of velocities suggested by plate kinematic reconstructions (Fig. 4.10D; Meert et al., 1993; Zahirovic et al., 2015).

However, the smaller angular difference between the Xiajiang Group and Madiyi Formation poles relative to the Lower and Upper Grusdievbreen Formation poles could be reconciled with the TPW hypothesis if differential plate motion between South China and Svalbard is superimposed on TPW motion between ca. 813 and 805 Ma (Evans, 2003). For example, if rapid TPW occurred ca. 810 Ma, the Xiajiang Group and Madiyi Formation

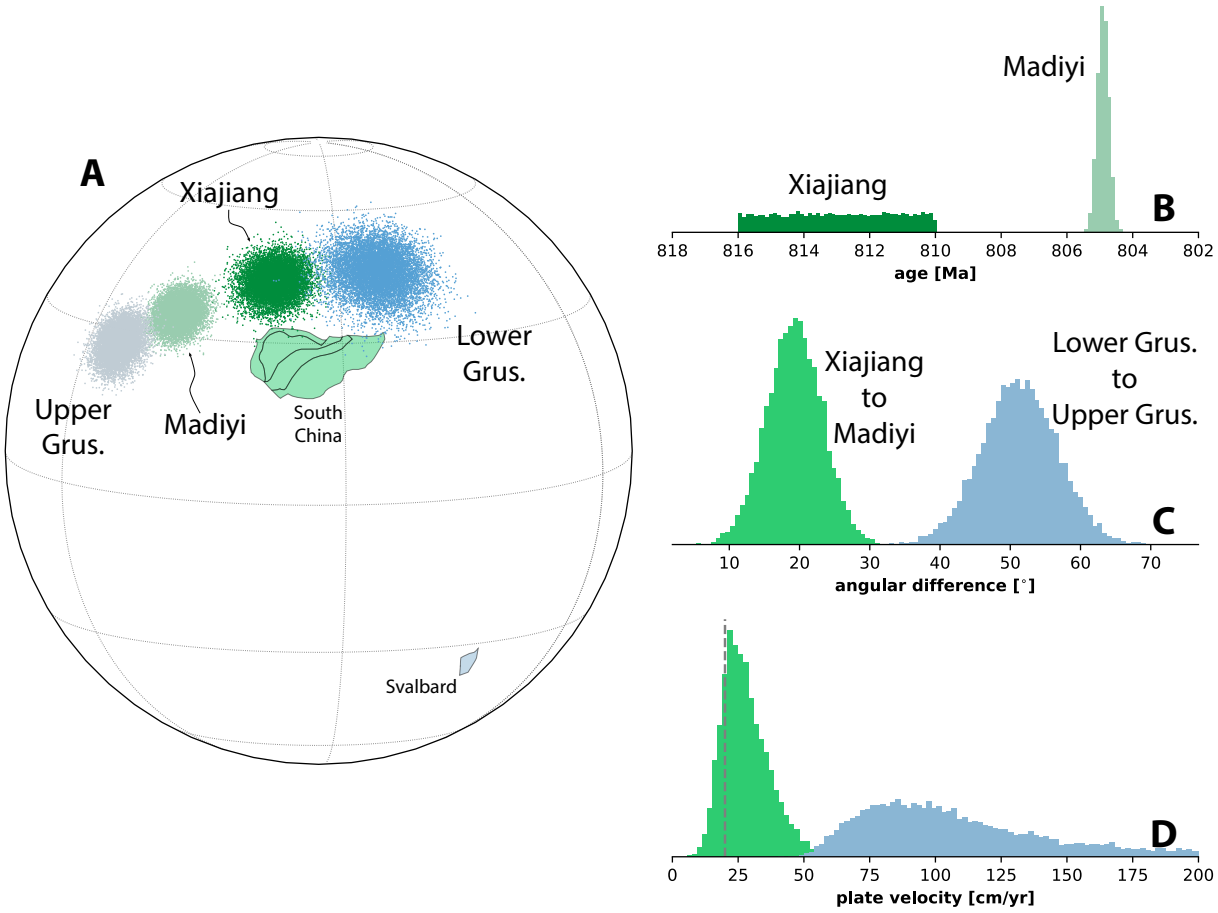

Figure 4.10: Results of Monte Carlo analysis of hypothesized ca. 810 Ma rapid true polar wander motion. **A)** Virtual geomagnetic poles (VGPs) for the Xiajiang Group, Madiyi Formation, and Lower and Upper Grusdievbreen Formation paleomagnetic poles randomly sampled from Fisherian distributions ($n = 10,000$). South China is shown in its present day location, and Svalbard is rotated such that the 4 poles lie along a great circle. **B)** Ages of the Xiajiang Group and Madiyi Formation poles randomly sampled from uniform and Gaussian distributions respectively. **C)** Angular difference between randomly selected VGP pairs in A. **D)** Plate velocity of South China implied by A and B, and the plate velocity of Svalbard implied by A and assuming that the Upper Grusdievbreen Formation pole is 1–10 m.y. younger than the Lower Grusdievbreen Formation pole. The dashed vertical line is the ∼20 cm/yr plate velocity limit suggested by Conrad and Hager (2001) and Zahirovic et al. (2015).

poles should lie along the great circle between the Lower and Upper Grusdievbreen Formation poles, implying a unique reconstruction for South China relative to Svalbard (Fig. 4.11). This configuration also aligns the great circle between the syn-Bitter Springs Stage Upper Grusdievbreen Formation and post-Bitter Springs Stage Svanbergfjellet Formation Svalbard poles with that of the syn-Bitter Springs Stage Madiyi Formation and post-Bitter Springs Stage Liantuo Formation South China poles (Fig. 4.11). In the TPW hypothesis,

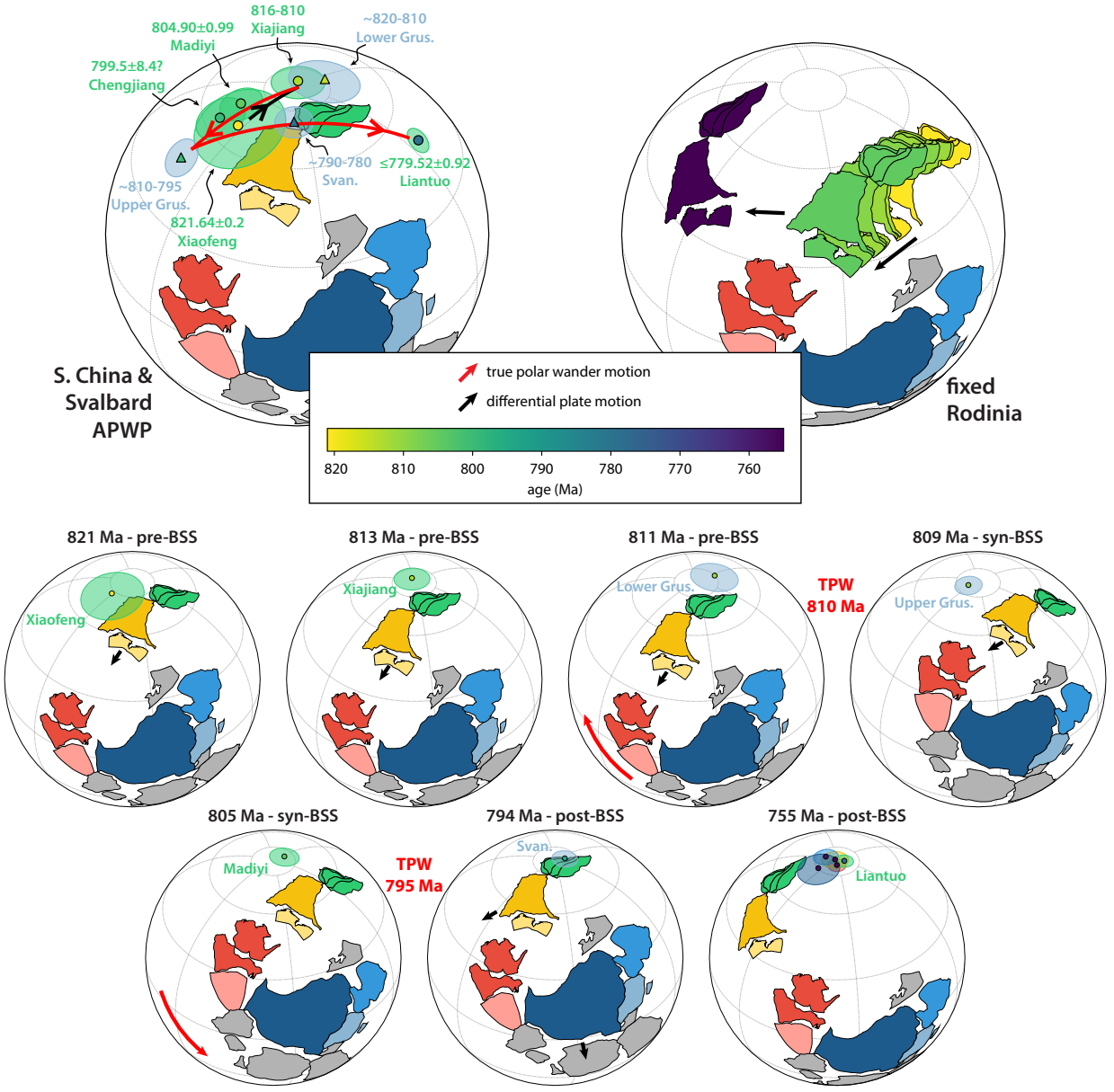

Figure 4.11: Continuous paleogeographic model if Tonian paleomagnetic poles from South China are interpreted as recording differential plate motion superimposed upon Bitter Springs Stage (BSS) true polar wander (TPW). In the upper left, the tectonic blocks are shown in a ca. 813 Ma reconstruction, and the apparent polar wander paths (APWPs) of South China and Svalbard are aligned along two great circles. In the upper right, Rodinia (Laurentia + associated cratons) is fixed in a ca. 755 Ma reconstruction to show the differential motion of South China-India-Rayner relative to Rodinia. The seven lower reconstructions show pre-, syn-, and post-BSS reconstructions in a celestial reference frame. Note that differential plate motion of South China-India-Rayner continues through ca. 810 Ma rapid TPW defined by the Lower and Upper Grusdievbreen Formation poles of Svalbard. Euler rotations for this paleogeographic model are shown in Table S9.

this second great circle would represent the second rapid TPW event ca. 795 Ma. However, South China could have continued to move via differential plate tectonics along the trajectory implied by the difference between the ca. 821 Ma Xiaofeng dikes and the ca. 813 Ma Xiajiang Formation poles through ca. 810 Ma TPW rotation (Fig. 4.11). In such a scenario, the differential plate tectonic motion of South China is approximately opposite the trajectory of the hypothesized TPW rotation (Fig. 4.11), which would be observed in the paleomagnetic record as a smaller angular difference between pre- to syn-Bitter Springs Stage paleomagnetic poles from South China than what would be predicted for TPW alone. Put another way, differential plate tectonic motion could have driven South China in the opposite direction of TPW motion, causing South China to move a smaller distance in a celestial reference frame relative to other tectonic blocks that were not experiencing such differential plate tectonic motion between ca. 813 and 805 Ma, such as Svalbard.

Importantly, if rapid TPW did occur ca. 810 Ma, and differential plate motion between South China and Svalbard ca. 813–805 Ma is superimposed upon that TPW motion to explain the smaller angular difference between the Xiajiang Group and Madiyi Formation poles relative to the Lower and Upper Grusdievbreen Formation poles, then it is required that South China was separate from Rodinia (i.e. the Separate model in Figure 4.8). It is well established that Svalbard was connected to Laurentia via Greenland until Silurian-Devonian translation along Greenland's margin and subsequent rifting away from Greenland in the Eocene (Torsvik and Cocks, 2016). Therefore, if South China was moving differentially relative to Svalbard ca. 813–805 Ma, South China must have been moving differentially relative to Rodinia, and therefore must have been separate from Rodinia. Furthermore, the alignment of paleomagnetic poles from South China and Svalbard along great circles places South China at high latitudes, with the long southeastern margin of the Cathaysia block facing Svalbard (Fig. 4.11). However, ca. 755 Ma paleomagnetic poles require that a Periphery model has South China-India-Rayner connected to Rodinia in a different orientation via northwestern Australia (Fig. 4.8). Even if the Lower Grusdievbreen Formation pole is interpreted as a Paleozoic overprint (Michalski et al., 2011), if the syn-Bitter Springs Stage Upper Grusdievbreen Formation and post-Bitter Springs Stage Svanbergfjellet Formation Svalbard poles are primary, rapid TPW could be interpreted to have occurred ca. 795 Ma. In this scenario, South China is still required to be separate from Rodinia in order to align the great circle between path with that of the syn-Bitter Springs Stage Madiyi Formation and post-Bitter Springs Stage Liantuo Formation South China poles (Fig. 4.11).

Regardless of whether the ca. 821 Ma to ca. 805 Ma poles are interpreted as recording TPW counteracted by plate tectonic motion or a relatively stable position of South China (as in Figure 4.6F), South China is peripheral or disconnected from Rodinia.

4.8 Conclusions

The geochronologic and paleomagnetic data developed from the Xiajiang Group constrain the amalgamation of the Yangtze and Cathaysia blocks of South China to have completed

between ca. 830 Ma and 815.73±0.18 Ma at high latitudes. A consistent high latitude position is implied by poles from ca. 821 Ma to 805 Ma with a continued high latitude position ca. 780 Ma following South China transiting over the pole. These paleolatitudes, as well as convergent orogenesis between the Yangtze and Cathaysia blocks and continued arc activity along the northwest margin of the South China craton during the Tonian and into the Cryogenian, cannot be reconciled with the Missing Link model that places South China in the core of a stable Rodinia continent. The angular difference in pole position between the ca. 813 Ma (pre-Bitter Springs Stage) Xiajiang Group pole and ca. 805 Ma (syn-Bitter Springs Stage) Madiyi Formation pole is significantly less than that predicted for the Bitter Springs Stage TPW hypothesis. The poles could be interpreted to indicate a relatively stable high latitude position for South China inconsistent with TPW. However, it is possible to interpret the poles as TPW rotation counteracted by plate tectonic motion. In this scenario, South China must be considered to be distinct from Rodinia. Whether or not the paleomagnetic poles are interpreted as recording TPW, they constrain South China to either have been connected to Rodinia along its periphery, or disconnected from the (super)continent entirely.

4.9 Acknowledgements

Research was supported by National Science Foundation grants EAR-1547434 and EAR-1547537 to N.L.S-.H. and F.A.M. CUGB research was supported by National Natural Science Foundation of China grant 41830215 to S.H.Z. Maoyan Zhu supported research logistics in the field. Oliver Abbitt prepared specimens for paleomagnetic analyses.

Bibliography

Abbott, L. D., Silver, E. A., Thompson, P. R., Filewicz, M. V., Schneider, C., and Abdoerrias, 1994, Stratigraphic constraints on the development and timing of arc-continent collision in northern Papua New Guinea: Journal of Sedimentary Research, vol. 64, pp. 169–183, doi: 10.1306/D4267F82-2B26-11D7-8648000102C1865D.

Aitken, J. D., 1981, Stratigraphy and sedimentology of the Upper Proterozoic Little Dal Group, Mackenzie Mountains, Northwest Territories: Mackenzie Mountains, Northwest Territories: Geological Survey of Canada, Paper, vol. 8110, pp. 47–81.

Alene, M., 1998, Tectonomagmatic evolution of the Neoproterozoic rocks of the Mai Kenetal-Negash area, Tigrai, northern Ethiopia: Ph.D. thesis, University of Turin.

Alene, M., Jenkin, G. R. T., Leng, M. J., and Darbyshire, D. P. F., 2006, The Tambien Group, Ethiopia: an early Cryogenian (ca. 800-735 Ma) Neoproterozoic sequence in the Arabian-Nubian Shield: Precambrian Research, vol. 147, pp. 79–99, doi: 10.1016/j.precamres.2006.02.002.

Ali, J., Hall, R., and Baker, S., 2001, Palaeomagnetic data from a Mesozoic Philippine Sea Plate ophiolite on Obi Island, Eastern Indonesia: Journal of Asian Earth Sciences, vol. 19, pp. 535–546, doi: 10.1016/s1367-9120(00)00053-5.

Ali, K. A., Azer, M. K., Gahlan, H. A., Wilde, S. A., Samuel, M. D., and Stern, R. J., 2010, Age constraints on the formation and emplacement of Neoproterozoic ophiolites along the Allaqi-Heiani Suture, south eastern desert of Egypt: Gondwana Research, vol. 18, pp. 583–595, doi: 10.1016/j.gr.2010.03.002.

Allègre, C. J., Louvat, P., Gaillardet, J., Meynadier, L., Rad, S., and Capmas, F., 2010, The fundamental role of island arc weathering in the oceanic Sr isotope budget: Earth and Planetary Science Letters, vol. 292, pp. 51–56, doi: 10.1016/j.epsl.2010.01.019.

Allen, R., Carter, A., Najman, Y., Bandopadhyay, P., Chapman, H., Bickle, M., Garzanti, E., Vezzoli, G., Andò, S., Foster, G., and et al., 2008, New constraints on the sedimentation and uplift history of the Andaman-Nicobar accretionary prism, South Andaman Island: Special Paper 436: Formation and Applications of the Sedimentary Record in Arc Collision Zones, pp. 223–255, doi: 10.1130/2008.2436(11).

Almeida, V. V., Janasi, V. A., Heaman, L. M., Shaulis, B. J., Hollanda, M. H. B., and Renne, P. R., 2018, Contemporaneous alkaline and tholeiitic magmatism in the Ponta Grossa Arch, Paraná-Etendeka Magmatic Province: Constraints from U-Pb zircon/baddeleyite and $^{40}Ar/^{39}Ar$ phlogopite dating of the José Fernandes Gabbro and mafic dykes: Journal of Volcanology and Geothermal Research, vol. 355, pp. 55–65, doi: 10.1016/j.jvolgeores.2017.01.018.

Arkin, Y., Beyth, M., Dow, D. B., Levitte, D., Haile, T., and Hailu, T., 1971, Geological map of Mekele Sheet area ND37-11 Tigre Province: Imperial Ethiopian Government, Ministry of Mines. Geological Survey of Ethiopia.

Arzamastsev, A. A. and Wu, F.-Y., 2014, U-Pb geochronology and Sr-Nd isotopic systematics of minerals from the ultrabasic-alkaline massifs of the Kola province: Petrology, vol. 22, pp. 462–479, doi: 10.1134/s0869591114050026.

Ashwal, L., Solanki, A., Pandit, M., Corfu, F., Hendriks, B., Burke, K., and Torsvik, T., 2013, Geochronology and geochemistry of Neoproterozoic Mt. Abu granitoids, NW India: Regional correlation and implications for Rodinia paleogeography: Precambrian Research, vol. 236, pp. 265–281, doi: 10.1016/j.precamres.2013.07.018.

Asmerom, Y., Jacobsen, S. B., Knoll, A. H., Butterfield, N. J., and Swett, K., 1991, Strontium isotopic variations of Neoproterozoic seawater: implications for crustal evolution: Geochimica et Cosmochimica Acta, vol. 55, pp. 2883–2894, doi: 10.1016/0016-7037(91)90453-C.

Audley-Charles, M., 2004, Ocean trench blocked and obliterated by Banda forearc collision with Australian proximal continental slope: Tectonophysics, vol. 389, pp. 65–79, doi: 10.1016/j.tecto.2004.07.048.

Audley-Charles, M. G., 1986, Rates of Neogene and Quaternary tectonic movements in the Southern Banda Arc based on micropalaeontology: Journal of the Geological Society, vol. 143, pp. 161–175, doi: 10.1144/gsjgs.143.1.0161.

Avigad, D., Stern, R. J., Beyth, M., Miller, N., and McWilliams, M. O., 2007, Detrital zircon U-Pb geochronology of Cryogenian diamictites and Lower Paleozoic sandstone in Ethiopia (Tigrai): age constraints on Neoproterozoic glaciation and crustal evolution of the southern Arabian-Nubian Shield: Precambrian Research, vol. 154, pp. 88–106, doi: 10.1016/j.precamres.2006.12.004.

Bailly, V., Pubellier, M., Ringenbach, J.-C., de Sigoyer, J., and Sapin, F., 2009, Deformation zone "jumps" in a young convergent setting; the Lengguru fold-and-thrust belt, New Guinea Island: Lithos, vol. 113, pp. 306–317, doi: 10.1016/j.lithos.2009.08.013.

Baldwin, S. L., Fitzgerald, P. G., and Webb, L. E., 2012, Tectonics of the New Guinea region: Annual Review of Earth and Planetary Sciences, vol. 40, pp. 495–520, doi: 10.1146/annurev-earth-040809-152540.

Ballantyne, P., 1992, Petrology and geochemistry of the plutonic rocks of the Halmahera ophiolite, eastern Indonesia, an analogue of modern oceanic forearcs: Geological Society, London, Special Publications, vol. 60, pp. 179–202, doi: 10.1144/gsl.sp.1992.060.01.11.

Banner, J. L. and Hanson, G. N., 1990, Calculation of simultaneous isotopic and trace element variations during water-rock interaction with applications to carbonate diagenesis: Geochimica et Cosmochimica Acta, vol. 54, pp. 3123–3137, doi: 10.1016/0016-7037(90)90128-8.

Bartley, J. K., Semikhatov, M. A., Kaufman, A. J., Knoll, A. H., Pope, M. C., and Jacobsen, S. B., 2001, Global events across the Mesoproterozoic-Neoproterozoic boundary: C and Sr isotopic evidence from Siberia: Precambrian Research, vol. 111, pp. 165–202, doi: 10.1016/S0301-9268(01)00160-7.

Bauerman, H., 1884, Geology of the Country Near the Forty-Ninth Parallel of North Latitude West of the Rocky Mountains: From Observations Made 1859–1861: Dawson Brothers, Montreal.

Baum, S. K. and Crowley, T. J., 2001, GCM response to Late Precambrian (∼590 Ma) ice-covered continents: Geophysical Research Letters, vol. 28, pp. 583–586, doi: 10.1029/2000GL011557.

Bellier, O., Sébrier, M., Seward, D., Beaudouin, T., Villeneuve, M., and Putranto, E., 2006, Fission track and fault kinematics analyses for new insight into the Late Cenozoic tectonic regime changes in West-Central Sulawesi (Indonesia): Tectonophysics, vol. 413, pp. 201–220, doi: 10.1016/j.tecto.2005.10.036.

Bereiter, B., Eggleston, S., Schmitt, J., Nehrbass-Ahles, C., Stocker, T. F., Fischer, H., Kipfstuhl, S., and Chappellaz, J., 2015, Revision of the EPICA Dome C CO_2 record from 800 to 600 kyr before present: Geophysical Research Letters, vol. 42, pp. 542–549, doi: 10.1002/2014gl061957.

Berends, C. J., de Boer, B., and van de Wal, R. S. W., 2020, Reconstructing the evolution of ice sheets, sea level and atmospheric co_2 during the past 3.6 million years: doi: 10.5194/cp-2020-52.

Bergman, S. C., Coffield, D. Q., Talbot, J. P., and Garrard, R. A., 1996, Tertiary tectonic and magmatic evolution of western Sulawesi and the Makassar Strait, Indonesia: evidence for a Miocene continent-continent collision: Geological Society, London, Special Publications, vol. 106, pp. 391–429, doi: 10.1144/gsl.sp.1996.106.01.25.

Berhe, S. M., 1990, Ophiolites in northeast and east Africa: implications for Proterozoic crustal growth: Journal of the Geological Society, vol. 147, pp. 41–57, doi: 10.1144/gsjgs.147.1.0041.

Berndt, M. E., Seyfried, W. E., and Beck, J. W., 1988, Hydrothermal alteration processes at midocean ridges: experimental and theoretical constraints from Ca and Sr exchange reactions and Sr isotopic ratios: Journal of Geophysical Research: Solid Earth, vol. 93, pp. 4573–4583, doi: 10.1029/JB093iB05p04573.

Berner, R. A., 2001, GEOCARB III: A revised model of atmospheric CO_2 over Phanerozoic time: American Journal of Science, vol. 301, pp. 182–204, doi: 10.2475/ajs.301.2.182.

Berner, R. A. and Caldeira, K., 1997, The need for mass balance and feedback in the geochemical carbon cycle: Geology, vol. 25, pp. 955–956, doi: 10.1130/0091-7613(1997)025⟨0955:TNFMBA⟩2.3.CO;2.

Berner, R. A., Lasaga, A. C., and Garrels, R. M., 1983, The carbonate-silicate geochemical cycle and its effect on atmospheric carbon dioxide over the past 100 million years: American Journal of Science, vol. 283, pp. 641–683.

Beyth, M., 1972, To the geology of central-western Tigre: Rheinisch Friedrich-Wilhelms-Universitaet.

Beyth, M., Avigad, D., Wetzel, H.-U., Matthews, A., and Berhe, S. M., 2003, Crustal exhumation and indications for Snowball Earth in the East African Orogen: north Ethiopia and east Eritrea: Precambrian Research, vol. 123, pp. 187–201, doi: 10.1016/S0301-9268(03)00067-6.

Bilardello, D., 2016, The do's and don'ts of inclination shallowing corrections: IRM Quarterly, vol. 26, pp. 1–11.

Bishop, J. W. and Sumner, D. Y., 2006, Molar tooth structures of the Neoarchean Monteville Formation, Transvaal Supergroup, South Africa. I: Constraints on microcrystalline $CaCO_3$ precipitation: Sedimentology, vol. 53, pp. 1049–1068, doi: 10.1111/j.1365-3091.2006.00801.x.

Blackburn, T. J., Olsen, P. E., Bowring, S. A., McLean, N. M., Kent, D. V., Puffer, J., McHone, G., Rasbury, E. T., and Et-Touhami, M., 2013, Zircon U-Pb geochronology links the End-Triassic extinction with the Central Atlantic Magmatic Province: Science, vol. 340, pp. 941–945, doi: 10.1126/science.1234204.

Bold, U., Smith, E. F., Rooney, A. D., Bowring, S. A., Buchwaldt, R., Dudás, F. Ő., Ramezani, J., Crowley, J. L., Schrag, D. P., and Macdonald, F. A., 2016, Neoproterozoic stratigraphy of the Zavkhan terrane of Mongolia: the backbone for Cryogenian and early Ediacaran chemostratigraphic records: American Journal of Science, vol. 316, pp. 1–63, doi: 10.2475/01.2016.01.

Boucot, A. J., Xu, C., Scotese, C. R., and Morley, R. J., 2013, Phanerozoic Paleoclimate: An Atlas of Lithologic Indicators of Climate: SEPM (Society for Sedimentary Geology), doi: 10.2110/sepmcsp.11.

Bowring, S. A., Grotzinger, J. P., Condon, D. J., Ramezani, J., Newall, M. J., and Allen, P. A., 2007, Geochronologic constraints on the chronostratigraphic framework of the Neoproterozoic Huqf Supergroup, Sultanate of Oman: American Journal of Science, vol. 307, pp. 1097–1145, doi: 10.2475/10.2007.01.

Brand, U., 2004, Carbon, oxygen and strontium isotopes in Paleozoic carbonate components: an evaluation of original seawater-chemistry proxies: Chemical Geology, vol. 204, pp. 23–44, doi: 10.1016/j.chemgeo.2003.10.013.

Brand, U. and Veizer, J., 1980, Chemical diagenesis of a multicomponent carbonate system-1: Trace elements: Journal of Sedimentary Research, vol. 50, pp. 1219–1236, doi: 10.1306/212F7BB7-2B24-11D7-8648000102C1865D.

Brantley, S. L., 2003, Reaction kinetics of primary rock-forming minerals under ambient conditions: Treatise on Geochemistry, pp. 73–117, doi: 10.1016/b0-08-043751-6/05075-1.

Brasier, M., McCarron, G., Tucker, R., Leather, J., Allen, P., and Shields, G., 2000, New U-Pb zircon dates for the Neoproterozoic Ghubrah glaciation and for the top of the Huqf Supergroup, Oman: Geology, vol. 28, pp. 175–178, doi: 10.1130/0091-7613(2000)28⟨175:NUZDFT⟩2.0.CO;2.

Brasier, M. D., Shields, G., Kuleshov, V. N., and Zhegallo, E. A., 1996, Integrated chemo- and biostratigraphic calibration of early animal evolution: Neoproterozoic-Early Cambrian of southwest Mongolia: Geological Magazine, vol. 133, pp. 445–485, doi: 10.1017/S0016756800007603.

Bright, R. M., Amato, J. M., Denyszyn, S. W., and Ernst, R. E., 2014, U-Pb geochronology of 1.1 Ga diabase in the southwestern United States: testing models for the origin of a post-Grenville large igneous province: Lithosphere, vol. 6, pp. 135–156, doi: 10.1130/L335.1.

Broecker, W. S. and Peng, T.-H., 1982, Tracers in the Sea: Eldigio Press, Palisades, N.Y., doi: 10.1017/S0033822200005221.

Buchan, K. L. and Ernst, R. E., 2004, Diabase dyke swarms and related units in Canada and adjacent regions: Geological Survey of Canada Map 2022A, doi: 10.4095/214883.

Buchan, K. L., Mertanen, S., Park, R. G., Pesonen, L. J., Elming, S.-Å., Abrahamsen, N., and Bylund, G., 2000, Comparing the drift of Laurentia and Baltica in the Proterozoic: the importance of key palaeomagnetic poles: Tectonophysics, vol. 319, pp. 167–198, doi: 10.1016/S0040-1951(00)00032-9.

Bureau of Geology and Mineral Resources of Guizhou Province, 1984, Regional geology of Guizhou Province: Geological Publishing House, Beijing.

Burgess, S. D. and Bowring, S. A., 2015, High-precision geochronology confirms voluminous magmatism before, during, and after Earth's most severe extinction: Science Advances, vol. 1, pp. 1–14, doi: 10.1126/sciadv.1500470.

Burgess, S. D., Bowring, S. A., Fleming, T. H., and Elliot, D. H., 2015, High-precision geochronology links the Ferrar large igneous province with early-Jurassic ocean anoxia and biotic crisis: Earth and Planetary Science Letters, vol. 415, pp. 90–99, doi: 10.1016/j.epsl.2015.01.037.

Bussert, R., 2010, Exhumed erosional landforms of the Late Palaeozoic glaciation in northern Ethiopia: Indicators of ice-flow direction, palaeolandscape and regional ice dynamics: Gondwana Research, vol. 18, pp. 356–369, doi: 10.1016/j.gr.2009.10.009.

Butterfield, N. J., 2015, Proterozoic photosynthesis – a critical review: Palaeontology, vol. 58, pp. 953–972, doi: 10.1111/pala.12211.

Calver, C. R., Crowley, J. L., Wingate, M. T. D., Evans, D. A. D., Raub, T. D., and Schmitz, M. D., 2013, Globally synchronous Marinoan deglaciation indicated by U-Pb geochronology of the Cottons Breccia, Tasmania, Australia: Geology, vol. 41, pp. 1127–1130, doi: 10.1130/G34568.1.

Cambiotti, G., Ricard, Y., and Sabadini, R., 2010, Ice age True Polar Wander in a compressible and non-hydrostatic Earth: Geophysical Journal International, vol. 183, pp. 1248–1264, doi: 10.1111/j.1365-246x.2010.04791.x.

Cao, W., Williams, S., Flament, N., Zahirovic, S., Scotese, C., and Müller, R. D., 2018, Palaeolatitudinal distribution of lithologic indicators of climate in a palaeogeographic framework: Geological Magazine, vol. 156, pp. 331–354, doi: 10.1017/s0016756818000110.

Carretier, S., Goddéris, Y., Delannoy, T., and Rouby, D., 2014, Mean bedrock-to-saprolite conversion and erosion rates during mountain growth and decline: Geomorphology, vol. 209, pp. 39–52, doi: 10.1016/j.geomorph.2013.11.025.

Carroll, S. A. and Knauss, K. G., 2005, Dependence of labradorite dissolution kinetics on $CO_{2(aq)}$, $Al_{(aq)}$, and temperature: Chemical Geology, vol. 217, pp. 213–225, doi: 10.1016/j.chemgeo.2004.12.008.

Cawood, P. A., Strachan, R. A., Pisarevsky, S. A., Gladkochub, D. P., and Murphy, J. B., 2016, Linking collisional and accretionary orogens during Rodinia assembly and breakup: Implications for models of supercontinent cycles: Earth and Planetary Science Letters, vol. 449, pp. 118–126, doi: 10.1016/j.epsl.2016.05.049.

Cawood, P. A., Wang, Y., Xu, Y., and Zhao, G., 2013, Locating South China in Rodinia and Gondwana: A fragment of greater India lithosphere?: Geology, vol. 41, pp. 903–906, doi: 10.1130/G34395.1.

Cawood, P. A., Zhao, G., Yao, J., Wang, W., Xu, Y., and Wang, Y., 2017, Reconstructing South China in Phanerozoic and Precambrian supercontinents: Earth-Science Reviews, doi: 10.1016/j.earscirev.2017.06.001.

Chan, N.-H., Mitrovica, J. X., Daradich, A., Creveling, J. R., Matsuyama, I., and Stanley, S., 2014, Time-dependent rotational stability of dynamic planets with elastic lithospheres: Journal of Geophysical Research: Planets, vol. 119, pp. 169–188, doi: 10.1002/2013je004466.

Charney, J. G., Arakawa, A., Baker, D. J., Bolin, B., Dickinson, R. E., Goody, R. M., Leith, C. E., Stommel, H. M., and Wunsch, C. I., 1979, Carbon dioxide and climate: a scientific assessment: National Academy of Sciences, Washington, DC.

Chatterjee, S. M., Roy Choudhury, M., Das, S., and Roy, A., 2017, Significance and dynamics of the Neoproterozoic (810 Ma) Phulad Shear Zone, Rajasthan, NW India: Tectonics, vol. 36, pp. 1432–1454, doi: 10.1002/2017tc004554.

Cloos, M., Sapiie, B., Quarles van Ufford, A., Weiland, R. J., Warren, P. Q., and McMahon, T. P., 2005, Collisional delamination in New Guinea: The geotectonics of subducting slab breakoff: Geological Society of America Special Papers, pp. 1–51, doi: 10.1130/2005.2400.

Coffin, M., Duncan, R., Eldholm, O., Fitton, J. G., Frey, F., Larsen, H. C., Mahoney, J., Saunders, A., Schlich, R., and Wallace, P., 2006, Large igneous provinces and scientific ocean drilling: Status quo and a look ahead: Oceanography, vol. 19, pp. 150–160, doi: 10.5670/oceanog.2006.13.

Cogné, J.-P. and Humler, E., 2006, Trends and rhythms in global seafloor generation rate: Geochemistry, Geophysics, Geosystems, vol. 7, pp. 1–17, doi: 10.1029/2005gc001148.

Colleps, C. L., McKenzie, N. R., Stockli, D. F., Hughes, N. C., Singh, B. P., Webb, A. A. G., Myrow, P. M., Planavsky, N. J., and Horton, B. K., 2018, Zircon (U-Th)/He thermochronometric constraints on Himalayan thrust belt exhumation, bedrock weathering, and Cenozoic seawater chemistry: Geochemistry, Geophysics, Geosystems, vol. 19, pp. 257–271, doi: 10.1002/2017gc007191.

Collins, A. S. and Windley, B. F., 2002, The tectonic evolution of central and northern Madagascar and its place in the final assembly of Gondwana: The Journal of Geology, vol. 110, pp. 325–339, doi: 10.1086/339535.

Condon, D., Zhu, M., Bowring, S., Wang, W., Yang, A., and Jin, Y., 2005, U-Pb ages from the Neoproterozoic Doushantuo Formation, China: Science, vol. 308, pp. 95–98, doi: 10.1126/science.1107765.

Condon, D. J., Schoene, B., McLean, N. M., Bowring, S. A., and Parrish, R. R., 2015, Metrology and traceability of U-Pb isotope dilution geochronology (EARTHTIME tracer

calibration part I): Geochimica et Cosmochimica Acta, vol. 164, pp. 464–480, doi: 10.1016/j.gca.2015.05.026.

Conrad, C. P. and Hager, B. H., 2001, Mantle convection with strong subduction zones: Geophysical Journal International, vol. 144, pp. 271–288, doi: 10.1046/j.1365-246x.2001.00321.x.

Cottam, M. A., Hall, R., Sperber, C., Kohn, B. P., Forster, M. A., and Batt, G. E., 2013, Neogene rock uplift and erosion in northern Borneo: evidence from the Kinabalu granite, Mount Kinabalu: Journal of the Geological Society, vol. 170, pp. 805–816, doi: 10.1144/jgs2011-130.

Courtillot, V. E. and Renne, P. R., 2003, On the ages of flood basalt events: Comptes Rendus Geoscience, vol. 335, pp. 113–140, doi: 10.1016/s1631-0713(03)00006-3.

Cox, G. M., Foden, J., and Collins, A. S., 2018a, Late Neoproterozoic adakitic magmatism of the eastern Arabian Nubian Shield: Geoscience Frontiers, doi: 10.1016/j.gsf.2017.12.006.

Cox, G. M., Halverson, G. P., Stevenson, R. K., Vokaty, M., Poirier, A., Kunzmann, M., Li, Z.-X., Denyszyn, S. W., Strauss, J. V., and Macdonald, F. A., 2016, Continental flood basalt weathering as a trigger for Neoproterozoic Snowball Earth: Earth and Planetary Science Letters, vol. 446, pp. 89–99, doi: 10.1016/j.epsl.2016.04.016.

Cox, G. M., Isakson, V., Hoffman, P. F., Gernon, T. M., Schmitz, M. D., Shahin, S., Collins, A. S., Preiss, W., Blades, M. L., Mitchell, R. N., and et al., 2018b, South Australian U-Pb zircon (CA-ID-TIMS) age supports globally synchronous Sturtian deglaciation: Precambrian Research, vol. 315, pp. 257–263, doi: 10.1016/j.precamres.2018.07.007.

Cox, G. M., Lewis, C. J., Collins, A. S., Halverson, G. P., Jourdan, F., Foden, J., Nettle, D., and Kattan, F., 2012, Ediacaran terrane accretion within the Arabian-Nubian Shield: Gondwana Research, vol. 21, pp. 341–352, doi: 10.1016/j.gr.2011.02.011.

Cox, G. M., Strauss, J. V., Halverson, G. P., Schmitz, M. D., McClelland, W. C., Stevenson, R. S., and Macdonald, F. A., 2015, Kikiktat volcanics of Arctic Alaska-melting of harzburgitic mantle associated with the Franklin large igneous province: Lithosphere, vol. 7, pp. 275–295, doi: 10.1130/L435.1.

Creveling, J. R., Mitrovica, J. X., Chan, N.-H., Latychev, K., and Matsuyama, I., 2012, Mechanisms for oscillatory true polar wander: Nature, vol. 491, pp. 244–248, doi: 10.1038/nature11571.

Crowhurst, P. V., Hill, K. C., Foster, D. A., and Bennett, A. P., 1996, Thermochronological and geochemical constraints on the tectonic evolution of northern Papua New Guinea: Geological Society, London, Special Publications, vol. 106, pp. 525–537, doi: 10.1144/gsl.sp.1996.106.01.33.

Cucciniello, C., 2010, U-Pb ages, Pb-Os isotope ratios, and platinum-group element (PGE) composition of the West-Central Madagascar flood basalt province: The Journal of Geology, vol. 118, pp. 523–541, doi: 10.1086/655012.

Cui, Y., Schubert, B. A., and Jahren, A. H., 2020, A 23 m.y. record of low atmospheric CO_2: Geology, doi: 10.1130/g47681.1.

Daly, R. A., 1912, Geology of the North American Cordillera at the forty-ninth parallel: US Government Printing Office.

Darmadi, Y., Willis, B., and Dorobek, S., 2007, Three-dimensional seismic architecture of fluvial sequences on the low-gradient Sunda Shelf, offshore Indonesia: Journal of Sedimentary Research, vol. 77, pp. 225–238, doi: 10.2110/jsr.2007.024.

Davies, H. L. and Jaques, A. L., 1984, Emplacement of ophiolite in Papua New Guinea: Geological Society, London, Special Publications, vol. 13, pp. 341–349, doi: 10.1144/gsl.sp.1984.013.01.27.

Davies, H. L. and Smite, I. E., 1971, Geology of eastern Papua: Geological Society of America Bulletin, vol. 82, pp. 3299–3312, doi: 10.1130/0016-7606(1971)82[3299:goep]2.0.co;2.

Davies, I. C., 1990, Geological and exploration review of the Tomori PSC, eastern Indonesia: Indonesian Petroleum Association Proceedings, 19th Annual Convention, doi: 10.29118/ipa.1845.41.67.

Davis, D. W. and Green, J. C., 1997, Geochronology of the North American Midcontinent rift in western Lake Superior and implications for its geodynamic evolution: Canadian Journal of Earth Sciences, vol. 34, pp. 476–488, doi: 10.1139/e17-039.

Davy, P. and Crave, A., 2000, Upscaling local-scale transport processes in large-scale relief dynamics: Physics and Chemistry of the Earth, Part A: Solid Earth and Geodesy, vol. 25, pp. 533–541, doi: 10.1016/s1464-1895(00)00082-x.

DeConto, R. M., Pollard, D., Wilson, P. A., Pälike, H., Lear, C. H., and Pagani, M., 2008, Thresholds for Cenozoic bipolar glaciation: Nature, vol. 455, pp. 652–656, doi: 10.1038/nature07337.

Delworth, T., 2006, Preface to the special section: Journal of Climate, vol. 19, pp. 641–641, doi: 10.1175/jcli9016.1.

Delworth, T. L., Broccoli, A. J., Rosati, A., Stouffer, R. J., Balaji, V., Beesley, J. A., Cooke, W. F., Dixon, K. W., Dunne, J., Dunne, K. A., and et al., 2006, GFDL's CM2 global coupled climate models. part i: Formulation and simulation characteristics: Journal of Climate, vol. 19, pp. 643–674, doi: 10.1175/jcli3629.1.

Denyszyn, S. W., Halls, H. C., Davis, D. W., and Evans, D. A., 2009, Paleomagnetism and U-Pb geochronology of Franklin dykes in High Arctic Canada and Greenland: a revised age and paleomagnetic pole constraining block rotations in the Nares Strait region: Canadian Journal of Earth Sciences, vol. 46, pp. 689–705, doi: 10.1139/E09-042.

Derry, L. A., 2010, A burial diagenesis origin for the Ediacaran Shuram-Wonoka carbon isotope anomaly: Earth and Planetary Science Letters, vol. 294, pp. 152–162, doi: 10.1016/j.epsl.2010.03.022.

Dessert, C., Dupré, B., François, L. M., Schott, J., Gaillardet, J., Chakrapani, G., and Bajpai, S., 2001, Erosion of Deccan Traps determined by river geochemistry: impact on the global climate and the $^{87}Sr/^{86}Sr$ ratio of seawater: Earth and Planetary Science Letters, vol. 188, pp. 459–474, doi: 10.1016/S0012-821X(01)00317-X.

Dessert, C., Dupré, B., Gaillardet, J., François, L. M., and Allègre, C. J., 2003, Basalt weathering laws and the impact of basalt weathering on the global carbon cycle: Chemical Geology, vol. 202, pp. 257–273, doi: 10.1016/j.chemgeo.2002.10.001.

Dimalanta, C. B. and Yumul, G. P., 2006, Magmatic and amagmatic contributions to crustal growth in the Philippine island arc system: Comparison of the Cretaceous and post-Cretaceous periods: Geosciences Journal, vol. 10, pp. 321–329, doi: 10.1007/bf02910373.

Domeier, M., 2018, Early Paleozoic tectonics of Asia: Towards a full-plate model: Geoscience Frontiers, vol. 9, pp. 789–862, doi: 10.1016/j.gsf.2017.11.012.

Dong, Y., Liu, X., Santosh, M., Chen, Q., Zhang, X., Li, W., He, D., and Zhang, G., 2012, Neoproterozoic accretionary tectonics along the northwestern margin of the Yangtze Block, China: Constraints from zircon U-Pb geochronology and geochemistry: Precambrian Research, vol. 196-197, pp. 247–274, doi: 10.1016/j.precamres.2011.12.007.

Donnadieu, Y., Goddéris, Y., Ramstein, G., Nedelec, A., and Meert, J., 2004a, A 'snowball Earth' climate triggered by continental break-up through changes in runoff: Nature, vol. 428, pp. 303–306.

Donnadieu, Y., Ramstein, G., Fluteau, F., Roche, D., and Ganopolski, A., 2004b, The impact of atmospheric and oceanic heat transports on the sea-ice-albedo instability during the Neoproterozoic: Climate Dynamics, vol. 22, pp. 293–306, doi: 10.1007/s00382-003-0378-5.

Donohoe, A. and Voigt, A., 2017, Why future shifts in tropical precipitation will likely be small: Geophysical Monograph Series, pp. 115–137, doi: 10.1002/9781119068020.ch8.

Dudas, F. O., Davidson, A., and Bethune, K. M., 1994, Age of the Sudbury diabase dykes and their metamorphism in the Grenville Province, Ontario: *In* Radiogenic ace and isotopic studies, Geological Survey of Canada, pp. 97–106.

Duebendorfer, E. M., 2002, Regional correlation of Mesoproterozoic structures and deformational events in the Albany-Fraser orogen, Western Australia: Precambrian Research, vol. 116, pp. 129–154, doi: 10.1016/s0301-9268(02)00017-7.

Dunlop, D. J. and Özdemir, Ö., 2001, Rock magnetism: fundamentals and frontiers, vol. 3: Cambridge University Press.

Edmond, J. M., 1992, Himalayan tectonics, weathering processes, and the strontium isotope record in marine limestones: Science, vol. 258, pp. 1594–1597, doi: 10.1126/science.258.5088.1594.

Elburg, M. and Foden, J., 1998, Temporal changes in arc magma geochemistry, northern Sulawesi, Indonesia: Earth and Planetary Science Letters, vol. 163, pp. 381–398, doi: 10.1016/s0012-821x(98)00143-5.

Emerson, S. and Hedges, J., 2008, Chemical oceanography and the marine carbon cycle: Cambridge University Press.

Ernst, R. E., Bleeker, W., Söderlund, U., and Kerr, A. C., 2013, Large igneous provinces and supercontinents: Toward completing the plate tectonic revolution: Lithos, vol. 174, pp. 1–14, doi: 10.1016/j.lithos.2013.02.017.

Ernst, R. E., Bond, D. P. G., Zhang, S.-H., Buchan, K. L., Grasby, S. E., Youbi, N., el Hafida, H., Bekker, A., and Doucet, L., 2019, LIP record through time and implications for secular environmental changes and GTS boundaries: *In* Ernst, R. E., Dickson, A., and Bekker, A., eds., Environmental Change and Large Igneous Provinces: The Deadly Kiss of LIPs, American Geophysical Union.

Ernst, R. E. and Buchan, K. L., 1993, Paleomagnetism of the Abitibi dyke swarm, southern Superior Province, and implications for the Logan Loop: Canadian Journal of Earth Sciences, vol. 30, pp. 1886–1897, doi: 10.1139/e93-167.

Ernst, R. E. and Buchan, K. L., 2001, Large mafic magmatic events through time and links to mantle-plume heads: *In* Special Paper 352: Mantle plumes: their identification through time, Geological Society of America, pp. 483–575, doi: 10.1130/0-8137-2352-3.483.

Ernst, R. E., Hamilton, M. A., Söderlund, U., Hanes, J. A., Gladkochub, D. P., Okrugin, A. V., Kolotilina, T., Mekhonoshin, A. S., Bleeker, W., LeCheminant, A. N., Buchan, K. L., Chamberlain, K. R., and Didenko, A. N., 2016, Long-lived connection between southern Siberia and northern Laurentia in the Proterozoic: Nature Geoscience, vol. 9, pp. 464–469, doi: 10.1038/ngeo2700.

Ernst, R. E., Wingate, M. T. D., Buchan, K. L., and Li, Z. X., 2008, Global record of 1600-700 ma Large Igneous Provinces (LIPs): implications for the reconstruction of the proposed Nuna (Columbia) and Rodinia supercontinents: Precambrian Research, vol. 160, pp. 159–178, doi: 10.1016/j.precamres.2007.04.019.

Ernst, R. E. and Youbi, N., 2017, How large igneous provinces affect global climate, sometimes cause mass extinctions, and represent natural markers in the geological record: Palaeogeography, Palaeoclimatology, Palaeoecology, vol. 478, pp. 30–52, doi: 10.1016/j.palaeo.2017.03.014.

Evans, D., Pesonen, L., Eglington, B., Elming, S.-Å., Gong, Z., Li, Z.-X., McCausland, P., Meert, J., Mertanen, S., Pisarevsky, S., Pivarunas, A., Salminen, J., Swanson-Hysell, N., Torsvik, T., Trindade, R., Veikkolainen, T., and Zhang, S., 2021, An expanding list of reliable paleomagnetic poles for Precambrian tectonic reconstructions: *In* Pesonen, L., Salminen, J., Elming, S.-Å., Evans, D., and Veikkolainen, T., eds., Ancient Supercontinents and the Paleogeography of the Earth, Elsevier.

Evans, D. A., 2003, True polar wander and supercontinents: Tectonophysics, vol. 362, pp. 303–320, doi: 10.1016/s0040-1951(02)000642-x.

Evans, D. A., Veselovsky, R. V., Petrov, P. Y., Shatsillo, A. V., and Pavlov, V. E., 2016, Paleomagnetism of Mesoproterozoic margins of the Anabar Shield: A hypothesized billion-year partnership of Siberia and northern Laurentia: Precambrian Research, vol. 281, pp. 639–655, doi: 10.1016/j.precamres.2016.06.017.

Evans, D. A. D., 2006, Proterozoic low orbital obliquity and axial-dipolar geomagnetic field from evaporite palaeolatitudes: Nature, vol. 444, pp. 51–55, doi: 10.1038/nature05203.

Evans, D. A. D., Beukes, N. J., and Kirschvink, J. L., 1997, Low-latitude glaciation in the Palaeoproterozoic era: Nature, vol. 386, pp. 262–266, doi: 10.1038/386262a0.

Evans, D. A. D., Li, Z. X., Kirschvink, J. L., and Wingate, M. T. D., 2000, A high-quality mid-Neoproterozoic paleomagnetic pole from South China, with implications for ice ages and the breakup configuration of Rodinia: Precambrian Research, vol. 100, pp. 313–334, doi: 10.1016/S0301-9268(99)00079-0.

Eyster, A., Weiss, B. P., Karlstrom, K., and Macdonald, F. A., 2019, Paleomagnetism of the Chuar Group and evaluation of the late Tonian Laurentian apparent polar wander path with implications for the makeup and breakup of Rodinia: GSA Bulletin, doi: 10.1130/b32012.1.

Fairchild, I. J., Einsel, G., and Song, T., 1997, Possible seismic origin of molar tooth structures in Neoproterozoic carbonate ramp deposits, north China: Sedimentology, vol. 44, pp. 611–636, doi: 10.1046/j.1365-3091.1997.d01-40.x.

Fairchild, I. J., Spencer, A. M., Ali, D. O., Anderson, R. P., Anderton, R., Boomer, I., Dove, D., Evans, J. D., Hambrey, M. J., Howe, J., and et al., 2018, Tonian-Cryogenian boundary sections of Argyll, Scotland: Precambrian Research, vol. 319, pp. 37–64, doi: 10.1016/j.precamres.2017.09.020.

Fantle, M. S. and Higgins, J., 2014, The effects of diagenesis and dolomitization on Ca and Mg isotopes in marine platform carbonates: Implications for the geochemical cycles of Ca and Mg: Geochimica et Cosmochimica Acta, vol. 142, pp. 458–481, doi: 10.1016/j.gca.2014.07.025.

Farr, T. G., Rosen, P. A., Caro, E., Crippen, R., Duren, R., Hensley, S., Kobrick, M., Paller, M., Rodriguez, E., Roth, L., and et al., 2007, The shuttle radar topography mission: Reviews of Geophysics, vol. 45, pp. 1–33, doi: 10.1029/2005rg000183.

Fekete, B. M., Vörösmarty, C. J., and Grabs, W., 1999, Global, composite runoff fields based on observed river discharge and simulated water balances: Global Runoff Data Centre Koblenz, Germany.

Fisher, D., 1974, Some more remarks on polar wandering: Journal of Geophysical Research, vol. 79, pp. 4041–4045, doi: 10.1029/jb079i026p04041.

Florisbal, L. M., Heaman, L. M., de Assis Janasi, V., and de Fatima Bitencourt, M., 2014, Tectonic significance of the Florianópolis Dyke Swarm, Paraná-Etendeka Magmatic Province: A reappraisal based on precise U-Pb dating: Journal of Volcanology and Geothermal Research, vol. 289, pp. 140–150, doi: 10.1016/j.jvolgeores.2014.11.007.

Foster, G. L., Royer, D. L., and Lunt, D. J., 2017, Future climate forcing potentially without precedent in the last 420 million years: Nature Communications, vol. 8, pp. 1–8, doi: 10.1038/ncomms14845.

France-Lanord, C. and Derry, L. A., 1997, Organic carbon burial forcing of the carbon cycle from Himalayan erosion: Nature, vol. 390, pp. 65–67, doi: 10.1038/36324.

Fritz, H., Abdelsalam, M., Ali, K. A., Bingen, B., Collins, A. S., Fowler, A. R., Ghebreab, W., Hauzenberger, C. A., Johnson, P. R., Kusky, T. M., Macey, P., Muhongo, S., Stern, R. J., and Viola, G., 2013, Orogen styles in the East African Orogen: A review of the Neoproterozoic to Cambrian tectonic evolution: Journal of African Earth Sciences, vol. 86, pp. 65–106, doi: 10.1016/j.jafrearsci.2013.06.004.

Gabet, E. J. and Mudd, S. M., 2009, A theoretical model coupling chemical weathering rates with denudation rates: Geology, vol. 37, pp. 151–154, doi: 10.1130/G25270A.1.

Gaillardet, J., Dupré, B., Louvat, P., and Allègre, C. J., 1999, Global silicate weathering and CO_2 consumption rates deduced from the chemistry of large rivers: Chemical Geology, vol. 159, pp. 3–30, doi: 10.1016/S0009-2541(99)00031-5.

Gallet, Y., Pavlov, V., Halverson, G., and Hulot, G., 2012, Toward constraining the long-term reversing behavior of the geodynamo: A new "Maya" superchron ∼1 billion years ago from the magnetostratigraphy of the Kartochka Formation (southwestern Siberia): Earth and Planetary Science Letters, vol. 339-340, pp. 117–126, doi: 10.1016/j.epsl.2012.04.049.

Galy, V., France-Lanord, C., Beyssac, O., Faure, P., Kudrass, H., and Palhol, F., 2007, Efficient organic carbon burial in the Bengal fan sustained by the Himalayan erosional system: Nature, vol. 450, pp. 407–410, doi: 10.1038/nature06273.

Gao, L., Chen, J., Dai, C., Ding, X., Wang, X., Liu, Y., Wang, M., and Zhang, H., 2014, SHRIMP zircon U-Pb dating of tuff in Fanjingshan Group and Xiajiang Group from Guizhou and Hunan Provinces and its stratigraphic implications: Geological Bulletin of China, vol. 33, pp. 949–959.

Gao, L.-Z., Dai, C.-G., Ding, X.-Z., Wang, M., Liu, Y.-X., Wang, X.-H., and Chen, J.-S., 2011, SHRIMP U-Pb dating of intrusive alaskite in the Fanjigshan Group and alaskite basal conglomerates: constraints on the deposition of the Xiajiang Group: Geology in China, vol. 38.

Gao, L. Z., Dai, C. G., Liu, Y. X., Wang, M., Wang, X. H., Chen, J. S., and Ding, X. Z., 2010, Zircon SHRIMP U-Pb dating of the tuffaceous bed of Xiajiang Group in Guizhou Province and its stratigraphic implication: Geology in China, vol. 37, pp. 1071–1080.

Garland, C. R., 1980, Geology of the Adigrat area: *In* Ministry of Mines Memoir No. 1, p. 51.

Geng, Y.-S., 2015, Neoproterozoic Era of South China Craton: Springer Geology, pp. 263–301, doi: 10.1007/978-3-662-47885-1_7.

Geologic Survey Division, 1963, Geological map of the Philippines: Tech. rep., Bureau of Mines, in coordination with the Board of Technical Surveys and Maps.

Gerlach, T., 2011, Volcanic versus anthropogenic carbon dioxide: Eos, Transactions American Geophysical Union, vol. 92, pp. 201–202, doi: 10.1029/2011eo240001.

Gislason, S. R. and Oelkers, E. H., 2003, Mechanism, rates, and consequences of basaltic glass dissolution: II. an experimental study of the dissolution rates of basaltic glass as a function of pH and temperature: Geochimica et Cosmochimica Acta, vol. 67, pp. 3817–3832, doi: 10.1016/s0016-7037(03)00176-5.

Goddéris, Y. and Donnadieu, Y., 2017, A sink- or a source-driven carbon cycle at the geological timescale? Relative importance of palaeogeography versus solid Earth degassing rate in the Phanerozoic climatic evolution: Geological Magazine, vol. 156, pp. 355–365, doi: 10.1017/S0016756817001054.

Goddéris, Y., Donnadieu, Y., Carretier, S., Aretz, M., Dera, G., Macouin, M., and Regard, V., 2017a, Onset and ending of the late Palaeozoic ice age triggered by tectonically paced rock weathering: Nature Geoscience, vol. 10, pp. 382–386, doi: 10.1038/ngeo2931.

Goddéris, Y., Donnadieu, Y., Nédélec, A., Dupré, B., Dessert, C., Grard, A., Ramstein, G., and François, L. M., 2003, The Sturtian 'snowball' glaciation: fire and ice: Earth and Planetary Science Letters, vol. 211, pp. 1–12, doi: 10.1016/S0012-821X(03)00197-3.

Goddéris, Y., Hir, G. L., Macouin, M., Donnadieu, Y., Hubert-Théou, L., Dera, G., Aretz, M., Fluteau, F., Li, Z. X., and Halverson, G. P., 2017b, Paleogeographic forcing of the strontium isotopic cycle in the Neoproterozoic: Gondwana Research, vol. 42, pp. 151–162, doi: 10.1016/j.gr.2016.09.013.

Göğüş, O. H., 2015, Rifting and subsidence following lithospheric removal in continental back arcs: Geology, vol. 43, pp. 3–6, doi: 10.1130/g36305.1.

Gold, D., White, L., Gunawan, I., and BouDagher-Fadel, M., 2017, Relative sea-level change in western New Guinea recorded by regional biostratigraphic data: Marine and Petroleum Geology, vol. 86, pp. 1133–1158, doi: 10.1016/j.marpetgeo.2017.07.016.

Gold, T., 1955, Instability of the Earth's axis of rotation: Nature, vol. 175, pp. 526–529, doi: 10.1038/175526a0.

Goodge, J. W. and Fanning, C. M., 2010, Composition and age of the East Antarctic Shield in eastern Wilkes Land determined by proxy from Oligocene-Pleistocene glaciomarine sediment and Beacon Supergroup sandstones, Antarctica: Geological Society of America Bulletin, vol. 122, pp. 1135–1159, doi: 10.1130/b30079.1.

Goodge, J. W., Vervoort, J. D., Fanning, C. M., Brecke, D. M., Farmer, G. L., Williams, I. S., Myrow, P. M., and DePaolo, D. J., 2008, A positive test of East Antarctica-Laurentia juxtaposition within the Rodinia supercontinent: Science, vol. 321, pp. 235–240, doi: 10.1126/science.1159189.

Hailu, T., 1975, Geological map of Adi Arkay: Addis Ababa: Tech. rep., Geological Survey of Ethiopia.

Hall, R., 1997, Cenozoic plate tectonic reconstructions of SE Asia: Geological Society, London, Special Publications, vol. 126, pp. 11–23, doi: 10.1144/gsl.sp.1997.126.01.03.

Hall, R., 2001, Cenozoic reconstructions of SE Asia and the SW Pacific: changing pattern of land and sea: *In* Metcalfe, I., Smith, J., Morwood, M., and Davidson, I., eds., Faunal and Floral Migrations and Evolution in SE Asia-Australasia, Swets and Zeitlinger, pp. 35–56.

Hall, R., 2002, Cenozoic geological and plate tectonic evolution of SE Asia and the SW Pacific: computer-based reconstructions, model and animations: Journal of Asian Earth Sciences, vol. 20, pp. 353–431, doi: 10.1016/s1367-9120(01)00069-4.

Hall, R., 2009, The Eurasian SE Asian margin as a modern example of an accretionary orogen: Geological Society, London, Special Publications, vol. 318, pp. 351–372, doi: 10.1144/sp318.13.

Hall, R., 2013a, Contraction and extension in northern Borneo driven by subduction rollback: Journal of Asian Earth Sciences, vol. 76, pp. 399–411, doi: 10.1016/j.jseaes.2013.04.010.

Hall, R., 2013b, The palaeogeography of Sundaland and Wallacea since the Late Jurassic: Journal of Limnology, vol. 72, pp. 1–17, doi: 10.4081/jlimnol.2013.s2.e1.

Hall, R., 2017, Southeast Asia: New views of the geology of the Malay Archipelago: Annual Review of Earth and Planetary Sciences, vol. 45, pp. 331–358, doi: 10.1146/annurev-earth-063016-020633.

Hall, R., Audley-Charles, M. G., Banner, F. T., Hidayat, S., and Tobing, S. L., 1988, Basement rocks of the Halmahera region, eastern Indonesia: a Late Cretaceous–early Tertiary arc and fore-arc: Journal of the Geological Society, vol. 145, pp. 65–84, doi: 10.1144/gsjgs.145.1.0065.

Hall, R. and Nichols, G., 2002, Cenozoic sedimentation and tectonics in Borneo: climatic influences on orogenesis: Geological Society, London, Special Publications, vol. 191, pp. 5–22, doi: 10.1144/gsl.sp.2002.191.01.02.

Hall, R., van Hattum, M. W., and Spakman, W., 2008, Impact of India–Asia collision on SE Asia: The record in Borneo: Tectonophysics, vol. 451, pp. 366–389, doi: 10.1016/j.tecto.2007.11.058.

Halverson, G. P., 2006, A Neoproterozoic Chronology, Springer Netherlands, Dordrecht, pp. 231–271: doi: 10.1007/1-4020-5202-28.

Halverson, G. P., Dudás, F. Ö., Maloof, A. C., and Bowring, S. A., 2007a, Evolution of the $^{87}Sr/^{86}Sr$ composition of Neoproterozoic seawater: Palaeogeography, Palaeoclimatology, Palaeoecology, vol. 256, pp. 103–129, doi: 10.1016/j.palaeo.2007.02.028.

Halverson, G. P., Hoffman, P. F., Schrag, D. P., Maloof, A. C., and Rice, A. H. N., 2005, Toward a Neoproterozoic composite carbon-isotope record: GSA Bulletin, vol. 117, pp. 1181–1207, doi: 10.1130/B25630.1.

Halverson, G. P., Maloof, A. C., and Hoffman, P. F., 2004, The Marinoan glaciation (Neoproterozoic) in northeast Svalbard: Basin Research, vol. 16, pp. 297–324, doi: 10.1111/j.1365-2117.2004.00234.x.

Halverson, G. P., Maloof, A. C., Schrag, D. P., Dudás, F. Ö., and Hurtgen, M., 2007b, Stratigraphy and geochemistry of a ca 800 Ma negative carbon isotope interval in northeastern Svalbard: Chemical Geology, vol. 237, pp. 5–27, doi: 10.1016/j.chemgeo.2006.06.013.

Hamilton, W. B., 1979, Tectonics of the Indonesian region: Professional Paper, p. 345, doi: 10.3133/pp1078.

Hanson, R. E., Crowley, J. L., Bowring, S. A., Ramezani, J., Gose, W. A., Dalziel, I. W. D., Pancake, J. A., Seidel, E. K., Blenkinsop, T. G., and Mukwakwami, J., 2004, Coeval large-scale magmatism in the Kalahari and Laurentian cratons during Rodinia assembly: Science, vol. 304, pp. 1126–1129, doi: 10.1126/science.1096329.

Harlan, S. S., Heaman, L., LeCheminant, A. N., and Premo, W. R., 2003, Gunbarrel mafic magmatic event: A key 780 Ma time marker for Rodinia plate reconstructions: Geology, vol. 31, pp. 1053–1056, doi: 10.1130/G19944.1.

Harrington, L., Zahirovic, S., Flament, N., and Müller, R. D., 2017, The role of deep Earth dynamics in driving the flooding and emergence of New Guinea since the Jurassic: Earth and Planetary Science Letters, vol. 479, pp. 273–283, doi: 10.1016/j.epsl.2017.09.039.

Harris, I., Jones, P., Osborn, T., and Lister, D., 2013, Updated high-resolution grids of monthly climatic observations - the CRU TS3.10 dataset: International Journal of Climatology, vol. 34, pp. 623–642, doi: 10.1002/joc.3711.

Harris, R., 2006, Rise and fall of the Eastern Great Indonesian arc recorded by the assembly, dispersion and accretion of the Banda Terrane, Timor: Gondwana Research, vol. 10, pp. 207–231, doi: 10.1016/j.gr.2006.05.010.

Hartmann, J., Jansen, N., Dürr, H. H., Kempe, S., and Köhler, P., 2009, Global CO_2-consumption by chemical weathering: What is the contribution of highly active weathering regions?: Global and Planetary Change, vol. 69, pp. 185–194, doi: 10.1016/j.gloplacha.2009.07.007.

Hartmann, J. and Moosdorf, N., 2012, The new global lithological map database GLiM: A representation of rock properties at the Earth surface: Geochemistry, Geophysics, Geosystems, vol. 13, pp. 1–37, doi: 10.1029/2012GC004370.

Hartmann, J., Moosdorf, N., Lauerwald, R., Hinderer, M., and West, A. J., 2014, Global chemical weathering and associated P-release - the role of lithology, temperature and soil properties: Chemical Geology, vol. 363, pp. 145–163, doi: 10.1016/j.chemgeo.2013.10.025.

Haug, G. H., Ganopolski, A., Sigman, D. M., Rosell-Mele, A., Swann, G. E. A., Tiedemann, R., Jaccard, S. L., Bollmann, J., Maslin, M. A., Leng, M. J., and Eglinton, G., 2005, North Pacific seasonality and the glaciation of North America 2.7 million years ago: Nature, vol. 433, pp. 821–825, doi: 10.1038/nature03332.

Haug, G. H. and Tiedemann, R., 1998, Effect of the formation of the Isthmus of Panama on Atlantic Ocean thermohaline circulation: Nature, vol. 393, pp. 673–676, doi: 10.1038/31447.

Heaman, L. M., LeCheminant, A. N., and Rainbird, R. H., 1992, Nature and timing of Franklin igneous events, Canada: implications for a Late Proterozoic mantle plume and

the break-up of Laurentia: Earth and Planetary Science Letters, vol. 109, pp. 117–131, doi: 10.1016/0012-821X(92)90078-A.

Heimsath, A. M., Dietrich, W. E., Nishiizumi, K., and Finkel, R. C., 1997, The soil production function and landscape equilibrium: Nature, vol. 388, pp. 358–361, doi: 10.1038/41056.

Hennig, J., Breitfeld, H. T., Hall, R., and Nugraha, A. S., 2017a, The Mesozoic tectono-magmatic evolution at the Paleo-Pacific subduction zone in West Borneo: Gondwana Research, vol. 48, pp. 292–310, doi: 10.1016/j.gr.2017.05.001.

Hennig, J., Hall, R., and Armstrong, R. A., 2016, U-Pb zircon geochronology of rocks from west Central Sulawesi, Indonesia: Extension-related metamorphism and magmatism during the early stages of mountain building: Gondwana Research, vol. 32, pp. 41–63, doi: 10.1016/j.gr.2014.12.012.

Hennig, J., Hall, R., Forster, M. A., Kohn, B. P., and Lister, G. S., 2017b, Rapid cooling and exhumation as a consequence of extension and crustal thinning: Inferences from the Late Miocene to Pliocene Palu Metamorphic Complex, Sulawesi, Indonesia: Tectonophysics, vol. 712-713, pp. 600–622, doi: 10.1016/j.tecto.2017.06.025.

Higgins, J. and Schrag, D., 2012, Records of Neogene seawater chemistry and diagenesis in deep-sea carbonate sediments and pore fluids: Earth and Planetary Science Letters, vol. 357-358, pp. 386–396, doi: 10.1016/j.epsl.2012.08.030.

Hildebrand, R. S., 1988, Implications of ash dispersal for tectonic models with an example from Wopmay orogen: Geology, vol. 16, pp. 1089–1091, doi: 10.1130/0091-7613(1988)016⟨1089:ioadft⟩2.3.co;2.

Hill, K. C. and Gleadow, A. J. W., 1989, Uplift and thermal history of the Papuan Fold Belt, Papua New Guinea: Apatite fission track analysis: Australian Journal of Earth Sciences, vol. 36, pp. 515–539, doi: 10.1080/08120098908729507.

Hilton, R. G., Gaillardet, J., Calmels, D., and Birck, J.-L., 2014, Geological respiration of a mountain belt revealed by the trace element rhenium: Earth and Planetary Science Letters, vol. 403, pp. 27–36, doi: 10.1016/j.epsl.2014.06.021.

Hodgskiss, M. S. W., Kunzmann, M., Poirier, A., and Halverson, G. P., 2018, The role of microbial iron reduction in the formation of Proterozoic molar tooth structures: Earth and Planetary Science Letters, vol. 482, pp. 1–11, doi: 10.1016/j.epsl.2017.10.037.

Hoffman, P. F., 1991, Did the breakout of Laurentia turn Gondwanaland inside-out?: Science, vol. 252, pp. 1409–1412, doi: 10.1126/science.252.5011.1409.

Hoffman, P. F., Abbot, D. S., Ashkenazy, Y., Benn, D. I., Brocks, J. J., Cohen, P. A., Cox, G. M., Creveling, J. R., Donnadieu, Y., Erwin, D. H., Fairchild, I. J., Ferreira, D., Goodman, J. C., Halverson, G. P., Jansen, M. F., Le Hir, G., Love, G. D., Macdonald, F. A., Maloof, A. C., Partin, C. A., Ramstein, G., Rose, B. E. J., Rose, C. V., Sadler, P. M., Tziperman, E., Voigt, A., and Warren, S. G., 2017, Snowball Earth climate dynamics and Cryogenian geology-geobiology: Science Advances, vol. 3, doi: 10.1126/sciadv.1600983.

Hoffman, P. F., Halverson, G. P., Domack, E. W., Maloof, A. C., Swanson-Hysell, N. L., and Cox, G. M., 2012, Cryogenian glaciations on the southern tropical paleomargin of Laurentia (NE Svalbard and East Greenland), and a primary origin for the upper Russoya (Islay) carbon isotope excursion: Precambrian Research, vol. 206-207, pp. 137–158, doi: 10.1016/j.precamres.2012.02.018.

Hoffman, P. F., Kaufman, A. J., Halverson, G. P., and Schrag, D. P., 1998, A Neoproterozoic Snowball Earth: Science, vol. 281, pp. 1342–1346, doi: 10.1126/science.281.5381.1342.

Hoffman, P. F. and Li, Z.-X., 2009, A palaeogeographic context for Neoproterozoic glaciation: Palaeogeography, Palaeoclimatology, Palaeoecology, vol. 277, pp. 158–172, doi: 10.1016/j.palaeo.2009.03.013.

Hoffman, P. F., Macdonald, F. A., and Halverson, G. P., 2011, Chemical sediments associated with Neoproterozoic glaciation: iron formation, cap carbonate, barite and phosphorite: *In* Arnaud, E., Halverson, G. P., and Shields-Zhou, G. A., eds., The Geological Record of Neoproterozoic Glaciations, Geological Society of London, vol. 36, chap. 5, pp. 67–80, doi: 10.1144/M36.5.

Hoffman, P. F. and Schrag, D. P., 2002, The snowball Earth hypothesis: testing the limits of global change: Terra Nova, vol. 14, pp. 129–155, doi: 10.1046/j.1365-3121.2002.00408.x.

Hoffmann, K.-H., Condon, D. ., Bowring, S. A., and Crowley, J. L., 2004, U-Pb zircon date from the Neoproterozoic Ghaub Formation, Namibia: Constraints on Marinoan glaciation: Geology, vol. 32, pp. 817–820, doi: 10.1130/G20519.1.

Hollanda, M. H. B. M., Archanjo, C. J., Renne, P. R., Ngonge, D. E., Castro, D. L., Oliveira, D. C., and Macêdo Filho, A. A., 2016, Evidence of an Early Cretaceous giant dyke swarm in northeast Brazil (South America): A geodynamic overview: Acta Geologica Sinica - English Edition, vol. 90, pp. 109–110, doi: 10.1111/1755-6724.12915.

Husson, J. M., Higgins, J. A., Maloof, A. C., and Schoene, B., 2015a, Ca and Mg isotope constraints on the origin of Earth's deepest C excursion: Geochimica et Cosmochimica Acta, vol. 160, pp. 243–266, doi: 10.1016/j.gca.2015.03.012.

Husson, J. M., Maloof, A. C., and Schoene, B., 2012, A syn-depositional age for Earth's deepest δ^{13}C excursion required by isotope conglomerate tests: Terra Nova, vol. 24, pp. 318–325, doi: 10.1111/j.1365-3121.2012.01067.x.

Husson, J. M., Maloof, A. C., Schoene, B., Chen, C. Y., and Higgins, J. A., 2015b, Stratigraphic expression of Earth's deepest $\delta^{13}C$ excursion in the Wonoka Formation of South Australia: American Journal of Science, vol. 315, pp. 1–45, doi: 10.2475/01.2015.01.

Hutchison, C. S., 1996, The "Rajang accretionary prism" and "Lupar Line" problem of Borneo: Geological Society, London, Special Publications, vol. 106, pp. 247–261, doi: 10.1144/gsl.sp.1996.106.01.16.

Ibarra, D. E., Caves, J. K., Moon, S., Thomas, D. L., Hartmann, J., Chamberlain, C. P., and Maher, K., 2016, Differential weathering of basaltic and granitic catchments from concentration-discharge relationships: Geochimica et Cosmochimica Acta, vol. 190, pp. 265 – 293, doi: 10.1016/j.gca.2016.07.006.

Ilao, K. A., Morley, C. K., and Aurelio, M. A., 2018, 3D seismic investigation of the structural and stratigraphic characteristics of the Pagasa Wedge, Southwest Palawan Basin, Philippines, and their tectonic implications: Journal of Asian Earth Sciences, vol. 154, pp. 213–237, doi: 10.1016/j.jseaes.2017.12.017.

Isson, T. T. and Planavsky, N. J., 2018, Reverse weathering as a long-term stabilizer of marine pH and planetary climate: Nature, vol. 560, pp. 471–475, doi: 10.1038/s41586-018-0408-4.

Jackson, M. and Swanson-Hysell, N. L., 2012, Rock magnetism of remagnetized carbonate rocks: another look: Geological Society, London, Special Publications, vol. 371, pp. 229–251, doi: 10.1144/sp371.3.

Jacobsen, S. B. and Kaufman, A. J., 1999, The Sr, C and O isotopic evolution of Neoproterozoic seawater: Chemical Geology, vol. 161, pp. 37–57, doi: 10.1016/S0009-2541(99)00080-7.

Jacobson, A. D., Blum, J. D., and Walter, L. M., 2002, Reconciling the elemental and Sr isotope composition of Himalayan weathering fluxes: insights from the carbonate geochemistry of stream waters: Geochimica et Cosmochimica Acta, vol. 66, pp. 3417–3429, doi: 10.1016/s0016-7037(02)00951-1.

Jaffey, A. H., Flynn, K. F., Glendenin, L. E., Bentley, W. C., and Essling, A. M., 1971, Precision measurement of half-lives and specific activities of ^{235}U and ^{238}U: Phys. Rev. C, vol. 4, pp. 1889–1906, doi: 10.1103/PhysRevC.4.1889.

Jagoutz, O., Macdonald, F. A., and Royden, L., 2016, Low-latitude arc-continent collision as a driver for global cooling: Proceedings of the National Academy of Sciences, vol. 113, pp. 4935–4940, doi: 10.1073/pnas.1523667113.

Ji, S., Nie, J., Lechler, A., Huntington, K. W., Heitmann, E. O., and Breecker, D. O., 2018, A symmetrical CO_2 peak and asymmetrical climate change during the middle Miocene:

Earth and Planetary Science Letters, vol. 499, pp. 134–144, doi: 10.1016/j.epsl.2018.07.011.

Jiang, Z., Liu, Q., Dekkers, M. J., Tauxe, L., Qin, H., Barrón, V., and Torrent, J., 2015, Acquisition of chemical remanent magnetization during experimental ferrihydrite-hematite conversion in Earth-like magnetic field-implications for paleomagnetic studies of red beds: Earth and Planetary Science Letters, vol. 428, pp. 1 – 10, doi: 10.1016/j.epsl.2015.07.024.

Jing, X., Yang, Z., Evans, D. A., Tong, Y., Xu, Y., and Wang, H., 2019, A pan-latitudinal Rodinia in the Tonian true polar wander frame: Earth and Planetary Science Letters, pp. 1–14, doi: 10.1016/j.epsl.2019.115880.

Jing, X.-q., Yang, Z., Tong, Y., and Han, Z., 2015, A revised paleomagnetic pole from the mid-Neoproterozoic Liantuo Formation in the Yangtze block and its paleogeographic implications: Precambrian Research, vol. 268, pp. 194–211, doi: 10.1016/j.precamres.2015.07.007.

Johansson, L., Zahirovic, S., and Müller, R. D., 2018, The interplay between the eruption and weathering of large igneous provinces and the deep-time carbon cycle: Geophysical Research Letters, vol. 45, doi: 10.1029/2017GL076691.

Johnson, P. R., 2014, An expanding Arabian-Nubian Shield geochronologic and isotopic dataset: defining limits and confirming the tectonic setting of a Neoproterozoic accretionary orogen: The Open Geology Journal, vol. 8, pp. 3–33, doi: 10.2174/1874262901408010003.

Johnson, P. R., Abdelsalam, M. G., and Stern, R. J., 2003, The Bi'r Umq-Nakasib Suture Zone in the Arabian-Nubian Shield: a key to understanding crustal growth in the East African Orogen: Gondwana Research, vol. 6, pp. 523–530, doi: 10.1016/S1342-937X(05)71003-0.

Johnson, P. R., Andresen, A., Collins, A. S., Fowler, A. R., Fritz, H., Ghebreab, W., Kusky, T., and Stern, R. J., 2011, Late Cryogenian-Ediacaran history of the Arabian-Nubian Shield: A review of depositional, plutonic, structural, and tectonic events in the closing stages of the northern East African Orogen: Journal of African Earth Sciences, vol. 61, pp. 167–232, doi: 10.1016/j.jafrearsci.2011.07.003.

Johnson, P. R. and Woldehaimanot, B., 2003, Development of the Arabian-Nubian Shield: perspectives on accretion and deformation in the northern East African Orogen and the assembly of Gondwana: Geological Society, London, Special Publications, vol. 206, pp. 289–325, doi: 10.1144/GSL.SP.2003.206.01.15.

Jones, D. S., Maloof, A. C., Hurtgen, M. T., Rainbird, R. H., and Schrag, D. P., 2010, Regional and global chemostratigraphic correlation of the early Neoproterozoic Shaler Supergroup, Victoria Island, Northwestern Canada: Precambrian Research, vol. 181, pp. 43–63, doi: 10.1016/j.precamres.2010.05.012.

Jourdan, F., Hodges, K., Sell, B., Schaltegger, U., Wingate, M., Evins, L., Söderlund, U., Haines, P., Phillips, D., and Blenkinsop, T., 2014, High-precision dating of the Kalkarindji large igneous province, Australia, and synchrony with the Early-Middle Cambrian (Stage 4-5) extinction: Geology, vol. 42, pp. 543–546, doi: 10.1130/g35434.1.

Kadarusman, A., Miyashita, S., Maruyama, S., Parkinson, C. D., and Ishikawa, A., 2004, Petrology, geochemistry and paleogeographic reconstruction of the East Sulawesi Ophiolite, Indonesia: Tectonophysics, vol. 392, pp. 55–83, doi: 10.1016/j.tecto.2004.04.008.

Kalnay, E., Kanamitsu, M., Kistler, R., Collins, W., Deaven, D., Gandin, L., Iredell, M., Saha, S., White, G., Woollen, J., Zhu, Y., Chelliah, M., Ebisuzaki, W., Higgins, W., Janowiak, J., Mo, K. C., Ropelewski, C., Wang, J., Leetmaa, A., Reynolds, R., Jenne, R., and Joseph, D., 1996, The NCEP/NCAR 40-year reanalysis project: Bulletin of the American Meteorological Society, vol. 77, pp. 437–471, doi: 10.1175/1520-0477(1996)077⟨0437:tnyrp⟩2.0.co;2.

Kao, S.-J., Hilton, R. G., Selvaraj, K., Dai, M., Zehetner, F., Huang, J.-C., Hsu, S.-C., Sparkes, R., Liu, J. T., Lee, T.-Y., and et al., 2014, Preservation of terrestrial organic carbon in marine sediments offshore Taiwan: mountain building and atmospheric carbon dioxide sequestration: Earth Surface Dynamics, vol. 2, pp. 127–139, doi: 10.5194/esurf-2-127-2014.

Kasbohm, J. and Schoene, B., 2018, Rapid eruption of the Columbia River flood basalt and correlation with the mid-Miocene climate optimum: Science Advances, vol. 4, pp. 1–8, doi: 10.1126/sciadv.aat8223.

Kastens, K., Mascle, J., Auroux, C., Bonatti, E., Broglia, C., Channell, J., Curzi, P., Emeis, K.-C., Glaçon, G., Hasegawa, S., Hieke, W., Mascle, G., McCoy, F., McKenzie, J., Mendelson, J., Müller, C., Réhault, J.-P., Robertson, A., Sartori, R., Sprovieri, R., and Torii, M., 1988, ODP Leg 107 in the Tyrrhenian Sea: insights into passive margin and back-arc basin evolution: Geological Society of America Bulletin, vol. 100, pp. 1140–1156, doi: 10.1130/0016-7606(1988)100⟨1140:OLITTS⟩2.3.CO;2.

Katili, J. A., 1978, Past and present geotectonic position of Sulawesi, Indonesia: Tectonophysics, vol. 45, pp. 289–322, doi: 10.1016/0040-1951(78)90166-x.

Katz, B., Elmore, R., and Engel, M., 1998, Authigenesis of magnetite in organic-rich sediment next to a dike: implications for thermoviscous and chemical remagnetizations: Earth and Planetary Science Letters, vol. 163, pp. 221–234, doi: 10.1016/s0012-821x(98)00189-7.

Kaufman, A. J., Knoll, A. H., and Narbonne, G. M., 1997, Isotopes, ice ages, and terminal Proterozoic earth history: Proceedings of the National Academy of Sciences, vol. 94, pp. 6600–6605, doi: 10.1073/pnas.94.13.6600.

Kendall, B., Creaser, R. A., and Selby, D., 2006, Re-Os geochronology of postglacial black shales in Australia: Constraints on the timing of "Sturtian" glaciation: Geology, vol. 34, pp. 729–732, doi: 10.1130/G22775.1.

Kennedy, M. J., Runnegar, B., Prave, A. R., Hoffmann, K.-H., and Arthur, M. A., 1998, Two or four Neoproterozoic glaciations?: Geology, vol. 26, pp. 1059–1063, doi: 10.1130/0091-7613(1998)026⟨1059:TOFNG⟩2.3.CO;2.

Kent, D. V., Kjarsgaard, B. A., Gee, J. S., Muttoni, G., and Heaman, L. M., 2015, Tracking the Late Jurassic apparent (or true) polar shift in U-Pb-dated kimberlites from cratonic North America (Superior Province of Canada): Geochemistry, Geophysics, Geosystems, vol. 16, pp. 983–994, doi: 10.1002/2015GC005734.

Kent, D. V. and Muttoni, G., 2008, Equatorial convergence of india and early Cenozoic climate trends: Proceedings of the National Academy of Sciences, vol. 105, pp. 16,065–16,070, doi: 10.1073/pnas.0805382105.

Kent, D. V. and Muttoni, G., 2013, Modulation of Late Cretaceous and Cenozoic climate by variable drawdown of atmospheric pCO_2 from weathering of basaltic provinces on continents drifting through the equatorial humid belt: Climate of the Past, vol. 9, pp. 525–546, doi: 10.5194/cp-9-525-2013.

Kessler, F.-L. and Jong, J., 2015, Tertiary uplift and the Miocene evolution of the NW Borneo Shelf margin: Berita Sedimentologi - Indonesian Journal of Sedimentary Geology, vol. 33, pp. 21–46.

Khudoley, A. K., Prokopiev, A. V., Chamberlain, K. R., Ernst, R. E., Jowitt, S. M., Malyshev, S. V., Zaitsev, A. I., Kropachev, A. P., and Koroleva, O. V., 2013, Early Paleozoic mafic magmatic events on the eastern margin of the Siberian craton: Lithos, vol. 174, pp. 44–56, doi: 10.1016/j.lithos.2012.08.008.

King, R. F., 1955, The remanent magnetism of artificially deposited sediments: Geophysical Journal International, vol. 7, pp. 115–134, doi: 10.1111/j.1365-246x.1955.tb06558.x.

Kingsbury, C. G., Kamo, S. L., Ernst, R. E., Söderlund, U., and Cousens, B. L., 2018, U-Pb geochronology of the plumbing system associated with the Late Cretaceous Strand Fiord Formation, Axel Heiberg Island, Canada: part of the 130-90 Ma High Arctic large igneous province: Journal of Geodynamics, vol. 118, pp. 106–117, doi: 10.1016/j.jog.2017.11.001.

Kirschvink, J. L., 1992, Late Proterozoic low-latitude global glaciation: The Snowball Earth: *In* Schopf, J., Klein, C., and Des Maris, D., eds., The Proterozoic Biosphere: A Multidisciplinary Study, Cambridge University Press, pp. 51–52.

Kirschvink, J. L., 1997, Evidence for a large-scale reorganization of early Cambrian continental masses by inertial interchange true polar wander: Science, vol. 277, pp. 541–545, doi: 10.1126/science.277.5325.541.

Kirschvink, J. L., Kopp, R. E., Raub, T. D., Baumgartner, C. T., and Holt, J. W., 2008, Rapid, precise, and high-sensitivity acquisition of paleomagnetic and rock-magnetic data: Development of a low-noise automatic sample changing system for superconducting rock magnetometers: Geochemistry, Geophysics, Geosystems, vol. 9, pp. 1–18, doi: 10.1029/2007gc001856.

Knauss, K. G., Nguyen, S. N., and Weed, H. C., 1993, Diopside dissolution kinetics as a function of pH, CO_2, temperature, and time: Geochimica et Cosmochimica Acta, vol. 57, pp. 285–294, doi: 10.1016/0016-7037(93)90431-u.

Knoll, A. H., Javaux, E. J., Hewitt, D., and Cohen, P., 2006, Eukaryotic organisms in Proterozoic oceans: Philosophical Transactions of the Royal Society of London B: Biological Sciences, vol. 361, pp. 1023–1038, doi: 10.1098/rstb.2006.1843.

Kozdrój, W., Kennedy, A. K., Johnson, P. R., Ziółkowska-Kozdrój, M., and Kadi, K., 2017, Geochronology in the southern Midyan terrane: a review of constraints on the timing of magmatic pulses and tectonic evolution in a northwestern part of the Arabian Shield: International Geology Review, vol. 60, pp. 1290–1319, doi: 10.1080/00206814.2017.1385425.

Krogh, T. E., Corfu, F., Davis, D. W., Dunning, G. R., Heaman, L. M., Kamo, S. L., Machado, N., Greenough, J. D., and Nakamura, E., 1987, Precise U-Pb isotopic ages of diabase dykes and mafic to ultra mafic rocks using trace amounts of baddeleyite and zircon: *In* Halls, H. C. and Fahrig, W. F., eds., Mafic dyke swarms, Geological Association of Canada, pp. 147–152.

Kump, L. R. and Arthur, M. A., 1997, Global Chemical Erosion during the Cenozoic: Weatherability Balances the Budgets, Springer US, Boston, MA, pp. 399–426: doi: 10.1007/978-1-4615-5935-1_18.

Kump, L. R., Brantley, S. L., and Arthur, M. A., 2000, Chemical weathering, atmospheric CO_2, and climate: Annual Review of Earth and Planetary Sciences, vol. 28, pp. 611–667, doi: 10.1146/annurev.earth.28.1.611.

Küster, D., Liégeois, J.-P., Matukov, D., Sergeev, S., and Lucassen, F., 2008, Zircon geochronology and Sr, Nd, Pb isotope geochemistry of granitoids from Bayuda Desert and Sabaloka (Sudan): evidence for a Bayudian event (920-900 Ma) preceding the Pan-African orogenic cycle (860-590 Ma) at the eastern boundary of the Saharan Metacraton: Precambrian Research, vol. 164, pp. 16–39, doi: 10.1016/j.precamres.2008.03.003.

Kuznetsov, A. B., Semikhatov, M. A., Maslov, A. V., Gorokhov, I. M., Prasolov, E. M., Krupenin, M. T., and Kislova, I. V., 2006, New data on Sr-and C-isotopic chemostratigraphy of the Upper Riphean type section (Southern Urals): Stratigraphy and Geological Correlation, vol. 14, pp. 602–628, doi: 10.1134/S0869593806060025.

Lague, D., 2013, The stream power river incision model: evidence, theory and beyond: Earth Surface Processes and Landforms, vol. 39, pp. 38–61, doi: 10.1002/esp.3462.

Lan, Z., Huyskens, M. H., Lu, K., Li, X.-H., Zhang, G., Lu, D., and Yin, Q.-Z., 2020, Toward refining the onset age of Sturtian glaciation in South China: Precambrian Research, vol. 338, p. 105,555, doi: 10.1016/j.precamres.2019.105555.

Lan, Z., Li, X., Zhu, M., Chen, Z.-Q., Zhang, Q., Li, Q., Lu, D., Liu, Y., and Tang, G., 2014, A rapid and synchronous initiation of the wide spread Cryogenian glaciations: Precambrian Research, vol. 255, pp. 401–411, doi: 10.1016/j.precamres.2014.10.015.

Lan, Z., Li, X.-H., Zhu, M., Zhang, Q., and Li, Q.-L., 2015, Revisiting the Liantuo Formation in Yangtze Block, South China: SIMS U-Pb zircon age constraints and regional and global significance: Precambrian Research, vol. 263, pp. 123–141, doi: 10.1016/j.precamres.2015.03.012.

Larsen, L. M., Pedersen, A. K., Tegner, C., Duncan, R. A., Hald, N., and Larsen, J. G., 2015, Age of Tertiary volcanic rocks on the West Greenland continental margin: volcanic evolution and event correlation to other parts of the North Atlantic Igneous Province: Geological Magazine, vol. 153, pp. 487–511, doi: 10.1017/s0016756815000515.

Lasaga, A. C., Soler, J. M., Ganor, J., Burch, T. E., and Nagy, K. L., 1994, Chemical weathering rate laws and global geochemical cycles: Geochimica et Cosmochimica Acta, vol. 58, pp. 2361–2386, doi: 10.1016/0016-7037(94)90016-7.

Le Heron, D. P., Busfield, M. E., and Prave, A. R., 2014, Neoproterozoic ice sheets and olistoliths: multiple glacial cycles in the Kingston Peak Formation, California: Journal of the Geological Society, vol. 171, p. 525, doi: 10.1144/jgs2013-130.

LeCheminant, A. N. and Heaman, L. M., 1989, Mackenzie igneous events, Canada: Middle Proterozoic hotspot magmatism associated with ocean opening: Earth and Planetary Science Letters, vol. 96, pp. 38–48, doi: 10.1016/0012-821X(89)90122-2.

Lécuyer, C., 2016, Seawater residence times of some elements of geochemical interest and the salinity of the oceans: Bulletin de la Société Géologique de France, vol. 187, pp. 245–260, doi: 10.2113/gssgfbull.187.6.245.

Li, G., Hartmann, J., Derry, L. A., West, A. J., You, C.-F., Long, X., Zhan, T., Li, L., Li, G., Qiu, W., Li, T., Liu, L., Chen, Y., Ji, J., Zhao, L., and Chen, J., 2016a, Temperature dependence of basalt weathering: Earth and Planetary Science Letters, vol. 443, pp. 59–69, doi: 10.1016/j.epsl.2016.03.015.

Li, J., Dong, S., Zhang, Y., Zhao, G., Johnston, S. T., Cui, J., and Xin, Y., 2016b, New insights into Phanerozoic tectonics of south China: Part 1, polyphase deformation in the Jiuling and Lianyunshan domains of the central Jiangnan Orogen: Journal of Geophysical Research: Solid Earth, vol. 121, pp. 3048–3080, doi: 10.1002/2015jb012778.

Li, L., Lin, S., Xing, G., Davis, D. W., Jiang, Y., Davis, W., and Zhang, Y., 2016c, Ca. 830 Ma back-arc type volcanic rocks in the eastern part of the Jiangnan orogen: Implications for the Neoproterozoic tectonic evolution of South China Block: Precambrian Research, vol. 275, pp. 209–224, doi: 10.1016/j.precamres.2016.01.016.

Li, X.-H., Li, W.-X., Li, Z.-X., Lo, C.-H., Wang, J., Ye, M.-F., and Yang, Y.-H., 2009, Amalgamation between the Yangtze and Cathaysia Blocks in South China: Constraints from SHRIMP U–Pb zircon ages, geochemistry and Nd–Hf isotopes of the Shuangxiwu volcanic rocks: Precambrian Research, vol. 174, pp. 117–128, doi: 10.1016/j.precamres.2009.07.004.

Li, Z., Li, X., Kinny, P., Wang, J., Zhang, S., and Zhou, H., 2003, Geochronology of Neoproterozoic syn-rift magmatism in the Yangtze Craton, South China and correlations with other continents: evidence for a mantle superplume that broke up Rodinia: Precambrian Research, vol. 122, pp. 85–109, doi: 10.1016/S0301-9268(02)00208-5.

Li, Z. X., Bogdanova, S. V., Collins, A. S., Davidson, A., Waele, B. D., Ernst, R. E., Fitzsimons, I. C. W., Fuck, R. A., Gladkochub, D. P., Jacobs, J., Karlstrom, K. E., Lu, S., Natapov, L. M., Pease, V., Pisarevsky, S. A., Thrane, K., and Vernikovsky, V., 2008, Assembly, configuration, and break-up history of Rodinia: a synthesis: Precambrian Research, vol. 160, pp. 179–210, doi: 10.1016/j.precamres.2007.04.021.

Li, Z.-X., Evans, D. A., and Halverson, G. P., 2013, Neoproterozoic glaciations in a revised global palaeogeography from the breakup of Rodinia to the assembly of Gondwanaland: Sedimentary Geology, vol. 294, pp. 219–232, doi: 10.1016/j.sedgeo.2013.05.016.

Li, Z.-X. and Evans, D. A. D., 2011, Late Neoproterozoic 40° intraplate rotation within Australia allows for a tighter-fitting and longer-lasting Rodinia: Geology, vol. 39, pp. 39–42, doi: 10.1130/g31461.1.

Li, Z. X., Evans, D. A. D., and Zhang, S., 2004, A 90° spin on Rodinia: possible causal links between the Neoproterozoic supercontinent, superplume, true polar wander and low-latitude glaciation: Earth and Planetary Science Letters, vol. 220, pp. 409–421, doi: 10.1016/S0012-821X(04)00064-0.

Li, Z.-X., Li, X.-h., Zhou, H., and Kinny, P. D., 2002, Grenvillian continental collision in south China: New SHRIMP U-Pb zircon results and implications for the configuration of Rodinia: Geology, vol. 30, pp. 163–166, doi: 10.1130/0091-7613(2002)030⟨0163:gccisc⟩2.0.co;2.

Li, Z.-X., Zhang, L., and Powell, C. M., 1995, South China in Rodinia: Part of the missing link between Australia–East Antarctica and Laurentia?: Geology, vol. 23, pp. 407–410, doi: 10.1130/0091-7613(1995)023⟨0407:scirpo⟩2.3.co;2.

Lin, M., Peng, S., Jiang, X., Polat, A., Kusky, T., Wang, Q., and Deng, H., 2016, Geochemistry, petrogenesis and tectonic setting of Neoproterozoic mafic-ultramafic rocks from the western Jiangnan orogen, South China: Gondwana Research, vol. 35, pp. 338–356, doi: 10.1016/j.gr.2015.05.015.

Loewen, M. W., Duncan, R. A., Kent, A. J. R., and Krawl, K., 2013, Prolonged plume volcanism in the Caribbean large igneous province: New insights from Curaçao and Haiti: Geochemistry, Geophysics, Geosystems, vol. 14, pp. 4241–4259, doi: 10.1002/ggge.20273.

Long, S., McQuarrie, N., Tobgay, T., and Grujic, D., 2011, Geometry and crustal shortening of the Himalayan fold-thrust belt, eastern and central Bhutan: Geological Society of America Bulletin, vol. 123, pp. 1427–1447, doi: 10.1130/b30203.1.

Lowenstein, T. K., 2001, Oscillations in Phanerozoic seawater chemistry: Evidence from fluid inclusions: Science, vol. 294, pp. 1086–1088, doi: 10.1126/science.1064280.

Ma, G., Li, H., Zhang, Z., et al., 1984, An investigation of the age limits of the Sinian System in South China: Bulletin of Yichang Institute of Geology and Mineral Resources, vol. 8, pp. 1–29.

Ma, H., Wang, Y., Huang, Y., and Xie, Y., 2019, Three-stage Mesozoic intracontinental tectonic evolution of South China recorded in an overprinted basin: evidence from stratigraphy and detrital zircon U-Pb dating: Geological Magazine, vol. 156, pp. 2085–2103, doi: 10.1017/s0016756819000451.

Macdonald, F. A., Schmitz, M. D., Crowley, J. L., Roots, C. F., Jones, D. S., Maloof, A. C., Strauss, J. V., Cohen, P. A., Johnston, D. T., and Schrag, D. P., 2010, Calibrating the Cryogenian: Science, vol. 327, pp. 1241–1243, doi: 10.1126/science.1183325.

Macdonald, F. A., Schmitz, M. D., Strauss, J. V., Halverson, G. P., Gibson, T. M., Eyster, A., Cox, G., Mamrol, P., and Crowley, J. L., 2018, Cryogenian of Yukon: Precambrian Research, vol. 319, pp. 114–143, doi: 10.1016/j.precamres.2017.08.015.

Macdonald, F. A., Swanson-Hysell, N. L., Park, Y., Lisiecki, L., and Jagoutz, O., 2019, Arc-continent collisions in the tropics set Earth's climate state: Science, vol. 364, pp. 181–184, doi: 10.1126/science.aav5300.

Macdonald, F. A. and Wordsworth, R., 2017, Initiation of Snowball Earth with volcanic sulfur aerosol emissions: Geophysical Research Letters, vol. 44, pp. 1938–1946, doi: 10.1002/2016GL072335.

MacLennan, S. A., Park, Y., Swanson-Hysell, N. L., Maloof, A. C., Schoene, B., Gebreslassie, M., Antilla, E., Tesema, T., Alene, M., and Haileab, B., 2018, The arc of the Snowball: U-Pb dates constrain the Islay anomaly and the initiation of the Sturtian glaciation: Geology, vol. 46, pp. 539–542, doi: 10.1130/G40171.1.

Madon, M., Kim, C. L., and Wong, R., 2013, The structure and stratigraphy of deepwater Sarawak, Malaysia: Implications for tectonic evolution: Journal of Asian Earth Sciences, vol. 76, pp. 312–333, doi: 10.1016/j.jseaes.2013.04.040.

Maffre, P., Ladant, J.-B., Moquet, J.-S., Carretier, S., Labat, D., and Goddéris, Y., 2018, Mountain ranges, climate and weathering. do orogens strengthen or weaken the silicate weathering carbon sink?: Earth and Planetary Science Letters, vol. 493, pp. 174–185, doi: 10.1016/j.epsl.2018.04.034.

Maher, K. and Chamberlain, C. P., 2014, Hydrologic regulation of chemical weathering and the geologic carbon cycle: Science, vol. 343, pp. 1502–1504, doi: 10.1126/science.1250770.

Maloof, A. C., Halverson, G. P., Kirschvink, J. L., Schrag, D. P., Weiss, B. P., and Hoffman, P. F., 2006, Combined paleomagnetic, isotopic, and stratigraphic evidence for true polar wander from the Neoproterozoic Akademikerbreen Group, Svalbard, Norway: GSA Bulletin, vol. 118, pp. 1099–1124, doi: 10.1130/B25892.1.

Maloof, A. C., Porter, S. M., Moore, J. L., Dudás, F. Ö., Bowring, S. A., Higgins, J. A., Fike, D. A., and Eddy, M. P., 2010, The earliest Cambrian record of animals and ocean geochemical change: Geological Society of America Bulletin, vol. 122, pp. 1731–1774, doi: 10.1130/B30346.1.

Manabe, S., 1969, Climate and the ocean circulation: the atmospheric circulation and the hydrology of the Earth's surface: Monthly Weather Review, vol. 97, pp. 739–774, doi: 10.1175/1520-0493(1969)097⟨0739:catoc⟩2.3.co;2.

Matsuyama, I., Mitrovica, J. X., Daradich, A., and Gomez, N., 2010, The rotational stability of a triaxial ice-age Earth: Journal of Geophysical Research, vol. 115, doi: 10.1029/2009jb006564.

Matsuyama, I., Nimmo, F., and Mitrovica, J. X., 2014, Planetary reorientation: Annual Review of Earth and Planetary Sciences, vol. 42, pp. 605–634, doi: 10.1146/annurev-earth-060313-054724.

Matthews, K. J., Maloney, K. T., Zahirovic, S., Williams, S. E., Seton, M., and Müller, R. D., 2016, Global plate boundary evolution and kinematics since the late Paleozoic: Global and Planetary Change, vol. 146, pp. 226–250, doi: 10.1016/j.gloplacha.2016.10.002.

Mattinson, J. M., 2005, Zircon U-Pb chemical abrasion ("CA-TIMS") method: Combined annealing and multi-step partial dissolution analysis for improved precision and accuracy of zircon ages: Chemical Geology, vol. 220, pp. 47–66, doi: 10.1016/j.chemgeo.2005.03.011.

McArthur, J., Howarth, R., and Shields, G., 2012, Strontium isotope stratigraphy: The Geologic Time Scale, pp. 127–144, doi: 10.1016/b978-0-444-59425-9.00007-x.

McArthur, J. M., Rio, D., Massari, F., Castradori, D., Bailey, T. R., Thirlwall, M., and Houghton, S., 2006, A revised Pliocene record for marine-$^{87}Sr/^{86}Sr$ used to date an interglacial event recorded in the Cockburn Island Formation, Antarctic Peninsula: Palaeogeography, Palaeoclimatology, Palaeoecology, vol. 242, pp. 126–136, doi: 10.1016/j.palaeo.2006.06.004.

McCabe, C. and Elmore, R. D., 1989, The occurrence and origin of Late Paleozoic remagnetization in the sedimentary rocks of North America: Reviews of Geophysics, vol. 27, p. 471, doi: 10.1029/rg027i004p00471.

McCormick, M. P., Thomason, L. W., and Trepte, C. R., 1995, Atmospheric effects of the Mt Pinatubo eruption: Nature, vol. 373, pp. 399–404, doi: 10.1038/373399a0.

McLean, N. M., Condon, D. J., Schoene, B., and Bowring, S. A., 2015, Evaluating uncertainties in the calibration of isotopic reference materials and multi-element isotopic tracers (EARTHTIME tracer calibration part II): Geochimica et Cosmochimica Acta, vol. 164, pp. 481–501, doi: 10.1016/j.gca.2015.02.040.

McLelland, J. M., Selleck, B. W., and Bickford, M. E., 2013, Tectonic evolution of the Adirondack mountains and Grenville orogen inliers within the USA: Geoscience Canada, vol. 40, pp. 318–352, doi: 10.12789/geocanj.2013.40.022.

Meert, J. G., der Voo, R. V., Powell, C. M., Li, Z.-X., McElhinny, M. W., Chen, Z., and Symons, D. T. A., 1993, A plate-tectonic speed limit?: Nature, vol. 363, pp. 216–217, doi: 10.1038/363216a0.

Meert, J. G., Pandit, M. K., and Kamenov, G. D., 2013, Further geochronological and paleomagnetic constraints on Malani (and pre-Malani) magmatism in NW India: Tectonophysics, vol. 608, pp. 1254–1267, doi: 10.1016/j.tecto.2013.06.019.

Merdith, A. S., Collins, A. S., Williams, S. E., Pisarevsky, S., Foden, J. D., Archibald, D. B., Blades, M. L., Alessio, B. L., Armistead, S., Plavsa, D., and et al., 2017, A full-plate global reconstruction of the Neoproterozoic: Gondwana Research, vol. 50, pp. 84–134, doi: 10.1016/j.gr.2017.04.001.

Metcalfe, I., 2013, Gondwana dispersion and Asian accretion: Tectonic and palaeogeographic evolution of eastern Tethys: Journal of Asian Earth Sciences, vol. 66, pp. 1–33, doi: 10.1016/j.jseaes.2012.12.020.

Meyers, S. R., Siewert, S. E., Singer, B. S., Sageman, B. B., Condon, D. J., Obradovich, J. D., Jicha, B. R., and Sawyer, D. A., 2012, Intercalibration of radioisotopic and astrochronologic time scales for the Cenomanian-Turonian boundary interval, Western Interior Basin, USA: Geology, vol. 40, pp. 7–10, doi: 10.1130/g32261.1.

Michalopoulos, P. and Aller, R. C., 1995, Rapid clay mineral formation in Amazon Delta sediments: Reverse weathering and oceanic elemental cycles: Science, vol. 270, pp. 614–617, doi: 10.1126/science.270.5236.614.

Michalski, K., Lewandowski, M., and Manby, G., 2011, New palaeomagnetic, petrographic and $^{40}Ar/^{39}Ar$ data to test palaeogeographic reconstructions of Caledonide Svalbard: Geological Magazine, vol. 149, pp. 696–721, doi: 10.1017/s0016756811000835.

Michel, L. A., Tabor, N. J., and Montañez, I. P., 2016, Paleosol diagenesis and its deep-time paleoenvironmental implications, Pennsylvanian-Permian Lodève Basin, France: Journal of Sedimentary Research, vol. 86, pp. 813–829, doi: 10.2110/jsr.2016.41.

Miller, N. R., Alene, M., Sacchi, R., Stern, R. J., Conti, A., Kröner, A., and Zuppi, G., 2003, Significance of the Tambien Group (Tigrai, N. Ethiopia) for Snowball Earth events in the Arabian-Nubian Shield: Precambrian Research, vol. 121, pp. 263–283, doi: 10.1016/S0301-9268(03)00014-7.

Miller, N. R., Stern, R. J., Avigad, D., Beyth, M., and Schilman, B., 2009, Cryogenian slate-carbonate sequences of the Tambien Group, Northern Ethiopia (I): Pre-"Sturtian" chemostratigraphy and regional correlations: Precambrian Research, vol. 170, pp. 129–156, doi: 10.1016/j.precamres.2008.12.004.

Milliman, J. D. and Farnsworth, K. L., 2013, River Discharge to the Coastal Ocean: A Global Synthesis: Cambridge University Press, doi: 10.1017/cbo9780511781247, URL http://dx.doi.org/10.1017/CBO9780511781247.

Mitrovica, J. X., Wahr, J., Matsuyama, I., and Paulson, A., 2005, The rotational stability of an ice-age earth: Geophysical Journal International, vol. 161, pp. 491–506, doi: 10.1111/j.1365-246x.2005.02609.x.

Molnar, P. and Cronin, T. W., 2015, Growth of the Maritime Continent and its possible contribution to recurring ice ages: Paleoceanography, vol. 30, pp. 196–225, doi: 10.1002/2014PA002752.

Monnier, C., Girardeau, J., Maury, R. C., and Cotten, J., 1995, Back-arc basin origin for the East Sulawesi ophiolite (eastern Indonesia): Geology, vol. 23, pp. 851–854, doi: 10.1130/0091-7613(1995)023⟨0851:baboft⟩2.3.co;2.

Monnier, C., Girardeau, J., Pubellier, M., Polvé, M., Permana, H., and Bellon, H., 1999, Petrology and geochemistry of the Cyclops ophiolites (Irian Jaya, East Indonesia): Consequences for the Cenozoic evolution of the north Australian margin: Mineralogy and Petrology, vol. 65, pp. 1–28, doi: 10.1007/bf01161574.

Montañez, I. P., 2013, Modern soil system constraints on reconstructing deep-time atmospheric CO_2: Geochimica et Cosmochimica Acta, vol. 101, pp. 57–75, doi: 10.1016/j.gca.2012.10.012.

Moquet, J.-S., Crave, A., Viers, J., Seyler, P., Armijos, E., Bourrel, L., Chavarri, E., Lagane, C., Laraque, A., Casimiro, W. S. L., and et al., 2011, Chemical weathering and atmospheric/soil CO_2 uptake in the Andean and Foreland Amazon basins: Chemical Geology, vol. 287, pp. 1–26, doi: 10.1016/j.chemgeo.2011.01.005.

Moquet, J.-S., Guyot, J.-L., Crave, A., Viers, J., Filizola, N., Martinez, J.-M., Oliveira, T. C., Sánchez, L. S. H., Lagane, C., Casimiro, W. S. L., and et al., 2016, Amazon River dissolved load: temporal dynamics and annual budget from the Andes to the ocean: Environmental Science and Pollution Research, vol. 23, pp. 11,405–11,429, doi: 10.1007/s11356-015-5503-6.

Moquet, J.-S., Guyot, J.-L., Morera, S., Crave, A., Rau, P., Vauchel, P., Lagane, C., Sondag, F., Lavado, C. W., Pombosa, R., and et al., 2018, Temporal variability and annual budget of inorganic dissolved matter in Andean Pacific Rivers located along a climate gradient from northern Ecuador to southern Peru: Comptes Rendus Geoscience, vol. 350, pp. 76–87, doi: 10.1016/j.crte.2017.11.002.

Morley, R. J. and Morley, H. P., 2013, Mid Cenozoic freshwater wetlands of the Sunda region: Journal of Limnology, vol. 72, pp. 18–35, doi: 10.4081/jlimnol.2013.s2.e3.

Moss, S. J. and Wilson, M. E. J., 1998, Biogeographic implications of the Tertiary palaeogeographic evolution of Sulawesi and Borneo: *In* Hall, R. and Holloway, J. D., eds., Biogeography and Geological Evolution of SE Asia, Backbuys Publishers Leiden, The Netherlands, vol. 133, pp. 133–163.

Mound, J. E., Mitrovica, J. X., Evans, D. A. D., and Kirschvink, J. L., 1999, A sea-level test for inertial interchange true polar wander events: Geophysical Journal International, vol. 136, pp. F5–F10, doi: 10.1046/j.1365-246x.1999.00791.x.

Mucci, A. and Morse, J. W., 1983, The incorporation of Mg^{2+} and Sr^{2+} into calcite overgrowths: influences of growth rate and solution composition: Geochimica et Cosmochimica Acta, vol. 47, pp. 217–233, doi: 10.1016/0016-7037(83)90135-7.

Müller, R. D., Sdrolias, M., Gaina, C., and Roest, W. R., 2008, Age, spreading rates, and spreading asymmetry of the world's ocean crust: Geochemistry, Geophysics, Geosystems, vol. 9, pp. 1–19, doi: 10.1029/2007GC001743.

Murphy, J. B., van Staal, C. R., and Keppie, J. D., 1999, Middle to late Paleozoic Acadian orogeny in the northern Appalachians: A Laramide-style plume-modified orogeny?: Geology, vol. 27, pp. 653–656, doi: 10.1130/0091-7613(1999)027⟨0653:mtlpao⟩2.3.co;2.

Myrow, P. M., Hughes, N. C., Derry, L. A., Ryan McKenzie, N., Jiang, G., Webb, A. A. G., Banerjee, D. M., Paulsen, T. S., and Singh, B. P., 2015, Neogene marine isotopic evolution and the erosion of Lesser Himalayan strata: Implications for Cenozoic tectonic history: Earth and Planetary Science Letters, vol. 417, pp. 142–150, doi: 10.1016/j.epsl.2015.02.016.

Nichols, G. J. and Hall, R., 1991, Basin formation and Neogene sedimentation in a backarc setting, Halmahera, eastern Indonesia: Marine and Petroleum Geology, vol. 8, pp. 50–61, doi: 10.1016/0264-8172(91)90044-2.

Niu, J., Li, Z.-X., and Zhu, W., 2016, Palaeomagnetism and geochronology of mid-Neoproterozoic Yanbian dykes, South China: implications for a c. 820–800 Ma true polar wander event and the reconstruction of Rodinia: Geological Society, London, Special Publications, vol. 424, pp. 191–211, doi: 10.1144/SP424.11.

Norton, K. P., Molnar, P., and Schlunegger, F., 2014, The role of climate-driven chemical weathering on soil production: Geomorphology, vol. 204, pp. 510–517, doi: 10.1016/j.geomorph.2013.08.030.

Nugraha, A. M. S. and Hall, R., 2018, Late Cenozoic palaeogeography of Sulawesi, Indonesia: Palaeogeography, Palaeoclimatology, Palaeoecology, vol. 490, pp. 191–209, doi: 10.1016/j.palaeo.2017.10.033.

Ojakangas, R. W., Morey, G. B., and Green, J. C., 2001, The Mesoproterozoic Midcontinent Rift System, Lake Superior Region, USA: Sedimentary Geology, vol. 141-142, pp. 421–442, doi: 10.1016/S0037-0738(01)00085-9.

Oliver, L., Harris, N., Bickle, M., Chapman, H., Dise, N., and Horstwood, M., 2003, Silicate weathering rates decoupled from the $^{87}Sr/^{87}Sr$ ratio of the dissolved load during Himalayan erosion: Chemical Geology, vol. 201, pp. 119–139, doi: 10.1016/s0009-2541(03)00236-5.

Pallister, J. S., Stacey, J. S., Fischer, L. B., and Premo, W. R., 1988, Precambrian ophiolites of Arabia: geologic settings, U-Pb geochronology, Pb-isotope characteristics, and implications for continental accretion: Precambrian Research, vol. 38, pp. 1–54, doi: 10.1016/0301-9268(88)90092-7.

Palmer, H. C., Merz, B. A., and Hayatsu, A., 1977, The Sudbury dikes of the Grenville Front region: paleomagnetism, petrochemistry, and K-Ar age studies: Canadian Journal of Earth Sciences, vol. 14, pp. 1867–1887, doi: 10.1139/e77-158.

Papanastassiou, D. and Wasserburg, G., 1968, Initial strontium isotopic abundances and the resolution of small time differences in the formation of planetary objects: Earth and Planetary Science Letters, vol. 5, pp. 361–376, doi: 10.1016/S0012-821X(68)80066-4.

Park, J. K., Norris, D. K., and Larochelle, A., 1989, Paleomagnetism and the origin of the Mackenzie Arc of northwestern Canada: Canadian Journal of Earth Sciences, vol. 26, pp. 2194–2203, doi: 10.1139/e89-186.

Park, Y., Maffre, P., Goddéris, Y., Macdonald, F. A., Anttila, E. S. C., and Swanson-Hysell, N. L., 2020a, Emergence of the Southeast Asian islands as a driver for Neogene cooling: Proceedings of the National Academy of Sciences, p. 202011033, doi: 10.1073/pnas.2011033117.

Park, Y., Swanson-Hysell, N. L., Macdonald, F. A., and Lisiecki, L., 2019, Evaluating the relationship between the area and latitude of large igneous provinces and Earth's long-term climate state: EarthArXiv, doi: 10.31223/osf.io/p9ndf.

Park, Y., Swanson-Hysell, N. L., MacLennan, S. A., Maloof, A. C., Gebreslassie, M., Tremblay, M. M., Schoene, B., Alene, M., Anttila, E. S., Tesema, T., and Haileab, B., 2020b, The lead-up to the Sturtian Snowball Earth: Neoproterozoic chemostratigraphy time-calibrated by the Tambien Group of Ethiopia: GSA Bulletin, vol. 132, pp. 1119–1149, doi: 10.1130/b35178.1.

Park, Y., Swanson-Hysell, N. L., Xian, H., Zhang, S., Condon, D. J., Fu, H., and Macdonald, F. A., submitted, Tonian paleomagnetism from South China permits an inclusive Rodinia or Bitter Springs Stage true polar wander, but not both: Journal of Geophysical Research: Solid Earth.

Parkinson, C., 1998a, Emplacement of the East Sulawesi Ophiolite: evidence from subophiolite metamorphic rocks: Journal of Asian Earth Sciences, vol. 16, pp. 13–28, doi: 10.1016/s0743-9547(97)00039-1.

Parkinson, C., 1998b, An outline of the petrology, structure and age of the Pompangeo Schist Complex of central Sulawesi, Indonesia: The Island Arc, vol. 7, pp. 231–245, doi: 10.1046/j.1440-1738.1998.00171.x.

Pehrsson, S. J. and Buchan, K. L., 1999, Borden dykes of Baffin Island, Northwest Territories: a Franklin U-Pb baddeleyite age and a paleomagnetic reinterpretation: Canadian Journal of Earth Sciences, vol. 36, pp. 65–73, doi: 10.1139/e98-091.

Peng, P., Bleeker, W., Ernst, R. E., Söderlund, U., and McNicoll, V., 2011, U-Pb baddeleyite ages, distribution and geochemistry of 925Ma mafic dykes and 900Ma sills in the North China craton: Evidence for a Neoproterozoic mantle plume: Lithos, vol. 127, pp. 210–221, doi: 10.1016/j.lithos.2011.08.018.

Peng, S., Kusky, T. M., Jiang, X. F., Wang, L., Wang, J. P., and Deng, H., 2012, Geology, geochemistry, and geochronology of the Miaowan ophiolite, Yangtze craton: Implications for South China's amalgamation history with the Rodinian supercontinent: Gondwana Research, vol. 21, pp. 577–594, doi: 10.1016/j.gr.2011.07.010, special Issue: Western Gondwana.

Pi, D.-H. and Jiang, S.-Y., 2016, U-Pb dating of zircons from tuff layer, sandstone and tillite samples in the uppermost Liantuo Formation and the lowermost Nantuo Formation in Three Gorges area, South China: Chemie der Erde - Geochemistry, vol. 76, pp. 103 – 109, doi: 10.1016/j.chemer.2015.12.003.

Pirajno, F., 2013, Large Igneous Provinces (Xiong'er, Dashigou, 827 Ma Event, Tarim, Emeishan) and the Yanshanian tectono-thermal Event of Eastern China, Springer Netherlands, Dordrecht, pp. 547–638: doi: 10.1007/978-94-007-4444-8-7.

Pirajno, F. and Hoatson, D. M., 2012, A review of Australia's large igneous provinces and associated mineral systems: Implications for mantle dynamics through geological time: Ore Geology Reviews, vol. 48, pp. 2–54, doi: 10.1016/j.oregeorev.2012.04.007.

Pisarevsky, S. A., Elming, S.-Å., Pesonen, L. J., and Li, Z.-X., 2014a, Mesoproterozoic paleogeography: Supercontinent and beyond: Precambrian Research, vol. 244, pp. 207–225, doi: 10.1016/j.precamres.2013.05.014.

Pisarevsky, S. A., Gladkochub, D. P., Konstantinov, K. M., Mazukabzov, A. M., Stanevich, A. M., Murphy, J. B., Tait, J. A., Donskaya, T. V., and Konstantinov, I. K., 2013, Paleomagnetism of Cryogenian Kitoi mafic dykes in South Siberia: Implications for Neoproterozoic paleogeography: Precambrian Research, vol. 231, pp. 372–382, doi: 10.1016/j.precamres.2013.04.007.

Pisarevsky, S. A., Wingate, M. T. D., Li, Z.-X., Wang, X.-C., Tohver, E., and Kirkland, C. L., 2014b, Age and paleomagnetism of the 1210Ma Gnowangerup-Fraser dyke swarm, Western Australia, and implications for late Mesoproterozoic paleogeography: Precambrian Research, vol. 246, pp. 1–15, doi: 10.1016/j.precamres.2014.02.011.

Pisarevsky, S. A., Wingate, M. T. D., Stevens, M. K., and Haines, P. W., 2007, Palaeomagnetic results from the Lancer 1 stratigraphic drillhole, Officer Basin, Western Australia, and implications for Rodinia reconstructions: Australian Journal of Earth Sciences, vol. 54, pp. 561–572, doi: 10.1080/08120090701188962.

Pollard, D. and DeConto, R. M., 2005, Hysteresis in Cenozoic Antarctic ice-sheet variations: Global and Planetary Change, vol. 45, pp. 9–21, doi: 10.1016/j.gloplacha.2004.09.011.

Pollard, D. and Kasting, J. F., 2005, Snowball Earth: A thin-ice solution with flowing sea glaciers: Journal of Geophysical Research: Oceans, vol. 110, pp. 1–16, doi: 10.1029/2004JC002525.

Pollock, M. D., Kah, L. C., and Bartley, J. K., 2006, Morphology of molar-tooth structures in Precambrian carbonates: influence of substrate rheology and implications for genesis: Journal of Sedimentary Research, vol. 76, pp. 310–323, doi: 10.2110/jsr.2006.021.

Polvé, M., Maury, R., Bellon, H., Rangin, C., Priadi, B., Yuwono, S., Joron, J., and Atmadja, R., 1997, Magmatic evolution of Sulawesi (Indonesia): constraints on the Cenozoic geodynamic history of the Sundaland active margin: Tectonophysics, vol. 272, pp. 69–92, doi: 10.1016/s0040-1951(96)00276-4.

Pratt, B. R., 1998, Molar-tooth structure in Proterozoic carbonate rocks: origin from synsedimentary earthquakes, and implications for the nature and evolution of basins and marine sediment: Geological Society of America Bulletin, vol. 110, pp. 1028–1045, doi: 10.1130/0016-7606(1998)110⟨1028:MTSIPC⟩2.3.CO;2.

Pubellier, M., Quebral, R., Rangin, C., Deffontaines, B., Muller, C., Butterlin, J., and Manzano, J., 1991, The Mindanao collision zone: a soft collision event within a continuous Neogene strike-slip setting: Journal of Southeast Asian Earth Sciences, vol. 6, pp. 239–248, doi: 10.1016/0743-9547(91)90070-e.

Pujol, M., Marty, B., Burgess, R., Turner, G., and Philippot, P., 2013, Argon isotopic composition of Archaean atmosphere probes early Earth geodynamics: Nature, vol. 498, pp. 87–90, doi: 10.1038/nature12152.

Qi, L., Cawood, P. A., Xu, Y., Du, Y., Zhang, H., and Zhang, Z., 2020, Linking South China to North India from the late Tonian to Ediacaran: Constraints from the Cathaysia Block: Precambrian Research, p. 105898, doi: 10.1016/j.precamres.2020.105898.

Qi, L., Xu, Y., Cawood, P. A., Wang, W., and Du, Y., 2019, Implications of 770 Ma rhyolitic tuffs, eastern South China Craton in constraining the tectonic setting of the Nanhua Basin: Lithos, vol. 324-325, pp. 842–858, doi: 10.1016/j.lithos.2018.12.004.

Quade, J., English, N., and DeCelles, P. G., 2003, Silicate versus carbonate weathering in the Himalaya: a comparison of the Arun and Seti River watersheds: Chemical Geology, vol. 202, pp. 275–296, doi: 10.1016/j.chemgeo.2002.05.002.

Raymo, M. E., 1991, Geochemical evidence supporting T. C. Chamberlin's theory of glaciation: Geology, vol. 19, pp. 344–347, doi: 10.1130/0091-7613(1991)019⟨0344:gestcc⟩2.3.co;2.

Raymo, M. E. and Ruddiman, W. F., 1992, Tectonic forcing of late Cenozoic climate: Nature, vol. 359, pp. 117–122, doi: 10.1038/359117a0.

Raymo, M. E., Ruddiman, W. F., and Froelich, P. N., 1988, Influence of late Cenozoic mountain building on ocean geochemical cycles: Geology, vol. 16, pp. 649–653, doi: 10.1130/0091-7613(1988)016⟨0649:iolcmb⟩2.3.co;2.

Ricard, Y., Spada, G., and Sabadini, R., 1993, Polar wandering of a dynamic earth: Geophysical Journal International, vol. 113, pp. 284–298, doi: 10.1111/j.1365-246x.1993.tb00888.x.

Ricci, J., Quidelleur, X., Pavlov, V., Orlov, S., Shatsillo, A., and Courtillot, V., 2013, New $^{40}Ar/^{39}Ar$ and K-Ar ages of the Viluy traps (Eastern Siberia): Further evidence for a relationship with the Frasnian-Famennian mass extinction: Palaeogeography, Palaeoclimatology, Palaeoecology, vol. 386, pp. 531–540, doi: 10.1016/j.palaeo.2013.06.020.

Richter, F. M., Rowley, D. B., and DePaolo, D. J., 1992, Sr isotope evolution of seawater: the role of tectonics: Earth and Planetary Science Letters, vol. 109, pp. 11–23, doi: 10.1016/0012-821X(92)90070-C.

Rooney, A. D., Macdonald, F. A., Strauss, J. V., Dudás, F. Ö., Hallmann, C., and Selby, D., 2014, Re-Os geochronology and coupled Os-Sr isotope constraints on the Sturtian

snowball Earth: Proceedings of the National Academy of Sciences, vol. 111, pp. 51–56, doi: 10.1073/pnas.1317266110.

Rooney, A. D., Strauss, J. V., Brandon, A. D., and Macdonald, F. A., 2015, A Cryogenian chronology: Two long-lasting synchronous Neoproterozoic glaciations: Geology, vol. 43, pp. 459–462, doi: 10.1130/G36511.1.

Rose, C. V., Swanson-Hysell, N. L., Husson, J. M., Poppick, L. N., Cottle, J. M., Schoene, B., and Maloof, A. C., 2012, Constraints on the origin and relative timing of the Trezona $\delta^{13}C$ anomaly below the end-Cryogenian glaciation: Earth and Planetary Science Letters, vol. 319-320, pp. 241–250, doi: 10.1016/j.epsl.2011.12.027.

Rothman, D. H., Hayes, J. M., and Summons, R. E., 2003, Dynamics of the Neoproterozoic carbon cycle: Proceedings of the National Academy of Sciences, vol. 100, pp. 8124–8129, doi: 10.1073/pnas.0832439100.

Sapin, F., Pubellier, M., Ringenbach, J.-C., and Bailly, V., 2009, Alternating thin versus thick-skinned decollements, example in a fast tectonic setting: The Misool–Onin–Kumawa Ridge (West Papua): Journal of Structural Geology, vol. 31, pp. 444–459, doi: 10.1016/j.jsg.2009.01.010.

Satyana, A. H., Nugroho, D., and Surantoko, I., 1999, Tectonic controls on the hydrocarbon habitats of the Barito, Kutei, and Tarakan Basins, Eastern Kalimantan, Indonesia: major dissimilarities in adjoining basins: Journal of Asian Earth Sciences, vol. 17, pp. 99–122, doi: 10.1016/s0743-9547(98)00059-2.

Sawaki, Y., Kawai, T., Shibuya, T., Tahata, M., Omori, S., Komiya, T., Yoshida, N., Hirata, T., Ohno, T., Windley, B. F., and Maruyama, S., 2010, $^{87}Sr/^{86}Sr$ chemostratigraphy of Neoproterozoic Dalradian carbonates below the Port Askaig Glaciogenic Formation, Scotland: Precambrian Research, vol. 179, pp. 150–164, doi: 10.1016/j.precamres.2010.02.021.

Schaller, M. F., Wright, J. D., and Kent, D. V., 2011, Atmospheric pCO_2 perturbations associated with the Central Atlantic Magmatic Province: Science, vol. 331, pp. 1404–1409, doi: 10.1126/science.1199011.

Schaller, M. F., Wright, J. D., Kent, D. V., and Olsen, P. E., 2012, Rapid emplacement of the Central Atlantic Magmatic Province as a net sink for CO_2: Earth and Planetary Science Letters, vol. 323-324, pp. 27–39, doi: 10.1016/j.epsl.2011.12.028.

Schellart, W. P., Lister, G. S., and Toy, V. G., 2006, A Late Cretaceous and Cenozoic reconstruction of the Southwest Pacific region: tectonics controlled by subduction and slab rollback processes: Earth-Science Reviews, vol. 76, pp. 191–233, doi: 10.1016/j.earscirev.2006.01.002.

Schellart, W. P., Stegman, D. R., and Freeman, J., 2008, Global trench migration velocities and slab migration induced upper mantle volume fluxes: Constraints to find an Earth reference frame based on minimizing viscous dissipation: Earth-Science Reviews, vol. 88, pp. 118–144, doi: 10.1016/j.earscirev.2008.01.005.

Schoene, B., Samperton, K. M., Eddy, M. P., Keller, G., Adatte, T., Bowring, S. A., Khadri, S. F. R., and Gertsch, B., 2014, U-Pb geochronology of the Deccan Traps and relation to the end-Cretaceous mass extinction: Science, vol. 347, pp. 182–184, doi: 10.1126/science.aaa0118.

Schopka, H., Derry, L., and Arcilla, C., 2011, Chemical weathering, river geochemistry and atmospheric carbon fluxes from volcanic and ultramafic regions on Luzon Island, the Philippines: Geochimica et Cosmochimica Acta, vol. 75, pp. 978–1002, doi: 10.1016/j.gca.2010.11.014.

Schrag, D. P., Higgins, J. A., Macdonald, F. A., and Johnston, D. T., 2013, Authigenic carbonate and the history of the global carbon cycle: Science, vol. 339, pp. 540–543, doi: 10.1126/science.1229578.

Sdrolias, M. and Müller, R. D., 2006, Controls on back-arc basin formation: Geochemistry, Geophysics, Geosystems, vol. 7, pp. 1–40, doi: 10.1029/2005gc001090.

Shackleton, N. J., Backman, J., Zimmerman, H., Kent, D. V., Hall, M. A., Roberts, D. G., Schnitker, D., Baldauf, J. G., Desprairies, A., Homrighausen, R., and et al., 1984, Oxygen isotope calibration of the onset of ice-rafting and history of glaciation in the North Atlantic region: Nature, vol. 307, pp. 620–623, doi: 10.1038/307620a0.

Shellnutt, J. G. and MacRae, N. D., 2012, Petrogenesis of the Mesoproterozoic (1.23 Ga) Sudbury dyke swarm and its questionable relationship to plate separation: International Journal of Earth Sciences, vol. 101, pp. 3–23, doi: 10.1007/s00531-010-0636-9.

Sherwood, S., Webb, M. J., Annan, J. D., Armour, K. C., Forster, P. M., Hargreaves, J. C., Hegerl, G., Klein, S. A., Marvel, K. D., Rohling, E. J., Watanabe, M., Andrews, T., Braconnot, P., Bretherton, C. S., Foster, G. L., Hausfather, Z., von der Heydt, A. S., Knutti, R., Mauritsen, T., Norris, J. R., Proistosescu, C., Rugenstein, M., Schmidt, G. A., Tokarska, K. B., and Zelinka, M. D., 2020, An assessment of Earth's climate sensitivity using multiple lines of evidence: Reviews of Geophysics, doi: 10.1029/2019rg000678.

Shevenell, A. E., 2004, Middle Miocene Southern Ocean cooling and Antarctic cryosphere expansion: Science, vol. 305, pp. 1766–1770, doi: 10.1126/science.1100061.

Shields, G. and Veizer, J., 2002, Precambrian marine carbonate isotope database: Version 1.1: Geochemistry, Geophysics, Geosystems, vol. 3, pp. 1 of 12–12 of 12, doi: 10.1029/2001GC000266.

Si, W. and Rosenthal, Y., 2019, Reduced continental weathering and marine calcification linked to late Neogene decline in atmospheric CO_2: Nature Geoscience, vol. 12, pp. 833–838, doi: 10.1038/s41561-019-0450-3.

Silver, E. A., McCaffrey, R., Joyodiwiryo, Y., and Stevens, S., 1983, Ophiolite emplacement by collision between the Sula Platform and the Sulawesi Island Arc, Indonesia: Journal of Geophysical Research: Solid Earth, vol. 88, pp. 9419–9435, doi: 10.1029/jb088ib11p09419.

Smith, A. G., 1968, The origin and deformation of some 'molar-tooth' structures in the Precambrian Belt-Purcell Supergroup: The Journal of Geology, vol. 76, pp. 426–443.

Smith, R. B. and Silver, E. A., 1991, Geology of a Miocene collision complex, Buton, eastern Indonesia: Geological Society of America Bulletin, vol. 103, pp. 660–678, doi: 10.1130/0016-7606(1991)103⟨0660:goamcc⟩2.3.co;2.

Söderlund, U., Elming, S.-Å., Ernst, R. E., and Schissel, D., 2006, The Central Scandinavian Dolerite Group-protracted hotspot activity or back-arc magmatism?: Constraints from U-Pb baddeleyite geochronology and Hf isotopic data: Precambrian Research, vol. 150, pp. 136–152, doi: 10.1016/j.precamres.2006.07.004.

Spada, G., Ricard, Y., and Sabadini, R., 1992, Excitation of true polar wander by subduction: Nature, vol. 360, pp. 452–454, doi: 10.1038/360452a0.

Spear, N., Holland, H. D., Garcia-Veígas, J., Lowenstein, T. K., Giegengack, R., and Peters, H., 2014, Analyses of fluid inclusions in Neoproterozoic marine halite provide oldest measurement of seawater chemistry: Geology, vol. 42, pp. 103–106, doi: 10.1130/G34913.1.

Steinberger, B. and O'Connell, R. J., 1997, Changes of the Earth's rotation axis owing to advection of mantle density heterogeneities: Nature, vol. 387, pp. 169–173, doi: 10.1038/387169a0.

Steinberger, B. and Torsvik, T. H., 2008, Absolute plate motions and true polar wander in the absence of hotspot tracks: Nature, vol. 452, pp. 620–623, doi: 10.1038/nature06824.

Steinberger, B. and Torsvik, T. H., 2010, Toward an explanation for the present and past locations of the poles: Geochemistry, Geophysics, Geosystems, vol. 11, pp. 1–19, doi: 10.1029/2009gc002889.

Stern, R. J., 1994, Arc-assembly and continental collision in the Neoproterozoic African Orogen: implications for the consolidation of Gondwanaland: Annual Review of Earth and Planetary Sciences, vol. 22, pp. 319–351, doi: 10.1146/annurev.ea.22.050194.001535.

Stocker, T., Qin, D., Plattner, G.-K., Tignor, M., Allen, S., Boschung, J., Nauels, A., Xia, Y., Bex, V., and Midgley, P., 2013, Climate Change 2013: The Physical Science Basis. Contribution of Working Group I to the Fifth Assessment Report of the Intergovernmental Panel on Climate Change: Cambridge University Press, 1535 pp.

Strauss, J. V., Rooney, A. D., Macdonald, F. A., Brandon, A. D., and Knoll, A. H., 2014, 740 Ma vase-shaped microfossils from Yukon, Canada: implications for Neoproterozoic chronology and biostratigraphy: Geology, vol. 42, pp. 659–662, doi: 10.1130/G35736.1.

Sugden, D. E., Marchant, D. R., Potter, N., Souchez, R. A., Denton, G. H., Swisher III, C. C., and Tison, J.-L., 1995, Preservation of Miocene glacier ice in East Antarctica: Nature, vol. 376, pp. 412–414, doi: 10.1038/376412a0.

Suggate, S. M., Cottam, M. A., Hall, R., Sevastjanova, I., Forster, M. A., White, L. T., Armstrong, R. A., Carter, A., and Mojares, E., 2014, South China continental margin signature for sandstones and granites from Palawan, Philippines: Gondwana Research, vol. 26, pp. 699–718, doi: 10.1016/j.gr.2013.07.006.

Swanson-Hysell, N. L., Kilian, T. M., and Hanson, R. E., 2015a, A new grand mean palaeomagnetic pole for the 1.11 Ga Umkondo large igneous province with implications for palaeogeography and the geomagnetic field: Geophysical Journal International, vol. 203, pp. 2237–2247, doi: 10.1093/gji/ggv402.

Swanson-Hysell, N. L. and Macdonald, F. A., 2017, Tropical weathering of the Taconic orogeny as a driver for Ordovician cooling: Geology, vol. 45, pp. 719–722, doi: 10.1130/G38985.1.

Swanson-Hysell, N. L., Maloof, A. C., Condon, D. J., Jenkin, G. R., Alene, M., Tremblay, M. M., Tesema, T., Rooney, A. D., and Haileab, B., 2015b, Stratigraphy and geochronology of the Tambien Group, Ethiopia: evidence for globally synchronous carbon isotope change in the Neoproterozoic: Geology, vol. 43, pp. 323–326, doi: 10.1130/G36347.1.

Swanson-Hysell, N. L., Maloof, A. C., Kirschvink, J. L., Evans, D. A. D., Halverson, G. P., and Hurtgen, M. T., 2012, Constraints on Neoproterozoic paleogeography and Paleozoic orogenesis from paleomagnetic records of the Bitter Springs Formation, Amadeus Basin, central Australia: American Journal of Science, vol. 312, pp. 817–884, doi: 10.2475/08.2012.01.

Swanson-Hysell, N. L., Ramezani, J., Fairchild, L. M., and Rose, I. R., 2019, Failed rifting and fast drifting: Midcontinent Rift development, Laurentia's rapid motion and the driver of Grenvillian orogenesis: GSA Bulletin, vol. 131, pp. 913–940, doi: 10.1130/b31944.1.

Swanson-Hysell, N. L., Rose, C. V., Calmet, C. C., Halverson, G. P., Hurtgen, M. T., and Maloof, A. C., 2010, Cryogenian glaciation and the onset of carbon-isotope decoupling: Science, vol. 328, pp. 608–611, doi: 10.1126/science.1184508.

Swanson-Hysell, N. L., Vaughan, A. A., Mustain, M. R., and Asp, K. E., 2014, Confirmation of progressive plate motion during the Midcontinent Rift's early magmatic stage from the Osler Volcanic Group, Ontario, Canada: Geochemistry, Geophysics, Geosystems, vol. 15, pp. 2039–2047, doi: 10.1002/2013GC005180.

Swanson-Hysell, N. L., Fairchild, L. M., and Slotznick, S. P., 2019, Primary and secondary red bed magnetization constrained by fluvial intraclasts: Journal of Geophysical Research: Solid Earth, vol. 124, pp. 4276–4289, doi: 10.1029/2018jb017067.

Swart, P. K., 2008, Global synchronous changes in the carbon isotopic composition of carbonate sediments unrelated to changes in the global carbon cycle: Proceedings of the National Academy of Sciences, vol. 105, pp. 13,741–13,745, doi: 10.1073/pnas.0802841105.

Swart, P. K. and Kennedy, M. J., 2012, Does the global stratigraphic reproducibility of δ^{13}C in Neoproterozoic carbonates require a marine origin? A Pliocene-Pleistocene comparison: Geology, vol. 40, pp. 87–90, doi: 10.1130/G32538.1.

Tack, L., Wingate, M. T. D., Liégeois, J.-P., Fernandez-Alonso, M., and Deblond, A., 2001, Early Neoproterozoic magmatism (1000-910 Ma) of the Zadinian and Mayumbian Groups (Bas-Congo): onset of Rodinia rifting at the western edge of the Congo craton: Precambrian Research, vol. 110, pp. 277–306, doi: 10.1016/S0301-9268(01)00192-9.

Tadesse, T., Hoshino, M., and Sawada, Y., 1999, Geochemistry of low-grade metavolcanic rocks from the Pan-African of the Axum area, northern Ethiopia: Precambrian Research, vol. 96, pp. 101–124, doi: 10.1016/S0301-9268(99)00008-X.

Tauxe, L., 2005, Inclination flattening and the geocentric axial dipole hypothesis: Earth and Planetary Science Letters, vol. 233, pp. 247 – 261, doi: 10.1016/j.epsl.2005.01.027.

Tauxe, L. and Kent, D. V., 1984, Properties of a detrital remanence carried by haematite from study of modern river deposits and laboratory redeposition experiments: Geophysical Journal International, vol. 76, pp. 543–561, doi: 10.1111/j.1365-246X.1984.tb01909.x.

Tauxe, L., Shaar, R., Jonestrask, L., Swanson-Hysell, N. L., Minnett, R., Koppers, A. A. P., Constable, C. G., Jarboe, N., Gaastra, K., and Fairchild, L., 2016, PmagPy: Software package for paleomagnetic data analysis and a bridge to the Magnetics Information Consortium (MagIC) Database: Geochemistry, Geophysics, Geosystems, vol. 17, pp. 2450–2463, doi: 10.1002/2016gc006307.

Tauxe, L. and Watson, G., 1994, The fold test: an eigen analysis approach: Earth and Planetary Science Letters, vol. 122, pp. 331–341, doi: 10.1016/0012-821x(94)90006-x.

Taylor, S. R., 1964, Abundance of chemical elements in the continental crust: a new table: Geochimica et Cosmochimica Acta, vol. 28, pp. 1273–1285, doi: 10.1016/0016-7037(64)90129-2.

Teklay, M., 1997, Petrology, geochemistry and geochronology of Neoproterozoic magmatic arc rocks from Eritrea: implications for crustal evolution in the southern Nubian Shield: Department of Mines-Ministry of Energy Mines and Water Resources-State of Eritrea.

Teklay, M., 2006, Neoproterozoic arc-back-arc system analog to modern arc-back-arc systems: evidence from tholeiite-boninite association, serpentinite mudflows and across-arc geochemical trends in Eritrea, southern Arabian-Nubian shield: Precambrian Research, vol. 145, pp. 81–92, doi: 10.1016/j.precamres.2005.11.015.

Teklay, M., Haile, T., Kröner, A., Asmerom, Y., and Watson, J., 2003, A back-arc palaeotectonic setting for the Augaro Neoproterozoic magmatic rocks of western Eritrea: Gondwana Research, vol. 6, pp. 629–640, doi: 10.1016/S1342-937X(05)71012-1.

Thorne, J., Cooper, M., and Claoué-Long, J., 2014, Guide to using the Australian mafic-ultramafic magmatic events GIS dataset: Archean, Proterozoic and Phanerozoic magmatic events: Geoscience Australia, doi: 10.11636/record.2014.039.

Tohver, E., Weil, A., Solum, J., and Hall, C., 2008, Direct dating of carbonate remagnetization by $^{40}Ar/^{39}Ar$ analysis of the smectite–illite transformation: Earth and Planetary Science Letters, vol. 274, pp. 524–530, doi: 10.1016/j.epsl.2008.08.002.

Torres, M. A., West, A. J., and Li, G., 2014, Sulphide oxidation and carbonate dissolution as a source of CO_2 over geological timescales: Nature, vol. 507, pp. 346–349, doi: 10.1038/nature13030.

Torsvik, T. H. and Cocks, L. R. M., 2016, Earth History and Palaeogeography: Cambridge University Press, doi: 10.1017/9781316225523.

Torsvik, T. H., Van der Voo, R., Preeden, U., Mac Niocaill, C., Steinberger, B., Doubrovine, P. V., van Hinsbergen, D. J., Domeier, M., Gaina, C., Tohver, E., Meert, J. G., McCausland, P. J. A., and Cocks, L. R. M., 2012, Phanerozoic polar wander, palaeogeography and dynamics: Earth-Science Reviews, vol. 114, pp. 325–368, doi: 10.1016/j.earscirev.2012.06.007.

Trenberth, K. E., Fasullo, J. T., and Mackaro, J., 2011, Atmospheric moisture transports from ocean to land and global energy flows in reanalyses: Journal of Climate, vol. 24, pp. 4907–4924, doi: 10.1175/2011jcli4171.1.

Trenberth, K. E., Stepaniak, D. P., and Caron, J. M., 2000, The global monsoon as seen through the divergent atmospheric circulation: Journal of Climate, vol. 13, pp. 3969–3993, doi: 10.1175/1520-0442(2000)013⟨3969:tgmast⟩2.0.co;2.

Tsai, V. C. and Stevenson, D. J., 2007, Theoretical constraints on true polar wander: Journal of Geophysical Research, vol. 112, doi: 10.1029/2005jb003923.

Turekian, K. K. and Wedepohl, K. H., 1961, Distribution of the elements in some major units of the Earth's crust: Geological Society of America Bulletin, vol. 72, pp. 175–192, doi: 10.1130/0016-7606(1961)72[175:DOTEIS]2.0.CO;2.

Tziperman, E., Halevy, I., Johnston, D. T., Knoll, A. H., and Schrag, D. P., 2011, Biologically induced initiation of Neoproterozoic snowball-Earth events: Proceedings of the National Academy of Sciences, vol. 108, pp. 15,091–15,096, doi: 10.1073/pnas.1016361108.

Uyeda, S. and Kanamori, H., 1979, Back-arc opening and the mode of subduction: Journal of Geophysical Research: Solid Earth, vol. 84, pp. 1049–1061, doi: 10.1029/JB084iB03p01049.

van de Wal, R. S. W., de Boer, B., Lourens, L. J., Köhler, P., and Bintanja, R., 2011, Reconstruction of a continuous high-resolution CO_2 record over the past 20 million years: Climate of the Past, vol. 7, pp. 1459–1469, doi: 10.5194/cp-7-1459-2011.

van de Weerd, A. A. and Armin, R. A., 1992, Origin and evolution of the Tertiary hydrocarbon-bearing basin in Kalimantan (Borneo), Indonesia: AAPG Bulletin, vol. 76, pp. 1778–1803.

Van Der Meer, D. G., Zeebe, R. E., van Hinsbergen, D. J. J., Sluijs, A., Spakman, W., and Torsvik, T. H., 2014, Plate tectonic controls on atmospheric CO_2 levels since the Triassic: Proceedings of the National Academy of Sciences, vol. 111, pp. 4380–4385, doi: 10.1073/pnas.1315657111.

van Hinsbergen, D. J. J., Steinberger, B., Doubrovine, P. V., and Gassmöller, R., 2011, Acceleration and deceleration of India-Asia convergence since the Cretaceous: Roles of mantle plumes and continental collision: Journal of Geophysical Research, vol. 116, doi: 10.1029/2010jb008051.

van Leeuwen, T. M. and Muhardjo, 2005, Stratigraphy and tectonic setting of the Cretaceous and Paleogene volcanic-sedimentary successions in northwest Sulawesi, Indonesia: implications for the Cenozoic evolution of Western and Northern Sulawesi: Journal of Asian Earth Sciences, vol. 25, pp. 481–511, doi: 10.1016/j.jseaes.2004.05.004.

van Leeuwen, T. M., Susanto, E. S., Maryanto, S., Hadiwisastra, S., Sudijono, Muhardjo, and Prihardjo, 2010, Tectonostratigraphic evolution of Cenozoic marginal basin and continental margin successions in the Bone Mountains, Southwest Sulawesi, Indonesia: Journal of Asian Earth Sciences, vol. 38, pp. 233–254, doi: 10.1016/j.jseaes.2009.11.005.

van Ufford, A. Q. and Cloos, M., 2005, Cenozoic tectonics of New Guinea: AAPG Bulletin, vol. 89, pp. 119–140, doi: 10.1306/08300403073.

Veevers, J. J. and Eittreim, S. L., 1988, Reconstruction of Antarctica and Australia at breakup (95 $\pm$ 5 Ma) and before rifting (160 Ma): Australian Journal of Earth Sciences, vol. 35, pp. 355–362, doi: 10.1080/08120098808729453.

Veizer, J., 1989, Strontium isotopes in seawater through time: Annual Review of Earth and Planetary Sciences, vol. 17, p. 141, doi: 10.1146/annurev.ea.17.050189.001041.

Villeneuve, M., Cornée, J.-J., Gunawan, W., Janin, M.-C., Butterlin, J., Saint-Marc, P., and Samodra, H., 2000, Continental block collision in the eastern arm of Sulawesi (Indonesia). Structure and geodynamic interpretation: Comptes Rendus de l'Académie des Sciences - Series IIA - Earth and Planetary Science, vol. 330, pp. 371–378, doi: 10.1016/s1251-8050(00)00163-4.

Villeneuve, M., Gunawan, W., Cornee, J.-J., and Vidal, O., 2001, Geology of the central Sulawesi belt (eastern Indonesia): constraints for geodynamic models: International Journal of Earth Sciences, vol. 91, pp. 524–537, doi: 10.1007/s005310100228.

Visser, W. A. and Hermes, J. J., 1962, Geological results of the exploration for oil in Netherlands New Guinea, carried out by the Netherlandsche Nieuw Guinee Petroleum Maatschappij, 1935-1960: Staatsdrukkerij-en Uitgeverijbedrijf.

Volpe, A. M. and Douglas Macdougall, J., 1990, Geochemistry and isotopic characteristics of mafic (Phulad Ophiolite) and related rocks in the Delhi Supergroup, Rajasthan, India: implications for rifting in the Proterozoic: Precambrian Research, vol. 48, pp. 167–191, doi: 10.1016/0301-9268(90)90061-t.

Voo, R. V. D. and Torsvik, T. H., 2012, The history of remagnetization of sedimentary rocks: deceptions, developments and discoveries: Geological Society, London, Special Publications, vol. 371, pp. 23–53, doi: 10.1144/sp371.2.

Vujovich, G. I. and Kay, S. M., 1998, A Laurentian? Grenville-age oceanic arc/back-arc terrane in the Sierra de Pie de Palo, Western Sierras Pampeanas, Argentina: Geological Society, London, Special Publications, vol. 142, pp. 159–179, doi: 10.1144/gsl.sp.1998.142.01.09.

Vujovich, G. I., van Staal, C. R., and Davis, W., 2004, Age constraints on the tectonic evolution and provenance of the Pie de Palo Complex, Cuyania Composite Terrane, and the Famatinian Orogeny in the Sierra de Pie de Palo, San Juan, Argentina: Gondwana Research, vol. 7, pp. 1041–1056, doi: 10.1016/s1342-937x(05)71083-2.

Walker, J. C. G., Hays, P. B., and Kasting, J. F., 1981, A negative feedback mechanism for the long-term stabilization of Earth's surface temperature: Journal of Geophysical Research, vol. 86, pp. 9776–9782, doi: 10.1029/jc086ic10p09776.

Wang, J. and Li, Z.-X., 2003, History of Neoproterozoic rift basins in South China: implications for Rodinia break-up: Precambrian Research, vol. 122, pp. 141 – 158, doi: 10.1016/S0301-9268(02)00209-7.

Wang, M., Dai, C., Chen, J., Wang, X., and Ma, H., 2016a, Neoproterozoic geochronologic framework of magmatism in Fanjingshan area and its tectonic implications: Geology in China, vol. 43, pp. 843–856.

Wang, M., Dai, C., Wang, X., Ma, H., Peng, C., and Yang, K., 2012, Sedimentation age of the Fanjingshan Group in East Guizhou Province: evidence from in-situ zircon LA-ICP-MS U-Pb dating: Acta Petrologica et Mineralogica, vol. 31, pp. 843–857.

Wang, T., Zhang, S., and Ramezani, J., 2016b, Age recalibration of the Xiaofeng dykes, South China, and its implications for true polar wander at ∼820 Ma: Acta Geologica Sinica - English Edition, vol. 90, p. 47, doi: 10.1111/1755-6724.12878.

Wang, W., Zhao, J.-H., Zhou, M.-F., Yang, S.-H., and Chen, F.-K., 2014, Neoproterozoic mafic-ultramafic intrusions from the Fanjingshan Region, South China: Implications for subduction-related magmatism in the Jiangnan Fold Belt: The Journal of Geology, vol. 122, pp. 455–473, doi: 10.1086/676596.

Wedepohl, K. H., 1995, The composition of the continental crust: Geochimica et Cosmochimica Acta, vol. 59, pp. 1217–1232, doi: 10.1016/0016-7037(95)00038-2.

Wei, Y., Peng, S., Jiang, X., Peng, Z., Peng, L., Li, Z., Zhou, P., and Zeng, X., 2012, SHRIMP zircon U-Pb ages and geochemical characteristics of the Neoproterozoic granitoids in the Huangling anticline and its tectonic setting: Journal of Earth Science, vol. 23, pp. 659–676, doi: 10.1007/s12583-012-0284-z.

Weil, A. B., Geissman, J. W., and Ashby, J. M., 2006, A new paleomagnetic pole for the Neoproterozoic Uinta Mountain supergroup, Central Rocky Mountain States, USA: Precambrian Research, vol. 147, pp. 234–259, doi: 10.1016/j.precamres.2006.01.017.

Weil, A. B., Geissman, J. W., Heizler, M., and der Voo, R. V., 2003, Paleomagnetism of Middle Proterozoic mafic intrusions and Upper Proterozoic (Nankoweap) red beds from the Lower Grand Canyon Supergroup, Arizona: Tectonophysics, vol. 375, pp. 199–220, doi: 10.1016/S0040-1951(03)00339-1, orogenic Belts, Regional and Global Tectonics: A Memorial Volume to Chris McAulay Powell.

Weiland, R. J. and Cloos, M., 1996, Pliocene-Pleistocene asymmetric unroofing of the Irian fold belt, Irian Jaya, Indonesia: Apatite fission-track thermochronology: Geological Society of America Bulletin, vol. 108, pp. 1438–1449, doi: 10.1130/0016-7606(1996)108⟨1438:ppauot⟩2.3.co;2.

West, A. J., 2012, Thickness of the chemical weathering zone and implications for erosional and climatic drivers of weathering and for carbon-cycle feedbacks: Geology, vol. 40, pp. 811–814, doi: 10.1130/g33041.1.

White, R. S., 1997, Mantle temperature and lithospheric thinning beneath the Midcontinent rift system: evidence from magmatism and subsidence: Canadian Journal of Earth Sciences, vol. 34, pp. 464–475, doi: 10.1139/e17-038.

Wingate, M. T., Campbell, I. H., Compston, W., and Gibson, G. M., 1998, Ion microprobe U-Pb ages for Neoproterozoic basaltic magmatism in south-central Australia and implications for the breakup of Rodinia: Precambrian Research, vol. 87, pp. 135–159, doi: 10.1016/S0301-9268(97)00072-7.

Wingate, M. T. D. and Giddings, J. W., 2000, Age and palaeomagnetism of the Mundine Well dyke swarm, Western Australia: implications for an Australia–Laurentia connection at 755 Ma: Precambrian Research, vol. 100, pp. 335–357, doi: 10.1016/S0301-9268(99)00080-7.

Wingate, M. T. D., Pisarevsky, S. A., and Evans, D. A. D., 2002, Rodinia connections between Australia and Laurentia: no SWEAT, no AUSWUS?: Terra Nova, vol. 14, pp. 121–128, doi: 10.1046/j.1365-3121.2002.00401.x.

Witts, D., Hall, R., Nichols, G., and Morley, R., 2012, A new depositional and provenance model for the Tanjung Formation, Barito Basin, SE Kalimantan, Indonesia: Journal of Asian Earth Sciences, vol. 56, pp. 77–104, doi: 10.1016/j.jseaes.2012.04.022.

Woodcock, N. H., 2004, Life span and fate of basins: Geology, vol. 32, pp. 685–688, doi: 10.1130/G20598.1.

Xian, H., Zhang, S., Li, H., Yang, T., and Wu, H., 2020, Geochronological and palaeomagnetic investigation of the Madiyi Formation, lower Banxi Group, South China: Implications for Rodinia reconstruction: Precambrian Research, vol. 336, pp. 1–13, doi: 10.1016/j.precamres.2019.105494.

Xiong, G., Wang, J., Wu, H., Zhang, H., Yu, Q., Yan, J., Jiang, X., Cui, X., and Wang, Z., 2014, Trace element and REE geochemistry of the Ediacaran Doushantuo Formation from Fanjingshan area, northeast Guizhou province, China: Carbonates and Evaporites, vol. 29, pp. 363–394, doi: 10.1007/s13146-014-0217-2.

Xu, Y.-G., Wei, X., Luo, Z.-Y., Liu, H.-Q., and Cao, J., 2014, The Early Permian Tarim large igneous province: Main characteristics and a plume incubation model: Lithos, vol. 204, pp. 20–35, doi: 10.1016/j.lithos.2014.02.015.

Yan, C., Shu, L., Faure, M., Chen, Y., and Huang, R., 2019, Time constraints on the closure of the Paleo-South China Ocean and the Neoproterozoic assembly of the Yangtze and Cathaysia blocks: Insight from new detrital zircon analyses: Gondwana Research, vol. 73, pp. 175–189, doi: 10.1016/j.gr.2019.03.018.

Yao, J., Cawood, P. A., Shu, L., and Zhao, G., 2019, Jiangnan Orogen, South China: A ∼970-820 Ma Rodinia margin accretionary belt: Earth-Science Reviews, vol. 196, p. 102,872, doi: 10.1016/j.earscirev.2019.05.016.

Yumul, G. P., 2007, Westward younging disposition of Philippine ophiolites and its implication for arc evolution: Island Arc, vol. 16, pp. 306–317, doi: 10.1111/j.1440-1738.2007.00573.x.

Yumul, G. P., Dimalanta, C. B., Tamayo, R. A., and Faustino-Eslava, D. V., 2013, Geological features of a collision zone marker: The Antique Ophiolite Complex (Western Panay, Philippines): Journal of Asian Earth Sciences, vol. 65, pp. 53–63, doi: 10.1016/j.jseaes.2012.08.017.

Zachos, J., Pagani, M., Sloan, L., Thomas, E., and Billups, K., 2001, Trends, rhythms, and aberrations in global climate 65 ma to present: Science, vol. 292, pp. 686–693, doi: 10.1126/science.1059412.

Zachos, J. C., Dickens, G. R., and Zeebe, R. E., 2008, An early Cenozoic perspective on greenhouse warming and carbon-cycle dynamics: Nature, vol. 451, pp. 279–283, doi: 10.1038/nature06588.

Zahirovic, S., Müller, R. D., Seton, M., and Flament, N., 2015, Tectonic speed limits from plate kinematic reconstructions: Earth and Planetary Science Letters, vol. 418, pp. 40–52, doi: 10.1016/j.epsl.2015.02.037.

Zahirovic, S., Müller, R. D., Seton, M., Flament, N., Gurnis, M., and Whittaker, J., 2012, Insights on the kinematics of the India-Eurasia collision from global geodynamic models: Geochemistry, Geophysics, Geosystems, vol. 13, pp. 1–25, doi: 10.1029/2011gc003883.

Zhai, Q.-g., Jahn, B.-m., Su, L., Ernst, R. E., Wang, K.-l., Zhang, R.-y., Wang, J., and Tang, S., 2013, SHRIMP zircon U-Pb geochronology, geochemistry and Sr-Nd-Hf isotopic compositions of a mafic dyke swarm in the Qiangtang terrane, northern Tibet and geodynamic implications: Lithos, vol. 174, pp. 28–43, doi: 10.1016/j.lithos.2012.10.018.

Zhang, J., Ye, T., Dai, Y., Chen, J., Zhang, H., Dai, C., Yuan, G., and Jiang, K., 2019, Provenance and tectonic setting transition as recorded in the Neoproterozoic strata, western Jiangnan Orogen: Implications for South China within Rodinia: Geoscience Frontiers, vol. 10, pp. 1823–1839, doi: 10.1016/j.gsf.2018.10.009.

Zhang, S., Jiang, G., and Han, Y., 2008, The age of the Nantuo Formation and Nantuo glaciation in South China: Terra Nova, vol. 20, pp. 289–294, doi: 10.1111/j.1365-3121.2008.00819.x.

Zhao, G., 2015, Jiangnan Orogen in South China: Developing from divergent double subduction: Gondwana Research, vol. 27, pp. 1173–1180, doi: 10.1016/j.gr.2014.09.004.

Zhao, J.-H., Asimow, P. D., Zhou, M.-F., Zhang, J., Yan, D.-P., and Zheng, J.-P., 2017, An Andean-type arc system in Rodinia constrained by the Neoproterozoic Shimian ophiolite in South China: Precambrian Research, vol. 296, pp. 93–111, doi: 10.1016/j.precamres.2017.04.017.

Zhao, J.-H., Zhou, M.-F., Yan, D.-P., Zheng, J.-P., and Li, J.-W., 2011, Reappraisal of the ages of Neoproterozoic strata in South China: No connection with the Grenvillian orogeny: Geology, vol. 39, pp. 299–302, doi: 10.1130/g31701.1.

Zhisheng, A., Kutzbach, J. E., Prell, W. L., and Porter, S. C., 2001, Evolution of Asian monsoons and phased uplift of the Himalaya–Tibetan plateau since Late Miocene times: Nature, vol. 411, pp. 62–66, doi: 10.1038/35075035.

Zhou, C., Tucker, R., Xiao, S., Peng, Z., Yuan, X., and Chen, Z., 2004, New constraints on the ages of Neoproterozoic glaciations in south China: Geology, vol. 32, pp. 437–440, doi: 10.1130/G20286.1.

Zhou, J.-C., Wang, X.-L., and Qiu, J.-S., 2009, Geochronology of Neoproterozoic mafic rocks and sandstones from northeastern Guizhou, South China: Coeval arc magmatism and sedimentation: Precambrian Research, vol. 170, pp. 27–42, doi: 10.1016/j.precamres.2008.11.002.

Zhou, M.-F., Malpas, J., Song, X.-Y., Robinson, P. T., Sun, M., Kennedy, A. K., Lesher, C., and Keays, R. R., 2002, A temporal link between the Emeishan large igneous province (SW China) and the end-Guadalupian mass extinction: Earth and Planetary Science Letters, vol. 196, pp. 113–122, doi: 10.1016/s0012-821x(01)00608-2.

Zhu, D.-C., Chung, S.-L., Mo, X.-X., Zhao, Z.-D., Niu, Y., Song, B., and Yang, Y.-H., 2009, The 132 Ma Comei-Bunbury large igneous province: Remnants identified in present-day southeastern Tibet and southwestern Australia: Geology, vol. 37, pp. 583–586, doi: 10.1130/g30001a.1.

Zhu, R., Potts, R., Pan, Y., Lü, L., Yao, H., Deng, C., and Qin, H., 2008, Paleomagnetism of the Yuanmou Basin near the southeastern margin of the Tibetan Plateau and its constraints on late Neogene sedimentation and tectonic rotation: Earth and Planetary Science Letters, vol. 272, pp. 97–104, doi: 10.1016/j.epsl.2008.04.016.

Appendix A

Supporting Information for "Emergence of the Southeast Asian islands as a driver for Neogene cooling"

These supplementary information materials provide details on the model framework used in this study. The code for the GEOCLIM model used in this study can be found at: https://github.com/piermafrost/GEOCLIM-dynsoil-steady-state/releases/tag/v1.0. The code that generated the inputs and analyzed the output of the GEOCLIM model can be found at: https://github.com/Swanson-Hysell-Group/2020_Southeast_Asian_Islands or https://doi.org/10.5281/zenodo.4021653.

A.1 Implementation of Lithology

We restricted the calculation of the weathering fluxes to the flux of dissolved Ca+Mg originating from continental silicate weathering, as they are essential for the long-term consumption of atmospheric CO_2 through silicate weathering. To calculate this flux, we need to assign the concentration of Ca and Mg (χ_{CaMg}) within the unweathered bedrock (Fig. 1 in the main text). Previous implementations of GEOCLIM have used a "diffuse lithology" where all exposed land is assigned the composition of bulk upper continental crust. These previous studies assumed that the weathering rates of all rocks was the same for each continental grid element, provided that the grid element was submitted to the same climatic conditions. Given that the hypothesis we seek to test involves the varying concentration of cations in different lithologies, we instead implement a more realistic lithologically-resolved version of the model.

The spatial distribution of lithologies is sourced from the Global Lithologic Map (GLiM) of Hartmann and Moosdorf (2012). The raw data takes the form of polygon vectors, where

GLiM ID	GLiM code	GLiM classification	GEOCLIM ID	GEOCLIM classification
1	su	unconsolidated sediments	6	sediments
2	vb	basic volcanic rocks	4	mafics
3	ss	siliciclastic sedimentary rocks	6	sediments
4	pb	basic plutonic rocks	4	mafics
5	sm	mixed sedimentary rocks	6	sediments
6	sc	carbonate sedimentary rocks	5	carbonates
7	va	acid volcanic rocks	2	felsics
8	mt	metamorphics	1	metamorphics
9	pa	acid plutonic rocks	2	felsics
10	vi	intermediate volcanic rocks	3	intermediates
11	wb	water bodies	0	water/ice
12	py	pyroclastics	2	felsics
13	pi	intermediate plutonic rocks	3	intermediates
14	ev	evaporites	5	carbonates
15	nd	no data	1	metamorphics
16	ig	ice and glaciers	0	water/ice

Table A.1: Grouping of 16 lithologic categories in GLiM Hartmann and Moosdorf (2012) to 6 broader categories for GEOCLIM.

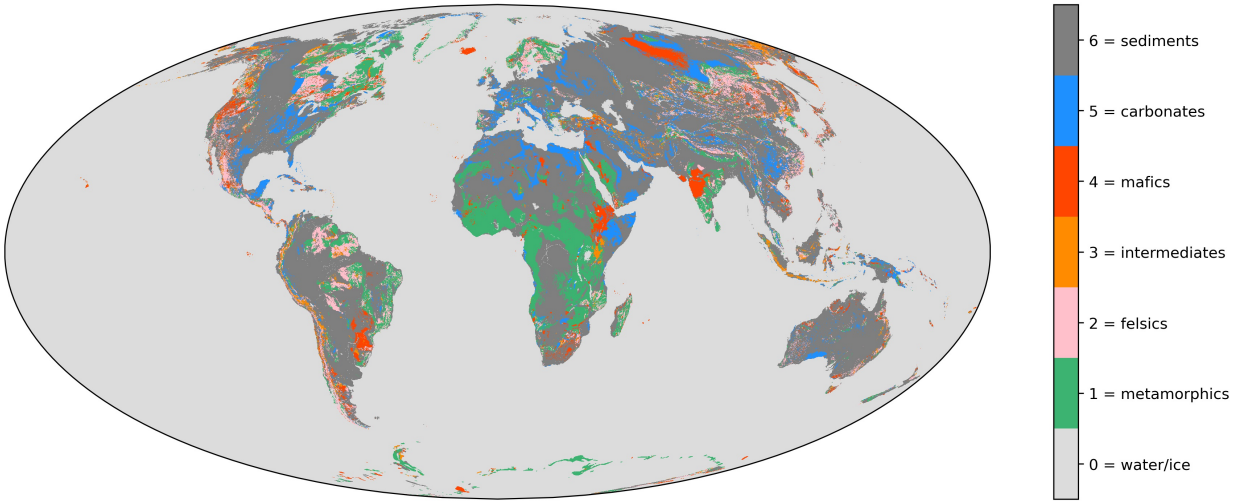

Figure A.1: Distribution of lithologies at $0.1° \times 0.1°$ resolution used in GEOCLIM modified from Hartmann and Moosdorf (2012).

each polygon is assigned one of 16 lithologic categories. We first group these 16 categories into 6 broader categories (metamorphic, felsic, intermediate, mafic, carbonate, and siliciclastic

sediment; Table A.1). Note that the siliciclastic sediment lithologic category also includes sedimentary sequences in which any carbonate is identified but is not the dominant lithology Hartmann and Moosdorf (2012). We then rasterize the polygon vectors to 0.1° × 0.1° resolution, where each pixel is assigned the lithologic category of the polygon that covers the greatest area in that pixel (i.e. the 'mode lithology'; Fig. A.1). To improve the computing time of GEOCLIM, we decrease the resolution of the raster to 0.5° × 0.5°. To do so, a 3-dimensional 720 × 360 × 7 matrix is created, in which the fraction of each 0.5° × 0.5° pixel covered by each of the 6 lithologic categories (or water/ice) is captured by the extra dimension. In this way, we calculate an area-weighted mean Ca+Mg concentration of the surface in each 0.5° × 0.5° pixel.

The Ca+Mg concentrations of felsic (1,521 mol/m^3), intermediate (4,759 mol/m^3), and mafic (10,317 mol/m^3) lithologies are assigned based on the mean of data compiled from EarthChem (www.earthchem.org/portal; calculations made in the code within the repository). For metamorphic and siliciclastic lithologies, we explore a range of feasible Ca+Mg concentrations during calibration of the silicate weathering component of GEOCLIM (*GEOCLIM Calibration*). This approach makes the simplifying assumption that all pixels of a given lithologic category share the same Ca+Mg concentration.

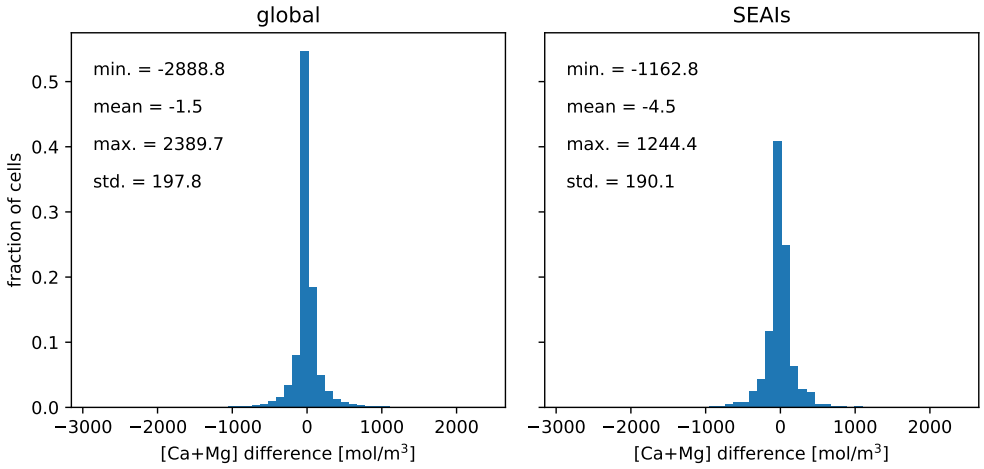

Figure A.2: Histograms showing the difference in the area-weighted mean Ca+Mg concentration of the surface in each 0.5° × 0.5° pixel that results from starting with an 0.1° × 0.1° GLiM raster versus an 0.05° × 0.05° GLiM raster. The left panel is calculated over all land pixels, whereas the right panel is calculated over land pixels in the SEAIs only. Both panels use the parameter values that produced the highest r^2 during calibration: metamorphic$_{Ca+Mg}$ = 2500 mol/m^3 and sediment$_{Ca+Mg}$ = 2000 mol/m^3.

We also explore the sensitivity of the area-weighted mean Ca+Mg concentration of the surface in each 0.5° × 0.5° pixel to the resolution of the underlying GLiM raster (Fig. A.2). We find that the difference in the area-weighted mean Ca+Mg concentration of the surface when using the 0.1° × 0.1° GLiM raster versus the 0.05° × 0.05° GLiM raster can be well explained by a tight Gaussian distribution (σ<200 mol/m^3) about a mean of ∼0 mol/m^3.

Therefore, using the lower-resolution GLiM raster does not overall bias our results to higher or lower area-weighted mean Ca+Mg concentrations of the surface, and only introduces some noise that has a magnitude that is significantly smaller than the most Ca+Mg-poor lithologic category (i.e. felsics, at 1,521 mol/m^3).

A.2 GEOCLIM Calibration

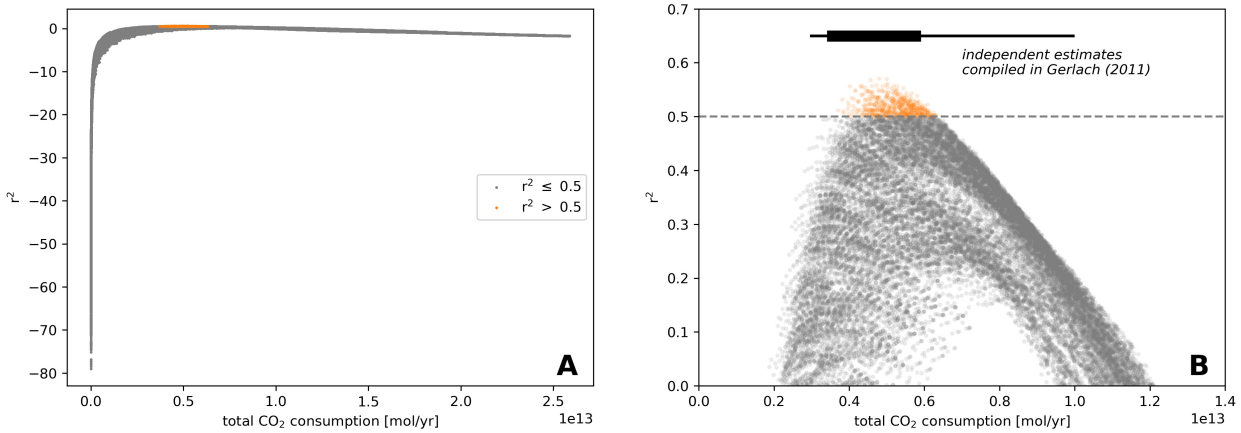

Figure A.3: A) Modeled global CO_2 consumption vs. the coefficient of determination (r^2) between modeled and data-constrained CO_2 consumption in each of the watersheds. Each point represents model output using one of the 93,600 parameter combinations (Table A.2). **B)** Same as A, but zoomed to the plotting space with positive coefficient of determination values. The black line represents the full range of estimates of the present-day non-anthropogenic global CO_2 emission rate compiled in Gerlach (2011). The black box represents the range of these estimates preferred by Gerlach (2011).

Experimental determinations of the activation energy (E_a; Equations 6 and 9) associated with the weathering of silicate minerals are variable (Brantley, 2003). However, multiple efforts to invert for E_a in basaltic watersheds with varying temperature have yielded values (41.6 ± 3.2 kJ/mol in Li et al., 2016a; 42.3 kJ/mol in Dessert et al., 2001) that are consistent with the lower end of activation energies of Ca+Mg bearing minerals in laboratory experiments such as that for diopside (40.5 ± 1.7 kJ/mol; Knauss et al., 1993) and for labradorite (42.1 kJ/mol; Carroll and Knauss, 2005). We use the value of 42 kJ/mol in our model runs. While we implement lithology-dependent Ca+Mg concentration, our implementation does not include lithology-dependent kinetics of mineral dissolution. Relative to felsic lithologies, mafic lithologies contain a higher concentration of minerals with faster dissolution kinetics (e.g. plagioclase). However, Ca+Mg from both felsic and mafic lithologies is predominantly sourced from minerals with faster dissolution kinetics, and we therefore use the same chemical weathering formulation (including the same activation energy) across lithologies.

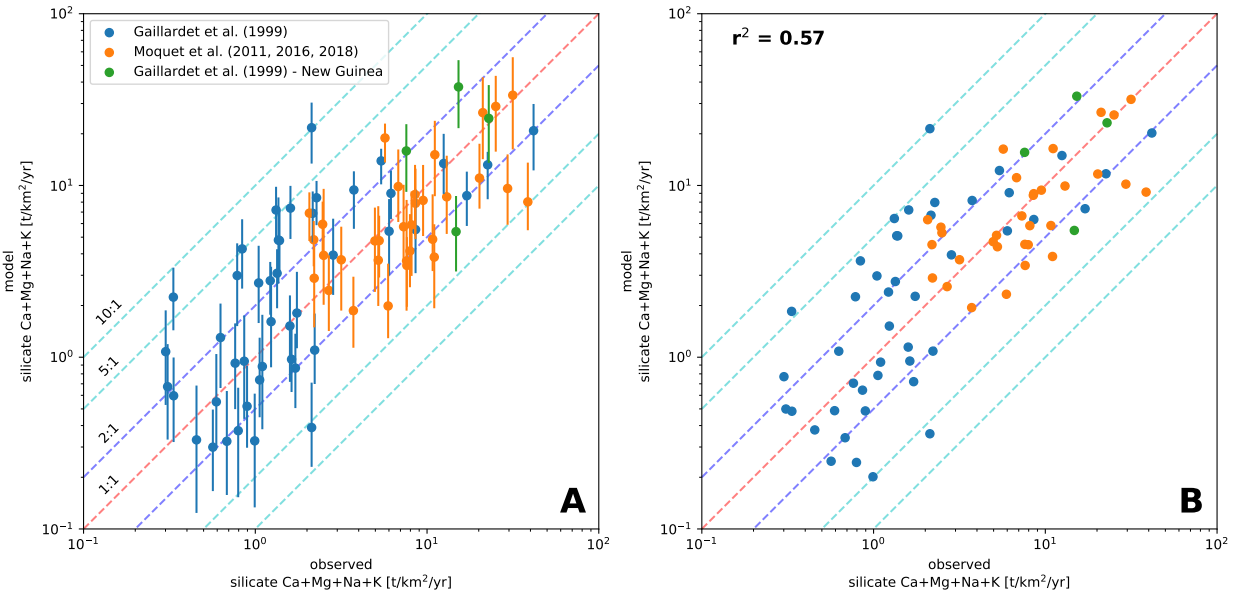

Figure A.4: Modeled vs. data-constrained CO_2 consumption in watersheds around the world. **A)** Each point represents a single watershed, and the y-value of the point shows the mean value of the 573 parameter combinations that produce individual watershed CO_2 consumption fluxes that approximate those estimated in the literature for the present-day (i.e. the orange points in Figure A.3). Whiskers extend to the minimum and maximum modeled watershed CO_2 consumption fluxes for the 573 parameters combinations. Watersheds within the compilation of Gaillardet et al. (1999) that are in the SEAIs (Fly, Kikori, Purari, and Sepik watersheds, all in New Guinea) are indicated in green. **B)** Same as A, but only showing the parameter combination that produced that highest r^2. The chemical weathering and regolith thickness maps of this parameter combination are shown in Figure A.5.

Within the equation that governs the physical erosion rate in GEOCLIM (Equation 8), the values of the exponents ($m = 0.5$ and $n = 1$) are supported by compilations (Lague, 2013). However, there is uncertainty in the value of the proportionality constant (k_e). Using the simplification of a uniform value, we therefore tune this value such that the total erosion flux in the model under present-day slope and runoff conditions (see below) matches the total erosion flux estimated in Milliman and Farnsworth (2013) (20×10^{12} kg/yr). Assuming that the density of eroded materials is 2500 kg/m^3, our tuned k_e value is 0.0029110 m^{1-m}/yr^{1-m}.

Within the equations that govern the chemical weathering rate in GEOCLIM, we identify the less constrained parameters: the proportionality constant that modifies the dependence of dissolution rate on runoff and temperature (k_d; Equation 9), the proportionality constant that modifies the dependence of dissolution rate on runoff only (k_w; Equation 9), the power constant that modifies the dependence of dissolution rate on the time that a rock particle has spent in the regolith (σ; Equation 4), and the proportionality constant that modifies the dependence of regolith production on runoff and temperature (k_{rp}; Equation 6). Furthermore, the Ca+Mg concentrations of metamorphic and siliciclastic sediment grid cells

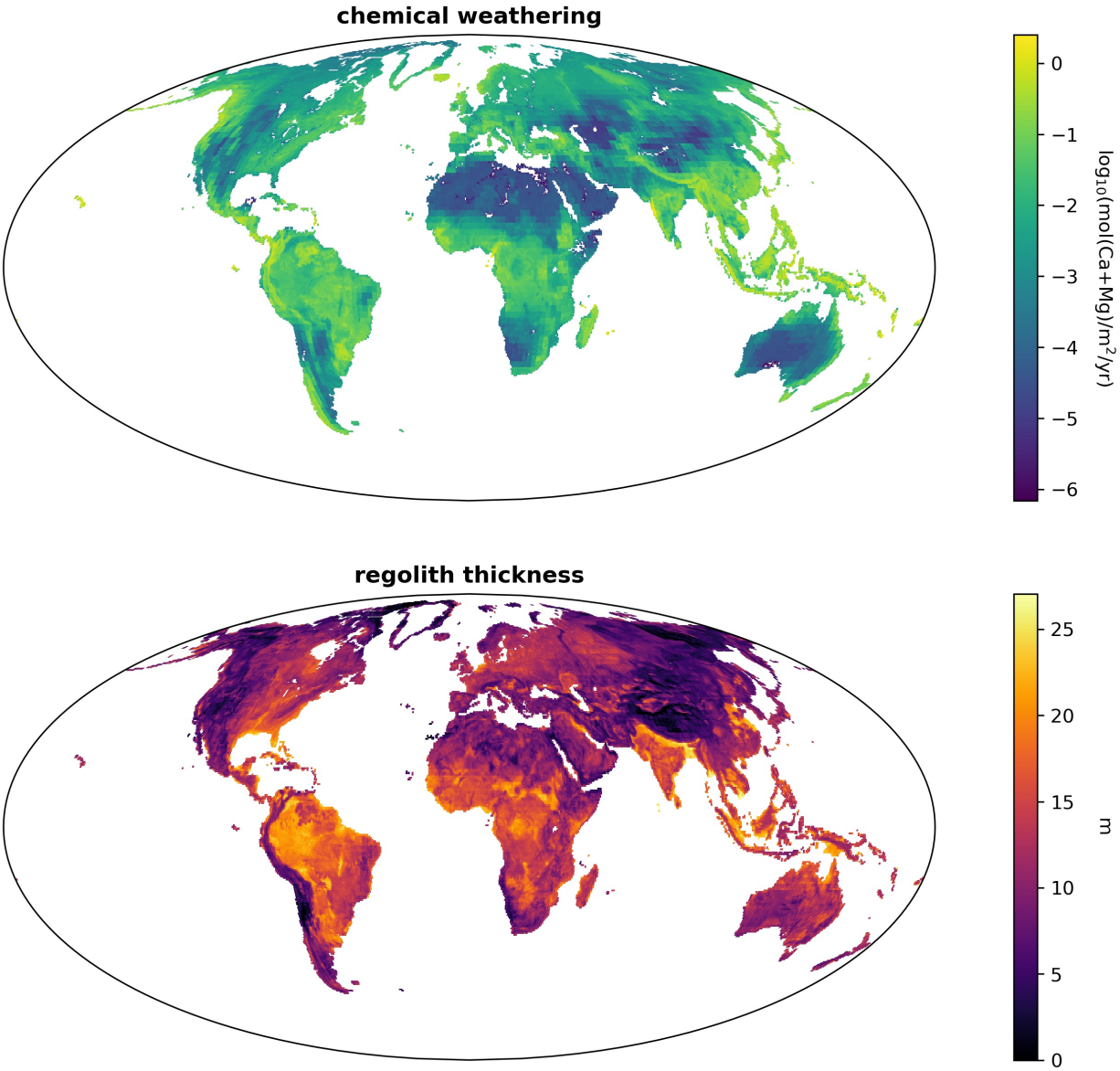

Figure A.5: Chemical weathering and regolith thickness maps associated with the GEOCLIM model run using the parameter combination that produced the highest r^2 (Fig. A.4B). Parameter values used for this model run are: $k_d = 5 \times 10^{-4}$, $k_w = 1$, $\sigma = -0.4$, $k_{rp} = 1 \times 10^{-2}$, metamorphic$_{Ca+Mg}$ = 2500 mol/m^3, sediment$_{Ca+Mg}$ = 2000 mol/m^3.

are difficult to define. We allow these parameters to vary within reasonable bounds during the calibration stage of GEOCLIM. In total, we test 93,600 unique parameter combinations (Fig. A.4; Table A.2).

We compute spatially-resolved long-term CO_2 consumption (i.e. Ca+Mg fluxes) using

k_d unitless	k_w unitless	σ unitless	k_{rp} unitless	$\mathbf{metamorphic_{Ca+Mg}}$ mol/m^3	$\mathbf{sediment_{Ca+Mg}}$ mol/m^3
1×10^{-5}	1×10^{-3}	-0.4	1.2×10^{-3}	1500	500
2×10^{-5}	2×10^{-3}	-0.2	2×10^{-3}	2000	1000
5×10^{-5}	5×10^{-3}	-0.1	3×10^{-3}	2500	1500
1×10^{-4}	1×10^{-2}	0	5×10^{-3}	3000	2000
2×10^{-4}	2×10^{-2}	0.1	1×10^{-2}	3500	2500
5×10^{-4}	5×10^{-2}	0.3	1.5×10^{-2}	4000	3000
1×10^{-3}	1×10^{-1}				
2×10^{-3}	2×10^{-1}				
5×10^{-3}	5×10^{-1}				
1×10^{-2}	1				

Table A.2: Values tested for poorly constrained parameters in the silicate weathering component of GEOCLIM. Every permutation of the listed values were tested (except those permutations where the Ca+Mg concentration of the sediments are higher than that of the metamorphics), resulting in 93,600 unique parameter combinations.

present-day runoff (UNH/GRDC Composite Runoff Fields V1.0; Fekete et al., 1999), temperature (CRU TS v.4.03; Harris et al., 2013), and slope (Shuttle Radar Topography Mission; Farr et al., 2007) fields. As described in the main text, we sum the computed CO_2 consumption over large-scale watersheds that appear in the global compilation of Gaillardet et al. (1999), as well as smaller-scale watersheds of the Amazon Basin (HYBAM network) in the compilation of Moquet et al. (2011), Moquet et al. (2016), and Moquet et al. (2018). The latter are nested watersheds, which requires upstream weathering fluxes to be subtracted from downstream fluxes. Watersheds for which this subtraction yields an aberrant value are not considered. 80 watersheds in total are used in this study. We calculate the coefficient of determination (r^2) between computed and measured CO_2 consumption in each of these basins:

$$r^2 = 1 - \frac{\sum \left[\log_{10}(M_i) - \log_{10}(O_i)\right]^2}{\sum \left[\log_{10}(O_i) - \overline{\log_{10}(O)}\right]^2}$$

M_i is the modeled CO_2 consumption over watershed i, O_i is the observed CO_2 consumption over watershed i, and $\overline{\log_{10}(O)}$ is the mean of the log of observed CO_2 consumption over all watersheds.

The majority of the original 93,600 parameter combinations produce CO_2 consumption maps with poor fits to the measured watershed data (Fig. A.3). Given that the coefficient of determination (r^2) is calculated using Equation A.2 rather than fitting a linear model, many of the combinations associated with particularly poor fits result in negative r^2 values (Fig. A.3). However, given the right permutation of parameters, GEOCLIM produces CO_2 consumption maps that fit the measured watershed data reasonably well. We eliminate

all parameter combinations that produce a $r^2 \leq 0.5$, which leaves 573 unique parameter combinations (Figs. A.3 and A.4).

Global CO_2 consumption calculated from these 573 parameter combinations ranges from 3.7×10^{12} mol/yr to 6.3×10^{12} mol/yr, with a mean of 5.2×10^{12} mol/yr. These estimates fall within the range of independently estimated outgassing rates for the present-day: the full range of estimates of the present-day non-anthropogenic global CO_2 emission rate compiled in Gerlach (2011) is $3.0–10.0\times10^{12}$ mol/yr, with the preferred range of those estimates being $3.4–5.9\times10^{12}$ mol/yr (Fig. A.3B).

Each parameter combination predicts a different total CO_2 consumption that should match the CO_2 degassing at steady-state. Hence, in the non-calibration GEOCLIM experiments, each parameter combination is used with its corresponding steady-state CO_2 degassing. In these estimates, we are not including the effects of reverse weathering (Michalopoulos and Aller, 1995) as it is not clear how it should be parameterized and it is interpreted to be a relatively minor flux in the Cenozoic (Isson and Planavsky, 2018). Formation of authigenic clays that scales with Ca and Mg concentration of riverine waters could decrease the CO_2 consumption associated with silicate weathering although the overall trend seen in this study would remain.

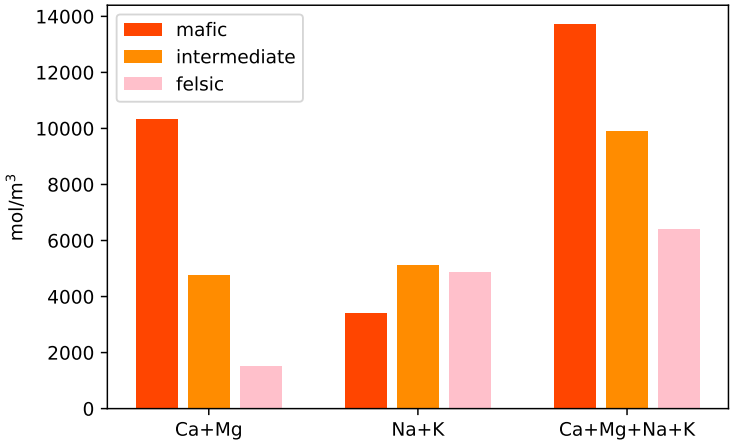

Figure A.6: Ca, Mg, Na, and K concentrations within mafic, intermediate, and felsic lithologies, as calculated based on the mean of data compiled from EarthChem.

A related issue is that our analysis focuses on the weathering of Ca and Mg silicates. Sources of alkalinity to the ocean include the four major cations of Ca, Mg, Na and K. A common approach for the long-term carbon cycle follows that of Berner et al. (1983) where an emphasis is placed on Ca and Mg with the weathering of Na and K silicates considered to not be a long-term sink of CO_2. The reasoning behind this assumption is that while weathering of these silicates can lead to transient uptake of CO_2, this uptake is balanced by release. The ultimate mechanism through which silicate weathering sequesters carbon is the incorporation of Ca+Mg carbonates into the lithosphere. Given that Na and K are not

precipitating carbonate, when simulating long term steady-state solutions, as we are here, it is valid to follow the approach of Berner et al. (1983) and not consider the Na and K cycles. Complexity arises given the long residence time of Na and K in seawater (∼45–80 m.y. for Na, and ∼8–10 m.y. for K; Emerson and Hedges, 2008; Lécuyer, 2016) and the lag between the generation of alkalinity and its consumption that could modulate the carbonate system. Dynamic modeling of the effects of the Na and K cycles on the long term carbon cycle is an area ripe for future research although uncertainty in their sinks and the timescale of the processes that control them make them difficult to parameterize. An alternative approach for estimating carbon sequestration associated with silicate weathering that sought to incorporate all four cations was taken by France-Lanord and Derry (1997) who used a formulation of $\Delta CO_2 = \Delta Mg + \Delta Ca + 0.15\Delta Na + 0.1\Delta K$. This relationship, also applied by Schopka et al. (2011), assumes that all Ca^{2+} and Mg^{2+} eventually forms carbonates and applies an estimate that 20% of K^+ and 30% of Na^+ exchanges for Ca and Mg and ultimately produces carbonate (and considers charge balance). Different parameterizations such as that of France-Lanord and Derry (1997) could modulate our estimates, but the importance of the emergence of the SEAIs on Neogene pCO_2 would remain unchanged. The relative importance of mafic lithologies also remains given that with significantly higher Ca+Mg concentrations and subequal Na+K concentrations to intermediate/felsic lithologies they have the highest Ca+Mg+Na+K concentrations (Fig. A.6).

A.3 Climate Model

For the climate model component of GEOCLIM, we use temperature and runoff fields from a subset of the GFDL CM2.0 experiments (Delworth, 2006; Delworth et al., 2006; available for download at https://nomads.gfdl.noaa.gov/dods-data/gfdl_cm2_0/) These experiments were performed in order to explore the effect of various changes in forcing agents on climate since ca. 1860 at 2.0° × 2.5° resolution. In the "1860 control" experiment, forcing agents representative of conditions ca. 1860 (including CO_2, CH_4, N_2O, O_3, sulfates, carbon, dust, sea salt, solar irradiance, and the distribution of land cover types) are held constant for 500 years after reaching equilibrium. pCO_2 in 1860 is assumed to be 286 ppm. In the "+1%/yr to 2×" experiment, initial conditions are taken from the "1860 control" experiment, then pCO_2 is prescribed to increase from 286 ppm at a compounded rate of +1% per year for 70 years, when pCO_2 reaches double (572 ppm) of the initial value. pCO_2 is then held constant until the end of the 280 year experiment. All non-CO_2 forcing agents are held constant. The "+1%/yr to 4×" experiment is identical to the "+1%/yr to 2×" experiment, except that pCO_2 is prescribed to increase for 140 years, when pCO_2 reaches quadruple (1144 ppm) of the initial value. pCO_2 is then held constant for 160 years. We take the mean of the last 100 years of each of these three experiments (when pCO_2 is being held constant at its final level) to obtain temperature and runoff fields for 286, 572, and 1144 ppm pCO_2 respectively. Temperature and runoff fields associated with pCO_2 values between the three modeled pCO_2 levels (286, 572, and 1144 ppm) are obtained through linear interpolation between the model

results.

Given that precipitation in the SEAIs is primarily driven by large-scale convective upwelling leading to high precipitation over both land and water (Donohoe and Voigt, 2017), the current approach of using a climate model forced by modern paleogeography for all SEAIs scenarios is a reasonable approximation for this region. However, for paleogeographic change that would have very significantly modified precipitation over broad swathes of land such as growth of the Himalaya, this approach of using modern climate model results is not viable. The climate model also assumes the present-day extent of ice-sheets for all $p\mathrm{CO}_2$ levels. However, without ice-sheets, the global climate would be warmer for a given $p\mathrm{CO}_2$ (hysteresis loop; Pollard and DeConto, 2005), but the amount of emergent land would be lower. We expect this bias to be minimal, as all of our modeled $p\mathrm{CO}_2$ estimates fall below the glaciation threshold for Antarctica.

A.4 Southeast Asian Islands Scenarios

We use geological data to quantify the changes in the area of the SEAIs over the past 15 m.y. (described in detail in *Paleoshoreline Reconstruction and Geological Synthesis*). To generate the lithologic map used in the "removed SEAIs" scenario (Fig. A.7), we remove all land associated with arc-continent collision in the SEAIs. To generate the lithologic map used in the "paleo-SEAIs" scenarios (Fig. A.7), we take the estimated paleoshorelines of the SEAIs for 15, 10, and 5 Ma, then remove all land that falls outside of these bounds. The slope and lithologic classification of each pixel is identical to that of the present day, provided that these pixels fall within the estimated paleoshorelines of the SEAIs for their respective time slice. This means that while we are changing the amount of emergent land, we are not changing the latitudinal or longitudinal position and are keeping the slope of emerged pixels the same. Given that similar distributions of lithology and slope are reasonable in the past and that latitudinal translation has been relatively minor, we consider this simplification to be reasonable to first-order (Fig. A.10). We then add land in the region that is not exposed today. The assignment of lithology, runoff, and slope for pixels on the Sunda Shelf is not trivial, given that the shelf is not currently exposed. As discussed in *Paleoshoreline Reconstruction and Geological Synthesis*, the Sunda Shelf is a flat-lying, relatively stable platform of continental crust. Islands between Malaysia/Sumatra and Borneo are composed of granite and are surrounded by shallow marine siliciclastic sediments (Darmadi et al., 2007; Hall, 2009, 2013b). However, basement highs of granite do not appear further to the northwest in the Gulf of Thailand, and seismic and drill core data suggest siliciclastic fluvial systems draining out toward the South China Sea when the Sunda Shelf was exposed (Darmadi et al., 2007). We therefore assign pixels of the Sunda Shelf between Malaysia/Sumatra and Borneo to be 50% felsic and 50% sediment, and pixels further to the north to be 100% sediment. For the slope, we take the mean slope value (0.0043 m/m) of relatively flat land on eastern Sumatra, and assign this value to all pixels of the Sunda Shelf. For the runoff, we linearly interpolate along latitude bands between present-day land pixels to obtain runoff values for

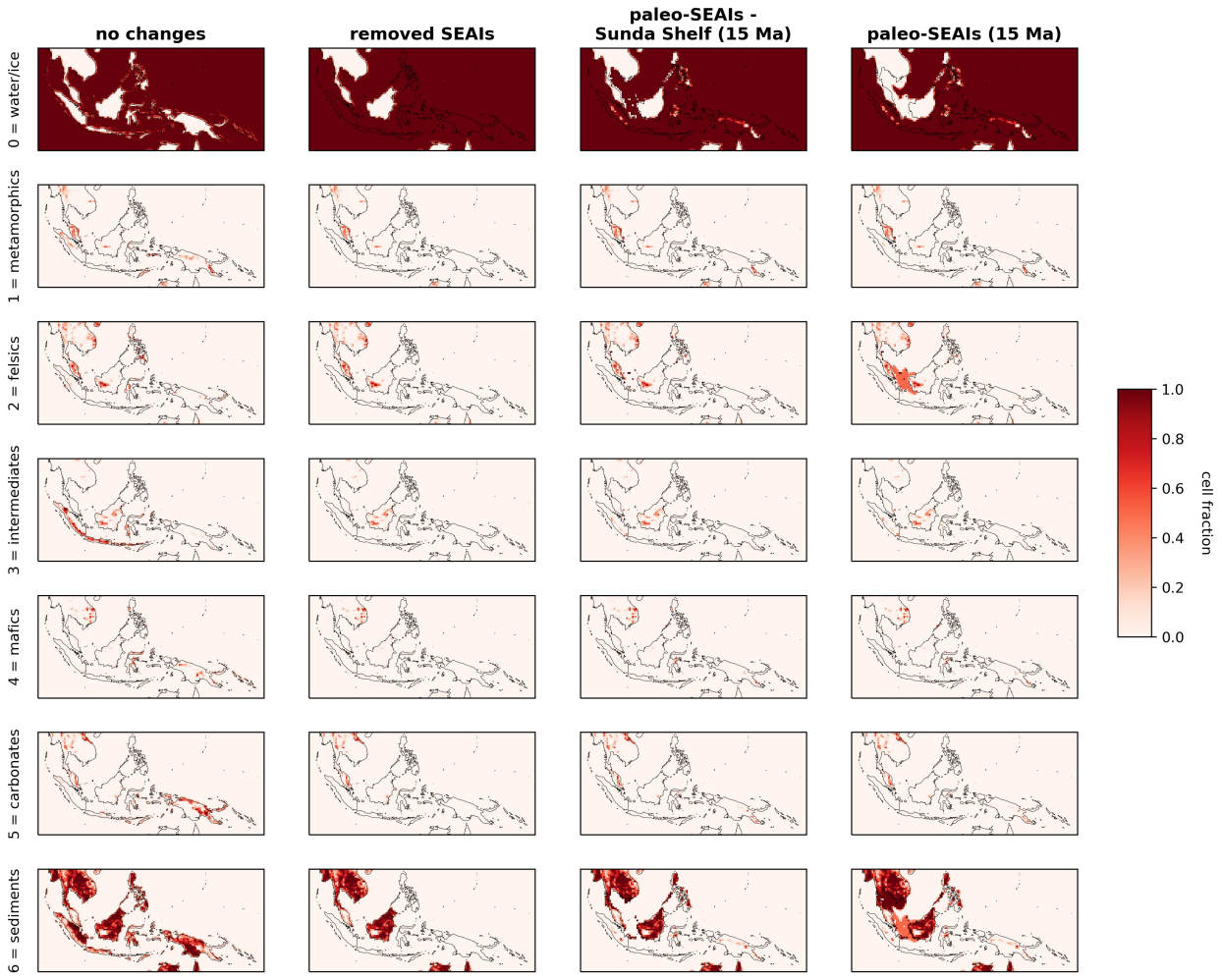

Figure A.7: 0.5° × 0.5° lithologic maps of the Southeast Asian islands (SEAIs) used to force GEOCLIM. Only the 15 Ma scenarios are shown here, but the 10 and 5 Ma scenarios would be similar, using the 10 and 5 Ma shorelines shown in Figure 1 of the main text instead. Each column represents a tested scenario. Each row represents a lithologic category. Solid black lines show present-day shorelines. Total areas of each lithologic category within the SEAIs for each of these tested scenarios is shown in Figure A.8.

the presently-submerged Sunda Shelf. This approach preserves large N-S variation in runoff associated with the large-scale Hadley circulation and therefore should be reasonable to first-order, although it does not accurately capture the smaller-scale interactions between land and ocean/atmosphere circulation. For other minor islands in the region that were exposed 15, 10, or 5 m.y. ago, but are currently submerged, we take the same approach as that described for the Sunda Shelf to generate the runoff field. For the slope and lithology, we take the mean slope and Ca+Mg concentrations from neighbouring pixels. We also remove the Greenland ice sheet in the "paleo-SEAIs" scenarios, to be consistent with Northern Hemi-

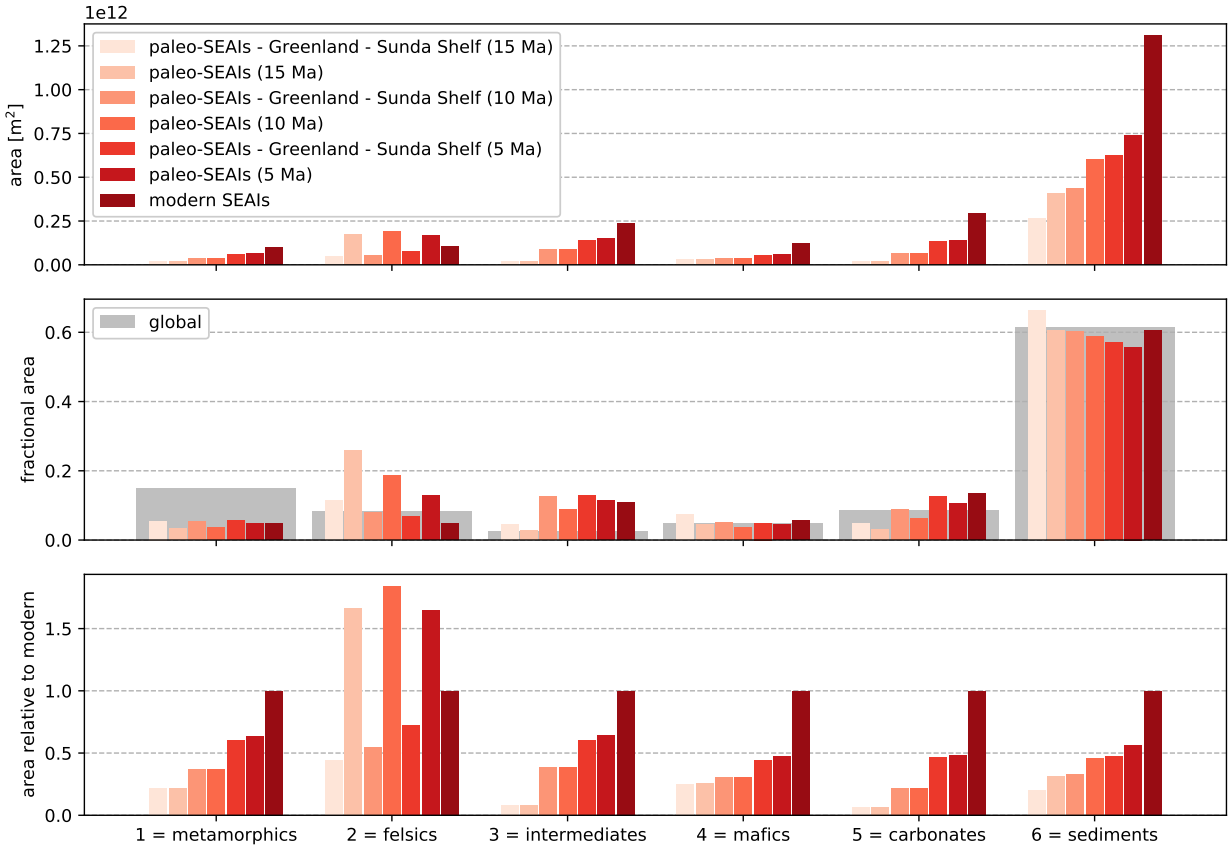

Figure A.8: Total area of the lithologic categories within the SEAIs for each tested scenario. Note that the grey bars in the middle panel indicate the fractional area of each lithologic category for the entire Earth.

sphere ice sheets developing after 5 Ma (Haug et al., 2005). The runoff field over Greenland is generated using the same method as that for the Sunda Shelf. For the slope, we take the mean slope value (0.0529 m/m) of land for which slope data exists around the edges of Greenland, and assign this value to all pixels of Greenland covered by the ice sheet. We also assign the Ca+Mg concentration of bulk continental crust to these pixels.

To explore the sensitivity of our results to the inclusion of the Sunda Shelf and the removal of the Greenland ice sheet, we also tested "paleo-SEAIs - Greenland" scenarios for 15, 10, and 5 Ma, which are identical to that of the "paleo-SEAIs" scenarios without the removal of the Greenland ice sheet. We also tested "paleo-SEAIs - Greenland - Sunda Shelf" scenarios for 15, 10, and 5 Ma, which are identical to that of the "paleo-SEAIs" scenarios without the inclusion of the Sunda Shelf and the removal of the Greenland ice sheet. We find that the estimated steady state $p\mathrm{CO}_2$'s for the "paleo-SEAIs - Greenland" and "paleo-SEAIs - Greenland - Sunda Shelf" scenarios are only marginally higher than those of the "paleo-SEAIs" scenarios (Fig. A.9), suggesting that our results are relatively insensitive to the

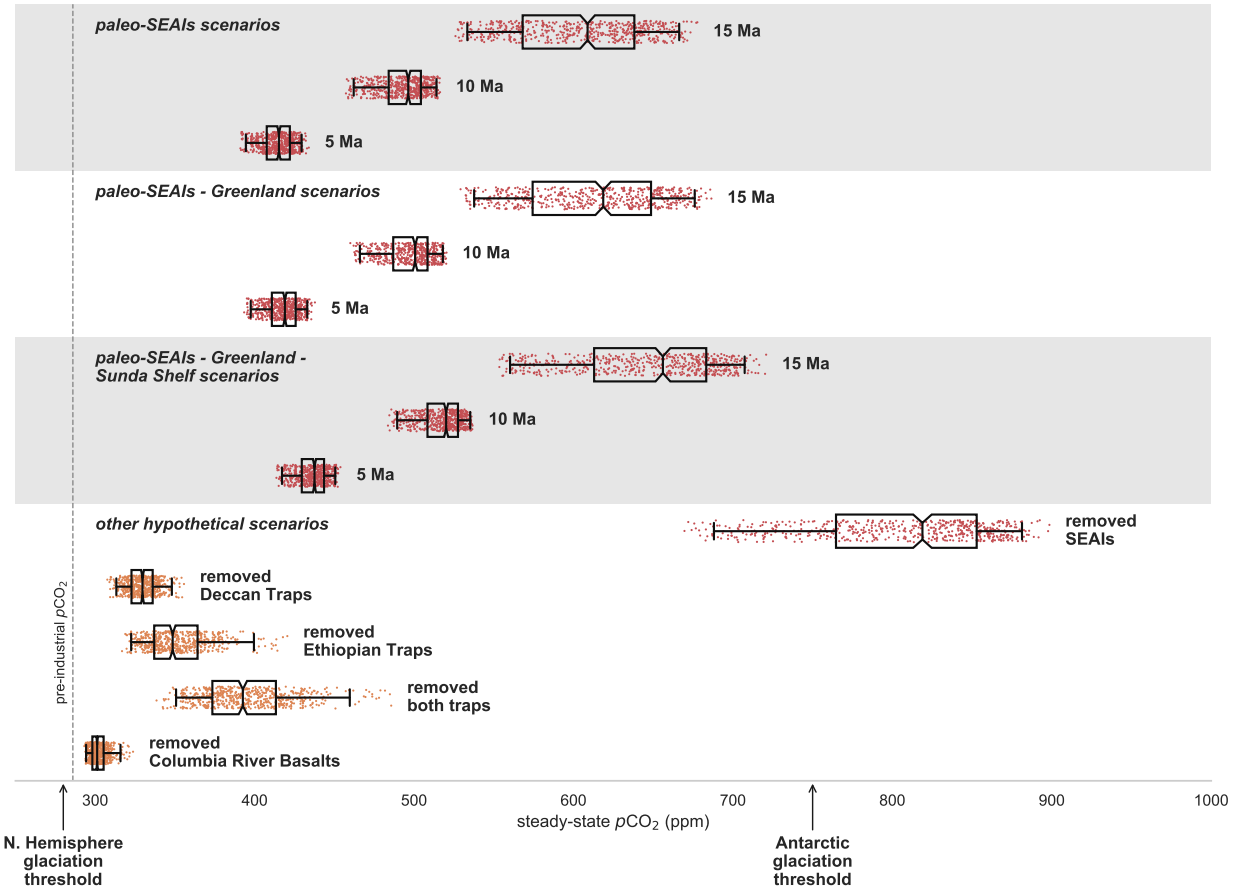

Figure A.9: Steady-state $p\mathrm{CO}_2$ estimates from GEOCLIM for the various scenarios discussed in the text. For each of the 13 scenarios, each point represents an estimate from one of the 573 unique parameter combinations that resulted in reasonable total global CO_2 consumption and most closely matched estimates of present-day CO_2 consumption in 80 watersheds around the world. The box encloses the middle 50% of the $p\mathrm{CO}_2$ estimates (i.e. the interquartile range), and the notch represents the median with its 95% confidence interval. The whiskers extend to the 2.5 and 97.5 percentile values. This figure is identical to Figure 2 in the main text, except for the addition of the scenarios used to test the sensitivity of the results to the inclusion of the Sunda Shelf and the removal of the Greenland ice sheet.

inclusion of the Sunda Shelf and the removal of the Greenland ice sheet. This insensitivity can be attributed to the low Ca+Mg concentrations of felsic and sediment lithologies in conjunction with the low relief across the Sunda Shelf, and the low runoff values at high latitudes.

Proxy-based $p\mathrm{CO}_2$ estimates for the past 20 m.y. are shown in Figure A.11 (Bereiter et al., 2015; Foster et al., 2017; Ji et al., 2018; Cui et al., 2020). Even when stringent quality criteria and the latest understanding of each of the $p\mathrm{CO}_2$ proxies have been applied to available $p\mathrm{CO}_2$ records, both significant uncertainty in the estimated $p\mathrm{CO}_2$ for any given

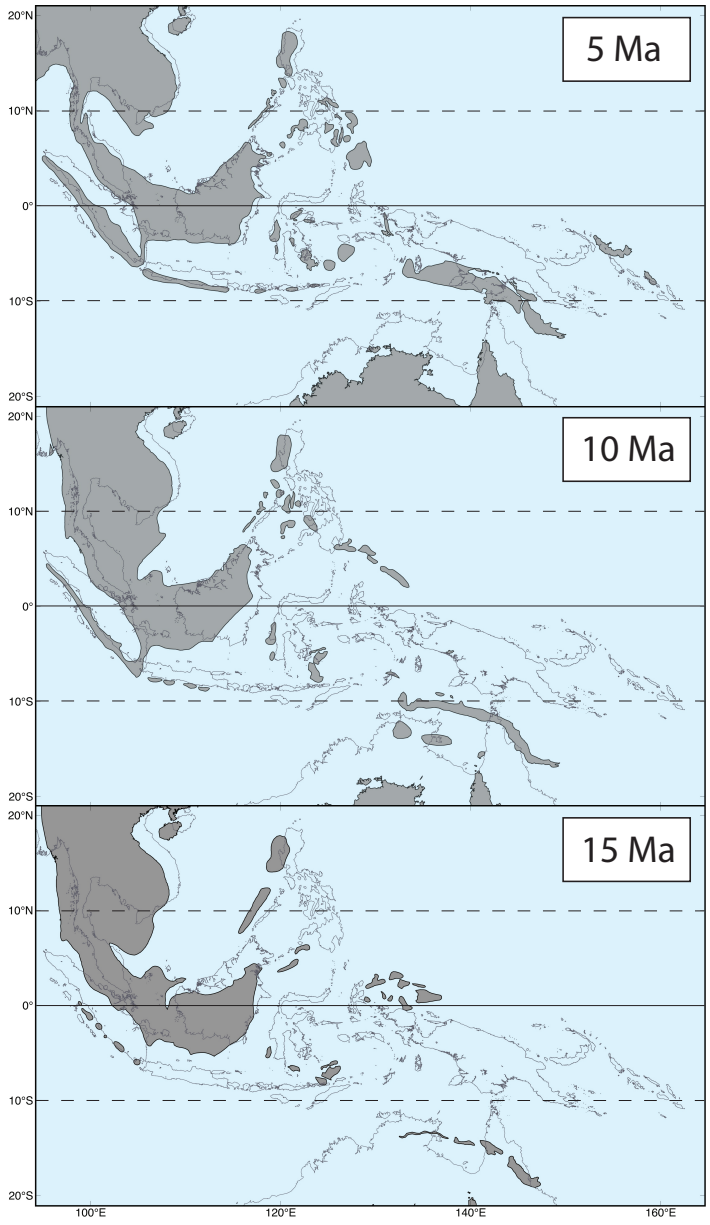

Figure A.10: Paleogeographically-reconstructed paleoshorelines for the SEAIs at 5, 10, and 15 Ma, using the paleoshoreline reconstruction of this study coupled to the paleogeographic model of Matthews et al. (2016).

data point as well as disagreement between techniques remain. Statistical methods that are often utilized in an attempt to extract trends from this data (e.g. locally-weighted scatter plot smoothing, LOWESS) evaluate the mean (with some weighting) of the highly scattered data in a given time interval. However, such methods are only appropriate for estimating

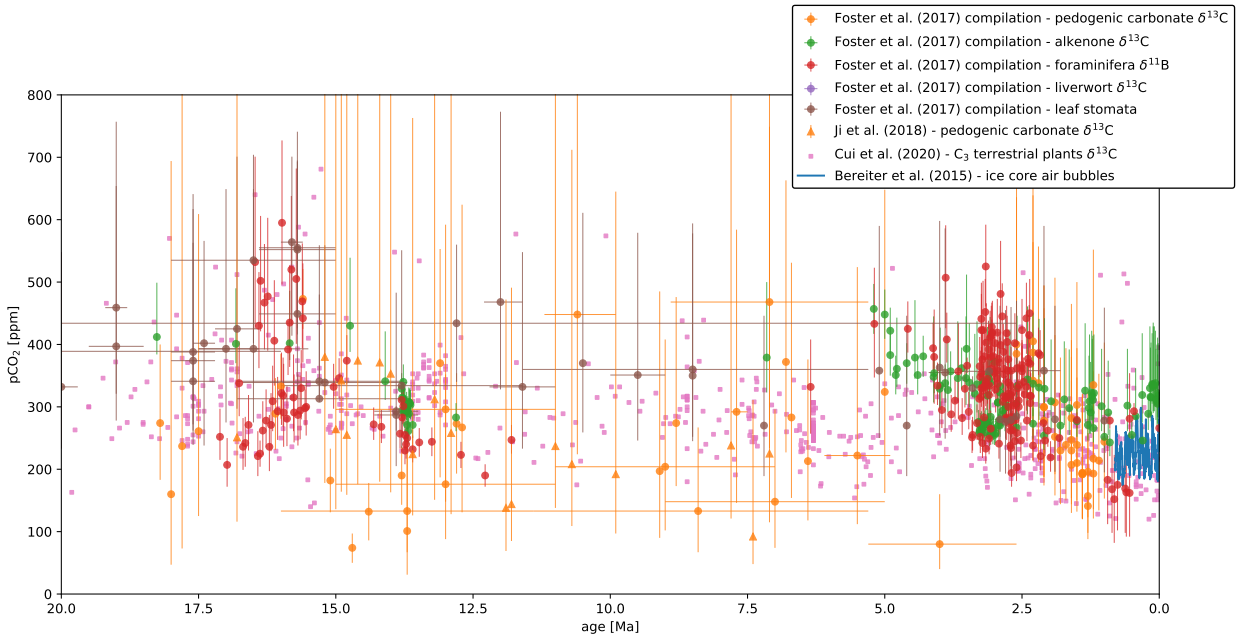

Figure A.11: Proxy-based $p\mathrm{CO}_2$ estimates for the past 20 m.y. For data that were compiled within Foster et al. (2017), error bars indicate standardized uncertainties. For the Ji et al. (2018) data, error bars represent the 16-84th percentile of resampled estimates. Individual data points from Cui et al. (2020) were not published with uncertainties. The Bereiter et al. (2015) data come from the EPICA Dome C ice core.

the "true" value at any given time interval in datasets in which individual data points are being drawn from a single distribution about a mean value. The $p\mathrm{CO}_2$ proxy compilation shown in Figure A.11 consists of several distinct techniques and samples, each with their own set of assumptions and associated probability distributions that influence their reported values. Therefore, running a regression through these values neglects the fact that some of these techniques/samples are likely more reliable than the others. Constraining how robust each $p\mathrm{CO}_2$ proxy technique is remains an important challenge, and as such the "true" $p\mathrm{CO}_2$ could plausibly lie anywhere within the full range of proxy-based $p\mathrm{CO}_2$ estimates for any given time interval. Nevertheless, our modeled $p\mathrm{CO}_2$ values for 15 Ma (Fig. A.9) resemble the higher end of proxy-based $p\mathrm{CO}_2$ estimates for the early-mid-Miocene. Given this scatter in the proxy-based $p\mathrm{CO}_2$ estimates, we instead infer the Neogene cooling trend from the Miocene benthic foram oxygen isotope record shown in Figure 1 in the main text.

A.5 Paleoshoreline Reconstruction and Geological Synthesis

Geological maps, stratigraphic data, and previous paleoshoreline compilations were used to calculate the changes in different types of subaerially exposed rocks in the SEAIs. Following Molnar and Cronin (2015), we analyzed the area changes of islands that are larger than $\sim$200 km^2 (Fig. 1 in main text). We also included changes in areas of submerged continental shelves that were previously exposed, like the Sunda Shelf. Larger islands were further divided into regions based upon their position on microplates as defined by Matthews et al. (2016). Miocene to present stratigraphic columns were compiled from each region to develop an age model for paleoenvironmental indicators. In general, carbonate strata and thin-bedded siliciclastic strata were assumed to be deposited in a subaqueous marine environment, whereas evidence for exposure and terrestrial siliciclastic deposits were used as indicators of a subaerial paleoenvironment. Following previous paleoshoreline compilations and these environmental indicators, paleoshorelines were outlined in QGIS to calculate areas for the Early Pliocene (5 Ma), Late Miocene (10 Ma), and Middle Miocene (15 Ma). The paleoshoreline reconstructions within the paleogeographic models broadly coincide with sub-Epoch boundaries (i.e. Early Miocene = 23–16 Ma, Middle Miocene = 15.99–11.61 Ma, Late Miocene = 11.6–5.4 Ma, Pliocene =5.39–3.8 Ma), but we recognize that the biostratigraphic resolution is an additional source of uncertainty.

Several new sources for paleoshoreline data have become available since Molnar and Cronin (2015). Particularly, for Sulawesi, we follow the recent stratigraphic compilation and paleoshorelines delineated by Nugraha and Hall (2018), and in New Guinea, we follow Gold et al. (2017) and Harrington et al. (2017). Although the outlines of our paleoshorelines are significantly different from those used for 5 Ma by Molnar and Cronin (2015) our calculated area is comparable.

Malay Peninsula and Sunda Shelf

Paleogeographic reconstructions of Peninsular Malaysia suggest that it has been largely exposed over the last 20 Ma (Hall and Nichols, 2002; Hall, 2013b). Although the majority of the Sunda Shelf is currently submerged, large portions of this flat-lying, relatively stable platform of continental crust were also emergent throughout the Neogene, and were repeatedly subaerially exposed during the Pleistocene as recently as the Last Glacial Maximum (Hall and Nichols, 2002). Similarities between the terrestrial biotas of Borneo and mainland Southeast Asia confirm the existence of land bridges on the Sunda Shelf throughout the Miocene (Moss and Wilson, 1998). Eocene through Miocene rifting of the South China Sea resulted in subsidence throughout the Sunda Shelf (Morley and Morley, 2013). Grabens associated with this subsidence became freshwater rift lakes that later transitioned to partially enclosed inland seas and extensive brackish or saline wetland environments. Palynological analysis suggests widespread swamp environments persisting through the Late Miocene (Morley and

Morley, 2013). Basement highs (e.g. the Natuna Arch, currently subaerially exposed as the largely granitic island of Natuna off SW Borneo, as well as the granitic Tin Islands south of the Malay Peninsula) are typically bounded by Paleogene to Neogene basins dominated by shallow marine clastic fill (Darmadi et al., 2007). Most paleogeographic reconstructions of the region incorporate some degree of exposure of the Sunda Shelf from 20 Ma onwards (Hall, 2013b; Madon et al., 2013), although it is omitted in the 5 Ma paleogeographic model of Molnar and Cronin (2015).

Borneo and Palawan

Our reconstructions of the paleoshorelines of Borneo and Palawan are largely informed by extant paleogeographic constructions detailed in Hall (2001, 2013a,b), as well as geologic maps and local shoreline reconstructions found in van de Weerd and Armin (1992); Witts et al. (2012); Madon et al. (2013); Kessler and Jong (2015). Comprised of Paleozoic to Mesozoic crustal components that were largely accreted to Sundaland by the late Cretaceous (Metcalfe, 2013), the southern and western portions of Borneo (SW Kalimantan) have been subaerially exposed throughout the Neogene (Hall, 2013a,b). A collision along the northern margin of Borneo associated with the initiation of rifting in the South China Sea resulted in the late Eocene uplift of the Central Range mountains (Hutchison, 1996), which provide sediment to basins along the Southern (Kalimantan) and northern (Sabah and Sarawak) coasts of the island. In the east, the Barito, Kutei, and Tarakan basins developed as a single area of subsidence (associated with the opening of the Makassar Straits in the Eocene) before the basins were isolated by Oligocene faulting and Miocene uplift (Witts et al., 2012). The Kutei Basin is characterized by eastward-prograding deltaic and shallow shelf deposits that have been steadily supplied with sediment from the Schwaner Mountains of SW Kalimantan and the Central Range (van de Weerd and Armin, 1992). North of the Kutei Basin, the deltaic deposits found in the Tarakan Basin similarly prograde eastward from the mid Miocene onward, fed by the northern drainages of the Central Range (Satyana et al., 1999). In SE Kalimantan, the Barito Basin is bounded to the east by the ophiolite-bearing Meratus Mountains. Sedimentological data suggests that the Meratus Mountains were not emergent until the Late Miocene (Witts et al., 2012).

Separated from the Paleozoic continental core of SW Borneo by the Lupar Line suture zone, the northern portion of Borneo (Sabah) is underlain by ophiolitic basement that extends to Palawan (Hall et al., 2008; Ilao et al., 2018). The Sarawak Basin and NW Borneo trough offshore Sabah host >10 km-thick Neogene sedimentary sequences, indicative of the extent and duration of exhumation in northern Borneo (Hall et al., 2008). The Late Oligocene/Early Miocene Sabah Orogeny resulted in the uplift of both Sabah and southern Palawan (Hall, 2013a), as well as the obduction of the Palawan ophiolite and Telupid ophiolite of northern Sabah. Under-thrusting of thinned passive-margin continental crust beneath these suprasubduction ophiolites resulted in Early to Middle Miocene exhumation and offshore unconformities (Hall et al., 2008). Early Miocene sediments in northern Sabah have a provenance from Palawan (Suggate et al., 2014), indicating that Palawan, like north-

ern Borneo, experienced uplift during the Sabah orogeny. However, initiation of back-arc extension in the Sulu Sea around 19 Ma (Hall, 2013a) resulted in the subsidence of the eastern Palawan Mountains, eliminating or reducing the role of Palawan as a sediment source for the Borneo trough. The 14 Ma Capoas Granite on Palawan and the 7.5 Ma Kinabalu Granite in Sabah are interpreted to be the result of crustal thinning related to pulses of regional backarc extension (Hall, 2013a). Thermochronological data from the Sabah highlands suggest extremely rapid uplift (7 km/m.y.) and exhumation during the latest Miocene and early Pliocene, resulting in the recent formation of Mt. Kinabalu, the tallest peak in Borneo (Cottam et al., 2013).

Sulawesi

For the paleoshorelines of Sulawesi, we largely followed the recent stratigraphic compilation and paleoshorelines compilation of Nugraha and Hall (2018). Geographically, Sulawesi can be divided into a central highland region flanked by North, South, Southeast, and East Arms. These arms have high relief (>3 km) that are separated by deep basins and broadly define Sulawesi's seven tectonic provinces: 1) the West Sulawesi magmatic arc of the South Arm, 2) the Central Sulawesi metamorphic Belt, 3) the Sangihe arc of the North Arm, 4) the East Sulawesi Ophiolite of the East Arm, 5) the southeast metamorphic belt of the Southeast Arm, and the microcontinental blocks of 6) Banggai-Sula and 7) Buton-Tukang Besi (Hamilton, 1979; Katili, 1978). Like SW Borneo, the North and South Arms, and much of Central Sulawesi, are underlain by continental blocks that rifted off of the Australian-Birds Head margin in the Jurassic and collided in the Cretaceous with Eurasian basement of Sundaland as part of the Woyla Arc system (Parkinson, 1998b; Hennig et al., 2016; Hall, 2017; Hennig et al., 2017a). After collision, subduction polarity reversed and a Cretaceous to Miocene SE-facing volcanic arc developed (Polvé et al., 1997; Elburg and Foden, 1998) that was connected to the paleo-Sunda Arc (Hall, 2002), also referred to as the Great Indonesian arc (Harris, 2006). The ophiolites of Sulawesi were generated in this arc system in a back-arc to intra-arc setting (Monnier et al., 1995) (but see Kadarusman et al., 2004 for an alternative view) and the largest fragments of the East Sulawesi ophiolite were detached from their metamorphic sole in the late Oligocene (32–28 Ma; Parkinson, 1998a) and thrust to the east above a west dipping slab (East Sulawesi block; Villeneuve et al., 2001). During the Early to Middle Miocene, the Tukang Besi-Buton block began to collide obliquely with the southeastern end of the Sunda Arc, causing ophiolite emplacement in West and SE Sulawesi, including Buton (Smith and Silver, 1991; Bergman et al., 1996).

The North Arm consists of Late Pliocene and younger volcanic rocks built upon Eocene to Early Miocene oceanic basalt, basaltic andesite, pelagic sediments, and metamorphic rocks (Elburg and Foden, 1998). Eocene to Early Miocene volcanic rocks formed above a NW dipping slab in an arc system that extended to West and South Sulawesi (van Leeuwen and Muhardjo, 2005). Gorontalo Bay is an extensional basin that formed in the Pliocene, and prior to that time, the East Sulawesi was attached to the North Arm of Sulawesi. After the Oligocene to Early Miocene accretion of the East Sulawesi ophiolite, the arc system stepped

out to the SE forming a Neogene (23–16 Ma) volcanic belt on the East arm (Kadarusman et al., 2004). In the Late Miocene, SE-dipping subduction was initiated below the North Arm, which continues today at the North Sulawesi Trough. North Sulawesi was not substantially emergent until the Pliocene (van Leeuwen and Muhardjo, 2005). Active volcanoes extend from the North Arm through the Sangihe Arc into the southern Philippines.

The East and Southeast Arms consist predominantly of mafic and ultramafic rocks of the East Sulawesi Ophoilite that are exposed for more than 10,000 km^2 (Monnier et al., 1995). The East Arm preserves a complete ophiolitic sequence underlain by a metamorphic sole, mélange, imbricate continental margin and crystalline basement with a blueschist metamorphic overprint (Silver et al., 1983; Monnier et al., 1995; Parkinson, 1998a). Locally, the structural thickness of the ophiolite exceeds 15 km with surface relief over 3 km (Kadarusman et al., 2004). Seventeen igneous K-Ar dates from the East Sulawesi ophiolite range from 93–32 Ma, clustering between 60 Ma and 40 Ma (Parkinson, 1998b). K-Ar dates on hornblende from the metamorphic sole yielded cooling ages between 36–23 Ma (Parkinson, 1998a; Villeneuve et al., 2001), which dates the initial emplacement of the East Sulawesi ophiolite as the north Sulawesi volcanic arc was underthrusted by the Sula spur (Australian crust) (Silver et al., 1983; Parkinson, 1998a); however, despite these relatively old ages of emplacement, it appears that the ophiolites on the East Arm were not substantially subaerially exposed and exhumed until the Miocene.

Collision of the Sula-Banggai block with the East margin of Sulawesi began in the latest Miocene and uplift accelerated in the early Pliocene (5.2 Ma to 3.8 Ma) and is associated with a major pulse of sedimentation in adjacent basins (Davies, 1990; Villeneuve et al., 2000). Off the northeast margin of the east arm of Sulawesi, Miocene platform carbonates on the Sula-Banggai block are overlain by Late Miocene to Early Pliocene ophiolite detritus in the Celebes mélange (Davies, 1990). Thus, although the East Sulawesi ophiolite was trapped/emplaced onto the composite Sundaland margin (i.e. a fragment of previously accreted Australian crust) between 36 Ma and 23 Ma, mafic and ultramafic rocks on the south and west arms appear to have not been substantially subaerially exposed in the south and west arms until after 15 Ma, and on the east arm until after 5 Ma.

West Sulawesi rifted from Borneo during the Eocene forming the Makassar Straits back arc basin behind a southwest-facing arc (Polvé et al., 1997). Eroded fragments of ophiolite and extensive belts of volcanic rocks are preserved on the West and South Arms of Sulawesi (Bergman et al., 1996; van Leeuwen et al., 2010). During the Middle Miocene (ca. 15–13 Ma), extensional faults in the Bone basin reversed, which was accompanied by uplift and erosion of the Bone Mountain ophiolite and Lamasi complex in West Sulawesi (Bergman et al., 1996; van Leeuwen et al., 2010). Shortening was likely due to the collision of the leading edge of the Buton-Tukang Besi block, which collided with Buton and the SE Arm of Sulawesi (Smith and Silver, 1991). Uplift and erosion is recorded by the presence of a major Middle Miocene unconformity and sedimentary breccias in marginal basins (Bergman et al., 1996; van Leeuwen et al., 2010). Uplift was diachronous, not effecting units below and to the west of the Lamasai ophiolite until the Middle Miocene (ca. 13 Ma) (van Leeuwen et al., 2010). Alkali volcanism ensued at ca. 11 Ma and is associated with a second phase of

extension and exhumation from the Late Miocene to Pliocene with fission track ages implying deep exhumation (Smith and Silver, 1991; Bergman et al., 1996; van Leeuwen et al., 2010).

Fission track ages from granitoids in central Sulawesi indicate rapid uplift of Central Sulawesi (200–700 m/m.y.) starting at about 5 Ma associated with movement on the Palo-Koro fault (Bellier et al., 2006). The fault system also shows a normal component with rapid exhumation of rock west of the fault in western Sulawesi – all fission track dates are younger than 5 Ma (Bellier et al., 2006). Just east of the Palo-Koro fault, the Palu Metamorphic Complex was exhumed in the Late Miocene to early Pliocene in the north (ca. 5.3 Ma) and later Pliocene in the south (ca. 3.1–2.7 Ma) at rates of up to 400 m/m.y. (Hennig et al., 2017b).

New Guinea and Halmahera

Paleoshoreline maps were georeferenced from several previous tectonic and paleogeographic analyses, most notably those of Nichols and Hall (1991); Cloos et al. (2005); Gold et al. (2017); Harrington et al. (2017). These studies were all based to varying degrees on lithological distributions, biostratigraphic, borehole data, and tectonic models. We complimented these data with our stratigraphic compilations for the region to provide further paleoenvironmental context.

Northern New Guinea, including the Melanesian Arc, was emplaced above the Australian plate during the Miocene (Hamilton, 1979; Cloos et al., 2005; van Ufford and Cloos, 2005; Baldwin et al., 2012). Two major ophiolite belts marking the suture – the Irian-Marum ophiolite belt (including the April ultramafics), and the Papuan Ultramafic Belt (PUB) – are preserved along the Central Range and Peninsular Range, respectively. South of the Irian-Marum ophiolites, the Ruffaer Metamorphic Complex constructed from the accretionary wedge, forms the spine of the Central Range (up to ∼5 km elevation today).

The Middle Miocene (16–14 Ma) basal Makats Formation contains siliciclastic sediment that was transported from the south into the forearc basin associated with the Irian-Marum ophiolite belt (Visser and Hermes, 1962; Cloos et al., 2005). The beginning of widespread synorogenic sedimentation to the south and on the Australian continental basement was later at ca. 12 Ma (van Ufford and Cloos, 2005). Mountain building began in Late Miocene time, ca. 8–7 Ma (van Ufford and Cloos, 2005; Baldwin et al., 2012), but major relief was not generated until the Pliocene (Weiland and Cloos, 1996). Similarly, the Marum ophiolite was uplifted between 8–5 Ma with 3–4 km of denudation (Crowhurst et al., 1996). An estimated 80–100 km of shortening has been accommodated by deformation on the south side of the Central Range (Hill and Gleadow, 1989; Cloos et al., 2005).

Along the Papuan Peninsula of Eastern New Guinea, the PUB was obducted above a north dipping slab during Oligocene arc-continent collision between Australian continental fragments and the Melanesian arc, but remained largely subaqueous until the Miocene (Davies and Smite, 1971; Davies and Jaques, 1984; van Ufford and Cloos, 2005). Miocene to present arc-continent collision in New Guinea has progressed from west to east. Exhumation of the Central Range accelerated over the past 4 m.y. which is interpreted to be the result of

slab-breakoff and buoyant uplift (Cloos et al., 2005). A change to left-lateral lateral motion on the northern coast of New Guinea at this time, caused the exhumation of ophiolites both along the coast (Monnier et al., 1999) and on the islands Obi (Ali et al., 2001) and Halmahera (Hall et al., 1988; Ballantyne, 1992). In eastern New Guinea, progressive jamming of the north-dipping subduction zone has caused major uplift over the past 4 Ma (van Ufford and Cloos, 2005), which is well dated with a change in provenance from continental to volcanic detritus (Abbott et al., 1994) and thermochronology (Hill and Gleadow, 1989).

In the Bird's Neck of western New Guinea, the Lengguru fold belt formed during Middle to Late Miocene clockwise rotation and obduction of the Weyland Terrane (Bailly et al., 2009). Recent counter-clockwise rotation has exhumed several core complexes and has produced Pliocene compressional deformation to the southwest in the Misool-Onin-Kumawa Ridge (Sapin et al., 2009).

Philippines

Our reconstructions of the paleoshorelines of the Phillipines were primarily informed by the paleogeographic reconstructions of Hall (1997), coupled with geologic maps of the archipelago (Geologic Survey Division, 1963). The Philippine ophiolites have been grouped in four distinct belts (Yumul, 2007). We combine belts 1 and 2 in an eastern suture zone and belts 3 and 4 in a western suture zone. Belts 1 and 2 were juxtaposed in the eastern suture zone during sinistral transpression, which resulted in Early Miocene uplift and deposition of coarse clastic sediments (Pubellier et al., 1991). The Palawan microcontinental block and Philippine mobile belt collided during late Early Miocene to early Middle Miocene resulting into the emplacement of the western ophiolites, with exhumation extending from the Late Miocene to the present (Yumul et al., 2013). In addition to collision, arc magmatism contributed significantly to crustal growth in the Philippines (Dimalanta and Yumul, 2006).

Sunda-Banda Arc

Paleoshoreline reconstructions of the Sunda-Banda Arc system relied largely on the work of Hall (2013a). The Sunda-Banda Arc system is composed of thick sequences of mixed sedimentary rocks and basement intruded and overlain by igneous rocks derived from continual arc magmatism through much of the Cenozoic (Hall, 2017). Sumatra is the largest island within the Sunda-Banda Arc system that stretches from the Andaman Sea in the northwest to the Banda Sea in the east. The western portion of the Sumatra is underlain by the Wolya ophiolite, which was obducted in the Cretaceous and exhumed in the Eocene to Oligocene (Allen et al., 2008), whereas the southeast corner on the islands of Bangka and Belitung is composed of granite basement of the Sunda Shelf (Hall, 2009, 2013b). Java is composed of a complex of E-W-striking deformational and magmatic belts (Audley-Charles, 2004). The belts have a volcanic arc in the south and a continental shelf to the north with an adjacent sedimentary basin (Audley-Charles, 2004). Bali and Flores are mostly volcanic with some sedimentary cover (Hall, 2009).

Exhumation of the modern Sunda-Banda Arc is the result of ongoing arc-continent collision with the subducting Australian Plate (Harris, 2006). From ca. 20–10 Ma, the majority of Sumatra and nearly all of Java were submerged, although Bangka and Belitung were exposed in addition to a portion of the greater Sunda Shelf (Hall, 2009, 2013b). Six major islands were subaerially exposed before 5 Ma: Sumatra, Belitung, Bangka, Java, Bali, and Flores. However, most of Sumatra and Java were elevated above sea level and emerged to their present exposures only since 5 Ma (Hall, 2009, 2013b). Most of the non-volcanic islands of the Outer Banda Arc emerged after 5 Ma, associated with slab roll-back and collision with the Australian continental margin (Audley-Charles, 2004; Harris, 2006; Hall, 2013b). In Timor and Sumba, arc-continent collision resulted in rapid uplift of deep marine sedimentary rocks to elevations >1 km above sea level with estimated average uplift rates of 1.5 km/m.y. (Audley-Charles, 1986).

Appendix B

Supporting Information for "The lead-up to the Sturtian Snowball Earth: Neoproterozoic chemostratigraphy time-calibrated by the Tambien Group of Ethiopia"

This document accompanies the discussion contained in the main text. All the Python code used for this study, as well as the associated data tables not included in this document, can be found at https://github.com/Swanson-Hysell-Group/2019_Tambien_Group. A release of this GitHub repository was also made and published at https://doi.org/10.5281/zenodo.3403180.

B.1 Construction of the Chemostratigraphic Composite

The main text contains a composite $\delta^{13}C$ and $^{87}Sr/^{86}Sr$ curves for the Tonian and Cryogenian that are time-calibrated by the record from Ethiopia and incorporate data from the literature from numerous sources. Additional details associated with the data sets within this composite are provided below. The Python code used to develop the composite as well as the associated data table can be found at: https://github.com/Swanson-Hysell-Group/2019_Tambien_Group.

Ethiopia

$\delta^{13}C$ and $^{87}Sr/^{86}Sr$ data from Ethiopia comes from the Tambien Group and are developed in Miller et al. (2009), Swanson-Hysell et al. (2015b), and this study. Combined with U-Pb ID-TIMS dates on zircons from Swanson-Hysell et al. (2015b) (815.29±0.32, 788.72±0.24, and

787.38±0.14 Ma) and new U-Pb ID-TIMS dates on zircons from MacLennan et al. (2018) (735.25±0.25, 719.58±0.56, and 719.68±0.46 Ma), the Tambien Group is now the source of the most temporally well-constrained pre-Sturtian chemostratigraphic dataset to date. We therefore use the Tambien Group $\delta^{13}C$ curve as the backbone for making correlations with other datasets. In the chemostratigraphic composite, the age of the initiation of the Sturtian Glaciation is set to 717 Ma (discussed further in the 'Onset of the Sturtian Snowball' section).

Svalbard

$\delta^{13}C$ and $^{87}Sr/^{86}Sr$ data from Svalbard come from the Akademikerbreen Group and are developed in Halverson et al. (2007a) and Halverson et al. (2007b). However, a slightly stricter threshold for $^{87}Sr/^{86}Sr$ diagenesis is applied to the data included in our composite than in the original publication ([Sr]<500 ppm). Additional $^{87}Sr/^{86}Sr$ data were published in Cox et al. (2016). The Polarisbreen Group, which unconformably overlies the Akademikerbreen Group, contains two separate diamictite units which have been interpreted to represent the Sturtian and Marinoan Glaciations respectively (Halverson et al., 2004). This correlation constrains the Akademikerbreen Group to have been deposited prior to the Sturtian Glaciation. No direct geochronological constraints exist for the Akademikerbreen Group although thermal subsidence models have been used to suggest a ca. 800 Ma age for the Bitter Springs stage (Maloof et al., 2006). Therefore, the $\delta^{13}C$ curve from the group is correlated to that of the Tambien Group by aligning the start and end of the Bitter Springs stage and the nadir of the 735 Ma Anomaly. This correlation results in a near constant sedimentation rate between these constraints, which is used to estimate the age of data that precedes the Bitter Springs stage.

Greenland

$\delta^{13}C$ and $^{87}Sr/^{86}Sr$ data from the Eleanore Bay Supergroup are developed in Cox et al. (2016). Halverson et al. (2004) approximated the age of the this succession to be ca. 800 Ma based on the correlation of lithological and $\delta^{13}C$ data to the Akademikerbreen Group of Svalbard, but no direct age constraints exist. Therefore, the age model is estimated based on aligning the $\delta^{13}C$ data with the $\delta^{13}C$ curve of the Akademikerbreen Group.

Australia

$\delta^{13}C$ data from the Bitter Springs Formation are developed in Swanson-Hysell et al. (2010). Further $^{87}Sr/^{86}Sr$ data are developed in Cox et al. (2016). Similar to the Akademikerbreen Group, the Bitter Springs Formation is unconformably overlain by Sturtian diamictite of the Areyonga Formation (Swanson-Hysell et al., 2010), and thus constrains the Bitter Springs Formation to have been deposited prior to the Sturtian Glaciation. However, no direct geochronological constraints exist for the Bitter Springs Formation. Therefore, the $\delta^{13}C$ curve from this group is correlated to that of the Tambien Group by aligning the start and end of the Bitter Springs stage. Again, this correlation results in a near constant sedimentation

rate between these constraints, which is used to estimate the age of data that post-dates the Bitter Springs stage. However, if the constant sedimentation rate is applied to $\delta^{13}C$ data from the Bitter Springs Formation preceding the Bitter Springs stage, there is a significant mismatch between these data and that of the Akademikerbreen Group. Therefore, these data were assigned slightly older ages than would be predicted by the constant sedimentation rate assumption in order to better match the $\delta^{13}C$ curves between these two sections.

Canada

$\delta^{13}C$ and $^{87}Sr/^{86}Sr$ data from Canada come from multiple studies and localities.

$\delta^{13}C$ data and geochronology from the Fifteenmile Group are developed in Macdonald et al. (2010). Additional $^{87}Sr/^{86}Sr$ data are developed in Cox et al. (2016). The Fifteenmile Group is unconformably overlain by temporally well-constrained (see the 'Onset of the Sturtian Snowball' section) Sturtian diamictite of the Upper Mount Harper Group (Macdonald et al., 2010). A U-Pb ID-TIMS date on zircons within a tuff of 811.51±0.25 Ma can be tied directly to this curve, and, combined with dates from the Tambien Group (787.38±0.14, 788.72±0.24, and 815.29±0.32 Ma), suggests global synchroneity of the Bitter Springs stage (Swanson-Hysell et al., 2015b). The nadir of the 735 Ma Anomaly can also be easily identified and correlated. Furthermore, $\delta^{13}C$ data that precede the Bitter Springs stage correlate well with data from the Akademikerbeen Group, and thus were correlated based on similar $\delta^{13}C$ values. However, unlike other sections in which the Bitter Springs stage is observed, the recovery from the interval of low $\delta^{13}C$ values appears to be much more gradual. Nevertheless, the end of the minimum $\delta^{13}C$ values is assumed to be correlative to the end of the Bitter Springs stage, and a roughly constant sedimentation rate was applied to the data between this age and the 735 Ma Anomaly nadir, excluding an unconformity interpreted to exist between PF1 and PF3 of the Fifteenmile Group (Macdonald et al., 2010).

$\delta^{13}C$ and $^{87}Sr/^{86}Sr$ data from the Little Dal Group are developed in Halverson (2006) and Halverson et al. (2007a). A slightly stricter threshold for $^{87}Sr/^{86}Sr$ diagenesis is applied to the data included in our composite ([Sr]<250 ppm and Mn/Sr>0.15) than in the original work. A basalt has been interpreted to conformably overlie the Little Dal Group (Aitken, 1981) and inferred to have erupted ca. 780 Ma based on geochemical similarity to mafic dikes and sills that intrude the Mackenzie Mountain Supergroup (Harlan et al., 2003). Given that the basalt has not been directly dated, there is some uncertainty associated with this interpretation. Nevertheless, correlating the $\delta^{13}C$ curve from the Little Dal Group to that of the Tambien Group by aligning the start and end of the Bitter Springs stage and assuming constant sedimentation rate throughout the rest of the section suggests that the top of the Little Dal Group is ca. 780 Ma, consistent with the inference of Harlan et al. (2003).

$\delta^{13}C$ and $^{87}Sr/^{86}Sr$ data and geochronology from the Coates Lake Group are developed in Halverson (2006), Halverson et al. (2007a), and Rooney et al. (2014). A Re-Os isochron date on black shales of 732.2±3.9 Ma can be tied directly to this curve as it comes from strata recording the recovery from the nadir of the 735 Ma $\delta^{13}C$ Anomaly. This date provides constraints on the temporal alignment of the curve. Given the uncertainty associated with

the date, the correlation is further refined by aligning the nadir and recovery of the excursion with the Tambien Group data.

$\delta^{13}C$ and $^{87}Sr/^{86}Sr$ data from the Shaler Supergroup are developed in Asmerom et al. (1991), although $^{87}Sr/^{86}Sr$ data with Mn/Sr>3 and $\delta^{18}O$ <-10‰ are considered to be altered. Further $\delta^{13}C$ data are developed in Jones et al. (2010). Age constraints on these strata are poor. However, the onset of the Bitter Springs Anomaly and the 735 Ma Anomaly as well as other minor inflexions in the $\delta^{13}C$ curve are identifiable in the data. Furthermore, lithostratigraphic correlations between the Shaler Supergroup and the Mackenzie Mountains Supergroup can be made. Therefore, the age model for these data is developed based on the correlation of the $\delta^{13}C$ curve as well as the lithostratigraphy between these two supergroups, as in Jones et al. (2010).

Scotland

$\delta^{13}C$ and $^{87}Sr/^{86}Sr$ data from the Dalradian Supergroup are developed in Sawaki et al. (2010). The carbonates from which these data are sourced unconformably underlie a glacial diamictite. Brasier et al. (2000) argues that $^{87}Sr/^{86}Sr$ values from these carbonates are too low (<0.7065) to be post-Sturtian, and therefore must be pre-Sturtian in age. Besides this argument, no direct geochronological constraints exist for the Dalradian Supergroup. Therefore, the $\delta^{13}C$ curve from this group is correlated to that of the Tambien Group by aligning the nadir of the 735 Ma Anomaly.

Russia

$\delta^{13}C$ and $^{87}Sr/^{86}Sr$ data from Siberia come from multiple sources.

$\delta^{13}C$ and $^{87}Sr/^{86}Sr$ data from the Proterozoic carbonates of the Uchur–Maya and Turukhansk regions of Siberia are developed in Bartley et al. (2001), with additional $^{87}Sr/^{86}Sr$ data from Cox et al. (2016). All available $^{87}Sr/^{86}Sr$ data from Bartley et al. (2001) had [Sr]<500 ppm, and as a result Mn/Sr>0.5 is the only threshold applied for diagenesis. Age constraints on these strata are poor. Therefore, the age model applied to these data was based on lithostratigraphic correlation to the Yenisey Ridge and Uchur Maya Region sections, which are temporally constrained to have been deposited ca. 1100-1000 Ma based on geochronological constraints of varying robustness (Gallet et al., 2012).

$\delta^{13}C$ and $^{87}Sr/^{86}Sr$ data from the Karatau Group of the Urals are developed in Kuznetsov et al. (2006), with additional $^{87}Sr/^{86}Sr$ data from (Cox et al., 2016). However, a slightly stricter threshold for $^{87}Sr/^{86}Sr$ diagenesis was applied to the data included in our composite ([Sr]<350 ppm and Mn/Sr>0.1). Correlation of microbiota across Siberia suggests that the group is younger than ca. 1030 Ma (Kuznetsov et al., 2006). However, no other direct age control is available for this group. Therefore, following Cox et al. (2016), the age model for the Karatau Group data is constructed based on the correlation of one ca. 970 Ma Turukhansk Uplift $^{87}Sr/^{86}Sr$ measurement to the start of the Karatau Group data.

Cryogenian Successions

Since Tambien Group chemostratigraphy is limited to the Tonian, our Cryogenian $\delta^{13}C$ and $^{87}Sr/^{86}Sr$ chemostratigraphic composite is a compilation of a number of other Cryogenian datasets. In general, correlations between datasets are made using absolute age constraints where possible - otherwise, characteristic negative $\delta^{13}C$ excursions (the ca. 659 Ma Rasthof Excursion, the ca. 655 Ma Taishir Anomaly, and the ca. 643 Ma Trezona Anomaly) are used to align datasets. Unless mentioned otherwise, the same criteria for diagenesis that were used for publication of the original datasets are applied here.

Mongolia

$\delta^{13}C$ and $^{87}Sr/^{86}Sr$ data from Mongolia come from the Tsagaan-Olam Group and are developed in Bold et al. (2016) and Brasier et al. (1996). Given that data from this group span the entirety of the Cryogenian and into the Ediacaran, we use it as the backbone for our Cryogenian composite. For both datasets we apply a [Sr]<500 ppm and Mn/Sr>0.3 threshold for $^{87}Sr/^{86}Sr$ diagenesis.

The age model for these data follows that of Bold et al. (2016). A minimum age for the end of the Sturtian Glaciation is constrained by the following: U-Pb ID-TIMS on zircon from a tuffaceous bed overlying Sturtian diamicite in south China yields an age of 662.9±4.3 Ma (Zhou et al., 2004), a Re-Os isochron on black shales overlying Sturtian diamictite in northwest Canada yields an age of 662.4±4.6 Ma (Rooney et al., 2014), and a Re-Os isochron on black shales overlying Sturtian diamictite in Mongolia yields an age of 659.0±4.5 Ma (Rooney et al., 2015). A maximum age for the end of the Sturtian Glaciation is constrained by U-Pb ID-TIMS on zircon from a tuff interbedded with Sturtian diamictite in Australia, which yields an age of 663.03±0.11 Ma (Cox et al., 2018b). Therefore, for our Cryogenian composite, we set the age of the end of the Sturtian Glaciation (and therefore the age of the base of the Tsagaan-Olam Group) to 660 Ma.

A maximum age for the start of the Marinoan Glaciation comes from a U-Pb SHRIMP age on zircon from a tuff underlying Marinoan diamictite in south China of 654.5±3.8 Ma (Zhang et al., 2008). However, this tuff is separated from the Marinoan diamictite by a major disconformity, and so the age for the start of the Marinoan Glaciation is likely significantly younger than this U-Pb SHRIMP age. Therefore, following Bold et al. (2016), we set the age for the start of the Marinoan Glaciation in our composite to be 640 Ma.

The end of the Marinoan Glaciation is tightly temporally constrained. Zircons from a volcanic ash within and just above Marinoan diamictite in south China yielded U-Pb ID-TIMS dates of 635.5±0.6 and 635.2±0.6 Ma respectively (Condon et al., 2005). This constraint is consistent with U-Pb ID-TIMS dates from zircon from tuffs within Marinoan diamictite of 635.5±1.2 Ma in Namibia (Hoffmann et al., 2004), and 636.4±0.5 Ma in Tasmania, Australia (Calver et al., 2013).

Canada

$\delta^{13}C$, $^{87}Sr/^{86}Sr$, and geochronological data from the Hay Creek Group are developed in Rooney et al. (2014). A Re-Os isochron on black shales from within this group yielded an age of 662.4±4.6 Ma. The $\delta^{13}C$ and $^{87}Sr/^{86}Sr$ data correlate well with that from Mongolia.

Australia

$\delta^{13}C$ data from the Amadeus Basin and Adelaide Rift Complex are taken from Swanson-Hysell et al. (2010) for the composite. Amadeus Basin data from the Bitter Springs Formation are older than the Sturtian diamictite of the Areyonga Formation which unconformably overlie it. Re-Os isochrons developed for black shales above the Areyonga Formation yielded ages of 643.0±2.4 and 657.2±5.4 Ma (Kendall et al., 2006). Data from the Etina and Trezona Formations of the Adelaide Rift Complex come from between Sturtian and Marinoan glacial deposits. It remains unclear whether or not the Taishir and Trezona Excursions are time equivalent. In this compilation, they are taken to be distinct following Bold et al. (2016) such that the Trezona Anomaly and subsequent recovery occur temporally close to the initiation of the Marinoan Glaciation. The close temporal connection implied by this age model between the Trezona Anomaly and the initiation of the Marinoan Glaciation needs further work to be substantiated, although dropstones have been documented in the uppermost Trezona Formation (Rose et al., 2012). The data from the Adelaide Rift Complex shows that the $\delta^{13}C$ recovers from the nadir of the Trezona Anomaly over ∼200 m such that recovery from the excursion occurred prior to local ice advance (Rose et al., 2012). While this does not necessarily mean that there is a substantial separation in time between the Marinoan Glaciation and the nadir of the Trezona Anomaly, it does suggest that the $\delta^{13}C$ values recovered from the negative anomaly to values near 0‰ prior to glaciation.

Namibia

$\delta^{13}C$ and $^{87}Sr/^{86}Sr$ data from the Otavi Group are developed in Halverson et al. (2005) and Halverson et al. (2007a). We applied [Sr]<500 ppm and Mn/Sr>0.1 as the thresholds for $^{87}Sr/^{86}Sr$ alteration. Apart from the 635.5±1.2 Ma age from Hoffmann et al. (2004) constraining the end of the Marinoan Glaciation, no direct geochronological constraints exist for this data. Therefore, we align the Trezona Anomaly between the data from Australia and Namibia.

B.2 Geochronology

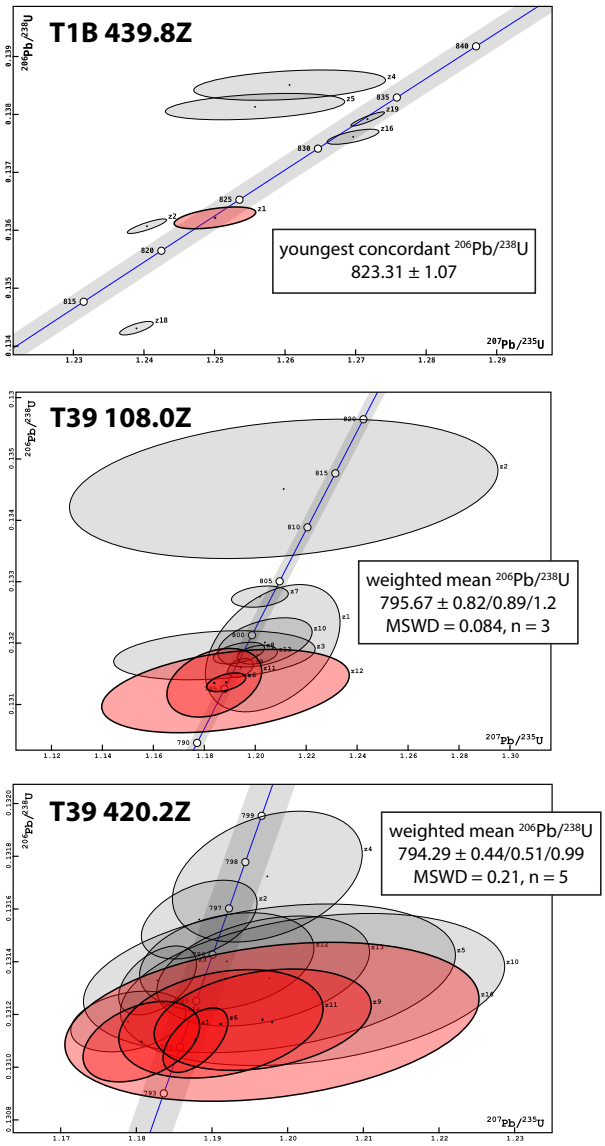

Figure B.1: Concordia diagrams for dates reported in this study. 2σ uncertainties are reported in the format ±X/Y/Z, where X is the internal (analytical) uncertainty in the absence of all external or systematic errors, Y is the uncertainty incorporating the U-Pb tracer calibration error, and Z is the uncertainty including X and Y, as well as the uranium decay constant uncertainty; MSWD = mean square of weighted deviates; n = number of zircon analyses included in the calculated date.

Table B.1: U-Pb data for analyzed zircons from T1B-439.8Z.

	Dates (Ma)								Composition				Isotopic Ratios						
fraction	^{a} $\frac{^{206}Pb}{^{238}U}$	± (2σ)	^{b} $\frac{^{207}Pb}{^{235}U}$	± (2σ)	^{a,b} $\frac{^{207}Pb}{^{206}Pb}$	± (2σ)	corr. coef.	^{c} % disc.	^{d} $\frac{Th}{U}$	^{e} Pb* (pg)	^{f} Pb_c (pg)	^{g} $\frac{Pb^*}{Pb_c}$	^{h} $\frac{^{206}Pb}{^{204}Pb}$	^{a,i} $\frac{^{206}Pb}{^{238}Pb}$	± (2σ%)	^{b,i} $\frac{^{207}Pb}{^{235}U}$	± (2σ%)	^{a,b,i} $\frac{^{207}Pb}{^{206}Pb}$	± (2σ%)
z1	823.31	1.07	823.43	2.61	823.76	8.55	0.51	0.10	0.34	23.13	0.61	37.96	2348.88	0.14	0.14	1.25	0.46	0.07	0.41
z2	822.49	0.71	819.07	1.26	809.80	3.20	0.85	-1.53	0.35	68.32	0.62	110.86	6810.02	0.14	0.09	1.24	0.22	0.07	0.15
z4	836.29	1.48	828.20	6.10	806.54	21.58	0.33	-3.65	0.53	13.16	0.86	15.23	908.36	0.14	0.19	1.26	1.08	0.07	1.03
z5	834.19	1.29	825.99	5.72	803.99	20.17	0.37	-3.72	0.67	13.33	0.80	16.67	958.46	0.14	0.16	1.26	1.01	0.07	0.96
z16	831.24	0.74	832.22	1.64	834.86	4.89	0.69	0.47	0.65	13.75	0.22	61.23	3610.31	0.14	0.10	1.27	0.29	0.07	0.23
z17	855.05	0.73	855.83	1.17	857.86	2.59	0.92	0.36	0.73	32.33	0.18	181.54	10466.28	0.14	0.09	1.32	0.20	0.07	0.12
z18	812.48	0.67	818.40	1.08	834.51	2.95	0.73	2.67	0.75	42.34	0.32	130.41	7480.36	0.13	0.09	1.24	0.19	0.07	0.14
z19	832.98	0.69	833.16	1.06	833.64	2.36	0.90	0.12	0.57	47.38	0.18	266.55	15958.64	0.14	0.09	1.27	0.19	0.07	0.11

Notes:
Colored rows indicate fractions included in the calculation of the reported sample age.
Isotopic dates calculated using $\lambda 238 = 1.55125 \times 10^{-10}$ and $\lambda 235 = 9.8485 \times 10^{-10}$ (Jaffey et al., 1971).
[a] Corrected for initial Th/U disequilibrium using radiogenic ^{208}Pb and Th/U[magma] = 3.50000.
[b] Corrected for initial Pa/U disequilibrium using initial fraction activity ratio $[^{231}Pa]/[^{235}U] = 1.10000$.
[c] % discordance = 100 - (100 × ($^{206}Pb/^{238}U$ date) / ($^{207}Pb/^{206}Pb$ date))
[d] Th contents calculated from radiogenic ^{208}Pb and ^{230}Th-corrected $^{206}Pb/^{238}U$ date of the sample, assuming concordance between U-Pb Th-Pb systems.
[e] Total mass of radiogenic Pb.
[f] Total mass of common Pb.
[g] Ratio of radiogenic Pb (including ^{208}Pb) to common Pb.
[h] Measured ratio corrected for fractionation and spike contribution only.
[i] Measured ratios corrected for fractionation, tracer and blank.

Table B.2: U-Pb data for analyzed zircons from T39-108.0Z.

	Dates (Ma)								Composition				Isotopic Ratios						
	[a]		[b]		[a,b]			[c]	[d]	[e]	[f]	[g]	[h]	[a,i]		[b,i]		[a,b,i]	
fraction	$\frac{^{206}Pb}{^{238}U}$	$\pm$ (2σ)	$\frac{^{207}Pb}{^{235}U}$	$\pm$ (2σ)	$\frac{^{207}Pb}{^{206}Pb}$	$\pm$ (2σ)	corr. coef.	% disc.	$\frac{Th}{U}$	Pb* (pg)	Pb_c (pg)	$\frac{Pb^*}{Pb_c}$	$\frac{^{206}Pb}{^{204}Pb}$	$\frac{^{206}Pb}{^{238}Pb}$	$\pm$ (2σ%)	$\frac{^{207}Pb}{^{235}U}$	$\pm$ (2σ%)	$\frac{^{207}Pb}{^{206}Pb}$	$\pm$ (2σ%)
z1	798.88	5.90	803.74	12.16	817.26	41.88	0.41	2.29	0.57	1.59	0.25	6.29	395.48	0.13	0.79	1.21	2.19	0.07	2.00
z2	813.64	6.45	805.73	38.62	783.94	142.22	0.26	-3.75	0.56	0.54	0.30	1.78	125.78	0.13	0.84	1.21	6.94	0.07	6.77
z3	798.22	2.28	793.16	18.38	778.96	68.88	0.25	-2.43	0.51	4.01	1.13	3.54	233.74	0.13	0.30	1.18	3.34	0.07	3.28
z6	795.71	0.87	795.30	3.56	794.14	12.54	0.49	-0.16	0.47	5.66	0.27	20.81	1297.81	0.13	0.12	1.19	0.65	0.07	0.60
z7	803.66	0.98	801.43	5.14	795.22	18.90	0.27	-1.02	0.43	4.03	0.31	12.82	813.30	0.13	0.13	1.20	0.93	0.07	0.90
z8	798.42	1.01	797.63	4.66	795.41	16.56	0.46	-0.34	0.58	5.09	0.31	16.30	993.36	0.13	0.13	1.19	0.84	0.07	0.79
z9	797.04	0.88	797.93	2.31	800.40	8.21	0.36	0.46	0.73	12.47	0.33	38.31	2223.30	0.13	0.12	1.19	0.42	0.07	0.39
z10	799.42	2.28	802.34	8.53	810.47	30.06	0.42	1.40	0.50	2.01	0.20	10.01	628.68	0.13	0.30	1.20	1.54	0.07	1.44
z11	795.67	3.19	793.15	8.65	786.05	31.21	0.33	-1.18	0.44	2.11	0.27	7.93	509.16	0.13	0.43	1.18	1.57	0.07	1.49
z12	794.90	3.87	795.18	22.55	795.97	82.26	0.38	0.18	0.42	1.37	0.39	3.54	238.72	0.13	0.52	1.19	4.09	0.07	3.92
z13	798.28	0.88	800.97	3.63	808.48	13.15	0.31	1.30	0.43	5.40	0.28	19.34	1218.11	0.13	0.12	1.20	0.65	0.07	0.63

Notes:
Colored rows indicate fractions included in the calculation of the reported sample age.
Isotopic dates calculated using $\lambda 238 = 1.55125\times10^{-10}$ and $\lambda 235 = 9.8485\times10^{-10}$ (Jaffey et al., 1971).
[a] Corrected for initial Th/U disequilibrium using radiogenic ^{208}Pb and Th/U[magma] = 3.50000.
[b] Corrected for initial Pa/U disequilibrium using initial fraction activity ratio $[^{231}Pa]/[^{235}U] = 1.10000$.
[c] % discordance = 100 - (100 × ($^{206}Pb/^{238}U$ date) / ($^{207}Pb/^{206}Pb$ date))
[d] Th contents calculated from radiogenic ^{208}Pb and ^{230}Th-corrected $^{206}Pb/^{238}U$ date of the sample, assuming concordance between U-Pb Th-Pb systems.
[e] Total mass of radiogenic Pb.
[f] Total mass of common Pb.
[g] Ratio of radiogenic Pb (including ^{208}Pb) to common Pb.
[h] Measured ratio corrected for fractionation and spike contribution only.
[i] Measured ratios corrected for fractionation, tracer and blank.

Table B.3: U-Pb data for analyzed zircons from T39-420.2Z.

	Dates (Ma)							Composition					Isotopic Ratios						
fraction	[a] $\frac{^{206}Pb}{^{238}U}$	± (2σ)	[b] $\frac{^{207}Pb}{^{235}U}$	± (2σ)	[a,b] $\frac{^{207}Pb}{^{206}Pb}$	± (2σ)	corr. coef.	[c] % disc.	[d] $\frac{Th}{U}$	[e] Pb* (pg)	[f] Pb_c (pg)	[g] $\frac{Pb^*}{Pb_c}$	[h] $\frac{^{206}Pb}{^{204}Pb}$	[a,i] $\frac{^{206}Pb}{^{238}Pb}$	± (2σ%)	[b,i] $\frac{^{207}Pb}{^{235}U}$	± (2σ%)	[a,b,i] $\frac{^{207}Pb}{^{206}Pb}$	± (2σ%)
z1	794.12	0.87	791.62	3.59	784.58	12.98	0.38	-1.18	0.69	11.98	0.49	24.28	1391.39	0.13	0.12	1.18	0.65	0.07	0.62
z2	796.76	0.85	795.17	3.55	790.74	12.69	0.42	-0.73	0.87	15.22	0.59	25.79	1415.45	0.13	0.11	1.19	0.64	0.07	0.60
z3	795.44	0.75	792.62	2.40	784.69	8.35	0.48	-1.33	0.76	23.62	0.59	40.01	2239.52	0.13	0.10	1.18	0.44	0.07	0.40
z4	797.69	1.41	799.35	5.80	803.97	20.92	0.34	0.82	0.73	13.69	0.91	15.02	857.80	0.13	0.19	1.20	1.05	0.07	1.00
z5	795.49	1.61	799.47	11.36	810.60	41.75	0.31	1.90	0.64	12.24	1.71	7.15	427.13	0.13	0.21	1.20	2.05	0.07	2.00
z6	794.15	0.70	794.95	1.99	797.18	6.68	0.55	0.42	0.77	43.52	0.87	50.28	2801.05	0.13	0.09	1.19	0.36	0.07	0.32
z9	794.59	1.09	799.06	6.63	811.54	24.38	0.28	2.12	1.20	8.79	0.62	14.19	731.99	0.13	0.15	1.20	1.20	0.07	1.17
z10	795.25	1.64	802.10	11.70	821.19	42.92	0.30	3.19	1.06	10.65	1.38	7.70	416.84	0.13	0.22	1.20	2.11	0.07	2.06
z11	794.51	1.17	796.51	6.26	802.10	23.04	0.28	0.98	0.69	5.42	0.40	13.43	776.60	0.13	0.16	1.19	1.13	0.07	1.10
z12	795.85	1.05	796.87	5.34	799.70	19.65	0.27	0.51	1.16	10.71	0.61	17.46	903.55	0.13	0.14	1.19	0.97	0.07	0.94
z13	795.65	1.19	799.10	6.49	808.72	23.61	0.35	1.65	0.66	5.25	0.40	13.04	760.42	0.13	0.16	1.20	1.17	0.07	1.13
z14	794.55	0.66	790.82	3.54	780.29	13.14	0.29	-1.80	1.30	10.90	0.40	27.31	1363.19	0.13	0.09	1.18	0.64	0.07	0.62
z16	794.55	1.72	799.63	12.64	813.80	46.60	0.29	2.40	0.66	7.30	1.14	6.40	382.41	0.13	0.23	1.20	2.28	0.07	2.23

Notes:
Colored rows indicate fractions included in the calculation of the reported sample age.
Isotopic dates calculated using $\lambda 238 = 1.55125 \times 10^{-10}$ and $\lambda 235 = 9.8485 \times 10^{-10}$ (Jaffey et al., 1971).
[a] Corrected for initial Th/U disequilibrium using radiogenic ^{208}Pb and Th/U[magma] = 3.50000.
[b] Corrected for initial Pa/U disequilibrium using initial fraction activity ratio $[^{231}Pa]/[^{235}U] = 1.10000$.
[c] % discordance = 100 - (100 × ($^{206}Pb/^{238}U$ date) / ($^{207}Pb/^{206}Pb$ date))
[d] Th contents calculated from radiogenic ^{208}Pb and ^{230}Th-corrected $^{206}Pb/^{238}U$ date of the sample, assuming concordance between U-Pb Th-Pb systems.
[e] Total mass of radiogenic Pb.
[f] Total mass of common Pb.
[g] Ratio of radiogenic Pb (including ^{208}Pb) to common Pb.
[h] Measured ratio corrected for fractionation and spike contribution only.
[i] Measured ratios corrected for fractionation, tracer and blank.

Figure B.2: **(A)** Photograph of the lava flow T1b-439.8Z. **(B)** Photograph of the ignimbrite T39-108.0Z, with feldspar phenocrysts and fiammed lithic clasts. **(C)** Photograph of the 30 cm rhyolitic tuff T39-420.2Z, with normally graded lapilli at the base. Hammer points up section in all panels.

B.3 Diagenetic Considerations

Isotope Conglomerate Test

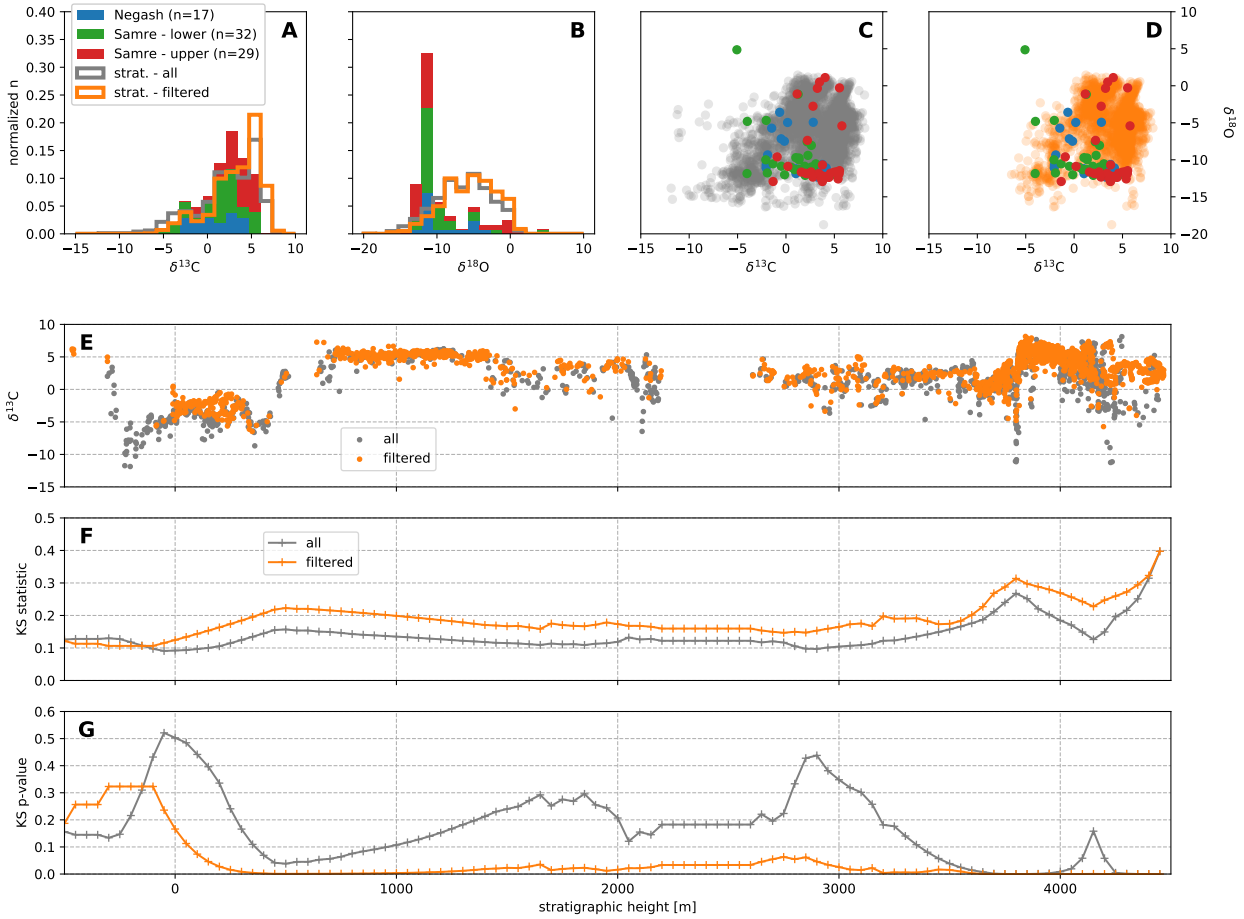

Figure B.3: **(A)** and **(B)** Histograms of δ^{13}C and δ^{18}O values of carbonate clasts within the diamictite of the Negash Formation of both the Negash Syncline and Samre Fold-Thrust Belt, compared to all *in situ* Tambien Group carbonate samples. Both filtered and unfiltered (all) versions of the *in situ* carbonate data are shown (see main text for a discussion of the filtering method). **(C)** and **(D)** Cross plots of δ^{13}C vs δ^{18}O for the clasts and *in situ* carbonate samples. **(E)** Filtered and unfiltered versions of the *in situ* carbonate δ^{13}C data against cumulative stratigraphic height. **(F)** Degree of correlation (as quantified by the Kolgomorov-Smirnov statistic) between the *in situ* carbonate δ^{13}C data with the carbonate clasts within the diamictite as samples below a given cumulative stratigraphic height (x-axis) are removed (i.e. the x-axis represents the depth of erosion). Low values suggest that the two datasets are drawn from the same distribution. See accompanying text for further details. **(G)** Kolgomorov-Smirnov statistic p-value. High values suggest that the two datasets are drawn from the same distribution.

We compare δ^{13}C and δ^{18}O values of the carbonate clasts from within diamictite of the

Negash Formation of the Negash Syncline and Samre Fold-Thrust Belt. In general, the distribution of clast $\delta^{13}C$ values is similar to that of the *in situ* Tambien Group carbonates (Fig. B.3A). However, the filtering technique proposes that the stratigraphic distance of a sample to the closest siliciclastic unit is a reasonable predictor for $\delta^{13}C$ alteration in *in situ* Tambien Group carbonates. If such a scenario applied equally to the diamictite clasts, we might expect the $\delta^{13}C$ of the clasts to be pulled to more negative values relative to the *in situ* carbonates since most of the samples in the *in situ* stratigraphy were extracted from carbonate horizons thicker than the diamictite clasts, but such a distribution is not observed.

There are several potential explanations for this apparent inconsistency. First, as discussed in the main text, samples that fall below the threshold d may or may not have had their carbon isotopic composition altered. And so, even though the majority of sampled diamictite clasts have a radius <0.2 m, the $\delta^{13}C$ of a significant proportion of these samples need not have been affected by secondary alteration. Second, it is possible that carbon is better buffered in the diamictite relative to the rest of the Tambien Group. Unless 100% of the diamictite's matrix was produced via scouring and redeposition of pre-Snowball Earth siliciclastics with associated organic matter, the matrix likely contains less low $\delta^{13}C$ organic carbon relative to the siliciclastic units of the underlying Tambien Group, given that organic productivity was suppressed during the Snowball Earth (Hoffman et al., 2017). The presence of extra-basinal clasts within the diamictite (see main text) suggests that at least some of the protolith was sourced from distal bedrock, and thus the organic component of the diamictite's matrix was likely diluted relative to undisturbed Tambien Group siliciclastics. Third, given that glacial erosion generates a bimodal sediment size distribution (fine grains from scouring and larger clasts from plucking) from the same rock, the sampled carbonate clasts in the diamictite are likely accompanied by fine carbonate sand from the same rock. This relatively carbonate-rich diamictite matrix would help to buffer the carbon isotopic composition of diamictite clasts against changes in $\delta^{13}C$ in a way that siliciclastic units within the *in situ* Tambien Group stratigraphy would not be able to. Finally, it is possible that our sampling of clasts from the diamictite is not representative of the bulk population. The total number of diamictite clasts sampled (n = 78) is substantially smaller than the total number of samples from *in situ* Tambien Group carbonates (n = 3139). Furthermore, diamictite clasts were only sampled from three discrete stratigraphic horizons, which may have been more carbonate buffered relative to the rest of the diamictite.

$\delta^{18}O$ values of the diamictite clasts are distinctly different from the spread in values observed in the *in situ* stratigraphy, and cluster at ∼-12‰ (Fig. B.3B). This difference suggests that, unlike the carbon isotopic composition, the oxygen isotope composition of the carbonate clasts was significantly more overprinted following deposition of the diamictite than that of the *in situ* carbonates. This difference in post-depositional alteration likely arises from the fact that the carbonate clasts in the diamictite are embedded within a predominantly siliciclastic matrix and are therefore less carbonate buffered against altering fluids, whereas most of the samples in the *in situ* stratigraphy were extracted from carbonate horizons thicker than the diamictite clasts and are therefore more likely to be carbonate buffered. Since carbon is more rock-buffered against altering fluids than oxygen, the $\delta^{13}C$ of

the clasts are more likely to preserve primary values.

Glacial erosion during the Sturtian Glaciation likely preferentially eroded the upper Tambien Group in most places instead of eroding all the way to the base of the Tambien Group. To assess how deep the bulk of glaciers eroded into Tambien Group stratigraphy, we divided the Tambien Group chemostratigraphic composite data collected from the *in situ* stratigraphy (Fig. B.3E) into several equal length (50 m) stratigraphic windows, and randomly selected the same number of samples from each of these windows. This Monte Carlo approach is necessary to avoid bias toward relatively heavily sampled intervals of the stratigraphy. We then quantified the similarity in distributions between the δ^{13}C of the Monte Carlo sampled *in situ* stratigraphy with that of the diamictite clasts using the two sample Kolmogorov-Smirnov (KS) statistic, which tests whether two sets of samples are consistent with being drawn from the same distribution. Low KS statistics and high p-values suggest that the two samples are drawn from the same distribution. We then simulate shallower erosion by iteratively excluding the lowest of these stratigraphic windows and recalculating the KS statistic, moving up the stratigraphy (Fig. B.3F and G). In general, we find that the two distributions are closest when the 'erosion height' is close to the bottom of the Tambien Group ($\sim$0 m in Fig. B.3F and G) and near the middle of the Tambien Group ($\sim$2900 m). We also observe a distinct trough/peak near the top of the Tambien Group ($\sim$4200 m), although the KS statistic/p-value is not as low/high as at the bottom or near the middle of the Tambien Group. Furthermore, the filtered version of the *in situ* carbonate δ^{13}C data (see main text) matches the clast data more poorly than all of the *in situ* carbonate δ^{13}C data, likely as a result of similar post-depositional alteration mechanisms operating throughout the entirety of the Tambien Group. Ultimately, this analysis illustrates the fact that a relatively large proportion of the diamictite clasts have relatively low δ^{13}C ($<0‰$), and thus the clast δ^{13}C distribution matches the *in situ* carbonate δ^{13}C distribution when the 'erosion height' is such that it includes a high proportion of samples within the Bitter Springs stage, the Didikama-Matheos excursion, and/or carbonate samples that have likely experienced secondary alteration pulling them to lower δ^{13}C values. Observations of the facies of clasts within the diamictite suggest that they were sourced predominantly from the Matheos and/or Mariam Bohkahko formations (see main text), and thus an 'erosion height' of $\sim$2900 m or $\sim$4200 m would be consistent with these facies. The KS statistic/p-value at these 'erosion heights' is low/high enough such that we cannot reject the null hypothesis that the diamictite clasts and the *in situ* carbonate samples from above these heights come from the same distribution. However, we note that erosion into the Mariam Bohkahko/Matheos formations is not observed locally where the diamictite is deposited. This observation requires that the clasts derive from carbonates time-equivalent to these formations deposited elsewhere in the basin, or from carbonates deposited in another basin within an Arabian-Nubian terrane.

Sample Proximity to Siliciclastic Units

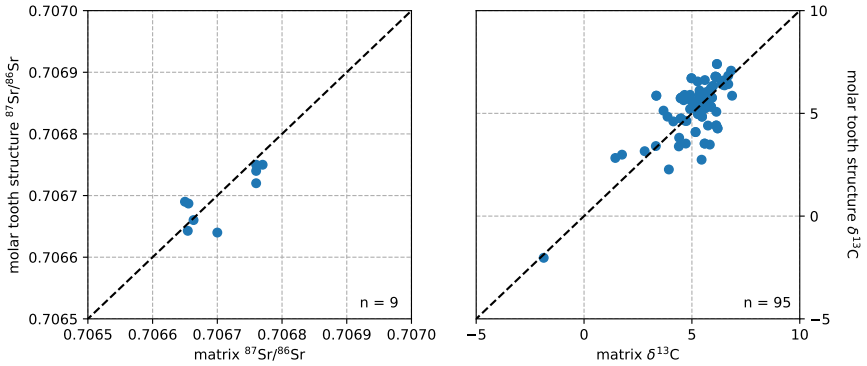

Figure B.4: Cross plots of carbonate matrix vs. adjacent molar tooth structure calcite $^{87}Sr/^{86}Sr$ and $\delta^{13}C$ from Tambien Group samples that meet the filtering thresholds for alteration (see main text). Dashed black lines are the 1:1 lines - samples that fall on these lines have identical isotopic composition between the matrix and molar tooth structure carbonate. The isotopic composition of the matrix is similar to that of adjacent molar tooth structures, and no systematic offsets can be identified.

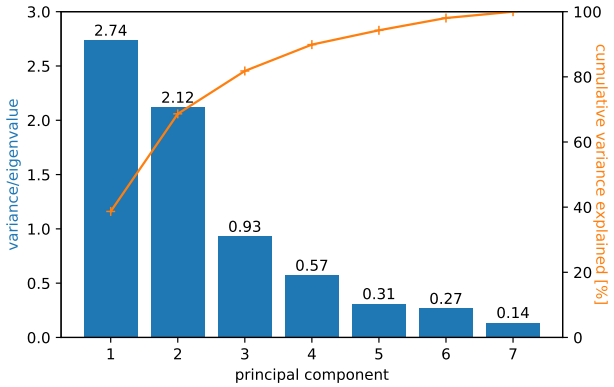

Figure B.5: Eigenvalues and cumulative variance explained for the 7 principal components in the principal components analysis (also known as a scree plot). Notably, the magnitude of the eigenvalues (and the percent variance explained) drops off sharply after the second principal component, indicating that the first two principal components capture the most significant sources of variance in our dataset.

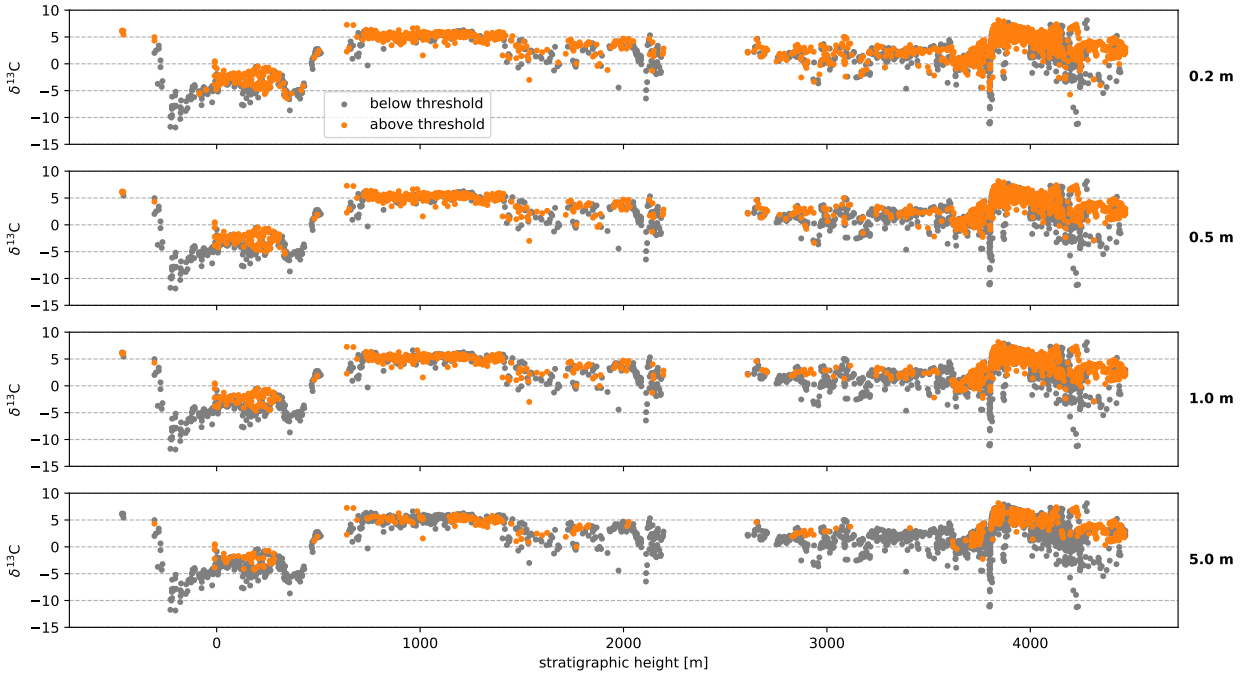

Figure B.6: Resulting composite chemostratigraphy of the Tambien Group as samples below a given d (shown on the right) are filtered out. Note that data that resolve the Didikama-Matheos excursion as well as the descent into and recovery out of the Bitter Springs stage are mostly removed under the $d = 0.2$ m threshold, and completely removed by $d = 0.5$ m.

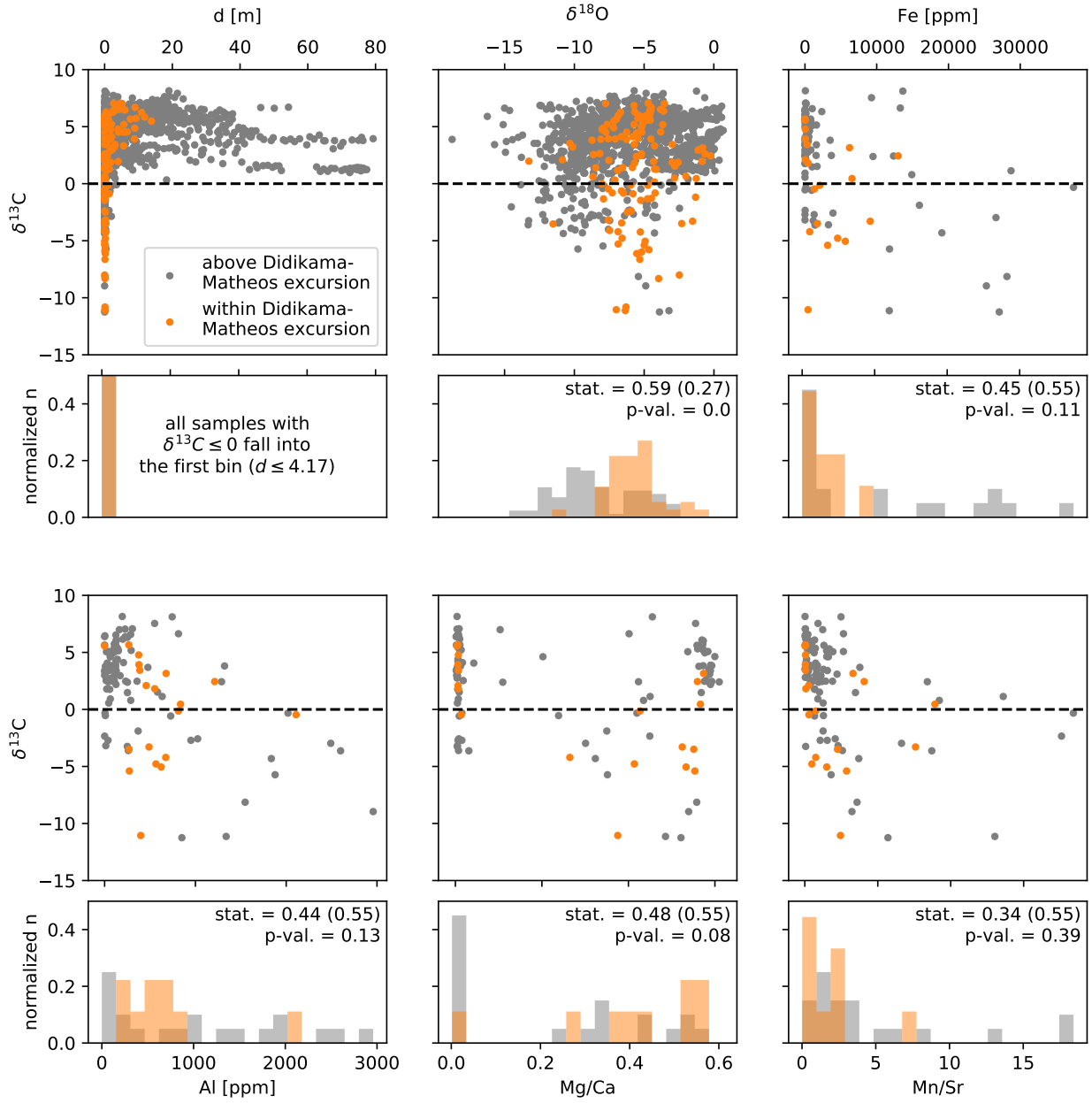

Figure B.7: Comparison of individual samples above the Didikama-Matheos excursion vs. samples within/adjacent to the Didikama-Matheos excursion. The normalized histograms under each scatter plot compare the distribution of samples with δ^{13}C $\leq$0‰ only. The 'stat.' and 'p-val.' refer to the Kolmogorov-Smirnov statistic and p-value respectively, with the value within the parentheses showing the critical Kolmogorov-Smirnov statistic for rejecting the null hypothesis (see text below).

As per conventions in statistics, the following discussion will use the term 'unit' to refer to an individual carbonate rock, and the term 'sample' to refer to a collection of 'units' from a population. Figure B.7 compares geochemical data of units above the Didikama-Matheos excursion to units within/adjacent to the Didikama-Matheos excursion. Units within the Didikama-Matheos excursion that record δ^{13}C $\leq$0‰ appear to exhibit lower Fe, Al, and Mn/Sr than units that record δ^{13}C $\leq$0‰ above the Didikama-Matheos excursion. This difference in distributions suggests that low δ^{13}C Didikama-Matheos excursion units have been less altered by the unbuffered fluids (see main text) than low δ^{13}C post-Didikama-Matheos excursion units, and thus provides support for the primary nature of the anomaly. To quantify this qualitative interpretation of the data, we compare the distributions of units with low δ^{13}C above the Didikama-Matheos excursion to units with low δ^{13}C within the Didikama-Matheos excursion by computing the two-sample Kolmogorov-Smirnov (KS) statistic. We also compute the critical KS statistic for rejecting the null hypothesis, which is given by $1.36\sqrt{\frac{N_1+N_2}{N_1N_2}}$, where N_1 and N_2 are the number of items in the two samples. If the computed KS statistic is above the critical KS statistic, or the p-value is below 0.05, we can reject the null hypothesis at the 95% confidence level that the two samples come from the same distribution. We find that the KS test yields ambiguous results for the Fe, Al, and Mn/Sr (Fig. B.7). For all three variables, the KS statistic is below the critical value, and the p-value is above 0.05. These results indicate that we cannot declare at the 95% confidence level that the two samples come from different distributions - instead, the test indicates that the samples may or may not come from the same distribution. However, the primary reason for this ambiguity is the small number of units used in the test. There are only 20 units with δ^{13}C $\leq$0‰ and element concentration data above the Didikama-Matheos excursion, and only 9 units with δ^{13}C $\leq$0‰ and element concentration within the Didikama-Matheos excursion, which results in a high critical KS statistic and thus a more 'difficult' test to achieve an unambiguous result in. Therefore, more element concentration data is required in order for the KS test to quantitatively reject the hypothesis at the 95% confidence level that units within the Didikama-Matheos excursion that record δ^{13}C $\leq$0‰ exhibit lower Fe, Al, and Mn/Sr than units that record δ^{13}C $\leq$0‰ above the Didikama-Matheos excursion.

Sr Isotopes

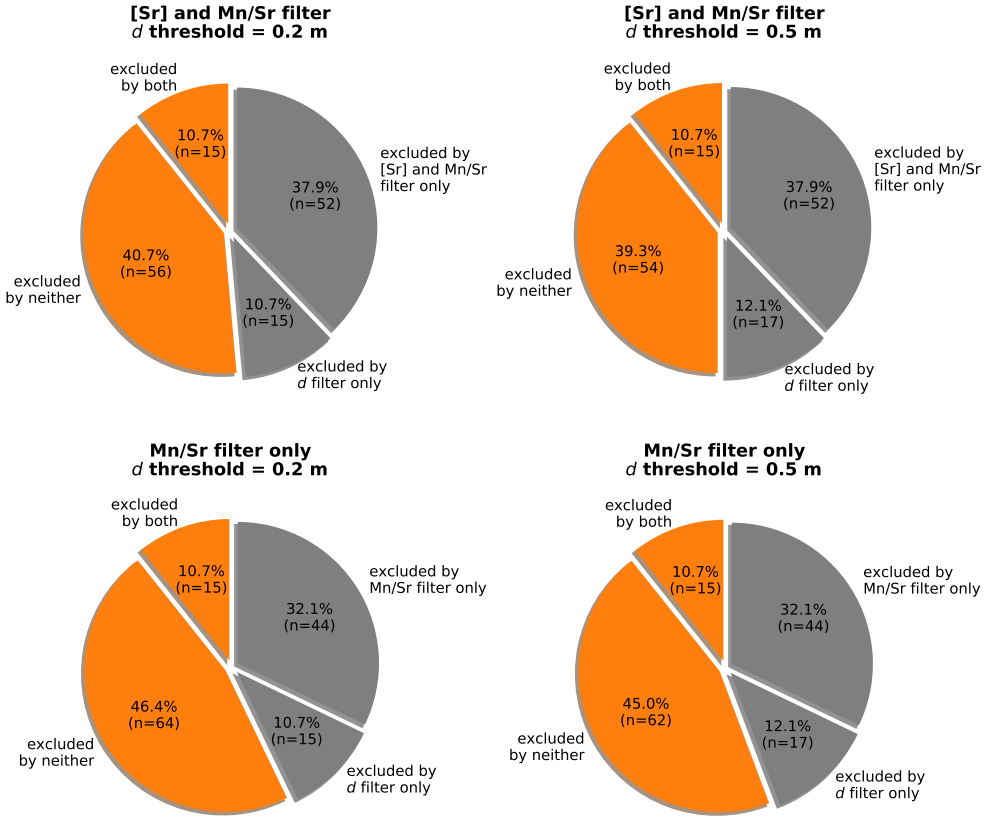

Figure B.8: Comparison of the application of the [Sr] and Mn/Sr filter and the filter based on distance to siliciclastics (d) to the $^{87}Sr/^{86}Sr$ data, for both $d = 0.2$ m and $d = 0.5$ m. Orange sectors denote classification agreement between the two filters, and grey sectors denote classification disagreement between the two filters. In the upper row, both the [Sr] and Mn/Sr thresholds are combined to filter samples. In the lower row, only the Mn/Sr threshold is used to filter samples.

Figure B.8 compares the application of the [Sr] and Mn/Sr filter and the filter based on distance to siliciclastics (d) to the $^{87}Sr/^{86}Sr$ data. When both the [Sr] and Mn/Sr thresholds are combined to filter samples (as in the main text), the [Sr] and Mn/Sr filter and the d filter only agree on classification for around half of the samples. This lack of agreement results from the fact that the principal components analysis used for the d filter (see main text) includes Mn/Sr, and not [Sr], as a variable in the analysis, since [Sr] in carbonates can vary considerably based on factors other than secondary alteration (e.g. calcite vs. aragonite, Husson et al., 2015a). Therefore, by using the Mn/Sr threshold only to filter samples, agreement between the Mn/Sr filter and the d filter improves. Still, considerable

disagreement between the two filters remain, which highlights the limitations of the d filter as discussed in the main text. Namely, that in addition to filtering out samples that have been altered, it is a rather blunt filter and may also filter out samples that retain relatively pristine geochemistry.

B.4 Pre-Sturtian $^{87}Sr/^{86}Sr$ and the Drivers of Planetary Cooling

LIP Analysis

Table B.4 lists the large igneous provinces (LIPs) that were included in the LIP analysis in the main text. The extent of each LIP was traced in QGIS to generate shapefiles, which were then added to a paleogeographic model (Swanson-Hysell et al., 2019) to extract the paleolatitude of the LIPs. We note that the LIP polygons were drawn to include the full areal extent of all dykes, sills, and volcanics interpreted to be associated with each LIP, which may lead to an overestimate of the true emplacement extents, since subsurface intrusions could extend over a broader area than the surface volcanics. Where available, the paleogeographic model honors the paleomagnetic poles listed in Table B.4.

Global Weathering Model

The Python code used to develop the global weathering model can be found at: https://github.com/Swanson-Hysell-Group/2019_Tambien_Group. Table B.5 shows the variables and equations used in the global weathering model.

Table B.4: Large igneous provinces included in the analysis conducted in the main text.

Name	Craton	Emplacement Age [Ma]	Emplacement Area [Mkm^2]	Polygon Centroid Emplacement Latitude	Age Reference	Polygon Reference	Paleomagnetic Pole Reference
Mackenzie	Laurentia	1267	2.983	11.4	LeCheminant and Heaman (1989)	Ernst and Youbi (2017)	Buchan et al. (2000)
CSDG	Baltica	1255	0.145	-24	Söderlund et al. (2006)	Ernst and Youbi (2017)	Pisarevsky et al. (2014a)
Sudbury	Laurentia	1235	0.056	7.7	Dudas et al. (1994)	Shellnutt and MacRae (2012)	Palmer et al. (1977)
Marnda Moorn	SW. Australia	1210	0.598	65.2	Pisarevsky et al. (2014b)	Ernst and Youbi (2017)	Pisarevsky et al. (2014b)
Abitibi	Laurentia	1141	0.229	48.2	Krogh et al. (1987)	Ernst and Youbi (2017)	Ernst and Buchan (1993)
Umkondo	Kalahari	1109	1.846	0.8	Hanson et al. (2004)	Ernst and Youbi (2017)	Swanson-Hysell et al. (2015a)
Keweenawan	Laurentia	1109	0.414	41.9	Davis and Green (1997)	Ernst and Youbi (2017)	Swanson-Hysell et al. (2014)
SW Laurentia	Laurentia	1090	0.776	28.7	Weil et al. (2003)	Bright et al. (2014)	Weil et al. (2003)
Warakurna - 1	SW. + N. Australia	1070	0.757	38.6	Wingate et al. (2002)	Ernst and Youbi (2017)	Wingate et al. (2002)
Warakurna - 2	SW. + N. Australia	1070	0.444	41.9	Wingate et al. (2002)	Ernst and Youbi (2017)	Wingate et al. (2002)
Dashigou	N. China	925	0.663	3.9	Peng et al. (2011)	Pirajno (2013)	-
Gangil-Mayumbia	Congo	920	0.333	-52.3	Tack et al. (2001)	Ernst and Youbi (2017)	-
Willouran-Gairdner - 1	S. Australia	827	0.345	24.3	Wingate et al. (1998)	Ernst and Youbi (2017)	-
Willouran-Gairdner - 2	S. Australia	827	0.171	29.3	Wingate et al. (1998)	Ernst and Youbi (2017)	-
SWCUC - 1	S. China	821	0.914	68.6	Wang et al. (2016b)	Ernst and Youbi (2017)	Li et al. (2004)
SWCUC - 2	S. China	821	0.411	65.6	Wang et al. (2016b)	Ernst and Youbi (2017)	Li et al. (2004)
Gunbarrel - 1	Laurentia	780	0.21	-7	Harlan et al. (2003)	Ernst and Youbi (2017)	Park et al. (1989)
Gunbarrel - 2	Laurentia	780	0.34	4.2	Harlan et al. (2003)	Ernst and Youbi (2017)	Park et al. (1989)
Mundine Well	N. Australia	755	0.21	25.6	Wingate and Giddings (2000)	Ernst and Youbi (2017)	Wingate and Giddings (2000)
Irkutsk	Siberia	724	0.154	13.6	Ernst et al. (2016)	Ernst et al. (2016)	-
Franklin	Laurentia	720	2.231	-2.3	Denyszyn et al. (2009)	Ernst and Youbi (2017)	Denyszyn et al. (2009)

Notes:
LIPs >0.1 Mkm^2 from the compilation in (Ernst et al., 2008) were included in the LIP analysis in the main text. Some LIPs are comprised of two separate polygons (denoted by 1 and 2).

Table B.5: Variables used in the global weathering model.

Term	Value/Equation	Note
Subaerial		
$[Ca]_{carb}$	302300 ppm	(1)
$[Mg]_{carb}$	47000 ppm	(1)
$[Sr]_{carb}$	610 ppm	(1)
$[Ca]_{rad}$	23750 ppm	(2)
$[Mg]_{rad}$	12800 ppm	(2)
$[Sr]_{rad}$	310 ppm	(2)
$[Ca]_{juv}$	71600 ppm	(3)
$[Mg]_{juv}$	45500 ppm	(3)
$[Sr]_{juv}$	465 ppm	(3)
Hydrothermal		
$H_{Mg-clays}$	$k \cdot [Mg]$	-
k	-	(4)
$H_{Ca-basalt}$	$\alpha_{Mg/Ca} \cdot H_{Mg-clays}$	-
$\alpha_{Mg/Ca}$	1	(5)
$H^{n}{}_{Sr-basalt}$	$\alpha_{Sr/Ca} \cdot H_{Ca-basalt}$	-
$\alpha_{Sr/Ca}$	0.0013	(6)
Precipitation		
$P_{Ca-carb}$	$W_{Mg-carb} + W_{Mg-rad} + W_{Mg-juv} - P_{Mg-carb} + W_{Ca-carb} + W_{Ca-rad} + W_{Ca-juv}$	(7)
$P_{Mg-carb}$	5×10^{10} mol/yr	(8)
$P_{Sr-carb}$	$(Sr/Ca)_{seawater} \cdot K_{Sr} \cdot P_{Ca-carb}$	-
K_{Sr}	0.2	(9)
^{87}Sr/^{86}Sr		
carbonate	0.70475	(10)
radiogenic	$BABI + (0.2783\left(\frac{Rb}{Sr}\right)_m(9.3485 + BABI))(1 - e^{-2\times10^9\lambda}) +$ $10(0.2783\left(\frac{Rb}{Sr}\right)_m(9.3485 + BABI))(1 - e^{-\lambda(t-2\times10^9)})$	(11)
juvenile	$BABI + (0.2783\left(\frac{Rb}{Sr}\right)_m(9.3485 + BABI))(1 - e^{-\lambda t})$	(11)

Notes:
(1) from Turekian and Wedepohl (1961)
(2) from Wedepohl (1995)
(3) taking the mean of Turekian and Wedepohl (1961) and Taylor (1964)
(4) flux of H_2O in hydrothermal systems, estimated to achieve desired initial steady state, then varied
(5) assumes 1:1 stoichiometry between Mg and Ca during weathering of the ocean crust
(6) from Maloof et al. (2010), calculated assuming 200 ppm Sr and 10 wt% CaO
(7) calculated iteratively assuming carbonate minerals are the only Ca sink
(8) estimated to achieve desired initial steady state
(9) homogeneous distribution coefficient for Sr in calcite from Mucci and Morse (1983)
(10) seawater has roughly constant $^{87}Sr/^{86}Sr$ ∼2-1 Ga (Shields and Veizer, 2002)
(11) these equations account of ^{87}Rb decay, where $BABI$ is the Basaltic Achondrite Best Initial ratio ($^{87}Sr/^{86}Sr$ =0.69897) from Papanastassiou and Wasserburg (1968), $\left(\frac{Rb}{Sr}\right)_m$ is Rb/Sr of the mantle (0.025), λ is the ^{87}Rb decay constant, and t is time since the origin of the Earth.

Appendix C

Supporting Information for "Tonian paleomagnetism from South China permits an inclusive Rodinia or Bitter Springs Stage true polar wander, but not both"

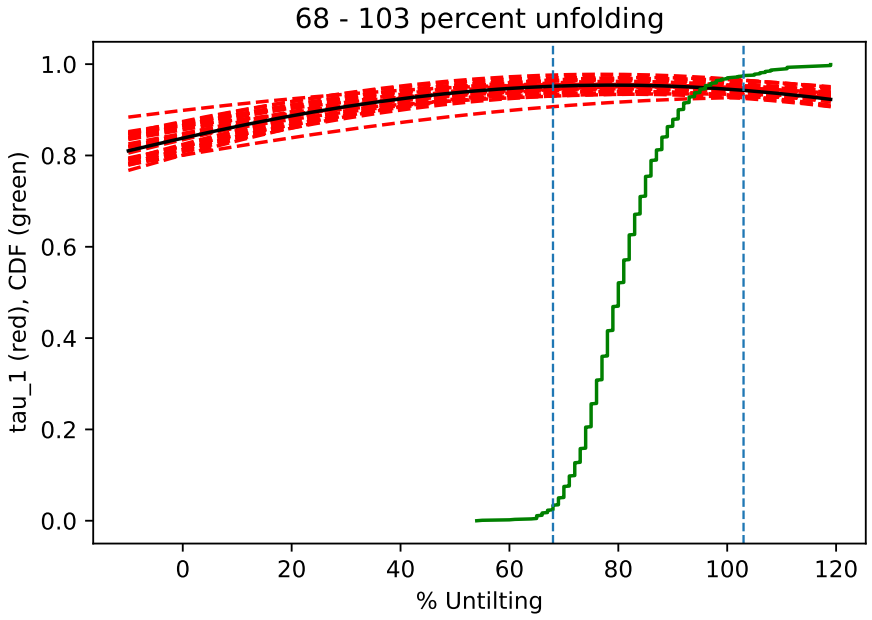

Figure C.1: Results of the bootstrap fold test (Tauxe and Watson, 1994) for the Xiajiang Group high-temperature component. The tightest grouping of site mean directions is obtained between 68 and 103% unfolding at the 95% confidence level. Since this range encompasses 100%, the high-temperature component passes the fold test, constraining the high-temperature component to have been acquired prior to Mesozoic folding of the Xiajiang Group (Li et al., 2016b; Ma et al., 2019).

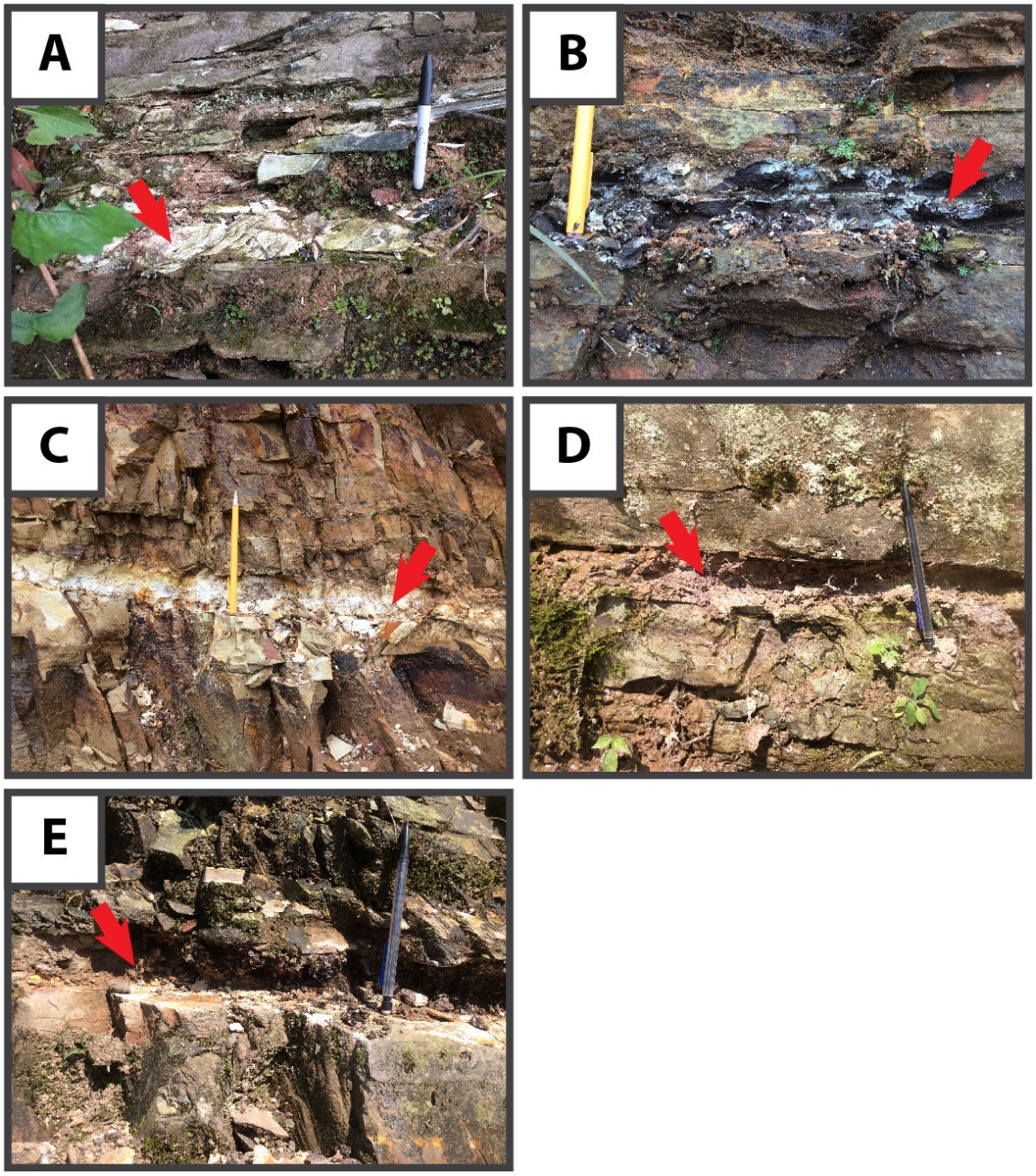

Figure C.2: Photographs of tuffs that yielded consistent and concordant CA-ID-TIMS $^{206}Pb/^{238}U$ zircon dates. Red arrows point to the sampled tuffs. **A)** H2-470. **B)** H3-60. **C)** H3-8. **D)** QR-74. **E)** L4-2. No photograph is available for sample L1-27.

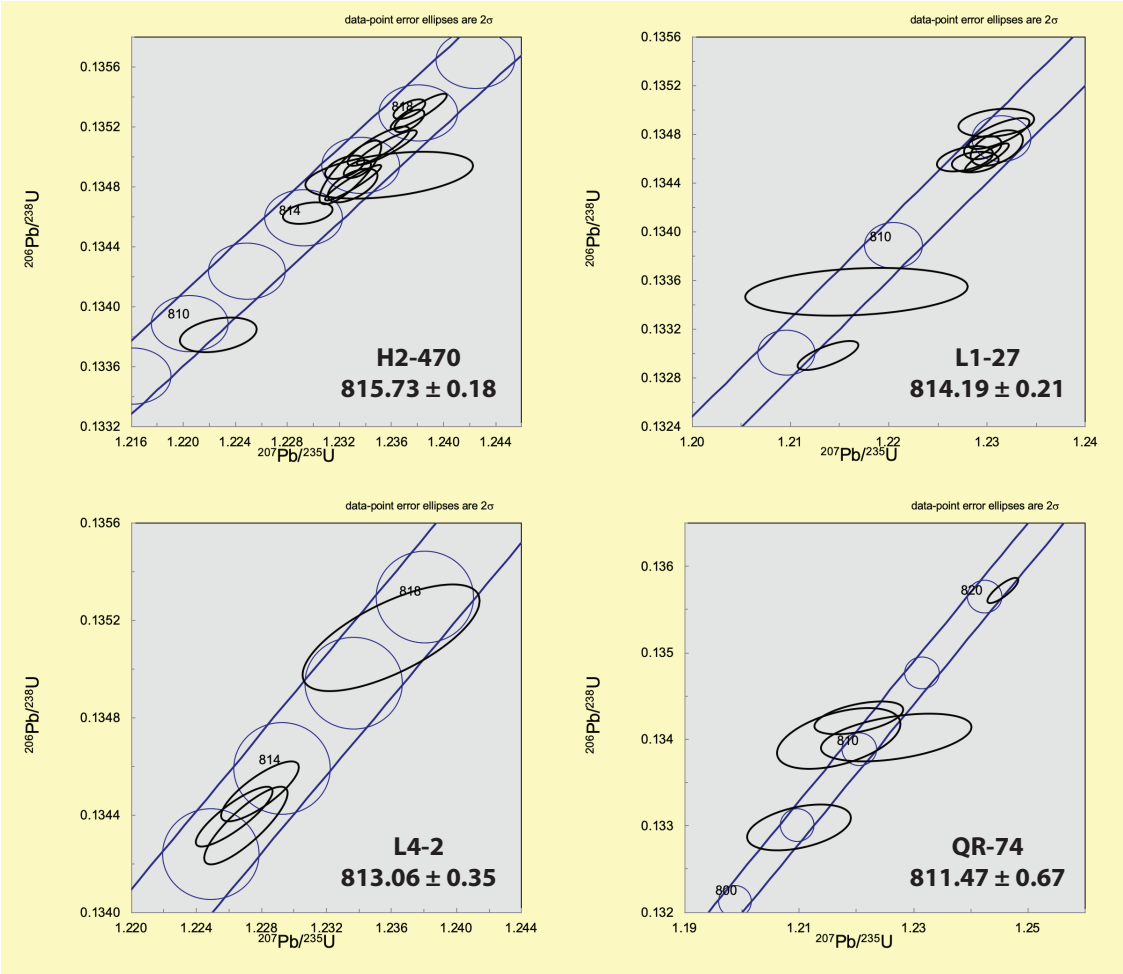

Figure C.3: Concordia diagrams for zircons from tuffs of the Xiajiang Group analyzed in this study. Individual zircon data are tabulated in Table SX.

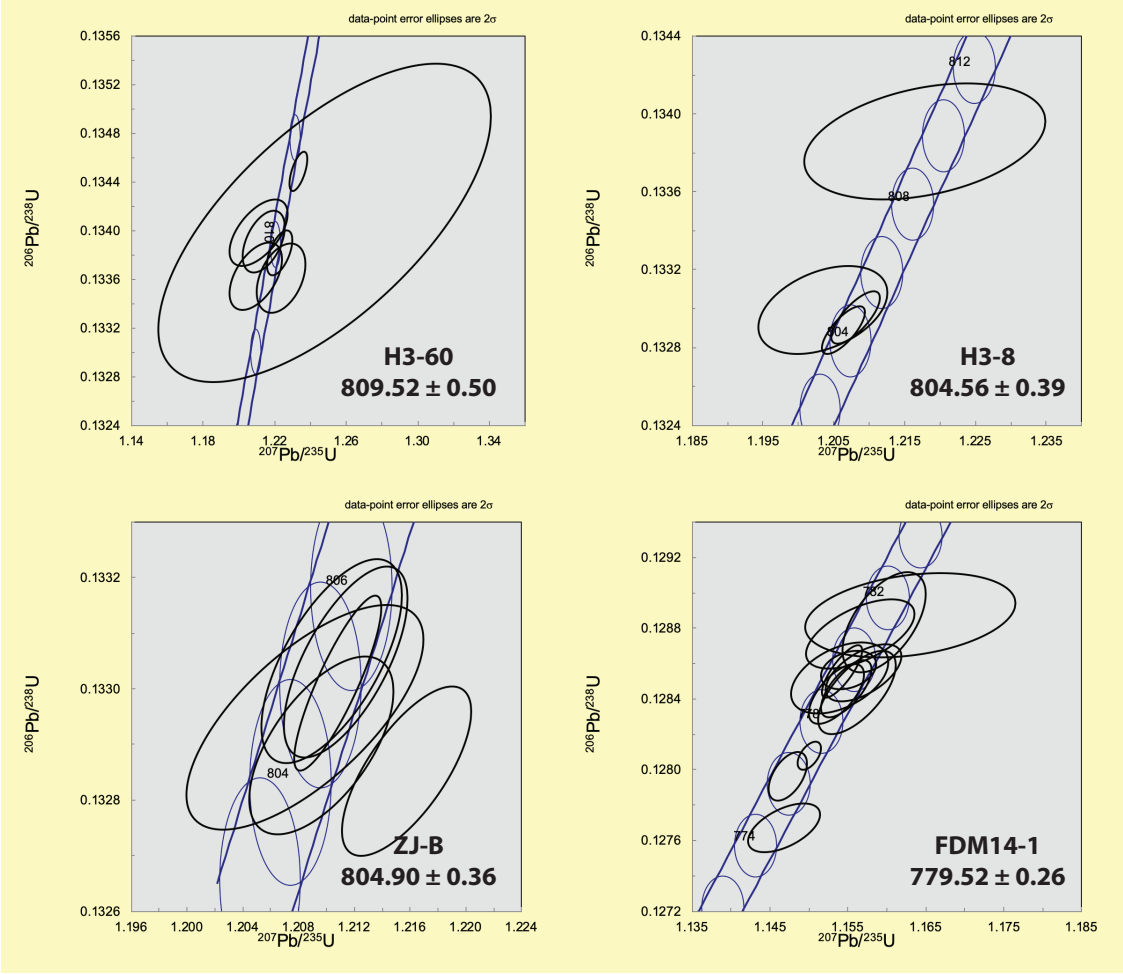

Figure C.4: Concordia diagrams for zircons from tuffs of the Xiajiang Group (H3-60 and H3-8), Madiyi Formation (ZJ-B), and Liantuo Formation (FDM14-1) analyzed in this study. Individual zircon data are tabulated in Table SX.

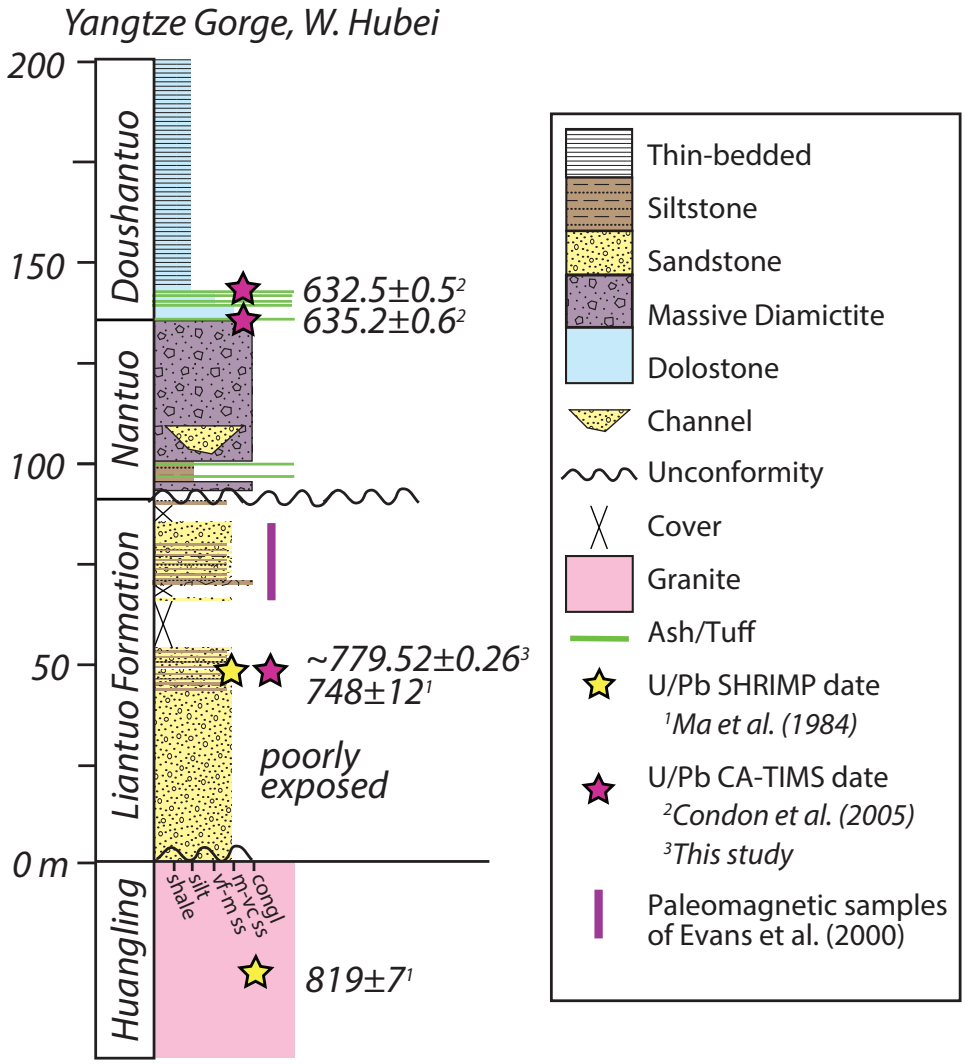

Figure C.5: Tonian-Cryogenian stratigraphy of the Yangtze Gorge, from where the paleomagnetic and geochronologic data for the Liantuo Formation are developed.

Table C.1: U-Pb data for analyzed zircons from H2-470.

	Dates (Ma)							Composition					Isotopic Ratios						
fraction	[a] $^{206}Pb/^{238}U$	± (2σ)	[b] $^{207}Pb/^{235}U$	± (2σ)	[a,b] $^{207}Pb/^{206}Pb$	± (2σ)	corr. coef.	[c] % disc.	[d] Th/U	[e] Pb* (pg)	[f] Pb_c (pg)	[g] Pb^*/Pb_c	[h] $^{206}Pb/^{204}Pb$	[a,i] $^{206}Pb/^{238}Pb$	± (2σ%)	[b,i] $^{207}Pb/^{235}U$	± (2σ%)	[a,b,i] $^{207}Pb/^{206}Pb$	± (2σ%)
z9	809.55	0.53	811.00	1.10	814.95	3.88	0.33	0.69	0.90	15.6	0.25	62.2	3392	0.133808	0.070220	1.222669	0.196189	0.066301	0.182537
z11	814.18	0.34	814.14	0.70	814.03	2.46	0.34	0.01	0.74	24.5	0.17	141.8	7993	0.134622	0.044107	1.229565	0.125086	0.066272	0.113043
z14	815.23	0.52	815.70	0.71	816.99	2.14	0.59	0.25	0.77	151.5	0.32	479.9	26838	0.134807	0.067705	1.232995	0.126378	0.066366	0.096844
z2	815.35	0.54	815.71	0.80	816.70	1.69	0.93	0.20	0.58	181.3	0.18	1013.2	59304	0.134828	0.070797	1.233019	0.143199	0.066356	0.074214
z3	815.62	0.72	816.98	2.39	820.70	8.28	0.41	0.65	0.62	95.6	5.15	18.6	1093	0.134876	0.093966	1.235816	0.424989	0.066484	0.394981
z7	815.73	0.99	815.63	0.88	815.35	1.90	0.82	-0.02	0.88	38.7	0.30	128.9	7036	0.134895	0.128998	1.232832	0.157563	0.066314	0.084703
z8	815.85	0.27	815.87	0.40	815.92	1.25	0.53	0.04	0.72	35.1	0.15	226.9	12842	0.134917	0.035031	1.233366	0.070632	0.066332	0.050324
z12	815.93	0.36	815.43	0.56	814.06	1.78	0.54	-0.20	0.78	23.6	0.16	148.4	8295	0.134931	0.047158	1.232398	0.100758	0.066273	0.078418
z1	816.69	0.53	816.90	0.84	817.48	1.95	0.90	0.13	0.76	132.2	0.74	179.4	10069	0.135064	0.069554	1.235639	0.150465	0.066381	0.087256
z4	816.73	0.61	816.60	0.88	816.24	2.11	0.83	-0.03	0.73	32.6	0.12	272.7	15417	0.135072	0.079228	1.234975	0.156380	0.066342	0.095355
z6	817.69	0.34	817.70	0.42	817.73	1.19	0.65	0.04	0.86	60.2	0.26	232.1	12723	0.135239	0.044110	1.237385	0.074873	0.066389	0.046714
z5	818.04	0.54	818.01	0.80	817.92	1.78	0.90	0.02	0.72	57.6	0.14	408.6	23141	0.135301	0.070555	1.238068	0.143195	0.066395	0.078665
z10	818.13	0.30	817.69	0.44	816.47	1.32	0.62	-0.17	0.76	50.0	0.16	311.7	17475	0.135318	0.038917	1.237363	0.079176	0.066349	0.053969
z16	826.68	0.32	824.61	0.43	819.04	1.27	0.61	-0.90	0.74	93.5	0.30	311.7	17581	0.136824	0.040989	1.252669	0.076810	0.066431	0.051484
z13	830.20	0.53	825.34	0.85	812.27	2.03	0.87	-2.17	0.75	62.5	0.38	164.3	9250	0.137445	0.068375	1.254296	0.149999	0.066216	0.091207
z15	844.63	0.31	837.47	0.90	818.55	3.17	0.28	-3.16	1.03	41.3	0.76	54.4	2879	0.139994	0.038917	1.281393	0.158093	0.066415	0.148349

Notes:
Colored rows indicate fractions included in the calculation of the reported sample age.
Isotopic dates calculated using $\lambda 238 = 1.55125\times10^{-10}$ and $\lambda 235 = 9.8485\times10^{-10}$ (Jaffey et al., 1971).
[a] Corrected for initial Th/U disequilibrium using radiogenic ^{208}Pb and Th/U[magma] = 2.8.
[b] Corrected for initial Pa/U disequilibrium using initial fraction activity ratio $[^{231}Pa]/[^{235}U] = 1.10000$.
[c] % discordance = 100 - (100 × ($^{206}Pb/^{238}U$ date) / ($^{207}Pb/^{206}Pb$ date))
[d] Th contents calculated from radiogenic ^{208}Pb and ^{230}Th-corrected $^{206}Pb/^{238}U$ date of the sample, assuming concordance between U-Pb Th-Pb systems.
[e] Total mass of radiogenic Pb.
[f] Total mass of common Pb.
[g] Ratio of radiogenic Pb (including ^{208}Pb) to common Pb.
[h] Measured ratio corrected for fractionation and spike contribution only.
[i] Measured ratios corrected for fractionation, tracer and blank.

Table C.2: U-Pb data for analyzed zircons from L1-27.

	Dates (Ma)								Composition				Isotopic Ratios						
fraction	$^{206}Pb/^{238}U$ [a]	± (2σ)	$^{207}Pb/^{235}U$ [b]	± (2σ)	$^{207}Pb/^{206}Pb$ [a,b]	± (2σ)	corr. coef.	% disc. [c]	Th/U [d]	Pb* (pg) [e]	Pb_c (pg) [f]	Pb*/Pb_c [g]	$^{206}Pb/^{204}Pb$ [h]	$^{206}Pb/^{238}Pb$ [a,i]	± (2σ%)	$^{207}Pb/^{235}U$ [b,i]	± (2σ%)	$^{207}Pb/^{206}Pb$ [a,b,i]	± (2σ%)
z5	804.84	0.56	806.95	1.16	812.78	3.42	0.72	1.01	0.73	50.5	0.82	61.7	3500	0.132980	0.073384	1.213839	0.207803	0.066232	0.160083
z6	807.82	0.91	808.27	4.24	809.52	15.58	0.22	0.24	0.79	7.0	0.63	11.1	638	0.133504	0.119942	1.216721	0.761579	0.066129	0.744112
z9	813.90	0.39	813.80	0.88	813.52	3.20	0.22	-0.02	0.85	27.2	0.32	85.4	4697	0.134572	0.050696	1.228808	0.156387	0.066256	0.149699
z8	814.06	0.48	813.32	1.08	811.29	3.66	0.43	-0.31	0.98	16.3	0.31	52.0	2787	0.134600	0.062729	1.227755	0.192831	0.066185	0.172067
z2	814.11	0.53	814.33	0.83	814.92	1.97	0.88	0.13	0.62	55.9	0.33	169.6	9852	0.134610	0.068803	1.229970	0.148922	0.066300	0.088455
z12	814.55	0.67	814.81	0.99	815.50	3.29	0.46	0.14	1.10	18.0	0.26	68.8	3583	0.134688	0.087437	1.231029	0.177274	0.066318	0.153859
z11	814.57	0.44	814.14	0.70	812.95	2.47	0.35	-0.17	0.87	19.5	0.23	86.0	4714	0.134691	0.058009	1.229554	0.125152	0.066238	0.113683
z4	815.24	0.59	814.91	1.15	814.02	3.28	0.75	-0.12	0.84	18.9	0.27	71.1	3926	0.134808	0.076864	1.231253	0.205803	0.066271	0.153331
z7	815.75	0.53	814.78	1.43	812.13	5.12	0.27	-0.41	0.88	9.1	0.27	33.0	1818	0.134898	0.069355	1.230966	0.254447	0.066212	0.242857

Notes:
Colored rows indicate fractions included in the calculation of the reported sample age.
Isotopic dates calculated using $\lambda 238 = 1.55125\times10^{-10}$ and $\lambda 235 = 9.8485\times10^{-10}$ (Jaffey et al., 1971).
[a] Corrected for initial Th/U disequilibrium using radiogenic ^{208}Pb and Th/U[magma] = 2.8.
[b] Corrected for initial Pa/U disequilibrium using initial fraction activity ratio $[^{231}Pa]/[^{235}U] = 1.10000$.
[c] % discordance = 100 - (100 × ($^{206}Pb/^{238}U$ date) / ($^{207}Pb/^{206}Pb$ date))
[d] Th contents calculated from radiogenic ^{208}Pb and ^{230}Th-corrected $^{206}Pb/^{238}U$ date of the sample, assuming concordance between U-Pb Th-Pb systems.
[e] Total mass of radiogenic Pb.
[f] Total mass of common Pb.
[g] Ratio of radiogenic Pb (including ^{208}Pb) to common Pb.
[h] Measured ratio corrected for fractionation and spike contribution only.
[i] Measured ratios corrected for fractionation, tracer and blank.

Table C.3: U-Pb data for analyzed zircons from L4-2.

	Dates (Ma)								Composition				Isotopic Ratios						
	[a] $\frac{^{206}Pb}{^{238}U}$	± (2σ)	[b] $\frac{^{207}Pb}{^{235}U}$	± (2σ)	[a,b] $\frac{^{207}Pb}{^{206}Pb}$	± (2σ)	corr. coef.	[c] % disc.	[d] $\frac{Th}{U}$	[e] Pb* (pg)	[f] Pb_c (pg)	[g] $\frac{Pb^*}{Pb_c}$	[h] $\frac{^{206}Pb}{^{204}Pb}$	[a,i] $\frac{^{206}Pb}{^{238}Pb}$	± (2σ%)	[b,i] $\frac{^{207}Pb}{^{235}U}$	± (2σ%)	[a,b,i] $\frac{^{207}Pb}{^{206}Pb}$	± (2σ%)
fraction																			
z5	812.67	0.73	812.99	0.96	813.86	2.20	0.84	0.18	0.64	28.3	0.17	170.0	9812	0.134357	0.096183	1.227035	0.171839	0.066266	0.100134
z3	812.88	0.57	812.67	0.88	812.09	2.13	0.85	-0.07	0.76	96.5	0.70	137.1	7703	0.134393	0.074304	1.226330	0.157528	0.066210	0.096556
z1	813.47	0.57	813.40	0.89	813.19	2.27	0.81	0.00	0.79	72.4	0.46	157.4	8784	0.134497	0.074341	1.227932	0.159174	0.066245	0.103450
z4	817.05	1.02	817.05	2.02	817.07	5.95	0.70	0.03	0.78	10.7	0.25	43.5	2442	0.135127	0.132953	1.235972	0.360619	0.066368	0.282745

Notes:
Colored rows indicate fractions included in the calculation of the reported sample age.
Isotopic dates calculated using $\lambda 238 = 1.55125 \times 10^{-10}$ and $\lambda 235 = 9.8485 \times 10^{-10}$ (Jaffey et al., 1971).
[a] Corrected for initial Th/U disequilibrium using radiogenic ^{208}Pb and Th/U[magma] = 2.8.
[b] Corrected for initial Pa/U disequilibrium using initial fraction activity ratio $[^{231}Pa]/[^{235}U] = 1.10000$.
[c] % discordance = 100 - (100 × ($^{206}Pb/^{238}U$ date) / ($^{207}Pb/^{206}Pb$ date))
[d] Th contents calculated from radiogenic ^{208}Pb and ^{230}Th-corrected $^{206}Pb/^{238}U$ date of the sample, assuming concordance between U-Pb Th-Pb systems.
[e] Total mass of radiogenic Pb.
[f] Total mass of common Pb.
[g] Ratio of radiogenic Pb (including ^{208}Pb) to common Pb.
[h] Measured ratio corrected for fractionation and spike contribution only.
[i] Measured ratios corrected for fractionation, tracer and blank.

Table C.4: U-Pb data for analyzed zircons from QR-74.

	Dates (Ma)								Composition				Isotopic Ratios						
	[a]		[b]		[a,b]			[c]	[d]	[e]	[f]	[g]	[h]	[a,i]		[b,i]		[a,b,i]	
fraction	$\frac{^{206}Pb}{^{238}U}$	$\pm$ (2σ)	$\frac{^{207}Pb}{^{235}U}$	$\pm$ (2σ)	$\frac{^{207}Pb}{^{206}Pb}$	$\pm$ (2σ)	corr. coef.	% disc.	$\frac{Th}{U}$	Pb* (pg)	Pb_c (pg)	$\frac{Pb^*}{Pb_c}$	$\frac{^{206}Pb}{^{204}Pb}$	$\frac{^{206}Pb}{^{238}Pb}$	$\pm$ $(2\sigma\%)$	$\frac{^{207}Pb}{^{235}U}$	$\pm$ $(2\sigma\%)$	$\frac{^{207}Pb}{^{206}Pb}$	$\pm$ $(2\sigma\%)$
z3	804.83	1.24	805.14	3.41	806.01	11.84	0.42	0.17	1.23	22.8	1.33	17.1	879	0.132978	0.163397	1.209897	0.614028	0.066018	0.564721
z16	810.71	1.64	808.35	4.05	801.85	13.64	0.48	-1.08	1.51	4.5	0.27	16.9	821	0.134012	0.215638	1.216885	0.726288	0.065887	0.650260
z11	810.75	1.28	812.97	4.90	819.06	17.07	0.44	1.02	2.16	4.4	0.29	15.3	661	0.134018	0.168352	1.226995	0.876654	0.066431	0.816287
z2	812.05	0.90	809.95	2.91	804.18	9.90	0.51	-0.95	0.78	6.1	0.23	26.3	1483	0.134247	0.117602	1.220376	0.521619	0.065960	0.471892
z8	820.43	0.67	821.41	1.00	824.08	2.43	0.82	0.48	0.53	51.0	0.34	151.9	9025	0.135722	0.086584	1.245585	0.176779	0.066591	0.111640
z12	851.34	3.08	860.05	15.02	882.58	52.25	0.23	3.57	0.82	4.8	1.62	3.0	182	0.141182	0.386791	1.332696	2.588865	0.068493	2.526201

Notes:
Colored rows indicate fractions included in the calculation of the reported sample age.
Isotopic dates calculated using $\lambda 238 = 1.55125\times10^{-10}$ and $\lambda 235 = 9.8485\times10^{-10}$ (Jaffey et al., 1971).
[a] Corrected for initial Th/U disequilibrium using radiogenic ^{208}Pb and Th/U[magma] = 2.8.
[b] Corrected for initial Pa/U disequilibrium using initial fraction activity ratio $[^{231}Pa]/[^{235}U] = 1.10000$.
[c] % discordance = 100 - (100 × ($^{206}Pb/^{238}U$ date) / ($^{207}Pb/^{206}Pb$ date))
[d] Th contents calculated from radiogenic ^{208}Pb and ^{230}Th-corrected $^{206}Pb/^{238}U$ date of the sample, assuming concordance between U-Pb Th-Pb systems.
[e] Total mass of radiogenic Pb.
[f] Total mass of common Pb.
[g] Ratio of radiogenic Pb (including ^{208}Pb) to common Pb.
[h] Measured ratio corrected for fractionation and spike contribution only.
[i] Measured ratios corrected for fractionation, tracer and blank.

Table C.5: U-Pb data for analyzed zircons from H3-60.

	Dates (Ma)								Composition					Isotopic Ratios						
fraction	$^{206}Pb/^{238}U$ [a]	± (2σ)	$^{207}Pb/^{235}U$ [b]	± (2σ)	$^{207}Pb/^{206}Pb$ [a,b]	± (2σ)	corr. coef.	% disc. [c]	Th/U [d]	Pb* (pg) [e]	Pb_c (pg) [f]	Pb*/Pb_c [g]	$^{206}Pb/^{204}Pb$ [h]	$^{206}Pb/^{238}Pb$ [a,i]	± (2σ%)	$^{207}Pb/^{235}U$ [b,i]	± (2σ%)	$^{207}Pb/^{206}Pb$ [a,b,i]	± (2σ%)
z89	808.42	1.31	811.45	5.14	819.76	18.09	0.40	1.41	0.90	5.4	0.52	10.3	576	0.133609	0.172358	1.223662	0.920442	0.066454	0.865681
z5	808.51	1.29	804.95	5.58	795.10	19.50	0.51	-1.66	1.19	6.8	0.46	14.6	763	0.133625	0.169577	1.209472	1.004012	0.065675	0.929277
z6	809.60	0.85	811.12	2.63	815.31	8.74	0.57	0.72	1.64	6.3	0.22	28.5	1338	0.133816	0.111624	1.222945	0.471028	0.066312	0.416759
z4	810.15	1.17	806.92	4.41	798.04	15.31	0.48	-1.49	1.06	5.6	0.42	13.5	723	0.133912	0.154026	1.213773	0.791331	0.065767	0.729865
z3	810.55	1.28	805.72	6.14	792.41	21.33	0.57	-2.25	0.70	5.2	0.48	10.9	639	0.133983	0.168169	1.211159	1.103179	0.065591	1.016252
z9	810.99	6.08	822.57	34.27	854.01	115.84	0.67	5.06	0.97	3.7	0.72	5.2	293	0.134062	0.797956	1.248158	6.078624	0.067555	5.576013
z24	813.41	0.75	815.79	1.91	822.30	6.02	0.63	1.12	0.18	7.8	0.24	33.0	2158	0.134487	0.098631	1.233197	0.339772	0.066535	0.286461
z30	832.33	3.35	836.95	5.23	849.22	15.68	0.58	2.02	0.53	5.2	0.33	15.8	956	0.137821	0.428971	1.280210	0.916686	0.067400	0.753347
z2	1686.09	2.05	1687.11	3.57	1688.38	7.24	0.45	0.14	0.82	12.2	0.86	14.2	789	0.298948	0.138089	4.267470	0.433978	0.103578	0.391116

Notes:
Colored rows indicate fractions included in the calculation of the reported sample age.
Isotopic dates calculated using $\lambda 238 = 1.55125\times10^{-10}$ and $\lambda 235 = 9.8485\times10^{-10}$ (Jaffey et al., 1971).
[a] Corrected for initial Th/U disequilibrium using radiogenic ^{208}Pb and Th/U[magma] = 2.8.
[b] Corrected for initial Pa/U disequilibrium using initial fraction activity ratio $[^{231}Pa]/[^{235}U] = 1.10000$.
[c] % discordance = 100 - (100 × ($^{206}Pb/^{238}U$ date) / ($^{207}Pb/^{206}Pb$ date))
[d] Th contents calculated from radiogenic ^{208}Pb and ^{230}Th-corrected $^{206}Pb/^{238}U$ date of the sample, assuming concordance between U-Pb Th-Pb systems.
[e] Total mass of radiogenic Pb.
[f] Total mass of common Pb.
[g] Ratio of radiogenic Pb (including ^{208}Pb) to common Pb.
[h] Measured ratio corrected for fractionation and spike contribution only.
[i] Measured ratios corrected for fractionation, tracer and blank.

Table C.6: U-Pb data for analyzed zircons from H3-8.

	Dates (Ma)								Composition				Isotopic Ratios						
	[a]		[b]		[a,b]			[c]	[d]	[e]	[f]	[g]	[h]	[a,i]		[b,i]		[a,b,i]	
fraction	$\frac{^{206}Pb}{^{238}U}$	± (2σ)	$\frac{^{207}Pb}{^{235}U}$	± (2σ)	$\frac{^{207}Pb}{^{206}Pb}$	± (2σ)	corr. coef.	% disc.	$\frac{Th}{U}$	Pb* (pg)	Pb_c (pg)	$\frac{Pb^*}{Pb_c}$	$\frac{^{206}Pb}{^{204}Pb}$	$\frac{^{206}Pb}{^{238}Pb}$	± (2σ%)	$\frac{^{207}Pb}{^{235}U}$	± (2σ%)	$\frac{^{207}Pb}{^{206}Pb}$	± (2σ%)
z18	804.34	0.57	803.51	1.16	801.23	3.36	0.75	-0.36	1.23	15.5	0.17	91.5	4632	0.132891	0.075104	1.206350	0.208574	0.065868	0.156792
z10	804.70	0.63	804.30	1.30	803.21	3.77	0.75	-0.16	0.92	13.6	0.20	68.5	3713	0.132954	0.083190	1.208067	0.233224	0.065930	0.176835
z22	804.92	1.05	802.18	3.41	794.60	12.04	0.39	-1.28	1.48	5.8	0.32	18.4	896	0.132993	0.138384	1.203463	0.614233	0.065660	0.573000
z23	809.85	1.38	808.78	6.36	805.83	22.85	0.35	-0.48	1.86	6.8	0.71	9.6	443	0.133861	0.181847	1.217825	1.141112	0.066012	1.090857

Notes:
Colored rows indicate fractions included in the calculation of the reported sample age.
Isotopic dates calculated using $\lambda 238 = 1.55125 \times 10^{-10}$ and $\lambda 235 = 9.8485 \times 10^{-10}$ (Jaffey et al., 1971).
[a] Corrected for initial Th/U disequilibrium using radiogenic ^{208}Pb and Th/U[magma] = 2.8.
[b] Corrected for initial Pa/U disequilibrium using initial fraction activity ratio $[^{231}Pa]/[^{235}U] = 1.10000$.
[c] % discordance = 100 - (100 × ($^{206}Pb/^{238}U$ date) / ($^{207}Pb/^{206}Pb$ date))
[d] Th contents calculated from radiogenic ^{208}Pb and ^{230}Th-corrected $^{206}Pb/^{238}U$ date of the sample, assuming concordance between U-Pb Th-Pb systems.
[e] Total mass of radiogenic Pb.
[f] Total mass of common Pb.
[g] Ratio of radiogenic Pb (including ^{208}Pb) to common Pb.
[h] Measured ratio corrected for fractionation and spike contribution only.
[i] Measured ratios corrected for fractionation, tracer and blank.

Table C.7: U-Pb data for analyzed zircons from ZJ-B.

	Dates (Ma)								Composition				Isotopic Ratios						
	[a]		[b]		[a,b]			[c]	[d]	[e]	[f]	[g]	[h]	[a,i]		[b,i]		[a,b,i]	
fraction	$\frac{^{206}Pb}{^{238}U}$	± (2σ)	$\frac{^{207}Pb}{^{235}U}$	± (2σ)	$\frac{^{207}Pb}{^{206}Pb}$	± (2σ)	corr. coef.	% disc.	$\frac{Th}{U}$	Pb* (pg)	Pb_c (pg)	$\frac{Pb^*}{Pb_c}$	$\frac{^{206}Pb}{^{204}Pb}$	$\frac{^{206}Pb}{^{238}Pb}$	± (2σ%)	$\frac{^{207}Pb}{^{235}U}$	± (2σ%)	$\frac{^{207}Pb}{^{206}Pb}$	± (2σ%)
z4	804.12	0.71	807.83	1.73	818.10	5.30	0.70	1.74	0.63	23.9	0.45	52.6	3059	0.132852	0.093875	1.215759	0.310700	0.066401	0.251380
z1	804.38	0.74	805.03	1.95	806.82	6.32	0.61	0.33	0.91	23.9	0.80	29.7	1625	0.132898	0.098018	1.209641	0.350970	0.066044	0.300053
z2	804.67	0.94	804.49	3.20	804.00	10.43	0.69	-0.05	0.64	17.7	0.91	19.4	1139	0.132949	0.123690	1.208474	0.575486	0.065955	0.496957
z5	805.02	0.73	805.55	1.17	807.04	2.84	0.86	0.28	0.73	21.8	0.19	112.8	6380	0.133011	0.096723	1.210789	0.209739	0.066051	0.131559
z6	805.23	0.80	805.83	1.66	807.48	5.05	0.67	0.32	0.46	7.1	0.19	37.0	2252	0.133048	0.105500	1.211388	0.298218	0.066064	0.239004
z3	805.24	0.85	805.36	1.88	805.70	5.85	0.65	0.09	0.61	8.1	0.23	34.9	2047	0.133050	0.112228	1.210372	0.338296	0.066008	0.277395

Notes:
Colored rows indicate fractions included in the calculation of the reported sample age.
Isotopic dates calculated using $\lambda 238 = 1.55125\times10^{-10}$ and $\lambda 235 = 9.8485\times10^{-10}$ (Jaffey et al., 1971).
[a] Corrected for initial Th/U disequilibrium using radiogenic ^{208}Pb and Th/U[magma] = 2.8.
[b] Corrected for initial Pa/U disequilibrium using initial fraction activity ratio $[^{231}Pa]/[^{235}U] = 1.10000$.
[c] % discordance = 100 - (100 × ($^{206}Pb/^{238}U$ date) / ($^{207}Pb/^{206}Pb$ date))
[d] Th contents calculated from radiogenic ^{208}Pb and ^{230}Th-corrected $^{206}Pb/^{238}U$ date of the sample, assuming concordance between U-Pb Th-Pb systems.
[e] Total mass of radiogenic Pb.
[f] Total mass of common Pb.
[g] Ratio of radiogenic Pb (including ^{208}Pb) to common Pb.
[h] Measured ratio corrected for fractionation and spike contribution only.
[i] Measured ratios corrected for fractionation, tracer and blank.

Table C.8: U-Pb data for analyzed zircons from FDM14-1.

	Dates (Ma)								Composition				Isotopic Ratios						
fraction	[a] $\frac{^{206}Pb}{^{238}U}$	± (2σ)	[b] $\frac{^{207}Pb}{^{235}U}$	± (2σ)	[a,b] $\frac{^{207}Pb}{^{206}Pb}$	± (2σ)	corr. coef.	[c] % disc.	[d] $\frac{Th}{U}$	[e] Pb* (pg)	[f] Pb_c (pg)	[g] $\frac{Pb^*}{Pb_c}$	[h] $\frac{^{206}Pb}{^{204}Pb}$	[a,i] $\frac{^{206}Pb}{^{238}Pb}$	± (2σ%)	[b,i] $\frac{^{207}Pb}{^{235}U}$	± (2σ%)	[a,b,i] $\frac{^{207}Pb}{^{206}Pb}$	± (2σ%)
z1	748.40	0.56	750.56	1.03	757.00	3.75	0.40	1.17	0.90	13.3	0.27	48.4	2643	0.123103	0.079758	1.094230	0.193393	0.064496	0.174627
z17	774.57	0.64	775.72	1.78	779.03	6.08	0.55	0.60	1.34	10.2	0.28	36.9	1837	0.127673	0.087745	1.146782	0.327690	0.065174	0.287456
z3	776.24	0.63	775.95	0.96	775.12	3.20	0.52	-0.11	0.80	19.3	0.29	67.0	3736	0.127964	0.086814	1.147263	0.177841	0.065054	0.148394
z4	776.90	0.38	777.25	0.57	778.28	1.85	0.53	0.20	1.50	35.7	0.29	122.7	5865	0.128079	0.051515	1.150022	0.104146	0.065151	0.081958
z8	778.89	0.79	778.89	1.37	778.91	4.19	0.65	0.03	1.47	21.9	0.32	69.6	3356	0.128427	0.107511	1.153495	0.251404	0.065171	0.196734
z15	778.95	1.10	780.15	1.90	783.60	5.77	0.66	0.62	1.35	12.5	0.23	55.0	2722	0.128438	0.149779	1.156169	0.348632	0.065316	0.272817
z9	779.07	0.75	779.49	1.24	780.71	3.68	0.68	0.24	1.31	17.3	0.25	70.0	3485	0.128459	0.102629	1.154767	0.227019	0.065227	0.171853
z7	779.40	0.94	779.09	2.41	778.20	8.46	0.45	-0.12	0.94	15.3	0.71	21.7	1184	0.128518	0.128658	1.153915	0.443332	0.065149	0.401136
z12	779.59	0.75	780.56	1.87	783.35	6.22	0.58	0.49	2.10	11.8	0.27	43.8	1878	0.128550	0.102596	1.157039	0.343867	0.065309	0.294178
z13	779.62	0.69	779.22	0.99	778.08	2.55	0.80	-0.17	0.96	29.3	0.21	138.1	7403	0.128556	0.094531	1.154197	0.182605	0.065145	0.116756
z5	779.67	0.50	779.65	1.36	779.59	5.02	0.30	0.02	1.08	8.9	0.24	37.2	1956	0.128565	0.068319	1.155104	0.250693	0.065192	0.236781
z16	780.83	0.92	780.36	2.68	779.02	9.09	0.58	-0.21	1.36	6.7	0.17	39.6	1960	0.128767	0.125367	1.156612	0.492453	0.065174	0.431265
z2	781.21	1.32	781.79	2.05	783.45	6.58	0.56	0.32	1.11	6.8	0.17	40.0	2089	0.128833	0.178839	1.159647	0.376544	0.065312	0.311606
z11	781.44	1.10	783.35	5.17	788.79	19.22	0.28	0.95	1.47	12.3	1.25	9.9	492	0.128874	0.149953	1.162970	0.947064	0.065478	0.915141
z14	795.30	0.68	794.22	1.31	791.16	3.99	0.66	-0.50	1.50	29.2	0.36	81.2	3889	0.131305	0.091416	1.186240	0.237625	0.065552	0.187365
z6	795.65	1.51	792.55	2.85	783.85	9.14	0.57	-1.48	1.12	31.0	1.14	27.1	1420	0.131365	0.202001	1.182660	0.517519	0.065324	0.433779

Notes:
Colored rows indicate fractions included in the calculation of the reported sample age.
Isotopic dates calculated using $\lambda 238 = 1.55125\times10^{-10}$ and $\lambda 235 = 9.8485\times10^{-10}$ (Jaffey et al., 1971).
[a] Corrected for initial Th/U disequilibrium using radiogenic ^{208}Pb and Th/U[magma] = 2.8.
[b] Corrected for initial Pa/U disequilibrium using initial fraction activity ratio $[^{231}Pa]/[^{235}U] = 1.10000$.
[c] % discordance = 100 - (100 × ($^{206}Pb/^{238}U$ date) / ($^{207}Pb/^{206}Pb$ date))
[d] Th contents calculated from radiogenic ^{208}Pb and ^{230}Th-corrected $^{206}Pb/^{238}U$ date of the sample, assuming concordance between U-Pb Th-Pb systems.
[e] Total mass of radiogenic Pb.
[f] Total mass of common Pb.
[g] Ratio of radiogenic Pb (including ^{208}Pb) to common Pb.
[h] Measured ratio corrected for fractionation and spike contribution only.
[i] Measured ratios corrected for fractionation, tracer and blank.

Table C.9: Euler rotation parameters used in the Bitter Springs Stage true polar wander model (Fig. 11 in the main text).

plate	**age (Ma)**	**latitude (°N)**	**longitude (°E)**	**angle (°)**	**relative plate**
spin axis	755	-7.6	-178.33	-16.15	mantle
spin axis	794	-7.6	-178.33	-16.15	mantle
spin axis	796	-0.57	133.44	-36.55	mantle
spin axis	809	-0.57	133.44	-36.55	mantle
spin axis	811	90.0	0.0	0.0	mantle
spin axis	821	90.0	0.0	0.0	mantle
Laurentia	755	43.4821	151.0109	-167.5558	spin axis
Laurentia	790	57.7447	147.6911	-175.862	spin axis
Laurentia	821	57.7447	147.6911	-175.862	spin axis
Greenland	755	67.5	-118.5	-13.8	Laurentia
Greenland	821	67.5	-118.5	-13.8	Laurentia
Amazonia	755	11.97	-47.01	-110.66	Laurentia
Amazonia	821	11.97	-47.01	-110.66	Laurentia
Parana Panema	755	0.67	103.22	-30.82	Amazonia
Parana Panema	821	0.67	103.22	-30.82	Amazonia
Rio de la Plata	755	0.67	103.22	-30.82	Amazonia
Rio de la Plata	821	0.67	103.22	-30.82	Amazonia
Baltica	755	75.8	-95.8	-59.2	Laurentia
Baltica	821	75.8	-95.8	-59.2	Laurentia
Scotland	755	78.64	161.9	-32.0	Laurentia
Scotland	821	78.64	161.9	-32.0	Laurentia
Svalbard	755	-81.0	125.0	68.0	Laurentia
Svalbard	821	-81.0	125.0	68.0	Laurentia
Siberia	755	77.0	98.0	137.0	Laurentia
Siberia	821	77.0	98.0	137.0	Laurentia
India	755	65.3333	103.3222	-29.8536	spin axis
India	790	24.9082	119.6524	-45.5154	spin axis
India	805	24.9082	119.6524	-45.5154	spin axis
India	821	21.5338	130.446	-67.842	spin axis
North China	755	52.9462	27.2366	61.9218	Laurentia
North China	821	52.9462	27.2366	61.9218	Laurentia
South China	755	6.7224	77.6921	67.9571	India
South China	821	6.7224	77.6921	67.9571	India
Kalahari	755	15.102	-25.2783	-157.5464	Laurentia
Kalahari	821	15.102	-25.2783	-157.5464	Laurentia
South Australia	755	-30.2638	-19.1192	-131.7445	Laurentia
South Australia	821	-30.2638	-19.1192	-131.7445	Laurentia
North Australia	755	-20.0	135.0	-40.0	South Australia
North Australia	821	-20.0	135.0	-40.0	South Australia
East Antarctica	755	-3.91	37.9	30.86	South Australia
East Antarctica	821	-3.91	37.9	30.86	South Australia
Rayner	755	1.8434	-165.1696	-91.8395	India
Rayner	821	1.8434	-165.1696	-91.8395	India

Notes:
(1) Model is defined between 821 Ma and 755 Ma.